

DESIGN FOR MANUFACTURABILITY AND YIELD
FOR NANO-SCALE CMOS

Series on Integrated Circuits and Systems

Series Editor: Anantha Chandrakasan
Massachusetts Institute of Technology
Cambridge, Massachusetts

Low Power Methodology Manual: For System-on-Chip Design
Michael Keating, David Flynn, Rob Aitken, Alan Gibbons, and Kaijian Shi
ISBN 978-0-387-71818-7

Modern Circuit Placement: Best Practices and Results
Gi-Joon Nam and Jason Cong
ISBN 978-0-387-36837-5

CMOS Biotechnology
Hakho Lee, Donhee Ham and Robert M. Westervelt
ISBN 978-0-387-36836-8

SAT-Based Scalable Formal Verification Solutions
Malay Ganai and Aarti Gupta
ISBN 978-0-387-69166-4, 2007

Ultra-Low Voltage Nano-Scale Memories
Kiyoo Itoh, Masashi Horiguchi and Hitoshi Tanaka
ISBN 978-0-387-33398-4, 2007

Routing Congestion in VLSI Circuits: Estimation and Optimization
Prashant Saxena, Rupesh S. Shelar, Sachin Sapatnekar
ISBN 978-0-387-30037-5, 2007

Ultra-Low Power Wireless Technologies for Sensor Networks
Brian Otis and Jan Rabaey
ISBN 978-0-387-30930-9, 2007

Sub-Threshold Design for Ultra Low-Power Systems
Alice Wang, Benton H. Calhoun and Anantha Chandrakasan
ISBN 978-0-387-33515-5, 2006

High Performance Energy Efficient Microprocessor Design
Vojin Oklobdzija and Ram Krishnamurthy (Eds.)
ISBN 978-0-387-28594-8, 2006

Abstraction Refinement for Large Scale Model Checking
Chao Wang, Gary D. Hachtel, and Fabio Somenzi
ISBN 978-0-387-28594-2, 2006

A Practical Introduction to PSL
Cindy Eisner and Dana Fisman
ISBN 978-0-387-35313-5, 2006

Thermal and Power Management of Integrated Systems
Arman Vassighi and Manoj Sachdev
ISBN 978-0-387-25762-4, 2006

Leakage in Nanometer CMOS Technologies
Siva G. Narendra and Anantha Chandrakasan
ISBN 978-0-387-25737-2, 2005

Statistical Analysis and Optimization for VLSI: Timing and Power
Ashish Srivastava, Dennis Sylvester, and David Blaauw
ISBN 978-0-387-26049-9, 2005

DESIGN FOR MANUFACTURABILITY AND YIELD FOR NANO-SCALE CMOS

by

CHARLES C. CHIANG

Synopsys Inc.

Mountain View, CA, USA

and

JAMIL KAWA

Synopsys Inc.

Mountain View, CA, USA



Springer

A C.I.P. Catalogue record for this book is available from the Library of Congress.

ISBN 978-1-4020-5187-6 (HB)

ISBN 978-1-4020-5188-3 (e-book)

Published by Springer,
P.O. Box 17, 3300 AA Dordrecht, The Netherlands.

www.springer.com

Printed on acid-free paper

The contributing authors of this book have used figures and content published in IEEE conferences and journals (© IEEE). Those figures and content from IEEE publications that are included in this book are printed with permission from the IEEE

All Rights Reserved

© 2007 Springer

No part of this work may be reproduced, stored in a retrieval system, or transmitted in any form or by any means, electronic, mechanical, photocopying, microfilming, recording or otherwise, without written permission from the Publisher, with the exception of any material supplied specifically for the purpose of being entered and executed on a computer system, for exclusive use by the purchaser of the work.

*To my wife Susan
(Show-Hsing) and my
daughters Wei Diana and
Ann - Charles*

*To my wife Zeina and my
children Nura, Tamara,
and Rami - Jamil*

Contents

List of Figures	xiii
List of Tables	xix
Preface	xxi
Acknowledgments	xxvii
1. INTRODUCTION	1
1.1 What is DFM/DFY	1
1.2 DFM/DFY Critical for IC Manufacturing	2
1.2.1 New Materials	3
1.2.2 Sub-wavelength Lithography	6
1.2.3 New Devices	9
1.2.4 Proliferation of Processes	12
1.2.5 Intra-die Variability	14
1.2.6 Error Free Masks Too Costly	15
1.2.7 Cost of a Silicon Spin	15
1.3 DFM Categories and Classifications	16
1.3.1 First Time Failures	16
1.3.2 Time Related Failures	17
1.4 How Do Various DFM Solutions Tie up with Specific Design Flows	17
1.5 DFM and DFY: Fully Intertwined	19
2. RANDOM DEFECTS	21
2.1 Types of Defects	21
2.2 Concept of Critical Area	22

2.3	Basic Models of Yield for Random Defects	23
2.4	Critical Area Analysis (CAA)	24
2.4.1	Classical Methods of CA Extraction	24
2.4.2	Approximations	25
2.4.3	Comparison of Approximate and Traditional CA	26
2.5	Mathematical Formulation of Approximation Method	26
2.5.1	Short Critical Area - Mathematical Formulation	27
2.5.2	Open Critical Area - Mathematical Formulation	31
2.6	Improving Critical Area	34
2.6.1	Cell Library Yield Grading	34
2.6.2	Average CA Yield Improvement	36
2.6.3	Weighted Average CA Yield Improvement	41
2.6.4	Key Benefits of the Proposed Algorithm	47
2.7	Experimental Results	48
2.7.1	Validation of Fast Critical Area Analysis Evaluation	48
2.7.2	Comparison of Critical Area Reductions	48
2.7.3	Discussion	50
2.8	Conclusions	51
3.	SYSTEMATIC YIELD - LITHOGRAPHY	53
3.1	Introduction	53
3.2	Optics Fundamentals	53
3.3	Basic Design Flow	55
3.4	Lithography and Process Issues	57
3.4.1	Masks Writing	57
3.4.2	Optical System Interactions	57
3.4.3	Resist	57
3.4.4	Etch	58
3.5	Resolution Enhancement Technique (RET)	58
3.5.1	Optical Proximity Correction (OPC)	59
3.5.2	Sub Resolution Assist Feature (SRAF)	63
3.5.3	Phase Shift Masks (PSM)	65
3.5.4	Off Axis Illumination (OAI)	71
3.6	Other Optical Techniques	73
3.6.1	Immersion Technology	73
3.6.2	Double Dipole Lithography (DDL)	73

3.6.3	Chromeless Phase Lithography (CPL)	74
3.7	Lithography Aware Routing	74
3.8	RET and Lithography Verification	75
3.8.1	Lithography Rule Check (LRC)	76
3.8.2	Pattern Simulation	77
3.9	Integrated Flow	77
3.9.1	Mask Preparation and Repair	77
3.9.2	Design Intent	79
3.9.3	Silicon vs. Layout	80
3.10	Yield Considerations	81
3.10.1	Cell Design Considerations	81
3.10.2	Yield Optimized Routing	82
3.11	Practical Application	83
3.11.1	Framing the problem	83
3.11.2	Potential Solutions	84
3.11.3	Proposed Solution	84
3.11.4	Framing the Solution - Definitions and Presentation	85
3.11.5	Litho-Hotspot Detection System	88
3.11.6	Summary & Results	95
3.12	DFM & DFY Centric Summary	96
3.13	Lithography Specific Summary	97
4.	SYSTEMATIC YIELD - CHEMICAL MECHANICAL POLISHING (CMP)	99
4.1	Introduction	99
4.2	The Dual Damascene Process	100
4.2.1	Via-first Dual-Damascene Process	101
4.2.2	The Dielectric	101
4.2.3	The Metal Barrier	101
4.3	Electroplating	102
4.3.1	Procedure Description	102
4.3.2	Electroplating Model	105
4.4	A Full Chip Simulation Algorithm	112
4.4.1	Case Selection	113
4.4.2	Tile Size and Interaction Length	115
4.4.3	Model Verification	116

4.4.4	Key Advantages of ECP Topography Model	121
4.5	CMP	121
4.5.1	CMP Process Description	122
4.6	Dummy Filling	124
4.6.1	Rule Based	125
4.6.2	Model Based	125
4.7	Application: ILD CMP Model Based Dummy Filling	127
4.7.1	Introduction	127
4.7.2	The 2-D Low-pass-filter CMP Model	128
4.7.3	The Dummy Filling Problem	128
4.7.4	The Linear Programming Method	129
4.7.5	The Min-variance Interactive Method	129
4.7.6	Improving the Detection Capability	132
4.7.7	Simulation Results	134
4.8	Application: Cu CMP Model Based Dummy Filling	139
4.8.1	Why Model Based Metal Filling?	139
4.8.2	Predictors of the Final (Post-CMP) Thickness Range	140
4.8.3	ECP Thickness Versus Final Thickness	141
4.8.4	Effective Density Versus Final Thickness	141
4.8.5	Details of the Proposed Metal Filling Algorithm	142
4.8.6	Experimental Results	148
4.8.7	Discussion of Results	148
5.	VARIABILITY & PARAMETRIC YIELD	151
5.1	Introduction to Variability and Parametric Yield	151
5.2	Nature of Variability	151
5.3	Source of Variability	152
5.3.1	Wafer Level Variability	153
5.3.2	Materials Based Variability	155
5.3.3	Atomistic Variability	157
5.3.4	Lithography Based Variability	157
5.3.5	Local Variability	159
5.3.6	Environmental Variability & Aging	159
5.3.7	Device and Interconnect Parameters Variability	162
5.4	Yield Loss Sources & Mechanisms	164
5.5	Parametric Yield	166

5.6	Parametric Yield Test Structures	167
5.7	Variability & Parametric Yield Summary & Conclusions	168
6.	DESIGN FOR YIELD	169
6.1	Introduction	169
6.2	Static Timing and Power Analysis	170
6.2.1	Overview	170
6.2.2	Critical Path Method (CPM)	171
6.3	Design in the Presence of Variability	172
6.4	Statistical Timing Analysis	173
6.4.1	Overview	173
6.4.2	SSTA: Issues, Concerns, and Approaches	175
6.4.3	Parametric and Delay Modeling PDFs	177
6.4.4	Correlation Issues	178
6.5	A Plurality of SSTA Methodologies	180
6.5.1	Early SSTA Approach: Using Continuous PDFs	180
6.5.2	Four Block-based Approaches	181
6.6	Bounding Approaches	185
6.7	Statistical Design Optimization	186
6.8	On Chip Optimization Techniques	188
6.8.1	Adaptive Body-biasing	190
6.8.2	Adaptive Voltage Scaling	191
6.8.3	A Combination	191
6.9	Summary: Design for Yield	192
6.9.1	Summary for SSTA	192
6.9.2	Summary for Statistical Design Optimization	192
7.	YIELD PREDICTION	195
7.1	Introduction	195
7.2	Yield Loss Sources & Mechanisms	196
7.3	Yield Modeling	196
7.3.1	Early Work in Yield Modeling	196
7.4	Yield Enhancement Mechanisms	199
7.4.1	IP Development	199
7.4.2	Synthesis	199
7.4.3	Placement and Routing	199

7.5	EDA Application I	200
7.5.1	Preliminary Definitions & the cdf Approach	200
7.5.2	Our Proposed Solution	201
7.5.3	A Brief Description of the Key Ideas	203
7.5.4	Example and Results	208
7.6	EDA Application II	211
7.6.1	Background	211
7.6.2	Variation Decomposition	212
7.6.3	Variations Handled by Hotspot Model	214
7.6.4	Application Example: CMP Yield	214
7.7	CMP Yield Prediction Model	215
7.7.1	Yield Prediction Algorithm	216
7.7.2	Simulation Examples	224
7.7.3	Recap and some conclusions	225
7.7.4	Summary and Conclusions	226
8.	CONCLUSIONS	227
8.1	The Case for a DFM/DFY Driven Design	227
8.2	Design Intent Manufacturing (Lithography) Centric DFM	228
8.3	Yield Centric DFM	229
8.4	DFM/DFY EDA Design Tools	229
8.4.1	Implementation	231
8.4.2	Physical Verification	235
8.4.3	Mask Synthesis	236
8.4.4	Mask Inspection	237
8.4.5	TCAD	239
8.4.6	Process Modeling and Simulation	239
8.5	Design Variability	240
8.6	Closing Remarks	240
	References	243
	Index	253

List of Figures

1.1	Cu Cross Section Showing Potential Problems	4
1.2	Basic Gate Illustration	4
1.3	$NA = I \sin \alpha$	8
1.4	Basic Example of OPC at 180nm	9
1.5	Example of Strong (180) PSM	9
1.6	Double-gate FET	10
1.7	TCAD Simulated FinFET	11
1.8	Layout of Multi-segment FinFET	11
1.9	Simulated 5nm MOSFET with Silicon Crystal Superimposed Next to A Bulk-CMOS Equivalent	13
1.10	Revenue as a Function of Design Cycle	16
1.11	Typical ASIC Design Flow	18
2.1	Short CA Between Two Wires Caused by Particles with Size x	22
2.2	Open CA on a Wire Caused by Particles with Size x	23
2.3	Intra-layers Defect Particle Resulting in an Open or Short	23
2.4	Typical Short Critical Area	28
2.5	Short Critical Area at Large Defect Size	28
2.6	Open Critical Area on Wire i	32
2.7	Example of Improving Poly Short CA and M1 Open CA	35
2.8	Illustration of Wire Pushing	40
2.9	Illustration of Wire-widening	47
2.10	Open Critical Area Correlation	48
2.11	Short Critical Area Correlation	49
3.1	Basic Optical Lithography IC Manufacturing System	54
3.2	Basic Design flow	56

3.3	Impact of OPC on Printability at 90 nm (Zero Defocus)	59
3.4	Silicon Wafer Image with/without OPC and with/without Defocus	60
3.5	Model Based OPC Flow	62
3.6	Layout	63
3.7	A Case Where Rule Based OPC Is Good Enough	63
3.8	OPC'd Geometry with Scatter Bars (SRAFs)	64
3.9	Printability of Isolated Feature, No Scatter Bar	64
3.10	Printability of Isolated Feature, with Scatter Bar	65
3.11	A Dark Field (Positive) Binary Mask	65
3.12	Basic Illustration of the Light-mask-resist Interaction	66
3.13	Illustration of Resolution Problem with Regular Mask	67
3.14	Illustration of the Resolution Enhancement Due to 180° Phase Inversion	68
3.15	Illustration of a Layout with Phase Assignment Conflict	68
3.16	Three Implementation of a Layout, Two have Phase Conflicts	69
3.17	Resolved Feature with PSM	69
3.18	Illustration of Concept of Attenuated PSM	70
3.19	Illustration of Off-axis Illumination	71
3.20	Eight Different Filtering Pupil Alternatives	72
3.21	Illustration the Different Between Conventional and Annular Illumination	72
3.22	Problem Place and Route Patterns	75
3.23	ICC Place and Route Tool Implementation of Via Doubling	75
3.24	Three Known Problem Patterns from a 65nm LRC Library	76
3.25	Design Flow Including OPC and LRC	78
3.26	Diffusion Mask Defects, Poly (Red) Superimposed for Illustration	79
3.27	Illustration of Steps Needed to Meet Design Intent	80
3.28	Silicon vs Layout Simulation Flow	81
3.29	Old Style “Compact” Layout vs Litho-friendly Cell Layout	82
3.30	Similar Layouts That Are Litho Hotspots	84
3.31	Range Pattern Staircase	85
3.32	Representation of Layout as Layout Matrix	86
3.33	Cutting-slice of Range Pattern staircase	87
3.34	Range Pattern “rocket”	88

3.35	Horizontal and Vertical Cutting-slices of Range Pattern Rocket	89
3.36	Flowchart of the Hotspot Detection System	90
3.37	Cutting-slice of Range Pattern Mountain	93
3.38	Layout Block Encoding	93
3.39	Drill and Fly	95
4.1	Simplified Cross Section of a Single and a Dual Damascene Process	100
4.2	Lithography Steps of a Via-first Dual Damascene Process	101
4.3	An Electroplating System [1]	103
4.4	Additive Absorption Behavior During ECP [2]	104
4.5	A Typical Topography After ECP Process	106
4.6	An Arbitrary Layout in Window with Size $D \times D$	107
4.7	Three Kinds of Post-ECP Topographies of a Wire	108
4.8	The Evolution of Topography in Case (1) Conformal-fill	110
4.9	The Evolution of Topography in Case (2) Super-fill	112
4.10	Framework of The Full-chip ECP Topography Simulator	114
4.11	Experimental Post-ECP Cu Topography from [1]	117
4.12	Experimental vs Simulation Results for (a) H and (b) S	118
4.13	Simulation of Surface Height and Absolute Step Height Under Different Interaction Lengths	120
4.14	Polish Table: A Picture of One Sector of A Polishing Table	122
4.15	A Break-down of the Details of A Polishing Station	123
4.16	Schema: A Schematic Representation of A Polishing Station	123
4.17	Surface Topography Profiles for Pitch Structures	125
4.18	Metal fill Illustrates the Rule Based (Traditional) vs Algorithmic (Alternative) Approach	126
4.19	Solutions of a Simple 1-D Problem	132
4.20	A Specific Case	133
4.21	The Discretization Error of LP	136
4.22	The CPU Time Comparison	137
4.23	The Effective Density of the LP Method	137
4.24	The Effective Density of the New Min-variance Iterative Method	138
4.25	Topography Results using CMP Simulator	140
4.26	Impact of ECP Thickness Range on Final Thickness Range	142
5.1	Illustrative Cross Section of a CMOS IC with Metallization	154

5.2	Planar Cross Section of a CMOS Device Showing Main Physical Parameters	154
5.3	Illustration of Interconnect Parameters for 2 Layers of Metal	155
5.4	Example of Metal LER	155
5.5	LER for Device Gate	156
5.6	Doping Fluctuations Are Pronounced at 45nm and Beyond	157
5.7	A Scan and Step Lithography System Representation	158
5.8	Die to Die Variability	159
5.9	I_{ds} within Die Variability	160
5.10	V_{th} within Die Variability	160
5.11	Correlation Length	161
5.12	A Temperature Distribution Map of a Typical Chip with a Core and Cache	161
5.13	Junction Temperature Distribution of a CMOS Device	162
5.14	Interconnect Cross Section	163
5.15	Defect Categories Distribution Trend as a Function of Technology Node	164
5.16	A Comprehensive Chart of the Sources of Yield Loss	165
5.17	A Well Designed Pattern for CMP Evaluation	168
6.1	Illustration of Gate Timing and Interconnect Timing	171
6.2	Illustration of CPM Method for Path In->out	172
6.3	Confidence Levels for 1σ , 2σ , and 3σ for a Normal Distribution	174
6.4	Probability Density Function for a Normal Distribution Function of a Variable x with $\mu = 0$ for Various Values of σ	174
6.5	Gate and Interconnect Delays Are Represented as PDFs in SSTA	177
6.6	Grid Model of Spatial Correlation	179
6.7	The Quad-tree Model for Spatially Correlated Variations	180
6.8	Illustration of the Computation of (a) Upper and (b) Lower Bounds for the CDF $X(t)$ for Paths a-b-d and a-c-e [3, 4]	186
6.9	Illustration of Upper and Lower Bound Functions	186
6.10	Statistical Optimization Results for Static Power	187
6.11	Statistical Design Optimization Always Superior to Worst Case	188
6.12	Block Diagram of Body-bias Implementation in [5]	189
6.13	Basic Illustration of Body Bias for P and N Devices	190

6.14	Block Diagram of a Combination of Adaptive Body Biasing and Adaptive Voltage Scaling	191
6.15	Optimization of Speed and Power Using Both Adaptive Voltage Scaling and Body Bias [5]	192
7.1	Defect Categories Distribution Trend as a Function of Technology Node	196
7.2	A Simplified Design Flow for Illustration Purposes	198
7.3	The Yield Prediction Flow in cdf Approach	201
7.4	Derivation of the Transformation “T” for Hot-spot Yield Scores	203
7.5	Distribution of Yield Measuring Variable and Yield Score Function	206
7.6	Approximation of $f()$ and $f^{-1}()$	207
7.7	The Complete Flow for Deriving the Transformation “T”	208
7.8	Rayleigh and Gaussian Distributions with Same Mean and Variance	209
7.9	Typical Post-CMP Topography [6]	215
7.10	Yield Prediction for The Case of Perfect Across-chip Correlation	217
7.11	Spatial Correlations of Random Variation as Function of Distances	218
7.12	Perfect Correlation Circles Surrounding Maximum Thickness Values	220
7.13	Flow Chart for Y_{max} Calculation	221
8.1	A Top-down View of Manufacturability and Yield Derailing Factors	228
8.2	OPC Alternatives for a Digitized Geometry	229
8.3	An EDA DFM/DFY Centric Design Flow	230
8.4	An Example of a DFM Optimized Cell Form	231
8.5	Table of Alternative Implementations of a Cell with Arcs	232
8.6	OPC Applicability Checking During Routing	233
8.7	Wire Spreading	233
8.8	Smart Metal Fill to Minimize Local ILD and Metal Thickness Variation	234
8.9	Illustration of Via Doubling	234
8.10	An Example of Prohibited Patterns	235
8.11	Data Fracturing	237
8.12	Mask Inspection Flow	238

8.13	Statistical vs Deterministic Design Delay Slack	240
8.14	Cross-bar Molecular Memory	241
8.15	Carbon Nano-tube Transistor [pqf]	241
8.16	Nano-fluidic Valve [zyx]	242

List of Tables

1.1	Cost of Defect Repair at Every Stage of Production	2
1.2	High K Oxide Materials and Their Dielectric Constants	5
1.3	Indicates the k_1 , NA Combinations vs Resolution	7
1.4	Light Wavelength Versus the Technology Node	7
1.5	Intra-die Variability Increase with Technology Node	15
1.6	Mask Preparation File Data Size - ITRS 2004	15
2.1	CA Results and Run Time in Shape Expansion Method and Our Method	26
2.2	Critical Area Optimization for Shorts	40
2.3	Short, Open, and Total Weighted Critical Area Reductions Comparison, with $w = 0.1$	49
2.4	Short, Open, and Total Weighted Critical Area Reductions Comparison, with $w = 10$	50
3.1	Litho-Hotspot Detection Results	96
4.1	Peak-peak Value and the Standard Deviation of Effective Density	132
4.2	Peak-peak Value and the Standard Deviation of Effective Density	138
4.3	Comparison of Different Metal Filling Results	149
6.1	Absolute and Relative Variability of Vt for Successive Technology Nodes	173
7.1	CD Variability Budget as a Function of Technology Node	196
7.2	A Possible CMP Hot Spot Specifications for 65nm	202
7.3	CMP Hot Spot Scoring (Based on CMP Hotspot Specifications)	204

7.4	Litho Hot Spot and Score Specifications (Derived from a Foundry Specs)	205
7.5	Simulation Results for the Case When True Distribution is Rayleigh ($\sigma_1 = 2, \sigma_2 = 3$)	210
7.6	Simulation Results for the Case When True Distribution is Laplace ($\sigma_1=2, \sigma_2=3; \mu_1=3, \mu_2=3.5$)	210
7.7	Yield Prediction under Different Radii of 'Perfect Correlation Circles (PCC)'	224
7.8	Yield Prediction for a Quicker Decrease of the Spatial Correlation	225

Preface

For any given industry striving to improve product quality, reliability, and yield on an ongoing basis is a fundamental task for the simple reason that higher product quality and reliability translates to higher sales, and higher yield translates to higher profitability. The electronic industry is no exception to that rule. In fact one of the driving considerations that transitioned the electronics industry from the era of discrete components to the era of the integrated circuit (IC) was the goal of achieving higher quality and reliability through less components to handle and assemble, and higher yields through smaller miniature devices. In this book we will focus on the technical aspects of manufacturability and yield as the industry moves well into the nano-era of integrated circuits.

Since the inception of the integrated circuits (IC) industry the manufacturing process has been based on optical lithography. The process of yield improvement focused on creating a cleaner processing environment (clean rooms) that reduced the number of particles in the manufacturing area which resulted in a lower number of random defects and thus higher yields, and on shrinking the design features that resulted in smaller die areas and thus more dies per wafer. Those two factors were on a collision course as smaller features meant that a smaller random particle could cause circuit defects that it did not cause when the geometries were more relaxed. Thus the requirement for cleaner fabrication facilities (clean rooms) and tighter process controls went hand in hand with shrinking geometric features.

Needless to say, along the IC progress path following Moore's law, solutions to challenges of high significance were required from all contributors to the manufacturing steps - from more accurate steppers, to lenses with larger numerical apertures, to illumination sources of light with shorter wavelengths, to mask writers (E-Beams) capable of parallel processing with tighter spot size and reasonable write time and throughput, to reticles with fewer defects, to new metal compounds capable of higher current densities, to more advanced etching materials and procedures, and to highly advanced metrology. And,

with every significant change there was a learning curve that resulted in a step back in yield until the particularities of each new step were fully understood and mastered, then yield was back on track and we moved forward. One such significant change was the use of Copper (Cu) instead of Aluminum (Al) or Al compounds; low K dielectrics was another such challenge, stacked vias with high aspect ratios, and the need for super planarization was also another significant challenge. Those four examples were by no means exclusive but were indeed major steps on the road to the nanometer era in IC manufacturing.

But, the IC optical manufacturing process found itself bumping its head against limitations rooted in physics that altered the learning curve process outlined in the last paragraph and called for a dramatically different approach not just to ensure yield improvement as we continue to shrink features, but to ensure that the manufacturability of smaller ICs is feasible in the first place. The IC industry was hitting barriers that threatened an end to the journey of optical lithography with an unpleasant outcome: zero yield; i.e. end of scalability. Moving from optical lithography to other means (atomic, molecular, self assembling structures, etc) meant a major discontinuity and a major disruption in the manufacturing and engineering techniques developed and mastered over the last fifty years at a staggering investment cost. Needless to say it is worth mentioning that re-training the design community in an alternative discipline of design cannot happen overnight either and will be very disruptive in nature should alternatives to the current manufacturing techniques emerge in short order. Simply put, the momentum of the optical lithography based IC industry is too strong to alter in such short order.

Optically, light source with a wavelength of 193 nano-meters (nm) was the end of the path in wavelength reduction with a big gap extending all the way to the 13nm extreme ultra-violet (EUV) light source. Efforts to develop 157nm and beyond came to a halt due to delays and to insurmountable technical challenges and we were faced with having to use 193nm light to print sub-90 nm features- features that are smaller than a half wave-length of the light source used. This called for a whole set of “engineering tricks” and techniques to extend the life of the 193nm based lithography. Also, on the materials front, “bulk” modeling of the behavior of dopant materials has quickly reached the end of its validity and quantum mechanical behavior of material needed to be taken into account. Unevenness in dopant distribution became very critical. Deterministic behavior had to be abandoned and replaced with statistical behavior and bulk properties had to be dealt with quantum mechanically. Single atomic layer gate oxides raised the need for high K gate dielectric with the challenge of making sure the electric field in the channel is not weakened. Fully salicided poly and metal gate options are considered to deal with this problem with a handful of new materials competing as candidates for the high k dielectric. The process of designing low K dielectric materials for intra-metal oxides

to reduce capacitance (improve speed) encountered big challenges in how to reduce K without increasing leakage. Not to be ignored is the complexity of the metallurgy and of other aspects of the manufacturing process. Via stacking and tighter metal pitches made planarization more critical than ever before; smart dummy fills that improved planarization without hurting the timing of a circuit became critical.

Thus designing for yield has changed to become designing for manufacturability and yield at the same time. The two go hand in hand - you cannot yield what you cannot manufacture. Also, faults impacting yield, which were dominated by particles (random defects) are not anymore the major mode of yield loss in ICs. Systematic variations impacting leakage, timing, and other manufacturing aspects in manufacturing are increasingly becoming the dominant factor; more so with every new technology node. Furthermore, the random component of variability which was strictly global in nature (die-die, wafer-wafer, lot-lot) has a new intra-die component of considerable significance.

In this book we start with a detailed definition of design for yield (DFY) and design for manufacturability (DFM) followed by a brief historical background of DFM/DFY where random (particle) defects were dominant and quickly move to the current challenges in manufacturability and yield and the solutions being devised to deal with those challenges for every step of a typical design flow. However, we do not present them in the order of steps in the typical design flow but in terms of categories that have logical and relational links.

In Chapter 1, after defining DFM/DFY and covering a brief historical perspective we go over why DFM/DFY has become so critical, we go through the classifications and categories of DFM and discuss what solutions are proposed for each problem and at what stage of the design flow, and through what tool(s) is such a problem addressed. We also start creating the logical link between DFM and DFY. Chapter 1 is a generic overview.

In Chapter 2 we cover a major random component of yield: critical area (CA), in depth. We discuss various algorithms used in critical area analysis (CAA) for extracting critical area of a design and evaluate them in terms of accuracy versus runtime. We cover techniques used in library design and in place and route that will improve the CA component of yield.

In Chapter 3 we move to define and explain the main systematic components of yield. We cover lithography in depth, explain the major problems associated with optical lithography, their root causes, and what remedies can be applied to solve them. We go over many examples of resolution enhancement techniques (RET) as it applies to the characteristics of light that we can manipulate in an effort to reduce the " k_1 " factor of the lithography system namely direction, amplitude, and phase. We discuss and analyze lithography aspects such as forbidden pitches, non-manufacturable patterns, etc. We discuss at length mask alternative styles, what problem is each alternative used to solve, their pros and

cons both technical and economical. We discuss mask preparation, generation, inspection, and repair. Lenses, filters, and illumination technologies are examined. Then we go over a practical design flow and examine what can be done at the routing stage after the major RET techniques are applied to the layout at the cell library design stage. We discuss lithography aware routing techniques. We also address various aspects of lithography rules checking and how it forms the link between classical design rule check (DRC) and manufacturability.

In Chapter 4 we cover the important planarization procedure of chemical mechanical polishing (CMP). We describe the process, identify the critical parameters that define it and the impact of each parameter on the overall planarization procedure. We cover Cu metallurgy, Cu deposition and etching and the following CMP steps, and address problems such as dishing and how they are related to the CMP parameters and to the neighboring metal patterns. We address the effects of the CMP variables and of the metal patterns on thickness variation in intra-metal insulating layers (ILD) and how that variation in turn affects manufacturability and yield. We cover the effect of metal patterns and local metal densities on ILD variation and get to the concept of metal “dummy fills”. We discuss and analyze rule based versus model based “dummy fills”. Finally, we address the ILD thickness variation on timing. Impacting parameters including resistance (R) and capacitance (C); and discuss how model based “smart fills” minimizes R and C variability, simultaneously.

In Chapter 5 we include a comprehensive coverage of variability and of variability’s impact on parametric yield. We discuss the growing significance of parametric yield in the overall yield picture. We discuss intra-die variability vs. inter-die variability. We cover the critical process parameters that have the most significant impact on parametric yield, discuss the sources of variability for those parameters, and the impact of the variability in each parameter on parametric yield. We touch on techniques for reducing parametric variability towards improving parametric yield. Coverage of parametric yield in this chapter is restricted mainly to the variability components of major parameters.

Chapter 6 integrates the knowledge acquired in the previous chapters towards the concept of design for yield. It stresses techniques to avoid manufacturability bottlenecks and addresses analysis tools and methodologies for both manufacturability and yield optimization. It introduces and covers statistical timing analysis and statistical design as more productive and mature alternatives to the classical case-file design methodologies.

Chapter 7 sums up the contribution of the components of yield- random and systematic, towards the goals of yield modeling and yield prediction. We introduce several comprehensive yield models that a designer can use towards evaluating the overall yield of a design as well as towards enabling the designer to do a sensitivity analysis in order to evaluate the impact of key parameters under certain design topologies on yield. Such sensitivity analysis can go a

long way towards enhancing yield by avoiding patterns and topologies that have adverse impact on yield.

Finally, Chapter 8 is a review and summation of all the concepts of DFM & DFY introduced in this book. It enables the DFM/DFY student or practicing engineer to regroup in few pages the most important concepts one should keep in mind when designing for manufacturability and yield.

CHARLES C. CHIANG AND JAMIL KAWA

Acknowledgments

Dr. Qing Su, Dr. Subarna Sinha, Dr. Jianfeng Luo, and Dr. Xin Wang of Synopsys, Inc., Mr. Yi Wang and Prof. Xuan Zeng from Fudan University, Shanghai, for their contribution to the materials presented in this book and Dr. Subarna Sinha, Dr. Qing Su, and Dr. Min-Chun Tsai of Synopsys, Inc, Huang-Yu Chen, Tai-Chen Chen, Szu-Jui Chou, Guang-Wan Liao, Chung-Wei Lin, and Professor Yao-Wen Chang of Taiwan University, Taipei, for their careful review of the manuscript and their valuable comments

Chapter 1

INTRODUCTION

1.1 What is DFM/DFY? Historical Prospective

Design for manufacturability (DFM) in its broad definition stands for the methodology of ensuring that a product can be manufactured repeatedly, consistently, reliably, and cost effectively by taking all the measures needed for that goal starting at the concept stage of a design and implementing these measures throughout the design, manufacturing, and assembly processes. It is a solid awareness that a product's quality and yield start at the design stage and are not simply a manufacturing responsibility. There are two motivations behind caring for DFM. Both motivations are rooted in maximizing the profit of any given project; the first is minimizing the cost of the final product of the project, and the second is minimizing the potential for loss associated with any defective parts that need to be replaced. In fact a study [7] estimates the cost of fixing a defective part at anywhere from 10 times to 10,000 times the initial cost of the part depending on the stage of the product cycle where the part is recalled (Table 1.1). Arguably, the numbers in Table 1.1 vary widely from product to product, and from industry to industry, but the trend in the scale of replacement cost is clear. You simply want to discover and eliminate any potential problem as close to the beginning of the product cycle as possible, preferably right at the design simulation and analysis stage.

The concept of DFM has been around for quite some time and has until recently stood by itself separate from "yield models" which were dedicated mainly to calculating yield as a function of defect densities. The concept of design for yield (DFY) is on the other hand a relatively new concept that stemmed from the fact that in the nano era of CMOS it is not sufficient to obey design rules, e.g., DFM rules, as the resulting yield could still be prohibitively low and therefore a new set of design procedures (model based) need to be applied to a design beyond manufacturability rules to ensure decent yield [8].

Table 1.1. Cost of Defect Repair at Every Stage of Production

Level of Completion	Cost to find and repair defect
Part itself	1X
At sub-assembly	10X
At final assembly	100X
At the dealer/distributor	1,000X
At the customer	10,000X

Also, in this book we will focus on the DFM for the semiconductor IC industry but we would like to mention outright that all the historical classical concepts of DFM such as component simplification, standardization, minimization of the number of modules to be assembled, avoiding tight tolerances, and design robustness still apply in one form or another to the IC industry although DFM (and DFY) in the IC industry has many particularities that are new and that are unique to it.

Some early works in DFM and DFY for the IC industry tried to differentiate between DFM & DFY along the lines that anything rule based is DFM and anything model based is DFY. We believe the concepts of DFM and DFY have converged and that it does not make any sense to try to draw any distinction. Therefore we will use DFM to mean DFM/DFY.

As we mentioned earlier DFM and DFY have always been tied together, in fact most of the time whenever DFM was discussed, both DFM and DFY were implied. Yet we recently encounter a special stress in the IC industry on the concept of DFY and that is really an effort to emphasize the added concept that yield is no longer a manufacturing issue but a collectively shared issue between all participants of a production process. It is a statement that the design and implementation teams hold as much, if not more, responsibility for yield than does the manufacturing team. In 2004 a study estimated the total financial loss due to yield in the IC industry at \$30 Billion dollars per year. That is why DFM/DFY is currently the most active area of research in the EDA industry.

1.2 Why is DFM/DFY Becoming Ever so Critical for IC Manufacturing?

Rarely have so many variables (factors) of a particular design and manufacturing process undergone significant fundamental changes simultaneously such as what we are witnessing today in the nanometer era of the IC industry. Further complicating matters in the emergence of structurally novel new devices (double gate devices, triple gate devices, and FinFETs) and the proliferation of dedicated sub-processes at every technology node directed toward meeting the needs of specific applications. Needless to say, the increase in the number of new variables introduced into the mix of any process renders the probability of

error due to a fault in any of those variables higher, and thus the need for a meticulous accountability of the impact of each variable on the overall process flow. In this section we will give a brief introduction to a plurality of those variables. A more detailed coverage of each variable is left for the body of the book.

1.2.1 New Materials

A quick count of the number of elements of the periodic table used in the IC industry from its inception until the onset of the nano era of CMOS and that used or being experimented with as a potential solution to one of the problems the industry is facing is very revealing. It is not an increase of ten or fifteen percent but rather a multiple of greater than four. In this section we will focus on the materials being used for metallurgy, for low K dielectric, high K dielectric, and engineered mechanical strain materials.

1.2.1.1 Copper

The switch from Aluminum (Al) and aluminum alloys to Copper (Cu) was a major and fundamental change. Aluminum metallurgy involved the deposition of aluminum (or aluminum alloy) all over the wafer and then the selective etch of that aluminum except for the traces forming the metal routes as defined by metal masks. The move to copper was needed as the wires were getting narrower and aluminum alloys could no longer deliver the current carrying capabilities needed by the circuitry. Copper had a higher current carrying capability, but, it couldn't be spun and etched the way aluminum could. Copper deposition is an electroplating procedure that will be described at length when chemical mechanical polishing (CMP) is discussed in Chapter 4. Metal migration (including open vias) was the main problem with Al but no other major problem was there. Figure 1.1 shows a typical cross section of a copper metallurgy for one layer and the slew of problems associated with it from dishing to field oxide loss, to erosion. Also, given that a typical CMOS process of 90 nm or beyond has no less than 8 metal layers, planarization of the layers becomes a must. CMP is used for that, and CMP issues are not trivial. Again it will be discussed at length in Chapter 4.

1.2.1.2 Low K and High K Dielectrics

Gate oxide scaling has resulted in gate oxide thickness reaching the limit of a few mono-atomic layers that is very hard to control. The only way to use thicker gate oxide and still maintain the proper gate coupling capacitance is to resort to higher dielectric (K) materials. Figure 1.2 shows a simple basic gate structure.

$$C_{ox} = K \times A/d \quad (1.1)$$

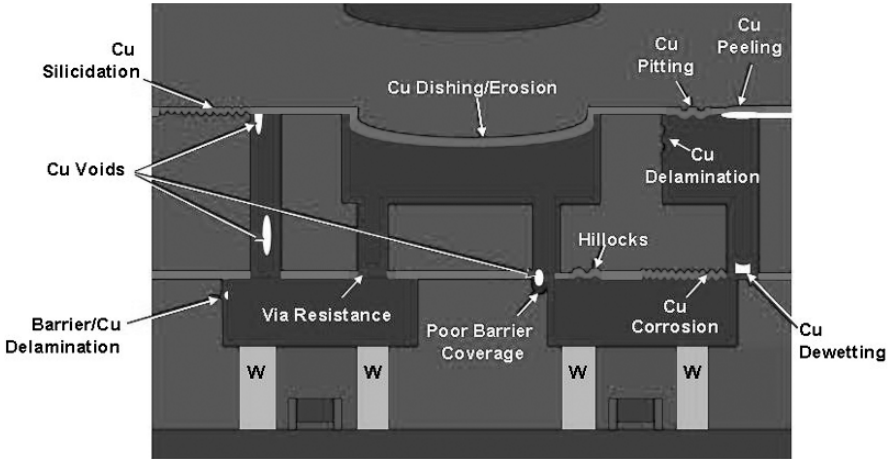


Figure 1.1. Cu Cross Section Showing Potential Problems

where C_{ox} is the gate capacitance, A is the cross sectional area and d is the oxide thickness.

An increase in the value of K allows for an unchanged C_{ox} with a larger value of d . The issue is not as simple as that, as other aspects such as poly field degradation, etc. calls for additional measures such as the use of metal gates with their own set of work function matching between the metal gate and polysilicon related problems. Nonetheless the dominant trend is for higher K dielectrics for gate oxide. Use of plasma nitrated dielectrics and high K dielectrics is growing. Table 1.2 lists few of the options being considered for high K oxides to achieve a variety of dielectric characteristics.

The exact opposite trend applies to inter-metal oxide layers (ILD). There, a lower K is desired to lower the capacitance of the underlying interconnect since with the increasing gate count of a typical design and shrinking device dimensions and supply voltages renders the interconnect delays as the dominant component of delay in most given critical paths; thus a reduction of C through a reduction of K is desirable. However, lower K means more porous material, and

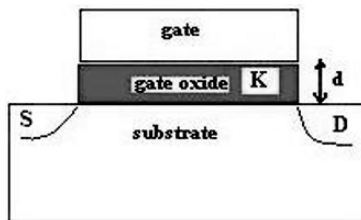


Figure 1.2. Basic Gate Illustration

Table 1.2. High K Oxide Materials and Their Dielectric Constants

SiO_2	3.9
Si_3N_4 / SiO_2	5
Si_3N_4	7
Al_2O_3	10
$HfSi_2O_3$	10-15
HfO_2	15-30
TiO_2	30-90
$BaSrTiO_3$	100-300

higher leakage. So, coming up with the proper materials with the appropriate desirable characteristics is not a trivial matter.

1.2.1.3 SiN and SiGe Layers for Induced Strained Silicon Engineering

One of the emerging techniques for selectively enhancing the mobility of p-carriers or n-carriers involves intentionally creating mechanical stress in the channel caused by the mismatch in the lattice structure at the interface between the native silicon and the induced material - namely SiN, SiC, or SiGe. There are compressive strain techniques and tensile techniques depending on which device we intend to enhance. Mobility of p-type or n-type carriers has been reported to be enhanced by as much as 50% due to mechanical stress. A recessed SiGe source and drain is used to enhance p-type performance through compressive stress while a SiC channel is an example of tensile stress used to enhance n-type performance. Two things are worth noting here: first, when a stress enhancement technique is used to enhance devices of one carrier type, it results in deterioration (though smaller in magnitude than the enhancement) in the opposite type carrier; second, the extent of enhancement or degradation of a certain carrier type due to stress engineering is very dependent on lattice orientation (Miller indexes) which determine the unstressed mobility characteristics of that carrier in the first place. This has implications on the permitted direction of gates orientation in physical layout which used to be a free variable.

1.2.1.4 Miscellaneous

We could go on and talk about photoresist materials being considered to control line edge roughness, a significant contributor to leakage, and materials being used for high-resolution and for phase manipulated masks, and the list goes on. The common theme is that there is an explosion in the materials and elements being used as we continue to shrink CMOS technology. We stressed the ones above due to their higher significance and relevance to the design cycle and to DFM/DFY.

1.2.2 Sub-wavelength Lithography

Sub-wavelength lithography will be covered in depth in Chapter 3, so our coverage of this issue here will be brief and will focus mainly on the chronological turning points in lithography and their impact on yield and manufacturability.

1.2.2.1 Some Basic Equations

Let us start by citing four characteristics of light that will guide our work in lithography related matters through the book. Light has wave properties namely wavelength, direction, amplitude, and phase. All lithography manipulation schemes revolve around manipulating one of those four characteristics. But, before addressing any issues impacting lithography it is useful to review some basic optical fundamentals. One such basic fundamental is that photoresist reacts to a threshold of light intensity (energy) and not to the wave shape nor its phase. We will need this fact later when we explain resolution enhancement through the use of phase-shift and others technologies. The other two fundamentals we would like to address briefly here are the two equations that describe the relation between resolution and depth of focus, the parameters of light wavelength, and the lens numerical aperture.

First is Rayleigh's equation for resolution

$$R = k_1 \times \lambda/NA \quad (1.2)$$

where R = resolution = minimum feature, k_1 = resolution constant, λ = wavelength of the light source, NA = numerical aperture which is a function of the lens and of the refraction index of the medium between the wafer and the lens of the contact aligner.

Depth of Focus (DOF):

$$DOF = k_2 \times \lambda/NA^2 \quad (1.3)$$

where DOF is defined as the range of items in focus in an image and λ = wavelength of the light source.

At this point we want to bring into attention few implications of the above two equations. The necessity of using the 193nm light source for the 45nm technology node implies an effort to increase NA and to reduce k_1 . While resolution improves with higher NA , DOF suffers at a squared rate of the increase in NA . The other point is that as k_1 is reduced to very low values (0.25) to meet the need of 45nm the proximity interaction effects of neighboring geometries increases complicating things further (we will not cover here the factors impacting k_1).

Table 1.3 before indicates the typical combination of NA and k_1 needed to meet technology requirements for 193 nm light source.

Table 1.3. Indicates the k_1 , NA Combinations vs Resolution

Light source λ	NA	k_1	Resolution
193nm	0.6	0.4	130nm
193nm	.75	.35	90nm
193nm	.85	.4	90nm
193nm	1	.34	65nm
193nm	1.1	.37	65nm
193nm	1.1	.25	45nm
193nm	1.2	.27	45nm
193nm	1.3	.3	45nm

Again, this topic will be covered at length in Chapter 3, but it important to note that as k_1 values drop below .4 heavy use of resolution enhancement techniques (RET) are needed to achieve any acceptable printability.

1.2.2.2 Light Sources

Table 1.4 shows the wavelength of the light source used versus the technology node processed using that source light. We obviously skipped many technology nodes but the point we wanted to stress here is that past the 130nm technology node the critical dimension (CD) of the featured technology is significantly less than half of the wavelength (λ) of the light source used in the lithography.

It is also significant to mention that efforts to develop a 157 nm illumination source has been all but abandoned in 2005 due to vast technical difficulties associated with the mask and photoresist technologies needed to go along with that light source. There is practically no serious candidate for a lithography light source beyond the ArF (Argon Fluoride) 193nm light source until the extreme ultra violet (EUV) light source with a wavelength of 13 nm. A lot of progress in the development of the EUV illumination source has been reported in the last several years with two “alpha” EUV systems installed in the year 2006 but any serious deployment of that source for full production is still many years away at best estimate.

1.2.2.3 Lens Technology

As Rayleigh’s equation (Equation 1.2) indicates a higher NA leads to an improved resolution limit. One of the techniques successfully used to improve the NA of the lens projection medium has been immersion technology where a drop of fluid is introduced between the lens and the exposed wafer. The change in the index of refraction in which the light source travels translates in this

Table 1.4. Light Wavelength Versus the Technology Node

Light source λ	436nm	365nm	248nm	193nm	193nm
Technology node	3,000nm	600nm	130nm	90nm	65nm

case to a shorter equivalent wavelength, thus improved resolution. The other technique is simply a direct improvement in the NA of the lens itself, however, this is capped at a theoretical limit of one and a practical limit around 0.8.

The NA of a lens is given by

$$NA = I \sin(\alpha) \quad (1.4)$$

Where I is the index of refraction of the media in which the lens is working. For air I is 1 putting a theoretical upper limit of 1 on the NA of a lens in air. Figure 1.3 is for the illustration of Equation 1.4.

With immersion technology where the medium is altered to water or oil, the index of refraction of some oils are as high as 1.5 allowing for an effective numerical aperture greater than one compared to the typical 0.6 ($\alpha = 32^\circ$) to 0.8 ($\alpha = 48^\circ$) range attainable through lens in air.

1.2.2.4 Resolution Enhancement Techniques (RET)

RET is defined as the set of optical and geometrical (layout) procedures performed individually or in any particular combination to enhance the printability of design features and to meet design intent. Figure 1.4 demonstrates the need for OPC in sub-wavelength lithography. Examples of layout procedures are optical proximity correction (OPC), which could be rule or model based, and which involves the addition of sub-resolution assist features (SRAF). An example of a combination of a layout-mask procedure would be phase-shift mask (PSM). Examples of optical procedures of RET includes off-axis illumination, pupil filtering, and multiple exposures. Since we will be covering these in detail in Chapter 3 we will limit our exposure of this topic to the basics.

Figure 1.5 is illustrations of the use of strong PSM for tight geometry resolution. The resist pattern to the left reflects the result of the exposure of a binary mask with a feature smaller than half of the light source wavelength. There is simply no resolution of the geometry whatsoever and the intended feature is totally missed. By applying strong PSM (right) the light interference due to

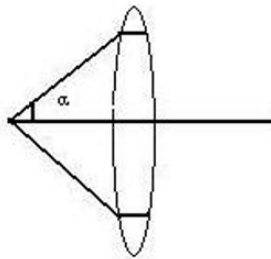


Figure 1.3. $NA = I \sin \alpha$

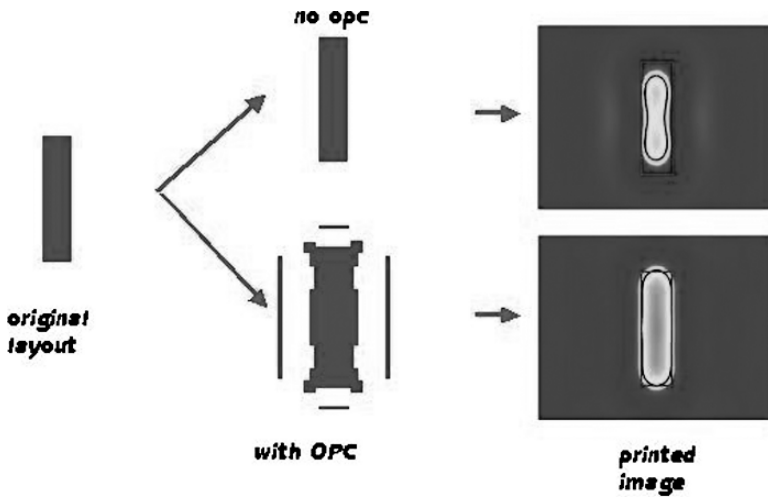


Figure 1.4. Basic Example of OPC at 180nm

the phase altered light wave allows a good resolution of the intended geometry. PSM is achieved by special processing of the mask based on a defined pattern to create a 180 degrees phase shift for light waves passing through the treated mask pattern.

1.2.3 New Devices

In this section we briefly touch on new devices in the context of the ever growing complexity of correctly extracting devices and interconnect, and in the context of growing complexity of process integration. The motivating factors are again dominated by power (especially leakage control) and performance considerations.

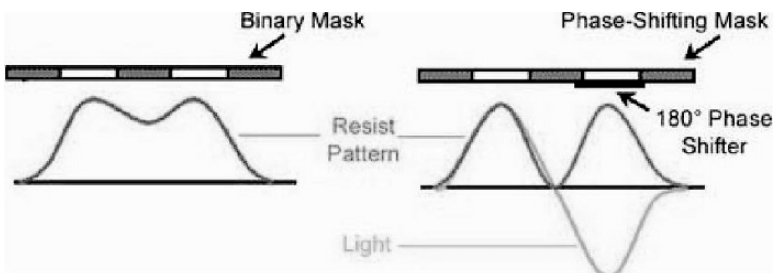


Figure 1.5. Example of Strong (180) PSM

1.2.3.1 Double-gates, Triple gates, and FinFETs

Double gates (Figure 1.6), triple-gates, and FinFETs (Figure 1.7) are all mainly a derivative of the desire to control leakage and short channel effects made worse by device scaling. The idea is rooted in the fact that most leakage occurs in the region far from the channel surface, therefore most of that leakage can be eliminated by having a thin body (shorter than channel length). The use of a double-gate, triple-gate, or finFET (triple gate with strict fin height (T_{si}) and fin width (W_{si}) ratio) will result in good controllability of both leakage and short channel effects without the need to resort to aggressive gate oxide scaling or heavy channel doping.

FinFET architecture is a bit restrictive for standard cell library generation but nonetheless manageable since most standard cell libraries use predetermined P/N device ratios to start with. Figure 1.8 shows an example of a multi-segment finFET layout for a standard cell implementation. However, it is worth noting (near term) that FinFET structures have been reported to have some structural reliability issues related to the mechanical stability of the fin structures. It is still not clear if FinFETs will be introduced any sooner than the 32 nm node. Most roadmaps still show bulk planar CMOS FETs at the 45nm node.

1.2.3.2 Silicon on Insulator (SOI)

The use of silicon on insulator is gaining ground as the cost differential between bulk CMOS and SOI continues to shrink and as the need for higher performance at lower power consumption grows (SOI delivers a technology node performance advantage at the same power level of an existing CMOS technology node, or, delivers same performance at a significantly reduced power- 15 to 20 percent). Originally partially depleted SOI was more dominant than fully depleted SOI. Uncertainties associated with history effects, characteristics of partially depleted SOI encouraged the move to fully depleted SOI. But, manufacturability issues associated with poor controllability of thresholds in fully depleted SOI reverted the interest back to partially depleted SOI.

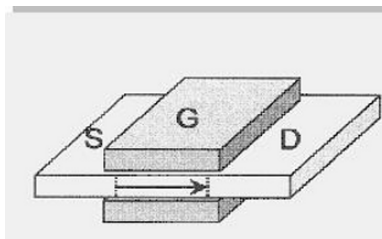


Figure 1.6. Double-gate FET

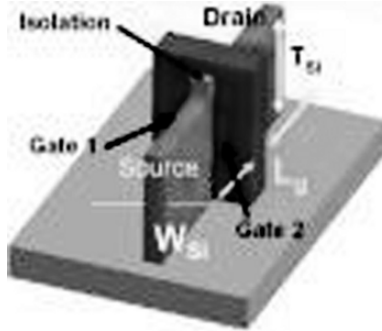


Figure 1.7. TCAD Simulated FinFET

We bring the issue of SOI in this section because of the reliability and predictability issues associates with SOI in terms of history effects and V_t control, localized thermal heating profiles, Electro-static Discharge (ESD), and other SOI specific concerns that need to be addressed carefully.

SOI, with both flavors of partially depleted and fully depleted, is not a new technology. But, given that FinFETs and triple gate structures and similar devices aimed at reducing leakage are not yet proven technologies for 45nm and beyond, the interest in partially depleted SOI is once again on the rise as an alternative solution. The shrinkage in the price differential between SOI and bulk CMOS is helping that trend.

1.2.3.3 Carbon Nanotube Devices, MEMS, and Molecular Devices

We will limit ourselves to the simple mention that the integration of emerging nano-devices of all flavors as well as MEMS and nano-fluidic devices with classical CMOS processes is gaining momentum and simply adds to the complexity of DFM and DFY issues. We specifically mention single walled carbon

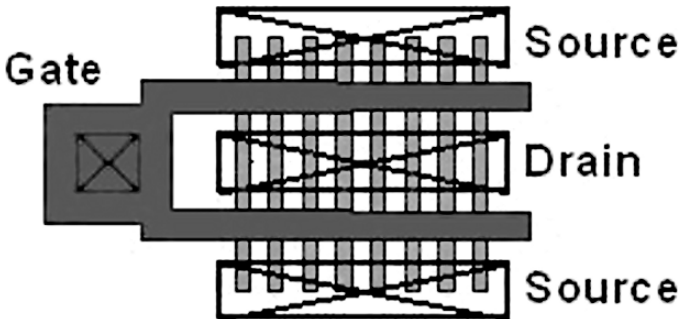


Figure 1.8. Layout of Multi-segment FinFET

nano-tubes (SWCNT) for via structures and nano wires (silicon and other materials) for devices and interconnect. We will not go into those issues with any depth as it is beyond the scope of this book but we simply wanted to alert the practicing engineer to keep a keen eye on these emerging technologies and their interaction and integration with the classical design flow.

1.2.4 Proliferation of Processes

Traditionally the fabrication facilities (FAB) owned DFM and DFY in the sense that the starting point of the design process was a hand over of the process design rules from the process engineers to the designers and the end point was the process engineers continuously tweaking the process to improve parameters causing marginal yield or high failure rates until a process is mature. As we have already stressed in this chapter and we'll be stressing throughout the book the concept of "hand over" or design rules of solid boundaries between various functionaries in the product cycle is long over. In this section we will tackle two issues characteristic of the nano era fabrication facilities namely the proliferation of many processes at any given technology node, and the complexities of those processes with what this implies to EDA tools in general and technology computer-aided design (TCAD) tools in particular.

1.2.4.1 Application Specific Processes

The presence of multi-flavors of any technology node in the form of low power oriented and high performance oriented processes dates back to the 0.6 μ m technology node, perhaps even before. But beyond the 90 nm node two factors have contributed to the further segregation and specialization of processes. One being power, or one should say the power crisis. With proliferation of hand held battery operated devices, and with idle (non-operating) leakage current becoming of comparable magnitude to operating current further division and segmentation within the power options has been exacerbated. The other originates in the level of integration where RF, analog, AMS, and digital functions need to co-exist with a very specific combination of power and performance. Therefore fine division lines entered the picture between processes resulting in separate technology roadmaps driven by the end products they are targeted for and the complexity of dealing with this plethora of processes increased significantly. Example will be: low cost, low power mobile, ultra low power biomedical, high performance, RF, etc.

1.2.4.2 Processing Complexities

We will not go in this introductory chapter into too many details of each of the process complexities except when it is related to EDA tools geared toward DFM / DFY, but nonetheless we enumerate many of the nano era process complexities

that impacts manufacturability and yield directly or indirectly. Most of those complexities are driven by scaling requirements (thin body, ultra shallow junctions, high dopant concentrations, etc) and power (leakage) requirements. To list but a few:

- Co-implantation of species to suppress diffusion
- Diffusion-less activation for ultra shallow junctions
- Diffusion free annealing processes
- Solid phase epitaxy (SPE)
- Spike annealing, flash annealing, and sub-melt laser annealing
- High-tilt high-current implantation (highly needed for double gates)
- Lateral dopant activation
- Through gate implants (TGI)
- Elevated source drain
- Dopant introduction via plasma immersion

1.2.4.3 DFM/DFY Applications for TCAD

One common derivative of the combination of the continuous scaling and the complexities of processing needed to achieve this scaling within tight power and performance constraints is added variability. One such example of variability that TCAD tools has to deal with is atomistic doping profiles for carriers and for minority dopants. Figure 1.9 is a TCAD simulation showing a continuum versus atomistic profiles of an MOS. Accordingly sub 10nm devices, expected

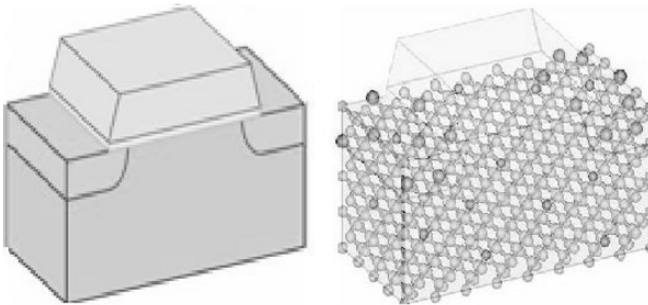


Figure 1.9. Simulated 5nm MOSFET with Silicon Crystal Superimposed Next to A Bulk-CMOS Equivalent

to be available around 2016 will have approximately 10 atoms along the effective channel length and the position of each silicon, dopant, or insulator atom having a microscopic impact on device characteristics. Therefore continuous doping profile models using Kinetic Monte-Carlo (KMC) simulators will not hold any longer and an atomistic statistical 3-D (quantum mechanical considerations) model will need to be implemented in order to correctly capture atomic interaction at that level.

Another DFM application is tied to layout dependency of the tensile stress profile created by the gate liner on the device performance. Stress engineering as pointed out earlier is widely used at 65 nm and beyond to enhance the performance of devices but that performance enhancement is highly layout dependent. Tools are currently developed that can analyze such dependency and extract profiles of layout hot spots as well as performance degradation as a function of position. We'll be covering this in more depth in Chapter 6.

1.2.5 Intra-die Variability

Linear and radial variability from die to die and wafer to wafer were the dominant sources of variability in the IC industry. The designer guard-banded a design against such variability through simulating across what was referred to as the process corners: slow, typical, and fast (these corners also covered environmental variability). The slow corner assumed variability in each parameter to reflect the worse effect on performance simultaneously. In other words it was worst case oxide thickness taking place at the same time as worst case threshold voltage (V_t) and the worst case effective channel length (L_{eff}). Add to that the fact a designer accounted for "worst case" environmental variables along with the slow process corner (high temperature and low supply voltage). Similarly the "best case" simulation accounted for the fastest effect for each parameter plus cold temperature and high supply voltage. Obviously that was an overkill on the part of the designer, but, still the methodology worked sufficiently well. Intra-die variability was insignificant.

The ITRS roadmap shows an annual growth in the die size of DRAM of roughly 3% annually to accommodate roughly 60% more components in keeping up with Moore's law (the 60% comes from technology sizing plus die size growth). That means the lithography field size for a 4 X stepper has to grow by 12% annually reducing the controllability and increasing intra-die variability. Now intra-die variability is very significant as Table 1.5 shows.

A significant portion of intra-die variability is systematic and is layout and pattern dependent and thus could be corrected for to some degree as we'll be covering in more detail in Chapter 5 but the rest of the variability is random and is best dealt with in a statistical approach.

One important point to make here regarding intra-die variability is that it is not limited to parameters such as V_t and t_{ox} which now have a higher percent

Table 1.5. Intra-die Variability Increase with Technology Node

L(nm)	250	180	130	90	65	45
Vt(mV)	450	400	330	300	280	200
σ -Vt(mV)	21	23	27	28	30	32
σ -vt/Vt	4.7%	5.8%	8.2%	9.3%	10.7%	16%

variation but geometries that were once treated as rectangular in cross section such as wires or uniform such as intra-metal oxide thickness can no longer be assumed as such and extraction tools need to take that into account.

1.2.6 Error Free Masks Too Costly

Mask writing equipment are expensive and their throughput is relatively low. Various rasterization techniques and parallel processing has sped mask writing some but the overall cost of a mask set is still a function of the mask write time which is in turn a function of size of the data to be written. Table 1.6 shows the explosion in data volume as we advance to the next technology node. What is most interesting about Table 6 is that the data volume was revised downward from the 2003 ITRS forecast. We'll be commenting on that later in the context for smart OPC but needless to say masks are becoming more expensive; and with the explosion of data points to be written to a mask and the growing field size, getting an error free mask is, in addition to being very expensive, quite hard to come by. This has resulted in the implementation of mask inspection EDA tools that can simulate the impact on a mask error on the overall print out and determining if that error needs to be re-worked or is tolerable. This is an increasingly growing (in size and importance) part of DFM/DFY tools.

1.2.7 Cost of a Silicon Spin

When we talk about the cost of a silicon spin we are talking about three different factors, all tied together, and all very costly. Figure 1.10 shows the typical life cycle of a new product. The typical time needed for a product from concept to first silicon is product dependent but is estimated on an average to be two years with a total cost anywhere from \$25 Million to \$40 Million. A typical re-spin is 6 months.

Now, the cost of a re-spin is interesting to figure out. From a materials and engineering time perspective it is no more than perhaps \$2 millions. But, if we look at the cost from a product life cycle point of view, it could be as high as

Table 1.6. Mask Preparation File Data Size - ITRS 2004

Year	2004	2007	2009
Node	90nm	65nm	45nm
Data	144GB	486GB	1,094GB

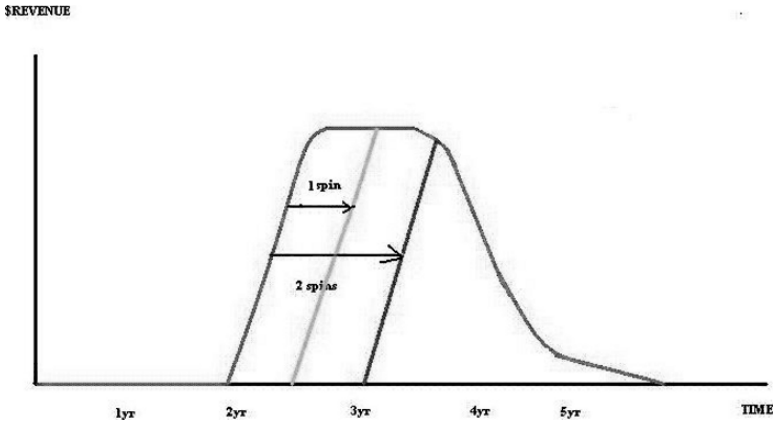


Figure 1.10. Revenue as a Function of Design Cycle

half the total revenue of the product. In fact being six months late to market for some products (Christmas season sales dependent) might cost the whole product cycle. Two re-spins and the product is most likely obsolete.

1.3 DFM Categories and Classifications

There are essentially two major categories of DFM/DFY namely first time loss and time related failures. In this book we focus on first time loss only although many of the time related failures can and should be addressed at the design stage, but are simply more appropriate for a circuits design book or a book on IC reliability and failure analysis than for a book dealing with DFM/DFY. We nonetheless enumerate most of them in an inclusive chart in Chapter 5 for those interested under the category of “physics related” (See Figure 5.16).

1.3.1 First Time Failures

First time failures refers to the situation where a chip comes out with a severity of functionality failure ranging from silicon that is fully operational but does not meet the product specification in timing, power, IEEE standards, or a combination of those issues, to silicon that comes out with fatal failures that is reflected in the chip simply showing no life at all. Here we are not referring to the silicon has a logic design catastrophic failure but rather a failure such as an open or a short caused by oversight in lithography artifacts that rendered a perfectly good logic design that passes all the classical verification tools prone to such unanticipated mode of failure. The focus of this book is dealing with the causes of first time failure and what can be done to reduce the probability of them ever taking place.

1.3.2 Time Related Failures

Time related failures are parts that exhibit failures in the field due to drift in certain parameters with time or due to the marginality of an aspect of the design that deteriorates with time until a failure occurs. Two examples of such a phenomena are metal migration and the drift in V_t of devices with time. A design can have a marginality in the current carrying capability of some interconnect, and the presence of a high current density in that interconnect weakens it over time in the form of a drift in the interconnect particles leading to additional thinning in the interconnect that leads to failure. There are EDA tools that are capable of analyzing a design for such weaknesses and catching them before a design is released. However, the same electro-migration phenomena could occur due to a lithography or a CMP related issue and not due to a current density violation reason. That aspect of failure is addressed in detail in this book. The other example of field failures we cited here is V_t shift with time. This is especially critical given the shallow junctions and the high doping concentrations characteristic of the nano-scale devices. This is the area of TCAD tools to make sure the design of device and process modules do not result in high electric fields that cause a severe enough drift in V_t with time such that it results in a device failure in the field.

As we mentioned at the very beginning of this chapter field failures are the most expensive type of failures and as such should be avoided at all costs. The time honored procedure in the IC industry to eliminate time related failures is to conduct static and dynamic burn-in tests where the parts (or a sample of the parts) undergo biased burn in for 1000 or 10,000 hours under the extreme environmental conditions that are specified IEEE standards and specifications. This procedure should ferret out most if not all such weaknesses in a design. Static burn-in eliminates weak links in what is known as infant mortality. The dynamic burn-in ensures that the device junctions encounter the same electric field profile they will undergo when the part is operating normally in the field executing the functionality it was designed to perform. Therefore it is of utmost importance that dynamic burn in vector sets be comprehensive and exhaustive. That is the extent of our coverage of time related failures in this book.

1.4 How Do Various DFM Solutions Tie up with Specific Design Flows

Since we strongly believe that manufacturability and yield should be designed in to a product from the very onset of the design process we strongly advocate a design flow approach for DFM/DFY. Obviously there is no single design flow followed across the industry, so the design flow we will use is one we believe to be a good and comprehensive example for a system on a chip (SOC) design.

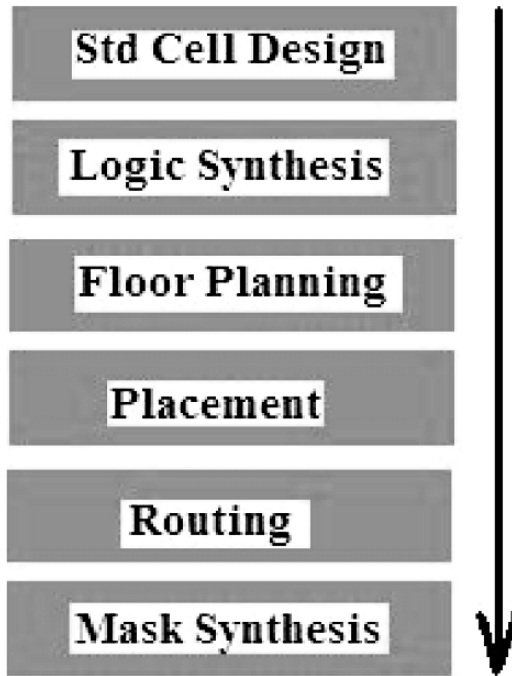


Figure 1.11. Typical ASIC Design Flow

Figure 1.11 shows a basic design flow for ASICs as an example but could be easily extended to a full System on Chip (SOC) design. The idea behind our design flow approach is to start at the very first step, analyze the issues that can impact manufacturability and yield, flag out any potential fatal problems, point out areas of improvements and their corresponding cost and assign a yield grade for each alternative. As an example, at the standard cell design level a cell layout is analyzed for CA failures and given a yield grade based on the vulnerability of the cell to CA failure, then an alternative layout is proposed that has a higher CA number. Such a cell might have a larger area, and perhaps even a performance (speed) cost. This alternative cell is given an appropriate yield grade as well. So, a yield grade will be an added arc for standard cells along the classical arcs of delay, power, area, and rise/fall time. This procedure is repeated throughout the whole design flow. An interesting issue arises when some alternatives have conflicting outcomes. An example of that will be the routing area where a procedure such as wire widening might improve the CA “opens” score of the design but worsens the CA “shorts” score of the design. This is why this methodology focuses at optimizing a weighted function of yield rather than maximizing yield. Maximizing yield might be too costly and might not be desirable. An obvious example of that would be using a 100%

defect free mask! A yield engine interacting with the various EDA design tools controlling such a flow is highly desirable to close the loop of interaction between the modules in the context of DFM/DFY.

1.5 DFM and DFY: Fully Intertwined

In summing up this chapter it is not hard for the reader to see the complexities associated with all aspects of the nano era IC manufacturing. Two major conclusions are self-evident. First, no single group owns the DFM and DFY responsibility, yet an oversight or the slightest error by one group or individual in the whole product flow is sufficient to either kill the product or to impact the product yield adversely and in a significant manner. It follows that close cooperation and open communications between the electronic design automation (EDA), design (including verification), mask preparation, fabrication, assembly, and testing communities is needed. It also suggests that this communication is a closed loop, two directional feed back. The second obvious conclusion is that functionality and yield can and should be designed into the product. By the time a design is committed to a mask it is too late and too expensive to try to do anything significant to impact functionality, reliability, or yield.

Chapter 2

RANDOM DEFECTS

Dealing with random defects in IC manufacturing and coming up with yield models that estimates yield as a function of die area and of the density of random defects dates back to the early sixties. The three most used yield models are the Poisson distribution model, the Seed's model, and the negative-binomial model. The Poisson and the negative-binomial models have emerged as dominant. We will limit our discussion to them.

2.1 Types of Defects

When we talk about random defects we refer to all types of defects that cannot be controlled or modeled in a predictable and systematic way. They include random particles in the resist or in the materials to be added or removed, or defects in the crystal structure itself that alters the intended behavior of the material and results in excessive leakage or in a shift in the device threshold (V_t) leading to the failure of the device. The failure modes resulting from these defects are

- 1 Opens
- 2 Shorts
- 3 Leakage
- 4 V_t shift
- 5 Variability in Mobility (μ)

Random defects as described above did not have to result in a total failure of the device but in a significant deterioration in its performance. A killer random defect was recognized as a defect that amounted to anywhere from $\frac{1}{10}$ to $\frac{1}{3}$ of

the critical dimension (CD) of the layer(s) it impacted. We enumerated the potential effects of particles for completeness. Defects resulting in leakage, V_t shift, μ shift are dealt with in infant mortality burn-in mentioned in Chapter 1. Here we only address CA in terms of opens and shorts. The early random defects yield models dealt with failure of Short and Open modes only, and it was a good approximation as short and open failure were the majority of the random defects. We extend it to address clustering effects which is becoming more relevant in the nano-era.

2.2 Concept of Critical Area

Critical area is a measure of a design's sensitivity to random particles. Critical area A_{cr} is defined as the region on the layout where contamination particles must fall to cause a catastrophic functional failure. A catastrophic failure is an open or a short. Based on the failure type (open or short) caused by the particles, the critical area can be categorized as open critical area or short critical area. The CA based random yield loss is a function of the open and short critical areas.

In the shape expansion method, the name is self evident in terms of the fact that "expanding" the circle needed to cause a short or an open define the particle size that causes such a short or open. Figures 2.1 and 2.2 illustrate the shape expansion method for the extraction of the short and open critical areas caused by the particles with radius $x/2$, or size x (shown as shaded areas in Figure 2.1 and 2.2).

Another example of open and short critical area between layers is shown in Figure 2.3. A typical example will be a particle (or a void) in the oxide between two conductors resulting in a short or a leakage path, another example will be a particle or a void in a via structure resulting in an open or in a high resistance via.

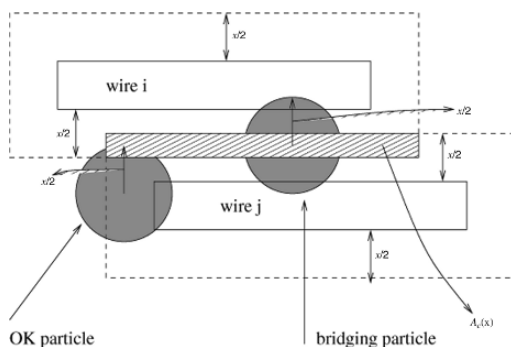


Figure 2.1. Short CA Between Two Wires Caused by Particles with Size x

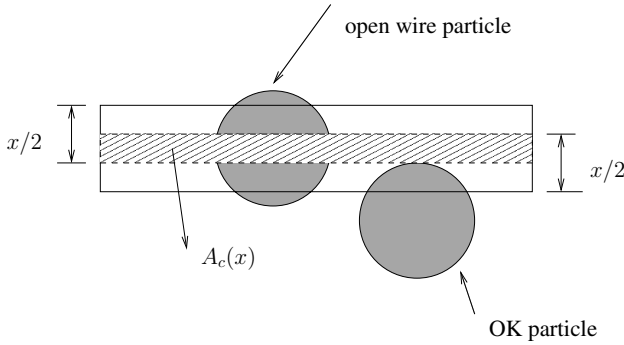


Figure 2.2. Open CA on a Wire Caused by Particles with Size x

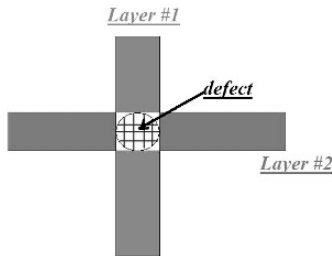


Figure 2.3. Intra-layers Defect Particle Resulting in an Open or Short

2.3 Basic Models of Yield for Random Defects

We will be devoting the next four chapters to deal with all other aspects of yield. So, we will cover yield here only as it relates to critical area in order to give the reader an idea of why extracting critical area and minimizing it is important.

As we mentioned, two of the most recognized yield models are the Poisson based yield Equation (Equation 2.1) and the negative binomial yield Equation (Equation 2.2) [9–12].

$$Y_r = e^{-A_{cr}D_0}. \tag{2.1}$$

$$Y_r = \frac{1}{(1 + \frac{A_{cr}D_0}{\alpha})^\alpha} \tag{2.2}$$

where Y_r denotes the random yield and D_0 refers to the particle density. A_{cr} is the critical area defined earlier in Section 2.2, which, as obvious from the Equation, is a key design yield determining parameter. The α is a “clustering parameter” introduced to correct the effect of defect clustering. It is especially useful for large devices where clustering is more significant to improve yield

prediction. It is also obvious that in order to maximize yield, that number needs to be minimized. In more advanced yield models, D_0 was replaced by D where D , rather than being a constant number D_0 is now a defect density distribution function $f(D)$. However, it is worth noting at this point that almost all yield models used by the IC industry for yield modeling fall into two categories: Poisson distribution based model and negative binomial distribution based model. We want to be clear at this point that we are not advocating one modeling method over the others. Different applications and the need for different levels of confidence as well as the design size might dictate which modeling method is most appropriate for that particular situation.

2.4 Critical Area Analysis (CAA)

In this section we will cover two standard methods of CA extraction namely the shape expansion method and the Monte Carlo method as well as a newly developed approximation method that exploits certain clustering phenomena of particle defects to result in a relatively accurate but fast method of CA extraction. The main differences between the first two standard methods and the approximate method are computation cost and accuracy. While the standard methods, also known in the industry as “exact” methods are accurate, they are computationally expensive. The approximate method on the other hand is close enough in accuracy especially when the CA calculation is needed to be performed in short order to make a decision in the routing stage for example among alternative options for the purpose of improving CA associated yield, yet it is computationally very efficient. Another benefit of the approximate method is that it makes CAA driven layout optimization possible.

2.4.1 Classical Methods of CA Extraction

The shape expansion based method is designed to compute the critical area for a particular given defect size. The critical area needs to be recomputed if the defect size is changed. The average critical area is calculated by integrating these critical areas at different defect sizes with defect size distribution function. The Monte Carlo method does not limit itself to any specific defect size. The generator simply generates random defects with their sizes following the given defect size distribution function. Both these methods suffer from the problem of huge run time for accurate estimation.

Once the critical areas for all the wires are computed, the geometric union of these areas gives the total critical area $A_c(x)$ at the defect size x . The average value of total critical area for all different defect sizes is calculated as

$$A_{cr} = \int_{x_{\min}}^{x_{\max}} A_c(x) f(x) dx \quad (2.3)$$

where x_{\min} and x_{\max} are the minimal and maximal defect sizes, $f(x)$ is the defect size distribution function.

For modern processes, it is widely accepted that the defect size distribution function is similar to Equation 2.4 [13–15].

$$f(x) = \begin{cases} \frac{x}{x_0^2} & \text{if } 0 < x \leq x_0, \\ \frac{x_0^2}{x^3} & \text{if } x_0 \leq x \leq x_{\max}, \end{cases} \quad (2.4)$$

where x_0 is the minimal spacing in the design rules.

At each particular defect size, the traditional shape expansion method computes the geometric union of the critical areas for all the wires to obtain the total critical area. Due to the existence of the overlaps between the geometry shapes, the total critical area is not a linear sum of each individual wire's critical area. Several algorithms (mostly based on scan-line or quad-tree data-structures) have been used for efficiently computing the geometric union. However, none of these methods can handle the geometric union analytically. Therefore there is no way to predict the total critical area at a different defect size. The whole extraction and computation procedure has to be repeated for different defect sizes. Thus we need approximation methods that can efficiently do that.

2.4.2 Approximations

As we mentioned earlier in the chapter using a shape expansion method for computing the CA of a particular design is an accurate but computation runtime expensive method [16–24], and the same applies to the Monte Carlo method [19, 20, 25]. It is not exactly practical for applications such as multi-layer metal routing where alternative yield improvement scenarios need to be evaluated by recomputing the CA of the design and the corresponding impact on yield for each proposed alteration to come up with an optimal solution. Thus, when the typical shape expanding technique is used, an approximation in the form of using a limited number of defect sample-sizes is used to speed up the calculation of CA. This introduces an inaccuracy in its own right reducing the significance of the accuracy of the method. Ways to speed up the on-the-fly calculation of CA within a particular step of the design flow has recently been an area of active research. The approach we describe in this section is a very efficient and promising approach that has been recently put into practice in the Synopsys ICC place and route suite with good results [26]. The approximation method is a shape expansion type of method, but it does not limit itself to any particular defect size. Furthermore, this approximation technique exploits well known and empirically proven defect clustering phenomena.

Table 2.1. CA Results and Run Time in Shape Expansion Method and Our Method

designs		traditional method		new method	
		results	run time	results	run time
design 1	short A_{cr}	2.8949e5	42 min	2.9426e5	41 sec
	open A_{cr}	5.8922e5	7 min	6.0319e5	24 sec
design 2	short A_{cr}	1.2450e6	3hr 14min	1.3970e6	3 min
	open A_{cr}	2.7109e6	24 min	2.7556e6	2 min
design 3	short A_{cr}	2.8225e6	5hr 8min	2.8387e6	3.5 min
	open A_{cr}	3.5000e6	29 min	3.5979e6	2.3 min
design 4	short A_{cr}	2.4867e6	5hr 51min	2.9197e6	3 min
	open A_{cr}	4.4026e6	23 min	4.5653e6	2 min

Thus there has been many attempts at coming up with an explicit analytical formulation of critical area [27] but almost all of them have the limitation of not properly dealing with the overlaps between critical areas of individual wires. Furthermore, some of them make the unrealistic assumption of a fixed wire width and wire spacing for the whole design, again impacting their accuracy.

In this method an explicit formula for the average critical area is generated. The layout-related parameters in the formula can be derived in one sweep through the objects of a layout. Therefore, if the traditional shape expansion-based method needs to compute the critical area m times for m different defect sizes, the proposed method can speed up the run time by at least a factor of m .

2.4.3 Comparison of Approximate and Traditional CA Extraction Techniques

In this section we present simulation results comparing the approximation method of calculating the average critical area presented here with the traditional shape expansion based method. We will discuss the details of the approximation method in the next section. We ran the proposed method and the traditional shape expansion method on 4 practical design layouts. The design sizes varied from $0.6mm \times 0.6mm$ to $1mm \times 1mm$. The data in Table 2.1 shows that both methods give very close results yet the proposed approximation method is dramatically faster than the traditional method (note that in the traditional method, we use 20 defect sizes to compute the average critical area).

2.5 Mathematical Formulation of Approximation Method

For this approach, an explicit formula for the total critical area is derived by introducing the concept of pseudo critical areas for the individual wires. Those areas are not overlapping with each other. The total critical area at any particular

defect size is formulated as the summation of those pseudo critical areas. That results are an explicit formula for the total critical area as a function of defect size and of some layout parameters such as wire width, length, and spacing. The integration over the defect size distribution function can be performed analytically as well. Therefore, the resulting average total critical area is also an explicit formula. The only free variables left in the final formula are the layout parameters.

With the explicit formula for short and for open critical areas available one only needs to go through all the objects in the layout once to extract the indicated layout parameters. At the end of extraction the extracted layout parameters are substituted into the formula and the average total critical area value is made available immediately for all different defect sizes.

This discussion on computational complexity is clearly for calculating the total average critical area. If one wants to identify the critical areas for only one particular defect size for the layout then there is no difference in the computational cost between this method and the traditional method. However this is highly unlikely since the average critical area is usually needed for the following two reasons

- 1 It is required to quantify yield loss due to all the random defects. Thus the average critical area is needed.
- 2 For layout optimization through critical area minimization it makes more sense to use the average critical area as a cost function to be minimized rather than the critical area of only one defect size.

2.5.1 Short Critical Area - Mathematical Formulation

If a pair of parallel wires (i, j) belonging to two different nets have portions adjacently visible to each other, as shown in Figure 2.4, then the critical area for this pair of wires at a particular defect size x is simply

$$A_c(x) = \begin{cases} 0 & \text{if } x < s_{ij}, \\ (x - s_{ij})b_{ij} & \text{if } x \geq s_{ij}. \end{cases} \quad (2.5)$$

where s_{ij} is the spacing between (i, j) . b_{ij} is the segment where i and j are visible to each other.

Equation 2.5 is an effort at formulating the critical area analytically. It has been used in [27]. There are two major problems with this formulation. One is that if the total critical area is computed as

$$A_c(x) = \sum_i \sum_{(nbr\ j\ of\ i)} A_{ij}(x) \quad (2.6)$$

where $nbr\ j\ of\ i$ means j is a visible neighbor of i . Therefore, the same critical area $A_{ij}(x)$ and $A_{ji}(x)$ is going to be double counted. Another major

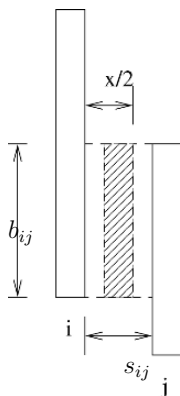


Figure 2.4. Typical Short Critical Area

problem with this formulation is that when the defect size is big, the critical area between a wire pair (i, j) might overlap with the critical area between another wire pair (i, k) as shown by area E in Figure 2.5. Equation 2.5 does not handle the overlap regions at all. The summation of such critical areas would result in double counting of these overlap regions.

In order to solve this problem, the total critical area is presented as the summation of some pseudo critical areas between every pair of visible wires $A_c(x) = \sum_i \sum_j \hat{A}_{ij}(x)$, where the pseudo critical area $\hat{A}_{ij}(x)$ is defined such that

$$\hat{A}_{ij}(x) \cap \hat{A}_{mn}(x) = \emptyset, \quad \forall (i, j) \neq (m, n).$$

However, note that the subscript (i, j) is order sensitive, i.e., $\hat{A}_{ij}(x) \neq \hat{A}_{ji}(x)$.

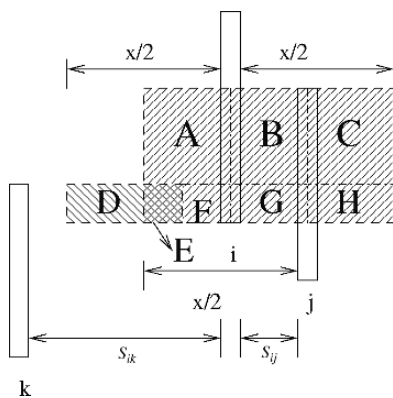


Figure 2.5. Short Critical Area at Large Defect Size

As shown in Figure 2.5, the wire i is split into two segments. One segment has one visible neighbor j on one side and no visible neighbor on the other side. The other segment has visible neighbors j and k on both sides.

For the segment of wire i that has a visible neighbor on only one side the pseudo critical area is defined as $\hat{A}_{ij}(x) \triangleq A + B/2$, $\hat{A}_{ji}(x) \triangleq B/2 + C$. Note that in this case the actual critical area between wires (i, j) is $A_{ij}(x) = A + B + C$. Thus $\hat{A}_{ij}(x) + \hat{A}_{ji}(x) = A_{ij}(x)$, $\hat{A}_{ij} \cap \hat{A}_{ji} = \emptyset$. Each region in the shaded area as shown in Figure 2.5 is included in only pseudo critical area only. Equation 2.7 defines $\hat{A}_{ij}(x)$ analytically for the segment of wire i that has a visible neighbor on only one side (the visible neighbor in this case is j).

$$\hat{A}_{ij}(x) \triangleq \begin{cases} 0, & \text{if } x \leq s_{ij}, \\ (x - s_{ij})b_{ij}/2, & \text{if } s_{ij} < x \leq 2s_{ij} + \min(w_i, w_j), \\ (s_{ij} + \min(w_i, w_j))b_{ij}/2 + (\frac{x}{2} - s_{ij} - \frac{\min(w_i, w_j)}{2})b_{ij}, & \text{if } 2s_{ij} + \min(w_i, w_j) < x \leq D_{\max}, \end{cases} \quad (2.7)$$

where b_{ij} is the length of the overlap portion between i and j , s_{ij} is the spacing between i and j , w_i, w_j are the wire-widths for the two wires, and D_{\max} is the maximum random defect size.

For the segment of the wire i that has visible neighbors on both sides the pseudo critical area is defined as $\hat{A}_{ij}(x) \triangleq F + G/2$, where the region F is the region of the critical area $A_{ij}(x)$ that goes to the other side of wire i but is not covered by the other side critical area $A_{ik}(x)$. The region E which is the overlap region between the critical areas $A_{ij}(x)$ and $A_{ik}(x)$, is included as part of the pseudo critical area $\hat{A}_{ik}(x)$. $\hat{A}_{ik}(x) \triangleq D/2 + E/2$. Note that the regions included by $\hat{A}_{ik}(x)$ should not go to the other side of wire i because that part has been covered by $\hat{A}_{ij}(x)$. The region H is already totally included as part of the pseudo critical area $\hat{A}_{ji}(x)$. Following these steps every region in the shaded area as shown in Figure 2.5 is included in only one pseudo critical area.

Equations 2.8, 2.9, and 2.10 define $\hat{A}_{ij}(x)$ analytically for a segment of wire i with visible neighbors on both sides. If $2s_{ij} + \min(w_i, w_j) < 2s_{ik} + \min(w_i, w_k)$:

$$\hat{A}_{ij}(x) \triangleq \begin{cases} 0, & \text{if } x \leq s_{ij}, \\ (x - s_{ij})b_{ij}/2, & \text{if } s_{ij} < x \leq 2s_{ij} + \min(w_i, w_j), \\ (s_{ij} + \min(w_i, w_j))b_{ij}/2 \\ + (\frac{x}{2} - s_{ij} - \frac{\min(w_i, w_j)}{2})b_{ij}, & \text{if } 2s_{ij} + \min(w_i, w_j) < x \leq \\ & s_{ij} + s_{ik} + w_i, \\ (s_{ij} + \min(w_i, w_j))b_{ij}/2 \\ + [(\frac{x}{2} - s_{ij} - \frac{\min(w_i, w_j)}{2}) - \\ (x - s_{ij} - s_{ik} - w_i)]b_{ij}, & \text{if } s_{ij} + s_{ik} + w_i < x \leq \\ & 2s_{ik} + 2w_i - \min(w_i, w_j), \\ (s_{ij} + \min(w_i, w_j))b_{ij}/2, & \text{if } 2s_{ik} + 2w_i - \min(w_i, w_j) \\ & < x \leq D_{\max}. \end{cases} \quad (2.8)$$

If $2s_{ij} + \min(w_i, w_j) > 2s_{ik} + \min(w_i, w_k)$:

$$\hat{A}_{ij}(x) \triangleq \begin{cases} 0, & \text{if } x \leq s_{ij}, \\ (x - s_{ij})b_{ij}/2, & \text{if } s_{ij} < x \leq 2s_{ij} + \min(w_i, w_j), \\ (s_{ij} + \min(w_i, w_j))b_{ij}/2 \\ + (\frac{x}{2} - s_{ij} - \frac{\min(w_i, w_j)}{2})b_{ij}, & \text{if } 2s_{ij} + \min(w_i, w_j) < x \leq \\ & 2s_{ij} + 2w_i - \min(w_i, w_k), \\ (s_{ij} + \min(w_i, w_j))b_{ij}/2 \\ + (w_i - \frac{\min(w_i, w_j)}{2} - \\ \frac{\min(w_i, w_k)}{2})b_{ij}, & \text{if } 2s_{ij} + 2w_i - \\ & \min(w_i, w_k) < x \leq D_{\max}. \end{cases} \quad (2.9)$$

If $2s_{ij} + \min(w_i, w_j) = 2s_{ik} + \min(w_i, w_k)$:

$$\hat{A}_{ij}(x) \triangleq \begin{cases} 0, & \text{if } x \leq s_{ij}, \\ (x - s_{ij})b_{ij}/2, & \text{if } s_{ij} < x \leq 2s_{ij} + \min(w_i, w_j), \\ (s_{ij} + \min(w_i, w_j))b_{ij}/2 \\ + (\frac{x}{2} - s_{ij} - \frac{\min(w_i, w_j)}{2})b_{ij}, & \text{if } 2s_{ij} + \min(w_i, w_j) < \\ & x \leq s_{ij} + s_{ik} + w_i, \\ (s_{ij} + \min(w_i, w_j))b_{ij}/2 \\ + (\frac{s_{ij} + s_{ik} + w_i}{2} - s_{ij} - \\ \frac{\min(w_i, w_j)}{2})b_{ij}, & \text{if } s_{ij} + s_{ik} + w_i < x \leq D_{\max}. \end{cases} \quad (2.10)$$

The total critical area at a particular defect size is the sum of all the pseudo critical areas shown in Equations 2.7, 2.8, 2.9, and 2.10. $A_c(x) = \sum_i \sum_j \hat{A}_{ij}(x)$.

By integrating $A_c(x)$ with the probability distribution function of the defect sizes in Equation 2.4 we have the averaged total short critical area A_{cr} as follows: For the segments of the wires that have only one side visible neighbor the average short critical area is:

$$A_{crS-1side} = \sum_i \sum_j x_0^2 b_{ij} \left[\frac{1}{4s_{ij}} + \frac{s_{ij}}{4D_{\max}^2} - \frac{1}{2D_{\max}} \right]. \quad (2.11)$$

For the segments of the wires that have visible neighbors on both sides, the average short critical area is as shown below:

If $2s_{ij} + \min(w_i, w_j) < 2s_{ik} + \min(w_i, w_k)$:

$$A_{crS-2side1} = \sum_i \sum_j x_0^2 b_{ij} \left[\frac{1}{4s_{ij}} - \frac{1}{2(s_{ij} + s_{ik} + w_i)} + \frac{1}{4(2s_{ik} + 2w_i - \min(w_i, w_j))} - \frac{s_{ik} + \min(w_i, w_j)}{4D_{\max}^2} \right]. \quad (2.12)$$

If $2s_{ij} + \min(w_i, w_j) > 2s_{ik} + \min(w_i, w_k)$:

$$A_{crS-2side2} = \sum_i \sum_j x_0^2 b_{ij} \left[\frac{1}{4s_{ij}} - \frac{1}{4(2s_{ij} + 2w_i - \min(w_i, w_j))} - \frac{s_{ij} + 2w_i - \min(w_i, w_j)}{4D_{\max}^2} \right]. \quad (2.13)$$

For $2s_{ij} + \min(w_i, w_j) = 2s_{ik} + \min(w_i, w_k)$:

$$A_{crS-2side3} = \sum_i \sum_j x_0^2 b_{ij} \left[\frac{1}{4s_{ij}} - \frac{1}{4(s_{ij} + s_{ik} + w_i)} - \frac{s_{ij} + w_i}{4D_{\max}^2} \right]. \quad (2.14)$$

2.5.2 Open Critical Area - Mathematical Formulation

Theoretically, the basic derivation fundamental ideas for the open critical area formula are a complement of the ideas used for the short critical area.

The middle wire in Figure 2.6 is the object for which the pseudo open critical area is formulated. It can be seen from this figure that for large defect sizes

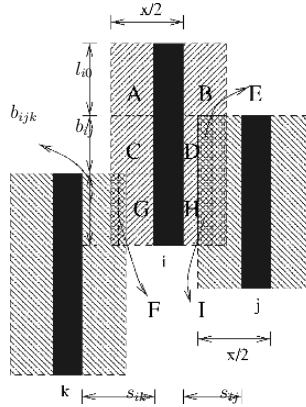


Figure 2.6. Open Critical Area on Wire i

the actual open critical area on wire i begins to overlap with those on wires j and k . In order to avoid counting the overlap regions more than once when calculating the total open critical area, the concept of pseudo open critical areas is introduced. For small defect sizes, when the actual open critical area on wire i has no overlap with the ones on any other objects, the pseudo open critical area is defined to be the same as the actual open critical area. As the defect size increases the pseudo open critical area grows. It should stop growing on the side when it begins to touch the open critical area of its visible neighbor on that same side. For the example shown in Figure 2.6 the pseudo open critical area for the mid wire i should be $\hat{A}_i(x) = A + B + C + D + E + F + G + H + I$. Regions E , F , and I are half of the overlapped shaded region in Figure 2.6 that is close to wire i .

For the segment of wire i that has no visible neighbors on either side as shown by the segment with length l_{i0} in Figure 2.6 the pseudo critical area is defined to be always the same as the actual open critical area because this part of the critical area never overlaps with those of the other wires. Its mathematical formulation is therefore:

$$\hat{A}_i(x) = \begin{cases} 0 & \text{if } x \leq w_i \\ (x - w_i)l_{i0} & \text{if } w_i < x \leq D_{\max} \end{cases} \quad (2.15)$$

Integrating Equation 2.15 with the defect size distribution function in Equation 2.4 results in the average pseudo critical area as:

$$\hat{A}_{0nbr} = x_0^2 l_{i0} \left[\frac{1}{2w_i} - \frac{1}{D_{\max}} + \frac{w_i}{2D_{\max}^2} \right]. \quad (2.16)$$

For the segment of the wire i that has visible neighbor on one side only as shown by the segment of length b_{ij} in Figure 2.6 the pseudo critical area is formulated as:

$$\hat{A}_{ij}(x) = \begin{cases} 0 & \text{if } x \leq w_i \\ (x - w_i)b_{ij} & \text{if } w_i < x \leq s_{ij} + w_i + w_j \\ \left(\frac{x}{2} - w_i + \frac{s_{ij} + w_i + w_j}{2}\right)b_{ij} & \text{if } s_{ij} + w_i + w_j < x \leq D_{\max} \end{cases} \quad (2.17)$$

Integrating Equation 2.17 with the defect size distribution function in Equation 2.4 results in the average pseudo critical area as:

$$\hat{A}_{1nbr} = x_0^2 b_{ij} \left[\frac{1}{2w_i} - \frac{1}{4(s_{ij} + w_i + w_j)} - \frac{1}{2D_{\max}} - \frac{s_{ij} - w_i + w_j}{4D_{\max}^2} \right]. \quad (2.18)$$

For the segment of the wire i that has visible neighbors on both sides as shown by the segment with length b_{ijk} in Figure 2.6, the pseudo critical area is formulated as follows: without loss of generality in this formulation we assume the spacing between wire pair (i, j) is not larger than that between wire pair (i, k) , i.e., $s_{ij} \leq s_{ik}$.

$$\hat{A}_{ijk}(x) = \begin{cases} 0 & \text{if } x \leq w_i \\ (x - w_i)b_{ijk} & \text{if } w_i < x \leq s_{ij} + w_i + w_j \\ \left(\frac{x}{2} - w_i + \frac{s_{ij} + w_i + w_j}{2}\right)b_{ijk} & \text{if } s_{ij} + w_i + w_j < x \leq \\ & s_{ik} + w_i + w_k \\ \left(\frac{s_{ij} + w_i + w_j}{2} + \frac{s_{ik} + w_i + w_k}{2} - w_i\right)b_{ijk} & \text{if } s_{ik} + w_i + w_k < x \leq D_{\max} \end{cases} \quad (2.19)$$

Integrating Equation 2.19 with the defect size distribution function in Equation 2.4, we have average pseudo critical area:

$$\hat{A}_{2nbr} = x_0^2 b_{ijk} \left[\frac{1}{2w_i} - \frac{1}{4(s_{ij} + w_i + w_j)} - \frac{1}{4(s_{ik} + w_i + w_k)} - \frac{w_j + w_k + s_{ij} + s_{ik}}{4D_{\max}^2} \right]. \quad (2.20)$$

Equations 2.16, 2.18 and 2.20 analytically describe the average pseudo open critical area for each kind of segment in a wire i . The total average open critical

area is the sum of all the average pseudo critical areas shown in these Equations. The explicit formula for the total average open critical area is:

$$A_{cr-open} = x_0^2 \sum_i \left(\sum_{nbr-j} \left(-\frac{b_{ij}}{4(s_{ij} + w_i + w_j)} - \frac{(s_{ij} + w_j)b_{ij}}{4D_{max}^2} \right) - \frac{l_{i1}}{2D_{max}} + \frac{w_i l_{i1}}{4D_{max}^2} - \frac{l_{i0}}{D_{max}} + \frac{w_i l_{i0}}{2D_{max}^2} + \frac{l_i}{2w_i} \right), \quad (2.21)$$

where l_i is the total length of the wire i , l_{i0} is the total length of the wire segments that have visible neighbors on one side only, b_{ij} is the length of the segment of wire i visible by neighbor j , s_{ij} is the spacing between wire i and its neighbor j , and D_{max} is the maximum defect size.

2.6 Improving Critical Area

In this section we will focus on the CA aspects of yield improvement. That is, reducing the critical area of any particular layer of an individual standard cell or of a whole routed design. In Chapter 6 we will present a comprehensive design flow view of yield yet it is important to emphasize at this point that yield optimization steps are all interlinked and must be dealt with collectively through a weighted total yield model. An example of that would be poly to poly spacing in a standard cell where the short CA for poly is improved but the diffusion capacitance of the impacted node is higher and thus might impact the performance of the cell, etc. This will be the only mention of that issue in this section as our focus here is limited to CA optimization.

2.6.1 Cell Library Yield Grading

In Chapter 1 we mentioned that designing for yield starts at the very basic steps of a design, and that yield could and should be designed in. In this section we will be covering the concept of yield grading for standard cells from the perspective of CA which is extensively covered in this chapter. Our choice of standard cell is a matter of practicality since standard cells are the basic building blocks of ASIC and SOC designs and since every standard cell is more or less unique and should be optimized individually for optimal CA yield; unlike structured arrays such as SRAFs where once the basic cell is optimized the task is practically complete.

In Figure 2.7 two examples are given of improving the short and open CA for poly and metal 1 respectively for a selected standard cell at no cost in area and hardly any cost in performance (node capacitance). For the poly gate shown the poly to poly spacing is labeled (a). We propose new positions for the poly gates as indicated in the white dotted lines to the right of the original gates. Obviously the contact to the power must be moved to the right as well. We did not show that here to avoid cluttering the figure. By doing that the shorts

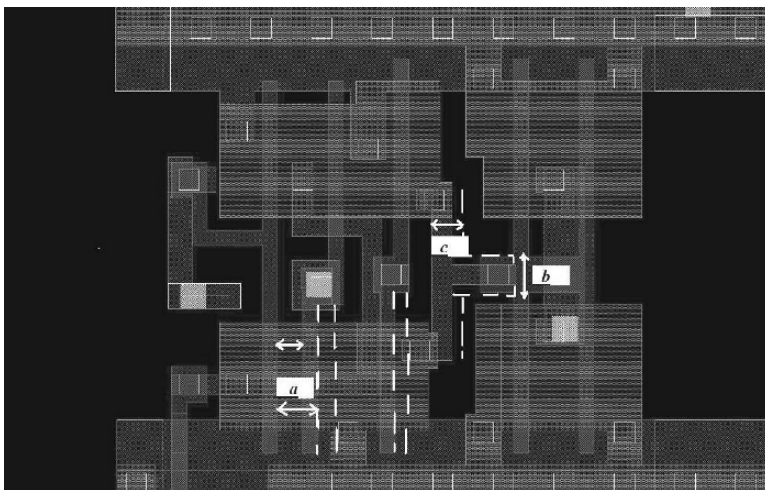


Figure 2.7. Example of Improving Poly Short CA and M1 Open CA

critical area for poly is improved as a result of the significant increase in (a), the distance to the next adjacent poly to the right is still much larger than the modified (a) and thus it does not take much figuring to realize that there is a net improvement in the poly CA number.

Similarly by widening the metal 1 around the contact (b) and metal 1 (c) it is obvious that the open CA for metal 1 is improved at practically absolutely no cost in area and practically no cost in performance.

Exercise:

- 1 Start with this layout and do all the poly and metal 1 widening and spreading that you believe will improve the open or short CA for poly and metal 1 without growing the size of the cell
- 2 Carry the exercise further to the limit of where improving the open CA will start hurting the short CA.
- 3 Do you think the change in parasitics is significant? Estimate impact on an unloaded cell and on a loaded cell (driving a fanout of 3).

The example we used in Figure 2.7 illustrates that there is a lot that can be done to improve the CA for opens and shorts for poly and metal 1 for a standard cell. Unfortunately most automatic layout generation tools are not that sophisticated and thus hand packing of the layout might be needed but it is worthwhile spending the time to do so as the library is built once and is used many times over.

Not all cells are as easy to exploit as the example we just gave. Some cells are pretty dense and hard to route in the first place. In such case multi-versions of

the cell are generated at the expense of area and performance (keeping things in perspective the interconnect delay is the dominant source of delay for a critical path in deep submicron). Another alternative would be weaker cells (less drive) if area is of the most importance.

Anyhow, what we want to stress in this section is that the classical arcs of delay, area, and power are not any more sufficient for choosing among alternatives in design synthesis. The added arc that is needed is the yield arc that is based on CA extraction and grading for poly, metal, vias, etc.

Coming up with the proper value for a yield metric for different versions of a cell is best done empirically through the use of test chips that have certain alternative equivalent structures positioned and repeated in such a way that the yield data gathered from them has statistical significance and merit. It is a tedious process but it is done once for a library (if the test structures are well thought through) and used repeatedly, also note that even a few percentage points of yield is worth the effort (typical yield differentials between alternatives are somewhere from zero to 7%).

Exercise: Although we will be covering lithography in the next chapter we encourage the reader with basic lithography knowledge to look at the same example of Figure 2.7 and add all the lithography artifacts that the reader believes will improve yield (such as contact enclosure, end of line extension etc.). Again, ask yourself if these artifacts will impact CA yield or performance. Always think of alternatives: what might a certain enhancement of a certain parameter do to other parameters?

2.6.2 Routing and Post Routing CA Yield Improvement - Average CA

Improving CA yield in the routing or post routing stage translates to one of two main operations. One is wire repositioning to improve the Short CA (wire spreading). The other is in the form of wire widening for Open CA. In this section we will discuss Short CA optimization by various wire-spreading algorithm. First we briefly cover the traditional approach of wire spreading which is a direct derivative of the traditional way of extracting CA. Then, we will go in detail into the “one iteration” optimization algorithm exploiting in Section 2.5.1 which has a higher level of accuracy and a much shorter execution time.

2.6.2.1 Traditional Routing and Post Routing Short CA Yield Improvement

Utilizing the available output of the traditional approaches for short CA extraction there are two main methodologies for routing and post routing short CA improvement [28–30]. One methodology starts with the extracted critical area value for one particular defect size, re-positioning a wire, and evaluates

the impact of the repositioning of the wire on the short CA to come up with the optimal wire position. Another methodology which is not much different does not restrict itself to optimizing wire positions for the short CA of one defect size but starts by moving the wire under question by a small amount, compute the change in the short CA, then repeat this process until no further improvement is obtained.

The first methodology of positioning the wires for optimizing the short CA for one defect size has a major flaw because a wire position that is optimal for short CA for a particular defect size is by default not optimal for any other defect size.

The second methodology which optimizes for the average CA is accurate but very time consuming as a re-calculation of the CA for all defect sizes has to be done for every iteration of wire movements.

2.6.2.2 Exploiting the Approximate CA Extraction Approach

Since the approximation approach of Section 2.5.1 calculates the CA in one iteration it is obvious that applying it to the second approach of the previous Section 2.6.2.1 is the optimal choice for wire spreading CA optimization. In this subsection we will go through a thorough formulation of using this approach to optimize yield through maximizing the average CA of a design.

2.6.2.3 Optimal Position of a Wire

In this section, we discuss how the optimal final position of a wire is computed. This is later used in our “one iteration” optimization. A wire’s optimal location depends on its position relative to all its visible neighbors and is calculated using the idea of the formulation based critical area evaluation. Since here we only consider the critical area around one particular wire the formula discussed earlier for a wire’s critical area has a slight change from the ones shown in Section 2.4.2. This is due to the fact that for the purpose of post layout optimization we are moving one wire at a time, therefore only the evaluation of critical area contributed by the wire pairs between the target wire and its visible neighbors is needed. For the purpose of simplicity in the presentation of the formulation we assume the maximum defect size $D_{\max} = \infty$, and consider only short critical area. Therefore the critical area between wire i and j for the segments of wire i that have one size only neighbor is

$$A_{cr-short}(i, j) = \left(\frac{1}{2s_{ij}} - \frac{1}{4(2s_{ij} + w_j)} \right) b_{ij}. \quad (2.22)$$

The critical area between wires i and j for the segments of wire i that have both side neighbors is:

$$A_{cr-short}(i, j) = \left(\frac{1}{2s_{ij}} - \frac{1}{4(2s_{ij} + w_j)} - \frac{1}{4(s_{ij} + s_{ik} + w_i)} \right) b_{ijk} \quad (2.23)$$

The critical areas of a wire i on its left and right sides are:

$$\begin{aligned}
 A_{cr}(i)_{left} &= \sum_{left-nbr-j} \frac{b_{ij}}{2s_{ij}} - \frac{b_{ij}}{4(2s_{ij}+w_j)} - \\
 &\quad \sum_{2-side-nbr} \frac{b_{ijk}}{4(s_{ij}+s_{ik}+w_i)}, \\
 A_{cr}(i)_{right} &= \sum_{right-nbr-k} \frac{b_{ik}}{2s_{ik}} - \frac{b_{ik}}{4(2s_{ik}+w_k)} - \\
 &\quad \sum_{2-side-nbr} \frac{b_{ijk}}{4(s_{ij}+s_{ik}+w_i)},
 \end{aligned} \tag{2.24}$$

If the wire width is kept unchanged, $s_{ij} + s_{ik} \triangleq m$ is a constant for any left neighbor wire j and right neighbor k . The final optimal spacing s_{ij}^* is

$$s_{ij}^* = \min_{s_{ij}} [A_{cr}(i)_{left} + A_{cr}(i)_{right}]. \tag{2.25}$$

The change between the optimal spacing and original spacing is the movement amount for this wire in order to minimize the critical area contributed by the wire pairs between this wire and its visible neighbors.

If we further approximate Equation 2.24 by replacing the summation with one neighbor only which contributes the most critical area on that side (or with the nearest visible neighbor on that side) and, assume same wire width for all the wires, we can calculate the optimal location for wire i explicitly:

$$s_{ij}^* = \frac{s_{ij} + s_{ik}}{1 + \sqrt{\frac{b_{ik}}{b_{ij}}}}. \tag{2.26}$$

Here $(s_{ij} + s_{ik})$ is the distance between the two side neighbors j and k . It is a constant because at this step we only move wire i .

Again, these assumptions are not necessary. If the exact solution is preferred it can be calculated without these assumptions. But the formula will be a little more complicated.

2.6.2.4 Optimization Algorithm Details

Here we describe the basic flow of the optimization algorithm and a few key implementation features. We focus on a single layer at one time and we leave vias untouched. Hence the only movable objects on a layer are the wires. Typically in routing each layer has a preferred direction of routing, either horizontal or vertical. Since the majority of the wires on a layer are in the preferred direction for that layer, the direction of movement is chosen to be perpendicular to the preferred direction on the layer, i.e., the horizontal wires are moved along the vertical axis and vice-versa. Furthermore, only the wires along the preferred direction are candidates for moving. For ease of explanation, let us

assume that we are optimizing a layer where the preferred direction is vertical. The algorithm works as follows:

- 1 For each vertical wire in the layer compute the difference between the critical areas on both sides. The difference between the critical areas on both sides is called the optimization potential.
- 2 Pick the wire with the largest optimization potential and shift it to the optimal location computed using Equation 2.26.
- 3 The optimization potentials of the visible neighbors of the shifted wire are re-computed (as their visible neighbors have changed) and Step 2 is repeated until all the movable objects have been processed once.

Note that once a wire is shifted to the optimal location it is locked and is not re-visited for the remainder of the iteration. Since the optimal location of a wire as computed in Equation 2.26 depends of the positions of the visible neighbors, it may help to run several iterations of the optimization routine to take into account these modifications.

In order to shift the wire to the final location (in Step 2 of the algorithm) without violating any DRC rules the following two steps have to be done efficiently:

- Spacing-visible neighbors : Find all the objects that are visible to the wire being moved modulo the spacing rules. We call these the *spacing-visible* neighbors to differentiate them from the visible neighbors used in the critical area computation. The *spacing-visible* neighbors of all the movable wires in the layout are computed in one sweep through the layout. An efficient variant of the algorithm outlined in [31] is used for the purpose. We leave the details of looking this up as an exercise to the reader.
- Wire-pushing: Given the *spacing-visible* neighbors and the optimal position of a wire push the wire to the specified optimal location. The basic idea of wire pushing is illustrated in Figure 2.8. Thus, the original wire is replaced by a set of horizontal and vertical wire segments such that most of the original wire is now located at the calculated optimal position while obeying the spacing rules of the given layer. The actual pushing algorithm is a modification of the well-known skyline algorithm [32].

Exercise Describe and outline the algorithm in [31]. How it can be used in the computing of spacing-visible neighbors?

2.6.2.5 Results

We also present some preliminary optimization results. The main objective of these experiments is to demonstrate the benefits of using the optimal position

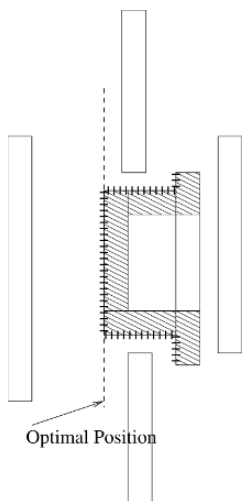


Figure 2.8. Illustration of Wire Pushing

computed in Section 2.6.2.3 for shifting the wires during optimization. To illustrate the advantage we compare this approach against a scheme where the wire is always pushed by a pre-specified amount in Step 2 of the algorithm (pushing by a pre-specified amount is commonly used in many commercial tools). The scheme where each wire is shifted by a pre-specified amount is referred to as the *Fixed* method, and the scheme where the wires are shifted by the optimal amount (as calculated by Equation 2.26) is referred to as *Optimal* method.

The results are shown in Table 2.2. Column 1 refers to the design; the number in parenthesis specifies the layer we worked on. The designs are the same four as we shown in Table 2.1. Column 2 specifies the number of movable objects on the layer. Columns 3, 4 and 5 specify the original critical area of the layer, the critical area after applying the fixed method, and the critical area after using the optimal method respectively. The results indicate that using the positions calculated by the method proposed in this book always produces much better results than moving the wire by a pre-specified amount. The runtime of both the approaches

Table 2.2. Critical Area Optimization for Shorts

Design	Movable seg.	short A_{cr} (Orig.)	short A_{cr} (Fixed)	short A_{cr} (Optimal)
design1(5)	2.8e03	7.494e03	7.095e03	6.430e03
design1(4)	9.396e03	1.094e05	9.994e04	9.921e04
design2(4)	20e03	2.300e05	2.300e05	2.267e05
design3(5)	14.051e03	2.035e05	1.982e05	1.960e05
design4(5)	12.62e03	2.807e05	2.628e05	2.604e05

are very comparable as computing the optimal position of a wire is very fast. Thus, this approach gives superior results at a negligible computational cost.

Exercise: Formulate the wire spreading problem for one of the two methodologies outlined in Section 2.6.2.1

2.6.3 Routing and Post Routing CA Yield Improvement - Weighted Average CA

In Section 2.6.2 we discussed three approaches for average short CA yield optimization, using mainly wire spreading without considering open CA. Short CA optimization was the focus in the past because in the processes at that time short defect was the dominating problem. However, in current deep sub-micro manufacturing process open defects are more of a problem. Hence both short CA and open CA (or total CA) need to be optimized. Optimizing only one of the two will not guarantee that total CA is improved. Furthermore, it is preferable for the total CA optimization algorithm in order to have the ability to address differing weights between short defects and open defects by adjusting the optimization heuristics automatically. The total CA is needed because of the defect clustering effect is an emerging fabric phenomena [33] where particles tend to selectively cluster in metal regions or in empty regions. Thus while the optimization algorithms are mathematically correct, they are unfortunately not realistic and do not necessarily result in improving yield. In fact they may result in worsening the yield. Since particles in the metal region can cause mainly opens and those in the empty region can mainly cause shorts, the primary effect of this variation is that the contribution of the short or open critical area to the random yield calculation can vary. This variation must be considered by the yield optimization solutions in order to ensure yield improvement at all times [34, 35].

Let's first revisit the rationale behind the typical short CA and open CA techniques - wire spreading and wire widening. If a pair of wires (i, j) belonging to different nets have segments visible to each other, as shown in Figure 2.1, their short critical area at a particular particle size x is (as shown in Equation 2.5)

$$A_c(x) = \begin{cases} 0 & \text{if } x < s_{ij}, \\ (x - s_{ij})b_{ij} & \text{if } x \geq s_{ij}. \end{cases} \quad (2.27)$$

where s_{ij} is the spacing between the two wires and b_{ij} is the visible length.

The open critical area on a wire for particle size x , as shown in Figure 2.2, is formulated as

$$A_o(x) = \begin{cases} 0 & \text{if } x \leq w_i, \\ (x - w_i)l_i & \text{if } w_i < x \leq D_{\max}, \end{cases} \quad (2.28)$$

where w_i is the wire width and l_i is the wire length.

After integrating the above equations with the particle size distribution function in Equation 2.4, and assuming the maximum particle size is infinity $D_{\max} = \infty$ we arrive at the following formula for average short and open critical areas:

$$A_s = \frac{b_{ij}}{2s_{ij}}, \quad (2.29)$$

$$A_o = \frac{l_i}{2w_i}. \quad (2.30)$$

Equation 2.29 shows that for same visible length b_{ij} an increase in spacing s_{ij} makes the short critical area smaller. This is the rationale behind wire-spreading techniques used to reduce the short critical area: move the wire or a segment of a wire away from the wire with which it has small spacing and large visible length. Similarly, Equation 2.30 clearly shows that wire-widening technique can effectively reduce the open critical area.

However, only the use of wire-spreading or wire-widening can negatively impact total critical area. For example wire-spreading typically introduces jogs and hence increases the wire length. Thus the actual wire length of the wire i is increased from l_i to $l_i + 2x$, where x is the move amount of the wire-spreading (i.e., the jog length). From Equation 2.30, the increase of wire length results in an increase of the open critical area. Therefore, after wire-spreading by amount x , the open critical area becomes $\hat{A}_o = \frac{l_i + 2x}{2w_i}$.

A similar effect is observed for wire-widening. Increase in the wire width reduces the open critical area but increases the short critical area. Widening the wire by y causes the following change in short critical area: $\hat{A}_s = \frac{b_{ij}}{2(s_{ij} - y/2)} + \frac{b_{ik}}{2(s_{ik} - y/2)}$.

Therefore it is not necessarily true that a random yield optimization algorithm based on minimizing only the short or open critical areas can always minimize the total critical area and thereby improve the total random yield.

2.6.3.1 Current Critical Area Minimization Methods

There has been a lot of work done to minimize critical area during routing or post-routing [28, 29]. However most of the techniques aim to minimize only the short or open critical area with the majority of emphasis on short critical area minimization. More recently new techniques have targeted both short and open critical area minimization simultaneously.

In this section, we discuss a commercially available prominent critical area minimization solution. The algorithm first does wire-spreading followed by wire-widening.

The wire-spreading step of the algorithm works as follows. The algorithm divides the entire routing region into switch-boxes and processes them one by one from sparse to dense. Within a switch-box wires longer than a pre-

specified threshold are candidates for spreading. For each such wire the two sides are analyzed and segments of the wire that only have a neighbor on one side are moved to the adjacent track away from its neighbor. Typically jogs are introduced to maintain connectivity between the displaced segment and the remainder of the wire. However, vias can also be moved if space on the upper and lower layers permits the lengthening of corresponding segments to maintain connectivity. We refer to the wire-spreading step of this method as the *track-based wire-spreading*.

As discussed before the introduced jogs increase the wire length and hence increase the open critical area. To counter this during the wire widening step of the algorithm the introduced jogs are widened as much as possible without introducing DRC errors while still maintaining connectivity.

2.6.3.2 Limitations of Current Method

In spite of performing both wire-spreading and wire-widening, the current method suffers from some key limitations. First, always performing wire-spreading before wire-widening is wasteful if the short critical area is not a dominant factor in the total yield loss of a given design. An example of such a scenario is when the original open critical area is much larger than the short critical area and hence contributes more to yield loss. Short critical area reduction in this case is undesirable and wasteful since it does not necessarily minimize the total critical area (the open critical area might increase) and could also introduce new problems like OPC issues due to the increased presence of jogs (OPC will be addressed in the next chapter).

In addition, the current static solution does not take into account the possibility that the short and open critical areas might not necessarily be equally weighted in the random yield calculation. This is a growing trend in current and future processes. Recall that in the yield model in Section 2.3, the yield relies on the product of $A_{cr}D_0$, where A_{cr} is critical area and D_0 is the particle density. With process advances, in many modern processes, it has been observed that the particles tend to selectively cluster in the metal or in empty regions of the chip, thus resulting in different densities in these regions [33]. For example, one fab we collaborated with found that the particle density in metal regions was much larger than the corresponding value in empty regions for one of their processes. Under these circumstances, it is not sufficient to only consider the critical area in the yield optimization algorithms. The different particle densities in the metal and empty regions also should be considered.

In this section, we introduce a modified total critical area formulation that takes clustering into account. Then we discuss a yield optimization solution that uses the new critical area formulation to efficiently combine wire-widening and wire-spreading to improve the total yield. This targeted approach ensures that random yield is always improved.

2.6.3.3 A Proposed Alternate Solution - Weighted Total Critical Area Formulation

The short critical areas are centered between the wires, and the open critical areas are centered on the wires. Theoretically, total critical area should be the union of short critical area and open critical area, because there might be overlaps between short and open critical areas for large particle sizes. However, in typical fabs, most particles are not too large resulting in a low probability of occurrence for the large particle sizes. Therefore, it is fair to approximate the total critical area as the sum of short critical area and open critical area.

As we discussed earlier in current processes starting at 90nm and moving below it has been observed that the particles are no longer uniformly distributed. Instead the particle distribution on metal regions and that on empty regions are uniform respectively but with different densities.¹

One way to handle this clustering effect in the current yield models is to use different particle densities D_0 for these two different regions. An equivalent way to handle this effect is to introduce weighting factors w_s and w_o for short and open critical areas while using the same average particle density D_0 . This is preferable as the routing tool can also use this weight information to guide the optimization suitably. Hence the weighted total critical area is formulated as

$$A_{wtotal} = w_s * A_{short} + w_o * A_{open} \quad (2.31)$$

It is clear that the weighted critical area is a proxy of the random yield and is the value that needs to be minimized for improving random yield. Hence it is used as the cost function to drive our algorithm for improving the total random yield.

2.6.3.4 Yield Optimization Algorithm Details

The proposed yield optimization algorithm works layer-by-layer. Thus, vias are not touched and the only movable objects on a layer are the wires². Typically, in routing, each layer has a preferred direction of routing, either horizontal or vertical. Since the majority of the wires on a layer are in the preferred direction, the direction of movement is chosen to be orthogonal to the preferred direction on the layer. Furthermore, only the wires along the preferred direction are candidates for moving.

The algorithm computes the optimization potential of all the wires. The optimization potential of a wire is a function of its weighted short and weighted

¹This clustering effect cannot be addressed by α in the Negative Binomial model ($Y_r = \frac{1}{(1 + \frac{A_{cr} D_0}{\alpha})^\alpha}$) since it does not distinguish between particles on the metal versus empty regions and also cannot accommodate uniform particle densities in each individual region.

²The proposed algorithm can be easily extended to the case where the vias can be moved as well.

open critical area and is a measure of both the severity of the problem in the local area and the flexibility available for improvement. The wire with the largest optimization potential is processed first and locked. It is widened or spread depending on the relationship between the ratio of the weighted open and the weighted short critical area of the wire and the corresponding ratio for the layer. This gives an indication as to which component of the critical area of the wire contributes more to the weighted critical area of the layer. The dominant component is then reduced using the appropriate technique, either widening or spreading. This results in a reduction in the weighted critical area of the wire. Subsequently, the optimization potentials of the remaining wires are updated as needed. Then, the wire with the largest optimization potential among the unlocked wires is picked and the process is repeated.

From the above description, we can see that the algorithm dynamically adjusts the number of wires that are widened and spread in accordance with the absolute values and the weighting factors of the open and short critical areas. The amount by which a wire is spread or widened also varies depending on the configuration of its neighboring wires and is described later in the section. Since the weighted critical area of the entire layer is simply the summation of the weighted critical areas of the individual wires, reductions on the weighted critical area of the wires ensures a reduction of the weighted critical area of the entire layer.

To summarize, the proposed algorithm takes the routed layer and the weighting factors of the open and short critical areas as input and works in the following sequence.

- 1 Compute the *layer_CA_ratio* which is a function of the weighted open and weighted short critical area of the layer.
- 2 For each preferred-direction wire in the layer, compute the *optimization potential*.
- 3 Pick the wire *i* with the largest optimization potential.
 - (a) Compute the *wire_CA_ratio* = (weighted open critical area/weighted short critical area) of *i*.
 - (b) If the *wire_CA_ratio* is greater than *layer_CA_ratio*, do *wire-widening*. Else, do *wire-spreading*.
 - (c) Re-compute the optimization potentials of the visible neighbors of *i* (as their visible neighbors have changed). Lock *i*.
- 4 Go to Step 3 if there is an unlocked preferred-direction wire.

In order to widen a wire or spread a wire without violating any DRC rules (Step 3 of the algorithm), the following steps have to be done efficiently:

- *Spacing-visible neighbors*: Find all the objects that are visible to the wire being moved, modulo the spacing rules. We call these the *spacing-visible*

neighbors to differentiate them from the visible neighbors used in the critical area computation. The *spacing-visible* neighbors of all the movable wires in the layout are computed in one sweep through the layout. An efficient variant of the algorithm outlined in [31] is used for the purpose. We skip the details here for the sake of brevity. The reader is encouraged to list them as an exercise.

- *Wire-spreading*: The spreading of a specific wire works as follows. First, the optimal position of the wire is computed. This is the position at which the short critical area is balanced on both sides and is typically set to be a multiple of the manufacturing grid. Given the *spacing-visible* neighbors and the optimal position, the wire is pushed to the specified optimal location. The basic idea of wire pushing is illustrated in Figure 2.8. The algorithm is a modification of the well-known skyline algorithm [32]. DRC rules are used to determine the desired distance from each *spacing-visible* neighbor and the skyline created from these displacements gives the final profile. Thus, the original wire is replaced by new wire segments such that most of the original wire is at the optimal position. Jogs are introduced to maintain connectivity. Suitable restrictions are imposed to ensure that the jog length is not smaller than a certain pre-specified amount, as lithographic correction methods like OPC tend to have problems with short jogs. We will refer to this wire-spreading step in our proposed algorithm as the *sensitivity-based* wire-spreading since it uses the critical area formulation to derive the movement amount of wire-spreading for each wire.

The *track-based* wire-spreading algorithm can also be used at this step for spreading a particular wire, as used in the *static* method. In Section 2.7, we show that both methods perform equally well for most cases, though the *sensitivity-based* wire-spreading algorithm tends to be more consistent in minimizing the short critical area.

- *Wire-widening*: A similar skyline-based method is used to determine the optimal widths of each segment of the wire. This time the *spacing-visible* neighbors on both sides are used. A skyline is generated for each side such that DRC rules are not violated. Then, a modified skyline that merges the two skylines (one of the skylines is flipped to ensure both are in the same direction) is computed and used to determine the optimal width of each wire segment. Again, suitable restrictions are imposed to ensure that too many short segments are not created. The basic idea is illustrated in Figure 2.9.

It should be noted that the algorithm has similar runtime complexity as the currently available static methods. This is because the algorithm processes each wire only once like the previous methods. The extra runtime overhead due to repeated local re-evaluations of the critical area of the neighboring wires is negligible as the neighbor relationship is maintained in a graph where a node

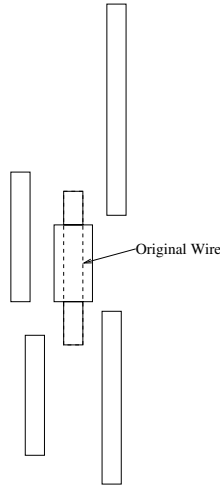


Figure 2.9. Illustration of Wire-widening

exists for every wire and an edge exists between any two wires that are visible to each other (i.e. a line can be drawn to intersect these wires and no other layout objects). Thus, a re-evaluation involves a lookup operation to find all the wires that have an edge to a given wire and an arithmetic evaluation to find the new values for the open and short critical area of the wire.

2.6.4 Key Benefits of the Proposed Algorithm

The algorithm uses the *layer_CA_ratio* and the *wire_CA_ratio* to decide which wires to widen and which ones to spread. The value of *layer_CA_ratio* decreases as the weighted open critical area contributes more to the total weighted critical area. Thus more wires are widened. Analogously, the value of *layer_CA_ratio* increases as the weighted short critical area dominates and more wires are spread.

Experimental results in Section 2.7 show that the proposed algorithm consistently reduces the weighted critical area when compared to the *static* method and obtains better optimization quality. This can be attributed to two reasons: (1) The algorithm dynamically selects the appropriate critical area minimization technique at each wire such that the weighted critical area of each wire and hence the whole layer is minimized. (2) A fast and incremental analysis engine is used during each iteration of the algorithm to obtain the most updated values of the weighted critical area. Thus, optimization decisions are actively driven by weighted critical area and take into account previous optimization decisions. This is in contrast to the static method where each wire is spread or widened by

the same amount independent of its contribution to the weighted critical area of the layer.

Another benefit is that the proposed solution also provides a framework that can incorporate any widening or spreading algorithms that process one wire at a time.

2.7 Experimental Results

In this section, we first show the correlation between the computed critical area values by fast analysis engine and the corresponding values from a fab. Then we present a comparison between the weighted critical area reductions obtained by the proposed algorithm and the static method.

2.7.1 Validation of Fast Critical Area Analysis Evaluation

An efficient internal critical area analysis engine is integrated in the router to quickly evaluate critical areas for the optimization algorithms, both locally and globally. This engine correlates very well with the golden critical area computation tool of a fab. Figures 2.10 and 2.11 are plots comparing our critical area computation with the tool from the fab for metal 4 of a 65nm layout. Similar good correlation results are observed on the other metal layers as well.

2.7.2 Comparison of Critical Area Reductions

We compared the critical area reductions from two methods: one is the current static method and the other is the proposed weighted critical area driven

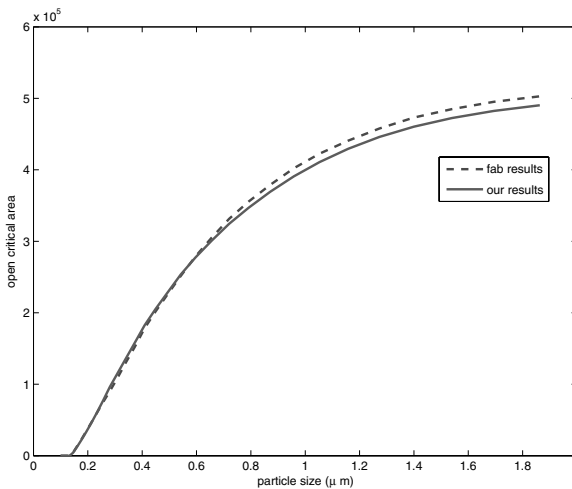


Figure 2.10. Open Critical Area Correlation

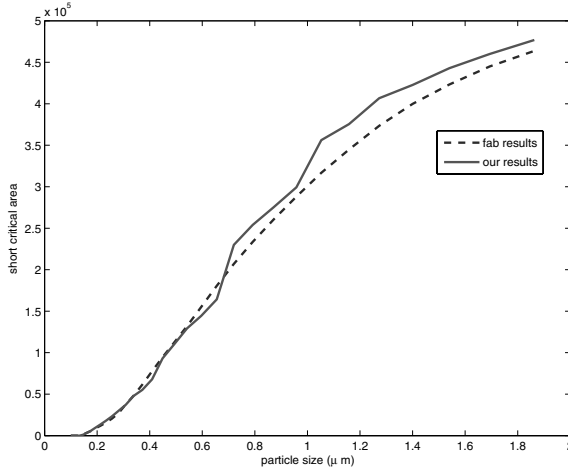


Figure 2.11. Short Critical Area Correlation

method. The experiments were performed on 7 routed layouts of practical designs. Layouts 1, 2, and 3 are from 65nm designs. Layouts 4, 5, 6, and 7 are from 90nm designs.

Table 2.3 shows the critical area reduction comparison when the weight $w = 0.1$. Here the weight is defined as $w = w_o/w_s$, where w_o and w_s are the relative weights for open and short critical area, as defined in Section 2.6.3.3. It is equivalent to the ratio of particle density in metal regions over that in empty regions. A small weight of $w = 0.1$ implies that short failures are more likely to happen and hence the contribution of the short critical area to the total weighted critical area computation is emphasized.

Table 2.4 shows the critical area reduction comparison when the weight $w = 10$. This weight implies the scenario that the open failures are more likely to happen; hence open critical area is emphasized in the total weighted critical area computation.

Table 2.3. Short, Open, and Total Weighted Critical Area Reductions Comparison, with $w = 0.1$

layouts	org. shortCA (μm^2)	org. openCA (μm^2)	static method			proposed method		
			short red.(%)	open red.(%)	total red.(%)	short red.(%)	open red.(%)	total red.(%)
1	8418.4	18304.5	15.3	-1.4	12.3	15.3	-7.3	11.2
2	4521.4	10331.4	22.1	-1.2	17.8	21.3	-2.3	16.9
3	543.9	2085.6	30.4	0.8	22.2	43.0	-0.7	30.9
4	60848.1	134078.3	-8.2	-9.7	-8.5	0	0.3	0
5	104574.3	162670.8	-45.4	-31.6	-43.6	17.3	-4.1	14.4
6	6703.8	22437.7	27.9	1.53	21.3	25.1	-1.8	18.3
7	14538.2	30049.2	7.5	-7.4	5.0	11.2	-3.3	8.7
Average					3.79			14.34

Table 2.4. Short, Open, and Total Weighted Critical Area Reductions Comparison, with $w = 10$

layouts	org. shortCA (μm^2)	org. openCA (μm^2)	static method			proposed method		
			short red.(%)	open red.(%)	total red.(%)	short red.(%)	open red.(%)	total red.(%)
1	8418.4	18304.5	15.3	-1.4	-0.7	-0.5	3.5	3.3
2	4521.4	10331.4	22.1	-1.2	-0.2	-2.2	10.0	9.5
3	543.9	2085.6	30.4	0.8	1.6	-0.9	8.0	7.8
4	60848.1	134078.3	-8.2	-9.7	-9.6	-0.01	0.14	0.14
5	104574.3	162670.8	-45.4	-31.6	-32.5	-0.03	0.29	0.27
6	6703.8	22437.7	27.9	1.53	2.3	-48.3	34.0	31.6
7	14538.2	30049.2	7.5	-7.4	-6.7	-33.0	24.9	22.2
Average					-6.54			10.69

In both Table 2.3 and Table 2.4, the original short and open critical areas of the 7 layouts are reported in the 2nd and 3rd column. The reductions in short, open, and total weighted critical areas obtained by static method are reported in columns 4–6. Columns 7–9 report the reductions in short, open, and total weighted critical areas obtained by our proposed method. The average improvement in the total weighted critical area reductions by the two methods are reported in the last row. The comparison of the average improvements clearly shows the advantage of our proposed method.

2.7.3 Discussion

It should be noted that for the *static* method, the open and short critical area reductions are identical for both tables. This is due to the fact that a static order of critical area reduction techniques is performed independent of the relative magnitudes of the short and open critical area or their relative weights. Hence, the weighted critical area of the whole layer is not always reduced. It is especially problematic for the scenario when weighted open critical area is more significant. Table 2.4 shows that for this case, the total weighted critical areas are worse for 5 out of 7 designs. This happens because wire-spreading is always performed first, which is wasteful when the weighted short critical area is smaller than the weighted open critical area.

On the other hand, our proposed method takes the different contributions of the weighted short and open critical areas into account. Therefore, the total weighted critical area is consistently improved. When the short critical area is emphasized ($w = 0.1$, as shown in Table 2.3), it is improved more. The average improvement on total weighted critical area for the 7 designs is 14.34%. Similarly, when open critical area is emphasized, ($w = 10$, as shown in Table 2.4), it is improved more. The average improvement on total weighted critical area for the 7 designs is 10.69%.

Another benefit of the proposed solution is that the wire-spreading technique in our algorithm is driven by critical area (we call it the *sensitivity-based* algorithm). The *track-based* algorithm can also be used for the wire-spreading portion of the proposed algorithm. However, as we can see from Table 2.3, even when short critical area is emphasized, the *track-based* algorithm can not always guarantee positive improvement in short critical area and total weighted critical

area. This happens because the short critical area is not directly used as a cost function to drive the wire-spreading³. In comparison, the *sensitivity-based* algorithm always guarantees positive improvement and hence consistently improves the random yield. One advantage of the *track-based* wire-spreading is that it makes the subsequent ECO steps easier. But the *sensitivity-based* method can also incorporate ECO by restricting the wire movement to only routing tracks or half tracks. While this might result in some reduction in optimization ability, it will still consistently reduce the short critical area.

It should be noted that both wire-spreading and wire-widening can impact timing. Wire-spreading increases the length of wires and can hence worsens timing. Wire-widening reduces wire resistance and increases capacitance slightly and can consequently cause setup violations. One should incorporate a simple timing model in our yield optimization algorithm to better control their impact on timing.

2.8 Conclusions

In this chapter we covered the concept of critical area of a design with its sub-categories of open and short critical areas and how CA is used in various basic random yield models. We covered classical derivation techniques and introduced a fast approximation technique that calculates the CA of a design in one pass. Then we covered the area of improving CA and thus yield at the basic cell level then at the routing and post routing level. The impact of defect clustering and of weighted open and short CA was addressed next and a CA optimization technique that deals with these aspects was covered in detail.

The concept of random yield optimization is perhaps the oldest and most thoroughly studied in the IC industry, yet it is no less important today at 65 nm and beyond than it was at 3nm and older technology nodes.

³Of course in practice, it is possible to make no change to the layout if a negative improvement in the short critical area is obtained.

Chapter 3

SYSTEMATIC YIELD - LITHOGRAPHY

3.1 Introduction

As technology advances from one technology node to the next in the nano era of CMOS processing one theme that must be carefully attended to is the transition from random to systematic failure modes as the main cause of yield loss. And, the deeper we go in the nano-era of technology the more systematic yield loss becomes the dominant yield loss determining factor. One of the main reasons for that is the decrease in the process parameter window and its implication on manufacturability and yield. Two factors: process excursion and process integration [36] makes the process parameter window tighter with every generation. Given that the Argon Fluoride (ArF) illumination source with a λ (wavelength) of 193nm remains for all practical purposes the main source of illumination for the optically driven IC manufacturing process at the 45 nm technology node and most likely at the 32nm node as well we are getting to the point where with the given tightening of the process window we are not guaranteed any wafer imprint for critical geometries at all without heavy manipulation of the drawn geometries and of the optical steps in the process flow. And, that is why the distinction between DFM and DFY becomes a mute point. You really cannot yield what you cannot manufacture in the first place. Dealing with lithography issues for the optical IC processing system is the key to manufacturability and yield. This chapter will focus specifically on lithography.

3.2 Optics Fundamentals

The basic system of optical lithography for IC manufacturing is shown in Figure 3.1. Its main components are the illumination source, a monochromatic source with a specific wavelength. For technology nodes currently in

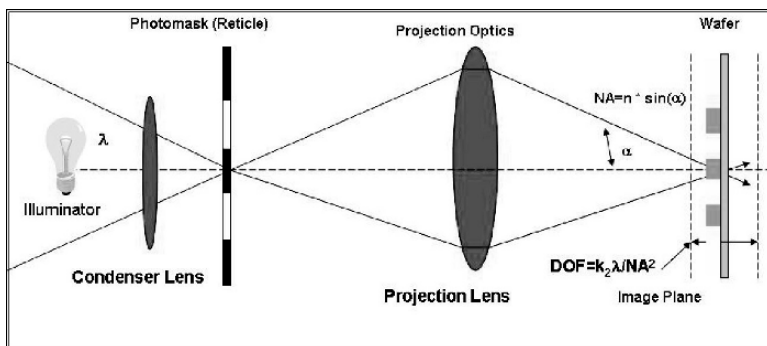


Figure 3.1. Basic Optical Lithography IC Manufacturing System

production and development the main two sources are Krypton Fluoride (KrF) with wavelength $\lambda = 248$ nm used in technology nodes 130 nm and higher, and ArF with wavelength $\lambda = 193$ nm used in technology nodes 130 nm and beyond. ArF is currently used in 90nm, 65nm, 45nm, and is the default expectation for the 32nm node given that efforts for developing the Fluorine (F2) 157 nm illumination source has been all but abandoned due to significant technical hurdles; and that EUV lithography is still years away from a full production mode.

The condensation lens shown next to the illumination source is for focusing the monochromatic light source on the 4x or 5x (4x most common) photo-mask. The illumination pupil (not shown here goes between illumination source and condenser lens) is optimized to maximize the process window and to simultaneously maintain the fidelity of the pattern [37]. The photo-mask (also known as reticle) is made of fused quartz on which a light absorbing material (chrome) is patterned reflecting the digitized geometry to be projected on the wafer. The next component in the projection lens, with a numerical aperture NA where $NA = n \cdot \sin(\alpha)$ and α is the angle shown in Figure 3.1. The n is a diffraction index characteristic of the medium of projection. It is one for air, greater than 1 for water or oil. It is easy to see from the equation for NA that the maximum theoretical value for NA is one. A more realistic range for NA is 0.65 to 0.85 for air as the medium, but with some oils experimented with recently the overall effective NA of greater than 1.25 can be achieved. The practice of applying a medium other than air between the projection lens and the wafer is known as immersion technology and has been used for the 90 nm node to improve resolution. The projection lens reduces the light that passes through the mask onto the wafer. Wafers are coated with a photoresist (positive or negative) and the projected light develops the photoresist such that the projected pattern (or its complement) is etched away with chemicals defining the pattern on the silicon wafer.

The optics of the system are covered by Rayleigh's Equations governing system resolution and depth of focus

$$\text{Resolution}(R) = k_1 \times \lambda / NA \quad (3.1)$$

$$\text{Depth of Focus}(DOF) = k_2 \times \lambda / NA^2 \quad (3.2)$$

Where λ = Exposure wavelength, NA = Numerical Aperture, k_1, k_2 = unit-less process "goodness" parameters or "scaling factors", typical range for k_1 0.25 - 0.7, and typical value of k_2 0.5 Reducing k_1 of a lithography system is an ongoing challenge for lithography tools manufacturers.

Note that by increasing NA, R increases but DOF suffers (Equations 3.1 and 3.2). Resolution, or critical dimension (CD), is defined as the half-pitch of dense lines and spaces pattern [38]. Maximum wafer CD = $0.25 \times \lambda / NA$. And, for a 4X projection max CD mask = λ / NA . Theoretical maximum NA in air is 1, and with immersion technology lets assume that a NA of 1.25 is achievable. That makes max CD mask is $0.8 \times \lambda$. Therefore for ArF with λ of 193nm that number is 155 nm for a mask and 39 nm for a wafer. Depth of focus is defined as the distance along the optical axis over which the image is in focus (Figure 3.1) or put differently it is the distance which the wafer plane can be moved (think flatness) while maintaining an acceptably sharp image of projection for that lens position. Another way of defining DOF is the distance between the negative focal failure point and the positive focal failure point of a given image [39].

3.3 Basic Design Flow

The flow chart of Figure 3.2 is typical of an ASIC or an SOC implementation. It has been the classical way of doing designs since the early days of the IC industry. Before the advent of 130nm a clean (verified) design GDSII was processed by a mask preparation software in terms of fracturing and bias and a mask was then produced (written). No further processing of the GDSII is needed. And, the idea is that for all practical purposes what you see (digitize) is what you get on the wafer.

That was the case when the half pitch of the feature produced was larger or comparable to the wavelength of the light source used for illumination. Once the half-pitch of the features became smaller than the incident light wavelength printability became an issue. Resolution enhancement techniques (RET) as well as lens manufacturing advances the optical medium manipulation, and light source polarization techniques became required to push the limits of the ArF light source capabilities.

Exercise: For ArF with $\lambda = 193\text{nm}$, a NA of 0.65, and a k_1 of 0.35 calculate the maximum possible resolution for the optical system (as was done in Section 3.2)

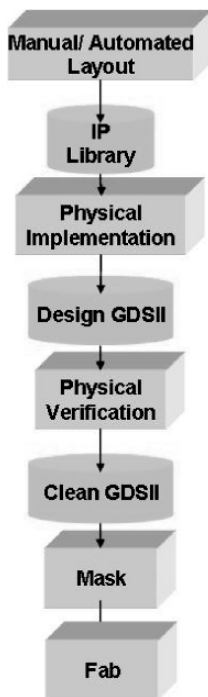


Figure 3.2. Basic Design flow

From Rayleigh’s resolution equation (Equation 3.1) it is obvious that in order to improve resolution for a given wavelength of the illumination source we need to minimize “ k_1 ” and maximize the numerical aperture “NA” of the projection lens. However, there is a fundamental limit for $k_1 = 0.25$ and, in order to achieve that limit we need to apply heavy RET, have optics of very low aberration, and apply resists that have increasingly higher dissolution contrast and smaller diffusion length [37]. Also, as Rayleigh’s DOF equation (Equation 3.2) for DOF indicates, every time we increase NA in an effort to improve the resolution of the optical system, DOF suffers and additional optical “workarounds” are needed to enhance DOF (increase k_2 , the fudge factor).

For the optical lithography part of the process one could look at the total margin in a feature [40] as:

$$\Delta feature = \Delta sizing + \Delta placement + \Delta edge + \Delta depth + \Delta transmission + \Delta slope \quad (3.3)$$

We will not go into the significance and detailed meaning of each term here beyond the self evident meaning gleaned from the equation. But it becomes clear that in order to establish a system of low k_1 there are many parameters to be monitored and closely controlled [37] namely lens aberrations,

pupil transmission, illumination profiles, illumination polarization, system vibrations, scattered light, exposure dose control, focus, and leveling control [41]. As we will see later in this chapter this basic flow did not survive for 90nm and beyond. More steps were needed increasing the complexity and cost of the flow.

3.4 Lithography and Process Issues

In this section we will touch briefly on the four main components that contribute to the overall integrity of the optical lithography design flow. We mention them and describe them briefly as they are the reason behind our need for RET.

3.4.1 Masks Writing

We will be covering mask writing and data preparation in Section 3.9 of this Chapter, but here we want to cover some basics associated with mask writing [42, 43] as it pertains to errors introduced into the lithography process and the consequences of these errors in terms of RET requirements.

Even without any RET mask making introduces errors associated with the limited capabilities and tolerances of the mask writing equipment (e-beam or laser) and the mask making starting material including absolute mask flatness. An error free mask is an expensive proposition.

3.4.2 Optical System Interactions

The goal of lithography is to end up with images on the wafer that satisfy certain tolerances, uniformities, and geometric integrity. Optical system limitations in terms of non-uniform exposure and defocus results in fluctuations in uniformity and linearity and sometimes results in printed geometries outside of the tolerances window for the process altogether. Add to that well know limitations and phenomena such as end of line shortening [44] and corner rounding which gets exacerbated in subwavelength lithography and one gets another compelling reason for RET implementation in the subwavelength lithography processing space. The issue of defocus deserves special attention as it gets critical in the overall lithography “budget” at 90 nm and beyond. The projected image from a mask on the wafer could result in a good CD under perfect focus conditions. But photoresist is a three-dimensional body with a particular topology and a finite thickness that experiences fluctuations due to the manufacturing process. This results in a finite defocus that can result in a poor projection of an image [44]. Such a defocus should be compensated for and budgeted for in the lithography process.

3.4.3 Resist

The basic simplified resist model is a threshold based model where the resist was fully developed for energy levels above the threshold and fully undeveloped

for any energy level lower than that threshold. The reality is a more complex model due to factors such as acid diffusion, standing waves, and post exposure diffusion [44]. The basic model was adequate for half pitch CDs greater than or comparable to the illumination source wavelength. More complicated resist models are needed for subwavelength lithography to capture these effects.

3.4.4 Etch

Etch is another non-uniform step in the lithography process flow. Part of the non-uniformity is due to loading effect of wafers and is thus radial in nature but nonetheless results in non-uniform distribution of etching agents across the wafer. Other reason of non-uniformity is pattern dependence. For the latter cause of non uniformity compensation in the form of “dummy fills” is possible. This issue will be treated in the next chapter.

3.5 Resolution Enhancement Technique (RET)

In section 3.2 we covered Rayleigh’s equations involving resolution and depth of focus and went through the calculations for the resolution limit for ArF with a 4X stepper optical system. It is thus obvious that with ArF as the source of illumination and as we pass the 100nm threshold resolution will suffer and something must be done towards achieving a wafer printability as close to the original digitized geometry as possible. Increasing the NA of the medium has limitations and causes a worsening of the DOF. While an enhanced NA system is applied, it is not sufficient to solve resolution issues and other techniques are certainly needed to compensate for the worsening depth of focus incurred in the process of improving resolution. The collective set of techniques applied to either the layout or the optical system towards achieving the good wafer printability goal is referred to as resolution enhancement techniques. They include, but are not limited to:

- Optical proximity correction (OPC)
- Phase-shift mask (PSM)
- Attenuated phase-shift mask (APSM)
- Off axis illumination (OAI)
- Double dipole lithography (DDL)
- Sub-resolution assist features (SRAF)

Some of those techniques such as OPC are referred to as “soft” RET. They involve geometric manipulation of the layout or adding scatter patterns. Other techniques such as PSM are considered “hard” RET and they involve physical etching of the mask quartz thickness. At 90 nm soft RET techniques were

most of the time sufficient to get by for a reasonable printability. At 45 nm a combination of soft and hard RET techniques are needed to achieve the same goals. In this section we will cover a plurality of those techniques.

Before getting into RET practices this is a good place to re-state the four characteristics of light as the basis of understanding what can be exploited towards improving resolution and DOF, and thus printability. These characteristics are:

- Wavelength: illumination source and traveling media defined
- Amplitude: that is what OPC manipulates
- Direction: illumination schemes defined (OAI)
- Phase: Mask medium and characteristics defined (PSM)

3.5.1 Optical Proximity Correction (OPC)

In the top row of Figure 3.3 the layout of a simple geometry at 90 nm is shown and its corresponding wafer image after the lithography process. The row below shows the same layout with OPC performed on it and the corresponding wafer image. The OPC'd image is much closer to the intended digitized geometry than the non-OPC'd one. This is the objective of applying OPC. But first lets define OPC. OPC is the process of modifying a drawn layout (modify the mask itself) in order to compensate for the non-ideal behavior of the lithography process and

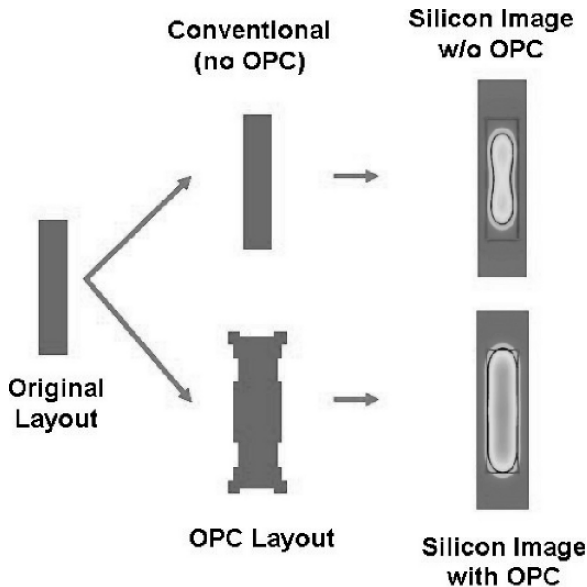


Figure 3.3. Impact of OPC on Printability at 90 nm (Zero Defocus)

in order to bring the final wafer printout as close to the original intended layout as possible. The procedure involves dividing the initial polygon into smaller and simpler segments and modifying the segments by adding or removing artifacts to the layout. OPC could be rule based or model based. In rule based OPC straightforward rules are applied to modify the underlying layout and simulating their effects while in model based OPC a feedback simulation system is applied back and forth on a geometry to end up with an optimal solution as close to the design intent as possible. It is important to stress that an exact inverse formulation mapping the desired wafer image back to layout does not exist and will be extremely complicated and non-linear if it were to exist because we are dealing with wave limit behavior of optics and three dimensional non-linear behavior of resist add to that the errors generated by an imperfect mask[45]. Thus it is important to know that there is no single OPC solution and that it is an interactive approximation based on simulation around a model in order to bring the printed image to within a specified tolerance (error) from the ideal desired image.

The main objectives of OPC are:

- 1 restore dimensional accuracy
- 2 increase overall process window
- 3 improve systematic and functional yield
- 4 improve chip performance

In the previous Figure 3.3 we showed the need for OPC at 90nm due to resolution effects only assuming zero defocus. Figure 3.4 simulates the OPC/non-OPC effects for resolution and defocus at 90nm and at 65 nm. It becomes

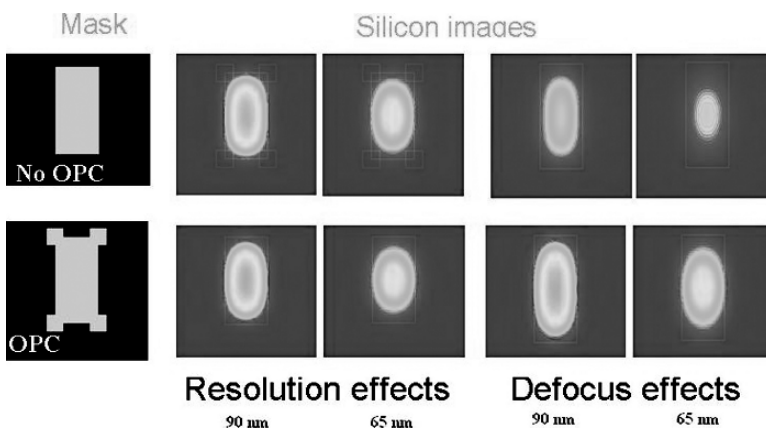


Figure 3.4. Silicon Wafer Image with/without OPC and with/without Defocus

clear that at 65nm and beyond OPC is not anymore a voluntary enhancement to improve printability but a necessity if any image is to be printed altogether.

3.5.1.1 Rule Based OPC

The two main categories of OPC are rule based and model based. Rule based is more simpler as it involves applying specific rules and recipes to specific geometries of various layers. Simulations are done first for a particular lithography system to come up with the geometry correction rules needed and to assess the effect of the performed OPC on the final image. Also, experimental data obtained from the lithography system in consideration is used to fine tune the geometric procedures. This has the great advantage of a fast correction time as no simulation is needed after the added OPC corrections [44]. Given that OPC is usually applied to a whole design being processed it is clear that applying rule based OPC is more manageable than the model based OPC which involves interactive simulation with more variables and is thus computationally expensive. However, rule based OPC might be inadequate in many cases and that leaves no alternative to model based OPC.

3.5.1.2 Model Based OPC

Model-based OPC is more complex and involves simulation of various process effects, which may be accomplished by computing a weighted sum of pre-simulated results for simple edges and corners that are stored in a library. Again the role of experimental data in constructing a model for proximity effects is crucial [46–48]. Some early models set up two separate models, one for the optics involved and another for the process parameters involved in an effort to simplify the optimization process [49–51]. Managing the large geometry database is CPU intensive, and the simulations involved in model-based OPC are even more CPU intensive since there is no closed form solution for the optimal layout. Thus applying OPC to a whole design using model based OPC is very time consuming. Model based OPC is needed to compensate for the higher systematic patterning distortions due to the lower k_1 lithography process [52]. One of the main drivers for model based OPC versus rule based OPC is dealing with isolated feature DOF issues which rule based OPC does not deal (in general) properly with. Convolution is the basis of most OPC modeling methods. The convolution process captures proximity effects at a specific point in the pattern by combining the influences of nearby pattern elements. The convolution kernel usually places a higher weight on the ambit of the evaluation point defined to include areas and patterns that are closest to it.

Figure 3.5 shows a simplified illustration of model based OPC. The initial layout (design intent) is run against the OPC model and an initial set of OPC modifications are applied followed by some quick simulations to determine the closeness of the resulting output image to the design intent. The process is

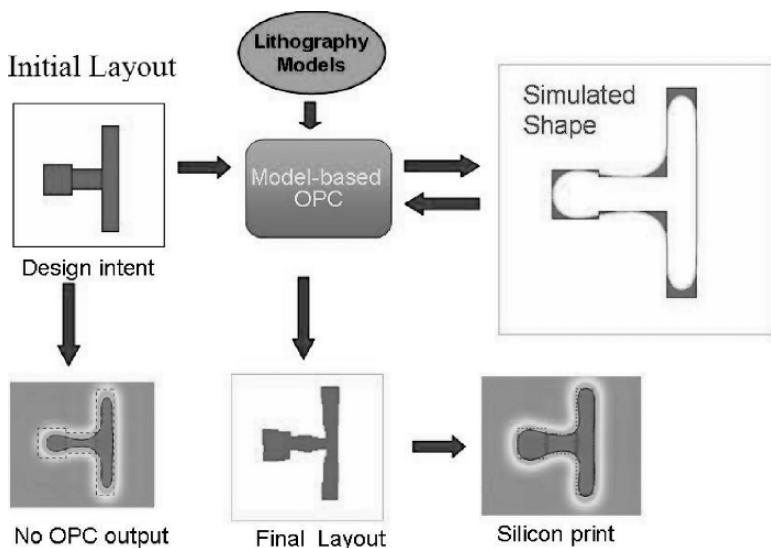


Figure 3.5. Model Based OPC Flow

repeated in a feedback loop until the output shape is within acceptable pre-determined tolerances from the design intent, then the process is stopped and the OPC'd shape is the shape that is fed to mask making tools after some further lithography verifications.

3.5.1.3 Just Enough OPC

By now we have established that model based OPC is more accurate than rule based OPC in achieving the design intent but is also more computationally expensive especially when applied to a whole design. Furthermore it usually results with many more added segments than rule based OPC. However, the cost differential does not stop at the computational expense. Mask manufacturing must be considered in terms of computational time for fracturing and verification, ease of application, and mask cost as well. Mask cost is a direct function of the write time which is also a direct function of the number of vertices, and the number of “shots” needed to capture the geometries after the process of fracturing.

The layout (left side) of Figure 3.6 shows a snap shot of a basic geometry to which model based OPC is applied. In the middle it shows the same layout after model based OPC is applied. Notice the extensive number of added vertices that resulted from this operation. The right side shows the OPC'd layout after fracturing. For the purposes of mask writing each fractured polygon is a “shot” to be written by the e-beam writer and adds to the expense of the mask [42, 43]. The concept of just enough OPC, also referred to as design intent driven OPC



Figure 3.6. Layout

is a bridge between the lack of accuracy of rule based OPC and the accurate but expensive model based OPC. Just enough OPC applies rule-based OPC to most cases and reserves the use of model based OPC to where it is really needed.

Figure 3.7 shows a case where applying model based OPC would have resulted with many additional vertices but would have had no advantage over a rule based OPC in terms of the quality of the final image.

To sum up this section on OPC, the main steps of OPC are:

- 1 Use optical resist model to determine the desired resist image needed (based on simulations).
- 2 Determine the optimal space in which the RET artifacts should be added.
- 3 Add artifacts needed to correct layout to within a pre-determined delta from the aerial image determined in 1.

3.5.2 Sub Resolution Assist Feature (SRAF)

One important measure of RET that is especially useful with illumination techniques that aim at controlling or making use of light interference patterns to enable the printing of very tight CDs, especially isolated pattern tight CDs is the use of scatter bars, also known as SRAFs which stands for Sub Resolution Assist Features. SRAFs are small lines placed on the mask to enhance the image of adjacent features without them being printed out. It is therefore critical that they be smaller than the resolving limit of the optics to ensure that they could

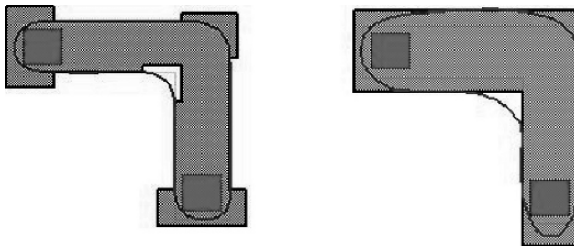


Figure 3.7. A Case Where Rule Based OPC Is Good Enough

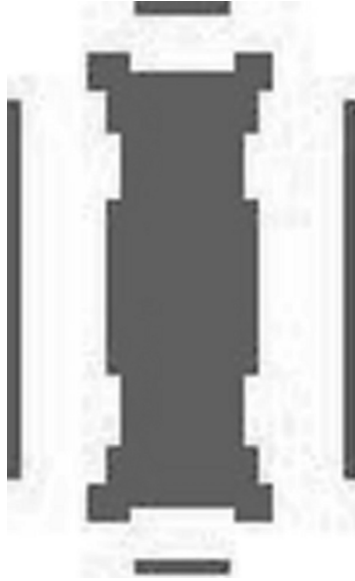


Figure 3.8. OPC'd Geometry with Scatter Bars (SRAFs)

never be erroneously printed out. Their main use is to reduce line end shortening and CD variations caused by proximity effects.

Figure 3.8 is an example of SRAFs used for both reducing end of line shortening and for proximity effects control. Figures 3.9 and 3.10 are a good illustration of the way in which scatter bars help with tight CD control of an isolated feature. We will be covering SRAFs further in the chapter when we discuss correct cell construction for proper lithography artifacts handling but it is nonetheless important to mention briefly at this point that a pre requisite for the ability to use SRAFs is that the original layout is constructed in such a way not to restrict the placement of these SRAFs. A stronger assertion

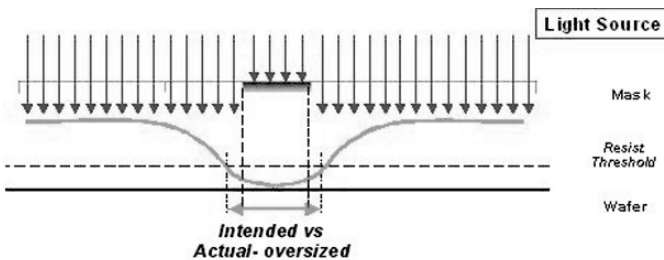


Figure 3.9. Printability of Isolated Feature, No Scatter Bar

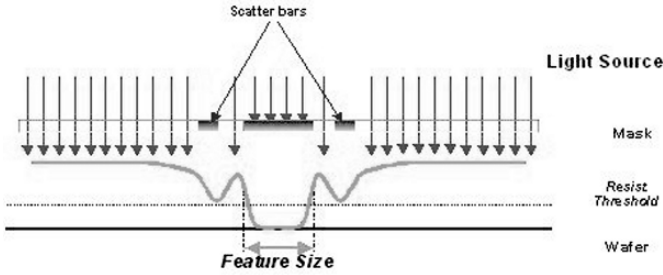


Figure 3.10. Printability of Isolated Feature, with Scatter Bar

would say not to obstruct the optimal placement of the SRAFs and not just their placements [53].

3.5.3 Phase Shift Masks (PSM)

Before getting into phase shift masks (PSM), attenuated phase shift masks (APSM), and other optical techniques for enhancing resolution and (or) DOF [54–56]. We will briefly go over the vanilla version of masks namely the binary mask. A binary mask is simply a flat surface made of clear quartz which is totally transparent to light and coated with chrome. Chrome is etched out for what represents the layout pattern to be printed. This is known as a dark field (positive) mask. The complement of that would be a clear field (negative) mask where the chrome represents the feature to be printed on the underlying wafer. Chrome is opaque and thus block light. Figure 3.11 is an illustration of a basic dark field binary mask.

Wafers are coated with photoresist, a polymer substance sensitive to light. It could be positive or negative photoresist. Positive photoresist areas of the wafers exposed to the light going through the quartz once developed by light

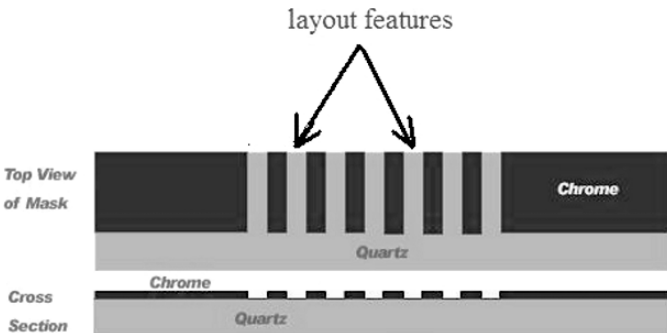


Figure 3.11. A Dark Field (Positive) Binary Mask

become soluble and are removed by etch. The unexposed photoresist hardens. The opposite is true for negative photoresist where the resist exposed to light hardens and the non-exposed becomes soluble.

It is important to note that the photo resist does not react to the incident light phase or amplitude but to the total intensity of light which is proportional to the square of the light amplitude. Also, it is important that the resist has a particular threshold of light intensity (characteristic of each particular resist) below which the resist does not react to the light and above which it does. It is not actually such a clean cut go/no-go type of a threshold as we will discuss in the coming sections. Figure 3.12 illustrates the basic interaction process of light, mask, and photo resist.

Given that we can have a dark or clear field mask, a positive or negative photo resist, that leaves us with a total of four possible combinations of mask and resist. The choice of what field type of mask and what type of resist to use has to do more with the feature to be processed and the properties of the resist as it impacts the accuracy of the image processed. An example would be a dark field with a positive photo resist for trenches. Next we will go over the problems associated with using standard binary masks with ArF 193 nm to process 90nm node features and beyond and go over some of the alternatives available.

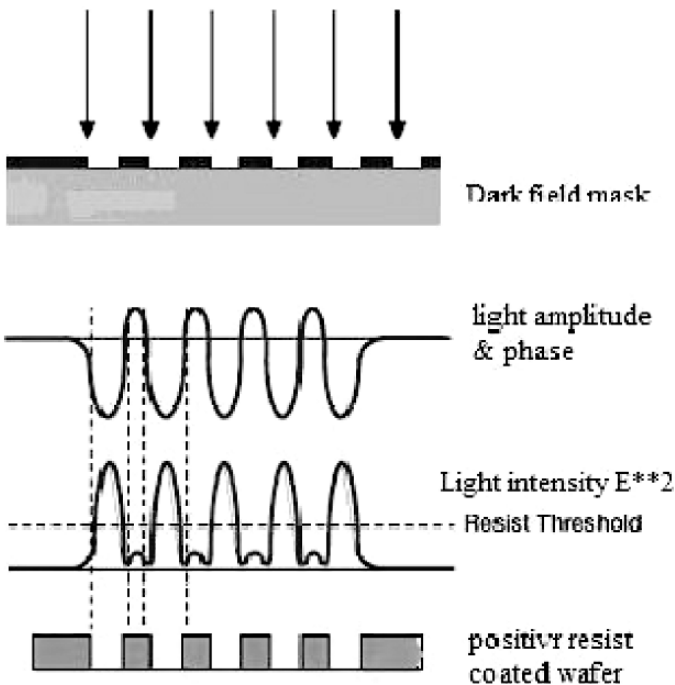


Figure 3.12. Basic Illustration of the Light-mask-resist Interaction

3.5.3.1 PSM (AltPSM)

One additional technique in the quest to extend the 193 nm illumination source's resolution and depth of focus is in the area of manipulating the light characteristics at the mask level by modulating the phase characteristics of the incident light over all or a part of the feature to be printed (or its complement). Figure 3.13 revisits the effect of a realistic "diffusion like" profile of a photoresist's reaction to incident light versus an absolute threshold with an binary cut-off characteristics. The reason for that has to do with the fact that the resist reacts to the light intensity and not to the light's phase, and as Figure 3.13 illustrates the effective intensity of light (amplitude square) where the two tails of the energy waves overlap result in a no-resolution outcome for the intended feature. The underlying photoresist is practically developed to the same level as the surrounding space.

In Figure 3.14 the center of the feature to be printed (chrome here) on the wafer forms the dividing line between a standard part of the quartz mask and a part etched back to result in a 180 degrees phase shift of the incident light. The destructive interference of the waves shown results in a clear cutoff in the

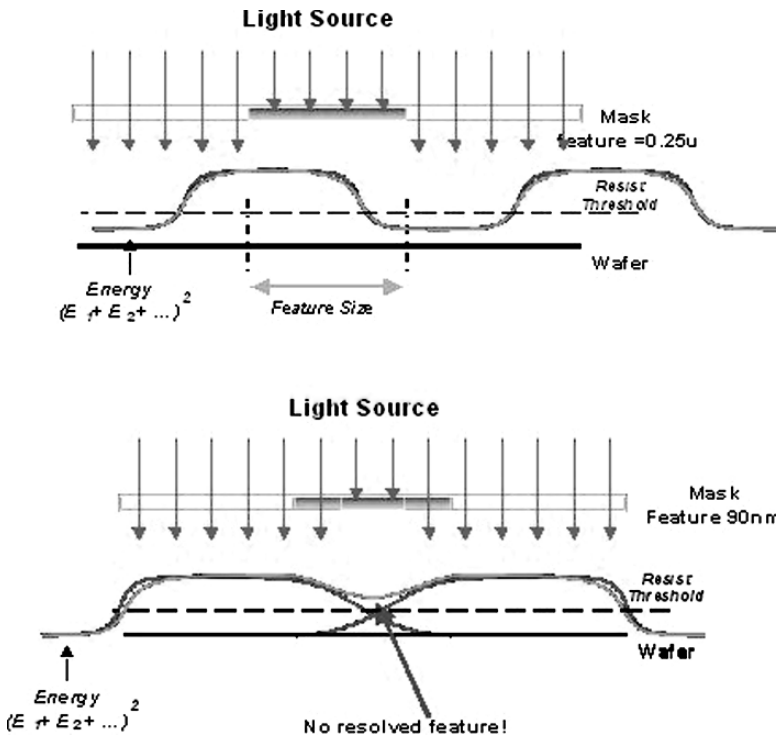


Figure 3.13. Illustration of Resolution Problem with Regular Mask

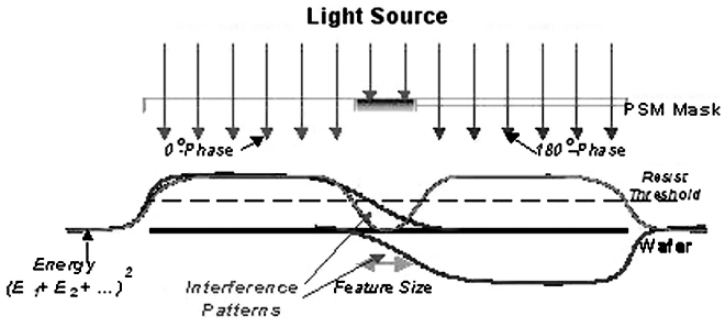


Figure 3.14. Illustration of the Resolution Enhancement Due to 180° Phase Inversion

energy profile with the photoresist representing the feature not experiencing any energy at or above the resist threshold. Thus resolution is enhanced and the feature printability is achieved. Thus this technique known as phase-shift mask (PSM) is very effective in printing tight features such as poly or contact. It is also referred to as alternating PSM or AltPSM as the phase assignments has to alternate for this technique to work.

From the illustration of Figure 3.14 the scheme for constructing a PSM mask is obvious, alternate phase assignments around the geometry of interest and that does it. But looking at Figure 3.15 and starting arbitrarily with either phase leads to a region where phase alteration on opposite sides of a geometry is not feasible. This is referred to as: phase coloring conflict.

Therefore one has to come up with an efficient technique to solve this conflict and allow for phase alteration when a phase conflict occurs. There are many techniques for phase conflict resolution. The majority of them involve splitting

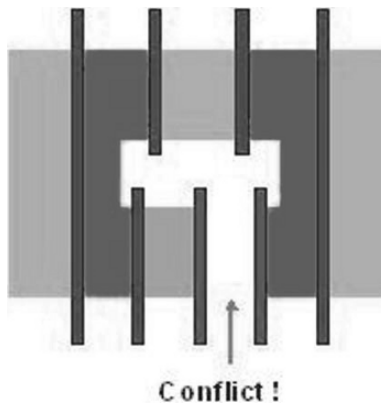
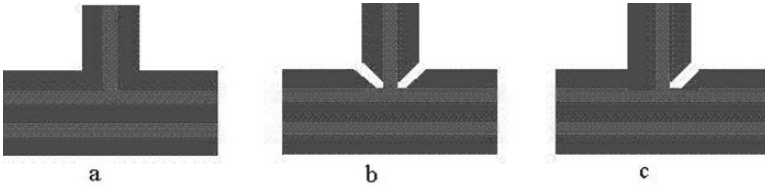


Figure 3.15. Illustration of a Layout with Phase Assignment Conflict



which one of these has no phase conflict?

Figure 3.16. Three Implementation of a Layout, Two have Phase Conflicts

a feature with a separator in such a way that the separator's introduction will not print out on the wafer (zero resolution for that part).

Exercise: Figure 3.16 tries assigning alternate phases for the structure shown. Is there a phase conflict? Will the artifacts introduced in (b) or (c) solve this conflict? Are both (b) and (c) viable solutions?

Figure 3.17 illustrates the benefits of PSM at 90 nm. However since we will be discussing several types of PSM and before going further we want to introduce an error factor for the mask part of the system: the mask error enhancement factor (MEEF) [38] is defined as:

$$MEEF = m \times \frac{\Delta CD_{wafer}}{\Delta CD_{mask}} \quad (3.4)$$

Where m is defined as the magnification of the projection optics.

It is important to observe that for low k_1 large changes in MEEF vs. feature size are observed [38] and it is observed that a large portion of the MEEF is related to mask topography effects. That translates to the need of tighter mask flatness and mask blank flatness. The 2004 ITRS roadmap has dictated a mask flatness improvement from 480nm to 192 nm and a mask substrate flatness from 90nm to 55nm simultaneously.

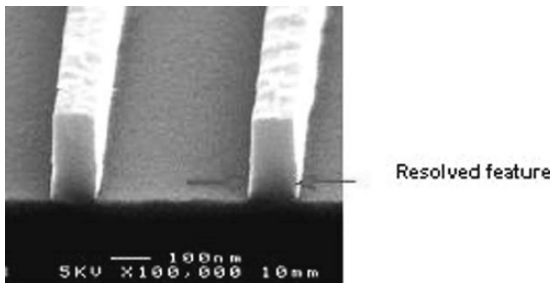


Figure 3.17. Resolved Feature with PSM

3.5.3.2 Attenuated PSM (APSM) (AttPSM)

In APSM patterns are formed by adjacent areas of quartz and other substances such as Molybdenum silicide (MoSi) which is opaque but unlike chrome allows for a percentage of the light (6 to 16%) to pass through. The thickness of the MoSi film is designed to make the small percentage of light that goes through it be 180 out of phase with the light going through the clear quartz (Figure 3.18). The idea is for the light passing through the MoSi to be too weak to develop the resist, yet form enough 180 modulation (interference) with the lobes of the incident light to cancel the “tail” end of the wave and make for a sharper pattern. APSM is most beneficial in imaging isolated contacts and trenches which requires both a low k_1 and a high NA [57]. APSM offers an increase in the image contrast, depth of focus, and exposure latitude.

One of the most important parameters in APSM is the transmission percentage. Higher transmission APSM provides added benefits for dense features patterning by scattering more light energy into the critical first diffraction orders [37]. Yet for dark field masks such as contacts high transmission APSM still provides good “isolated feature” focus margin. The main benefits of APSM over PSM are simpler design rules and lower cost. Thus it is a viable mask choice even for low volume designs. The major disadvantages of the APSM are a larger MEEF (defined earlier), being not as beneficial and effective as PSM, and finally, it works best with off-axis illumination (OAI) and thus creates forbidden pitches which is an inconvenience for layout.

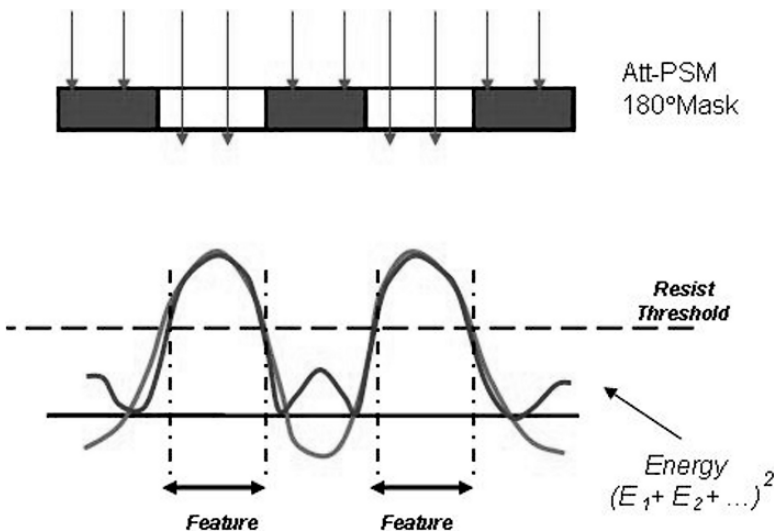


Figure 3.18. Illustration of Concept of Attenuated PSM

3.5.4 Off Axis Illumination (OAI)

OAI is the third work horse of the nano-era lithography besides OPC and PSM. It is a technique used to enhance depth of focus (DOF) especially when used with the proper dipole illumination source. OAI is as the name indicates an illumination that is off the main optical axis. It thus reduces significantly or eliminates altogether any on-axis component of the illumination. For the 65 nm node aggressive RET will be needed including a full phase-shifting methodology, chrome-less phase lithography as well as off axis illumination [40]. In order for OAI to work properly and effectively the shape and size of illumination must be determined in conjunction with the specific mask type and pattern being used.

Figure 3.19 illustrates pictorially the concept of off-axis illumination. The idea behind off axis illumination is that by tilting the illumination away from the normal incidence of the diffraction, the diffraction pattern of the mask is shifted spatially within the objective lens. This allows for more diffraction orders (frequency spectrum of diffracted light) to be transmitted through the lens allowing for better DOF for patterns with a tight pitch [58].

The shift in the diffracted light harmonics inwards in the projection lens is one-dimensional for tilting the illumination source through a conventional pupil. Thus an identical tilt in the opposite direction will produce the same effect. If instead a dipole is used with equal spacing from the center then the effect of the tilt is captured for both tilt directions and thus further improves the DOF by bringing more diffraction harmonics (on both sides with respect to the main zero

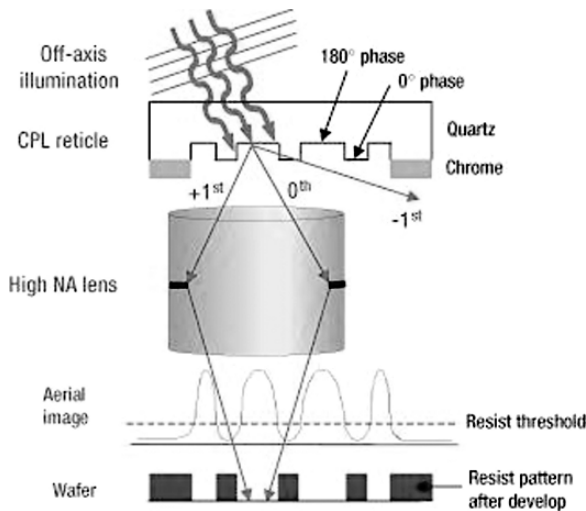


Figure 3.19. Illustration of Off-axis Illumination

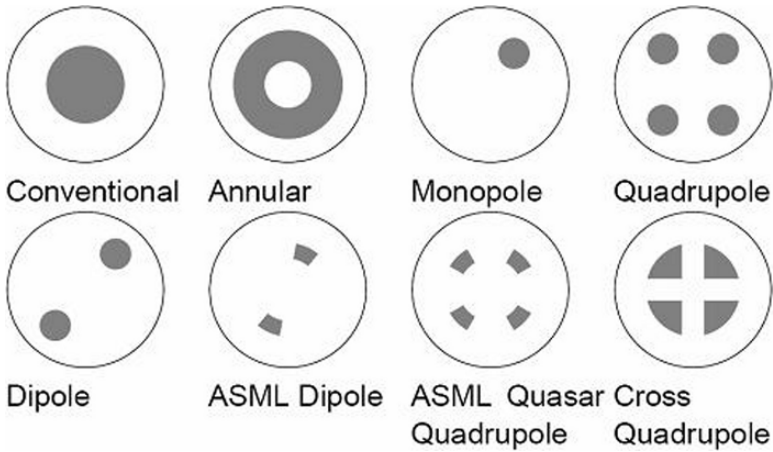


Figure 3.20. Eight Different Filtering Pupil Alternatives

degree illumination axis within the lens). Extending this principle further from dipole to 45-degree spaced quadrupole then we can capture the dipole effects for lines in the y-direction as well as in the x-direction. An annular extrapolation of the principle captures all orientations. Quadrupole and annular have been very useful for 65nm technology [59]. Figure 3.20 shows the eight varieties of illumination pupils mentioned in this discussion. Furthermore, Figure 3.21 illustrates the usefulness of annular illumination in its tilting away from normal incidences to amplify certain pitches.

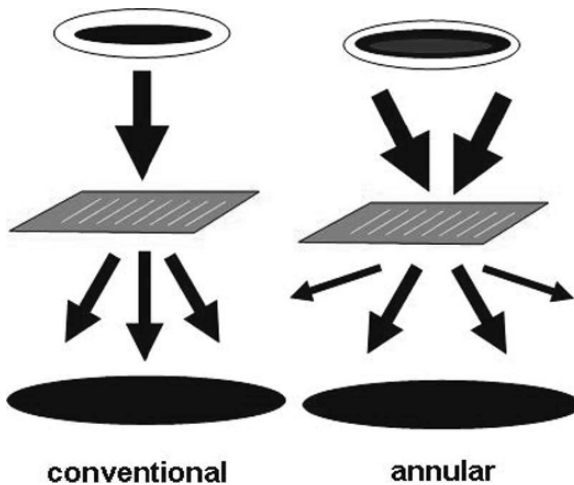


Figure 3.21. Illustration the Different Between Conventional and Annular Illumination

However, a particular angle for off-axis illumination optimizes DOF for a particular pitch. It will not work for any other pitch. Moreover, it might print nothing in another angle which happens to be the forbidden pitch. Thus the angle of off-axis illumination has to be worked out properly depending on the pitch of the pattern being processed.

3.6 Other Optical Techniques

3.6.1 Immersion Technology

We have already mentioned immersion lithography earlier. The principle is so simple one would think it is barely worth mentioning, yet it was one of the earliest techniques used to extend the capabilities of the 193 nm lithography. The principle is that the viscosity of water (later on other fluids such as a variety of oils) is higher than air and the change of speed of the light wave through such a medium translated to a shorter effective wavelength. The early application was in the form of a droplet of water, but now other oils have been experimented with. The early application of the technology had some problems in the form of bubbles manifesting between the lens and the translucent surface leading to non-uniformity. But since then this technology has been enhanced. With some oils an effective NA of as high as 1.3 is achievable.

3.6.2 Double Dipole Lithography (DDL)

Double dipole lithography (DDL) is an RET technique useful for ArF with $\lambda = 193\text{nm}$ using binary chrome masks with optical $k_1 < 0.35$ without resorting to hard RET techniques such as PSM, but it has its problems and limitations [60]. DDL uses extreme off-axis illumination. But, because DDL has a high contrast only for structures perpendicular to the dipole orientation DDL needs a pattern decomposition scheme into vertical and horizontal geometries, and needs double exposure, thus there is the added overlay issue from the separate image composition. Also, DDL is hard to apply to layers such as poly that is implemented with a clear mask and positive photo resist. For DDL scattering bars are needed as well as model based OPC to control background transmission during exposure. The width and placement of each scattering bar is a function of the vertical feature pitch and mask orientation [60]. DDL is one of the main contenders for low k_1 45 nm lithography. Because of the need for double exposure DDL's throughput is sacrificed but, the simplicity of the mask makes up for that. There are two types of shielding associated with DDL:

- 1 Main feature shielding (MFS) protects features that are oriented parallel to the dipole's long axis.
- 2 Background light shielding (BLS): that shielding minimizes background flare in the clear field area.

Needless to say EDA software has emerged to automate the decomposition scheme to allow for proper decomposition and proper application of OPC.

3.6.3 Chromeless Phase Lithography (CPL)

CPL is a single-exposure, single-mask technology. Some CPL users have demonstrated a depth of focus greater than 400-nm at the 65nm node for contacts and dense lines. With CPL the chrome is replaced by sub-resolution phase shifters. Every single line pattern is defined by two phase edges in CPL and the image contrast relies on the destructive interference at each phase edge. It works in that respect in a similar fashion to an attenuated PSM with OAI with the higher intensity and better resolution characteristic of that scheme. Yet CPL is more cost effective than PSM.

3.7 Lithography Aware Routing

Yield loss due to lithography limitations and oversight is one of the major sources of systematic yield loss that can be avoided if proper considerations are applied. Thus a lithography aware place and route system is essential for a manufacturable and high yielding design. Furthermore, RET performed after place and route is not only expensive but might not be feasible to perform all together once a design is past the routing stage [61]. The challenge becomes how to come up with the proper place and route program that is lithography aware but that is also CPU cycles requirements friendly. There are the two extreme solutions of adding a significant amount of design rules at the routing stage on one hand and doing full lithography simulation every time an incremental route is done to ensure the lithographic integrity of routing on the other hand. Both extremes are not practical. At 90 nm and beyond there are already too many detailed design rules to obey and follow. Adding a wish-list of recommended design rules of does and don'ts are very hard to implement on one hand and is very restrictive on the other hand. Doing full lithography simulations is very expensive. In between lies a full set of recognizable patterns and procedures that are known to be problematic or difficult to manipulate in order to enhance manufacturability and yield.

Via doubling, metal end of line extension in the direction of a single via, wire widening, and wire spreading are all examples of procedures that are relatively easy to implement and to exploit in a litho aware router. Looking for problematic patterns and dealing with them (or simply avoiding them when possible) during place and route is the proper optimal strategy for manufacturability and yield enhancement and is a better alternative to simulation. Figure 3.22 shows some examples of certain commonly occurring routing patterns that are DRC clean but are not yield or manufacturability friendly such as non-uniform pitches, very short jogs, and isolated wires.

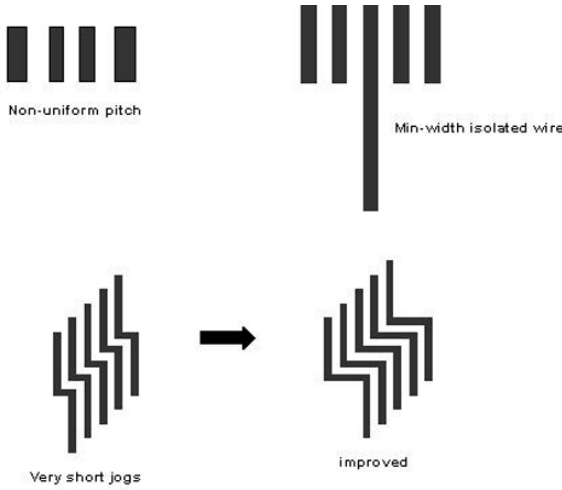


Figure 3.22. Problem Place and Route Patterns

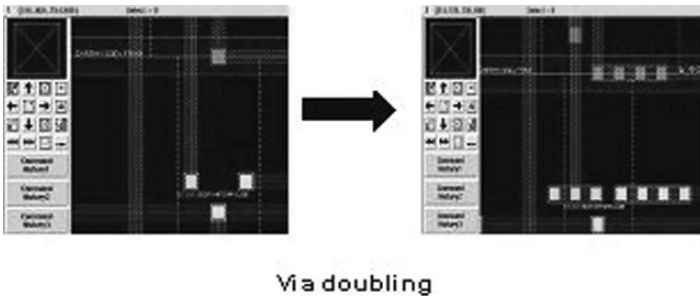


Figure 3.23. ICC Place and Route Tool Implementation of Via Doubling

Figure 3.23 shows an example of Synopsys’ ICC place and route greedy routine used to opportunistically exploit available spaces for via doubling and for end of line extension.

Another area closely related to routing is “smart” dummy-fill insertion to minimize inter-metal oxide thickness variability and thus improve DOF for metal and via processing. However that will be dealt with at length in the next chapter on chemical mechanical polishing (CMP).

3.8 RET and Lithography Verification

Applying OPC to a design without following that with optical rule check (ORC) is pretty dangerous [62]. ORC attempts to uncover potential failures of the OPC’d geometry at the wafer level. Recently, lithography rule check (LRC) has become the more common and the standard reference name for

ORC and we will use it in this book as well. In this section we will cover LRC, the procedure of using a library of recognized manufacturing problematic pattern and the research area of pattern simulation which attempts to build a library of potential problematic patterns for a new technology before there is enough wealth of experience to generate such a library from user data.

3.8.1 Lithography Rule Check (LRC)

As just mentioned in the first paragraph of this section the goal of LRC is to discover potential printed image failures at the wafer level through the simulation of the optical system's interaction with a given geometry influenced by its surroundings. For LRC to be useful it requires a very reliable simulation of the aerial and resist image at the wafer level, otherwise an overwhelming number of false errors will be reported by the simulation which is a very undesirable outcome [62]. Given that LRC applies an integrated optical system level aerial simulation it is very good at capturing the interaction of many layers of the process simultaneously. However, the main issue with that is that the simulation problem becomes unnecessarily intractable. Therefore the simulation is just limited to anywhere from one layer to a very few number of layers at a time [63, 64].

Figure 3.24 shows few examples of lithographically problematic patterns from a 65 nm library reported by a major foundry. As with the case of detailed routing covered earlier an LRC routine can attempt to catch problems by executing a set of detailed lithography rules on the whole design which has two inherent challenges

- 1 Difficulty of implementation as the rules become very exhaustive if they are to attempt to catch all lithography potential errors and we believe this is the easier of the two challenges. Also, many litho effects are non-linear. Furthermore, such rules can't properly model some lithography effects.

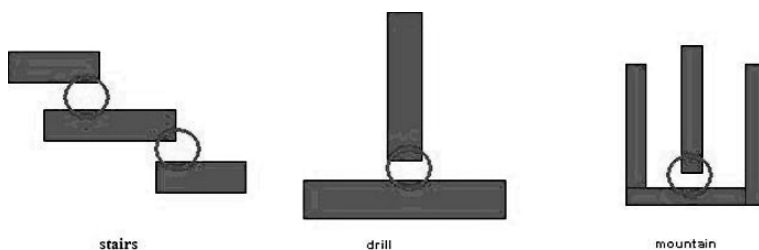


Figure 3.24. Three Known Problem Patterns from a 65nm LRC Library

- 2 A multitude of false positives (thousands) that such a routine generates which the designer has to go through one at a time to decide validity or lack of it and waive the false positive. A procedure that is time consuming and risky.

The other way of doing LRC is to frame the problem as follows:

- 1 Use silicon simulation to analyze layout printability for CDs, enclosures, bridging, and assist feature printing for pattern elements of a library.
- 2 Given a library of patterns and its range specifications, find all locations that match the pattern and score these matched locations.

For this procedure the designer can specify cost of each range specification for scoring the pattern matches.

3.8.2 Pattern Simulation

As we mentioned earlier in this section this is a hot area of research, it tries to use simulation based on a full optical and lithography flow to come up with a library of potential problematic patterns and assign a score to the impact of each pattern on manufacturability or yield.

3.9 Integrated Flow

Figure 3.25 shows a proposed design flow suitable for 90 nm and beyond. It has all the elements of the “old” design flow presented at the beginning of the chapter with some major differences that can be summed up as follows:

- 1 The new model is interactive with major feedback loops. It is not any longer top down. It is as much bottoms up as it is top down.
- 2 Fab based lithography models are the major driver of the bottoms up part of the flow. All the lithography centric blocks are built around the fab/process based litho model.
- 3 Furthermore the physical implementation starting at the IP libraries is built around OPC, PSM applicability, and printability models.
- 4 An added layer of physical verification in the form of design intent (silicon vs layout) verification is added to address and verify design intent.

3.9.1 Mask Preparation and Repair

A photomask is the first physical manifestation of the design. With the proliferation of strong RET requirements to push the capabilities of the ArF 193 nm lithography further, mask write time, and thus cost has gone up considerably. Mask write time is driven mainly by shot count determined by fractured

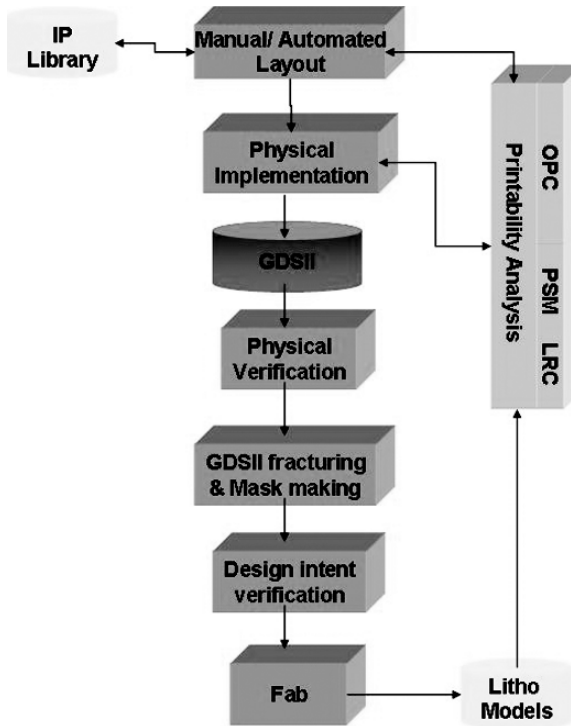


Figure 3.25. Design Flow Including OPC and LRC

results after PSM and OPC. But, what is equally important is that with so many geometries to write the probability of having an absolutely defect free mask is low. Also, insisting on a perfect mask will not only result in very expensive mask sets but will also make the turn around time (TAT) very long. Starting with blank mask specifications and moving through the process of mask making and inspection it is clear that a mask centric simulation is needed using experimentally anchored metrology operators as well as statistical analysis to study the layout RET specific mask requirements [40]. Per the ITRS roadmap blank flatness tolerances for both masks and wafers getting tighter. Mask flatness for tolerance is to be tightened from 480nm in 2002 to 192 nm in 2006 with a corresponding mask substrate flatness not to exceed 55nm. These are pretty tight tolerances for a mask

Thus mask preparation, inspection, and repair tools such as CATS (Synopsys) are very critical. These tools transcribe GDSII or OASIS polygon files into rectangles and trapezoids suitable for mask writers and prepares direct-write files. The next task these tools undertake is mask inspection which is a critical step in deciding to waive an error, repair it, or scrap the whole mask.

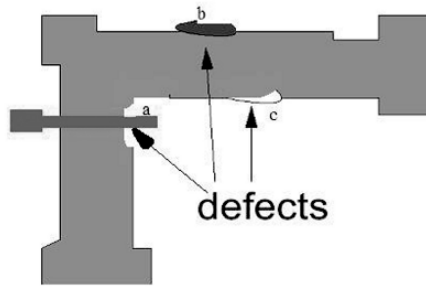


Figure 3.26. Diffusion Mask Defects, Poly (Red) Superimposed for Illustration

Figure 3.26 illustrates a mask layer under inspection (the red colored layer is superimposed on the mask image for illustration purposes only). The mask inspection software has to be able to simulate the effect of the defects, determine for example that defects b and c are irrelevant and can be waived while defect a is significant (assuming red is poly gate) and has to be fixed. Design detailed information including enough information about design intent is needed to enhance mask defect detection. Mask inspection itself is a detailed and time consuming procedure. Therefore there should be a way of identifying and thus focusing on critical areas such as gates, non-redundant vias, and metal line-end covering contacts. For non-critical areas a combination of no inspection altogether (such as metal fills) and basic inspection to some tolerances to filter out non-critical defects is needed.

3.9.2 Design Intent

In this subsection and the one that follows we will address the concept of design intent and the verification of design intent. We will start with a brief but important link between printability and design intent. Printability in the lithography sense is the ability to correctly and satisfactorily resolve the intended features on silicon using Photolithography. The “correctly” part of this definition is straightforward but the “satisfactorily” part needs some explanation. We have already addressed the difficulties associated with generating a perfect mask and with printing an image that is an exact replica of the digitized layout. In fact we know that given the limitation of the 193 nm lithography we are not going to get a replicate image of what we digitize even with strong RET. Therefore the concept of design intent comes to play. Is the printed image logically and functionally correct? And that is a bare minimum without which the design will not work. The second question to answer about the printed image is: is it satisfactory? That is does it fulfill the design intent? This is a very important

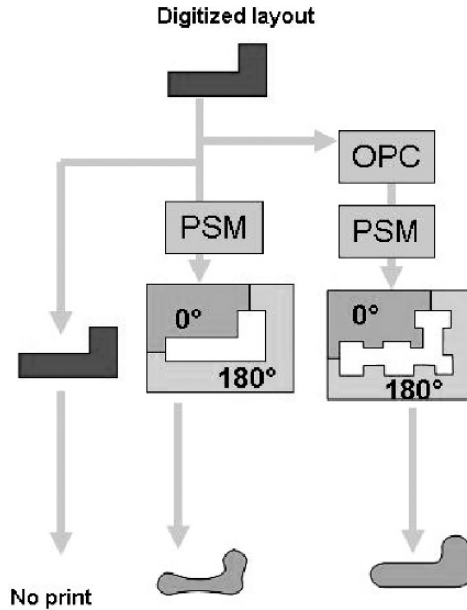


Figure 3.27. Illustration of Steps Needed to Meet Design Intent

question because it really determines the kind and extent of RET to be applied, the kind of mask and of illumination scheme to be followed and so on.

Figure 3.27 is very interesting in pointing out the complexity of the lithography scheme at 90 nm and beyond and the choices one has to make. First, no RET at all results in no silicon print at all- an unacceptable outcome. But with application of various RET schemes printability of different resolutions and quality is possible. Here comes the choice of what is good enough to reflect design intent? This is obviously a simplification to drive the point. At 45nm for example the right hand flow of both OPC and PSM is needed if there is to be any good printability, but the question becomes where to apply OPC and how much? We have covered this in “just enough OPC” and it boils down to the printability satisfying design intent.

3.9.3 Silicon vs. Layout

Silicon vs. layout has grown from its primitive form of extracting the active and passive devices with their connectivity from the digitized layout and comparing it to a netlist that represents an identical manifestation of the same design and checking for tolerances to a process of simulating all the steps of the lithographic process based on a compact model for each step to come up with a simulated printed image and checking that the simulated image does reflect the design intent of the designer.

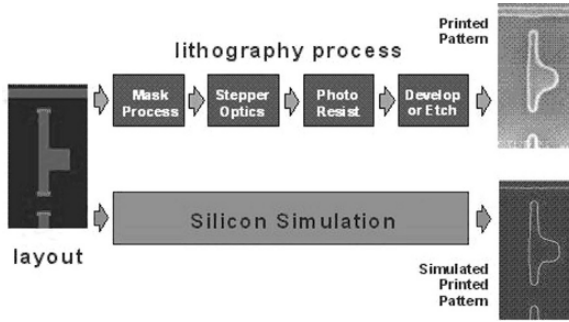


Figure 3.28. Silicon vs Layout Simulation Flow

Figure 3.28 is the flow of Synopsys' SiVI tool that does just that. The design intent allows the designer to evaluate what gets printed in the first place and what matters in a printed image vs. what can be tolerated. For example, a scatter bar in the layout is not a desirable element to be printed altogether. Also, it is o.k. for the poly over field area of a transistor for example to deviate from the digitized layout and have heavily rounded corners as long as the contact coverage is good, but such a thing is not tolerable for the transistor gate itself as it impacts performance significantly.

3.10 Yield Considerations

As we repeatedly emphasized there is no dividing line between DFM and DFY. The two have to be considered simultaneously in what is best described as a yield-centric DFM. The foundations of a yield-centric DFM is to introduce design changes at every step of the design flow, all the needed (and economically feasible) RET, and design process variations towards maximizing manufacturability and yield.

3.10.1 Cell Design Considerations

Lithography friendly design starts at the cell level. A proper lithographically correct design to start with is by far better than a more compact design that you are challenged to apply the proper RET artifacts to [61, 65]. The traditional way of optimizing the area or of using migration tools to automate and speed up the creation of standard cell is problematic. Figure 3.29 shows a 2-input NAND gate from a 130 nm standard cell library. In the layout on the left side we circled just a few of the lithography problematic spots had this layout style been migrated to 65 nm. On the right hand side is the same cell re-drawn to lithographically correct standards. We will leave it to the reader to draw few examples to see if there is really any area impact by drawing the cell lithographically correct in the first place versus coming up with the needed RET for printability, performance,

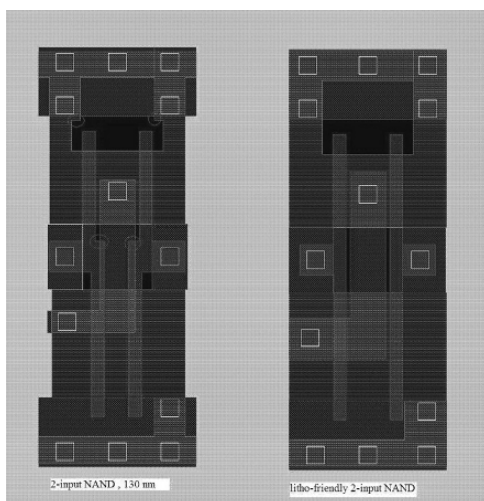


Figure 3.29. Old Style “Compact” Layout vs Litho-friendly Cell Layout

and yield. We hold to be obvious from the right hand part of Figure 3.29 that while RET will still be needed in many instances for printability, the yield characteristics of such a layout is far superior to the one on the left.

Exercise: Think of the desirability (or rather lack of desirability) of migrating complex standard cells from one technology node to a more advanced one without analyzing the power (especially leakage) implications of such a migration. Extend this exercise to SRAMs. Research the literature for the need of an 8-T SRAM cell vs the standard 6-T SRAM because of bit-line leakage considerations.

3.10.2 Yield Optimized Routing

Standard automatic routing was build around the idea of minimizing wire-length as that translates to better performance and minimizing congestion to ensure routability. Manufacturability and yield were not part of the scheme as routing paused no problem to either. In Chapter 2 we covered routing aspects of yield in terms of wire spreading and wire placement to optimize CA based yield. Here we will briefly touch on routing aspects related to manufacturability. We will limit it to resolution, printability, mask options and cost. We will cover the “dummy fill” yield enhancement aspects in the next Chapter when we discuss CMP in depth.

At 90 nm and beyond RET aware routing is not a matter of preference to enhance yield but a must to ensure manufacturability. In this chapter we also discussed the printability problems associated with short jogs, also, we discussed several mask alternatives that do better than others at printing isolated

artifacts such as isolated wires and contacts (PSM, APSM, OAI, etc). Those mask alternatives and the corresponding cost of processing vary significantly and must be taken into consideration (based on potential volume and part ASP) before choosing any specific course of optimization. In section 3.7 we discussed lithography aware routing and covered the basic preferable alternatives that should be followed for manufacturability. In summary, post routing yield enhancement processing has to balance many alternatives beyond the yield number to include the cost of the additional yield over the expected life of a design.

3.11 Practical Application: Lithography Hot-spot Detection Using Pattern Matching

3.11.1 Framing the problem

We have covered earlier in the chapter that with a low k_1 and high NA lithography system needed to develop nano-scale CDs of 65 nm and below heavy use of RET techniques are needed. Thus at the cell layout stage, and more importantly at the routing stage proper spacing considerations and neighbor interaction considerations are needed to be built in to allow for the application of the required RET. Also, applying RET solutions blindly (purely rule based) might be counter productive and might result with “hot-spots” such as poor printability or worse (such as shorts and opens). Thus metal routes need to be checked out against some rules to be supplied by fabs. Unfortunately fab supplied recommended rules fall short of what is needed for checking for potential hot spots because:

- (i) lithography interactions are non-local, they span a distance of over $1\mu\text{m}$ making local next neighbor rules inadequate.
- (ii) the large number of recommended rules making implementation and tracking difficult.
- (iii) no weight is given to each rule to reflect the yield impact of violating such a rule in a marginal way due to RET application.
- (iv) heavy RET could take the form of OPC only or scattering patterns, and a geometry that is perfectly OPC-able might actually be a hot spot because it is not scatter pattern SRAF-able Figure 3.30.

Figure 3.30 shows an example where two similar layouts could become litho-hotspots due to different RET constraints (the one on the left is “un-OPC-able” and the one on the right is “un-SRAF-able”).

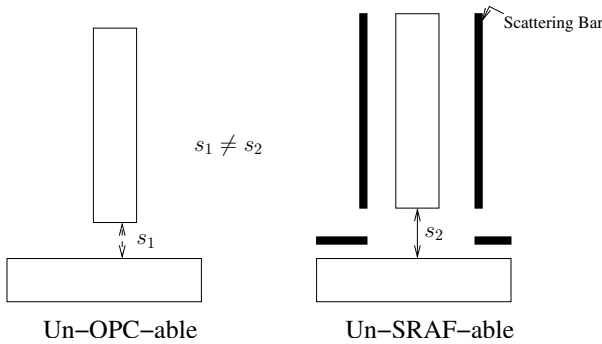


Figure 3.30. Similar Layouts That Are Litho Hotspots

3.11.2 Potential Solutions

One technique mentioned earlier in the chapter is the use of aerial image analysis to evaluate printability. One such application of this technique for addressing hot spot detection is found in [66, 67] where embedding an aerial image simulator into the router was proposed. One serious problem we see with this type of solution is the extent of false positives reported as well as other minor problems that are easy to fix. Dealing with false positives is very time consuming (for engineers) to say the least.

3.11.3 Proposed Solution

One solution we like is described in [68, 69] We will describe it in a more concise form in this section. The proposed solution is based on:

- (i) Accurately identify layout geometries that are most susceptible to the fluctuations of the lithography process and to the limitations of the RET techniques and thus are almost certain to print poorly and to impact yield negatively. This step is referred to as Litho hotspot detection.
- (ii) Generate a library of range patterns that captures geometries that are problematic to model or that are known to have adverse interaction with subsequent processing steps. Such a library is technology centric and fabrication facility centric as well. It is best for these libraries to be built and developed in collaboration with a fab but another alternative will be to use well established in-house RET flows to come up with layout patterns that cannot be corrected by the flow's RET schemes.
- (iii) These patterns are 2D layouts of geometries with each geometry representing a whole set (group) with a common or similar layout representation and a variability in spacing, length, and width between the components

of the geometries. This allows for a more compact library. Thus such a library deals with “range” patterns.

- (iv) Each range pattern is associated with a score according to yield impact of the problem pattern on hand. The router (designer) can have the flexibility of assigning the relative weights for each pattern based on the perceived impact on yield.

3.11.4 Framing the Solution - Definitions and Presentation

We will define here the concept of range pattern and the associated aspect of pattern matching. Also, we’ll go over what represents an appropriate format for layouts for the use in range pattern matching.

3.11.4.1 Range Pattern Definition and Layout Representation

First we define a range pattern as a DRC-correct two-dimensional layout of rectangles with additional specifications:

- 1 Widths and lengths of the rectangles can vary within certain user-specified bounds.
- 2 Spacing between pairs of rectangles can vary within certain user-specified bounds.
- 3 Optimal widths and lengths of the rectangles and optimal spacings between pairs of rectangles can be specified.
- 4 Constraints can be specified over linear combinations of the widths, lengths and spacings of the rectangles.

Figure 3.31 is an illustration of the definition given above.

As we mentioned earlier the scoring scheme is under the designer’s discretion but we need to stress that it only makes sense that a scoring scheme for a range pattern needs to weigh in factors contained in the range pattern such as line

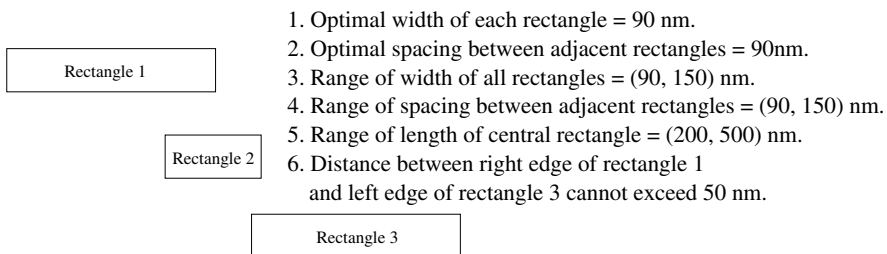


Figure 3.31. Range Pattern Staircase

widths and spacing in assigning a weight for a given situation. Two identical patterns with the only differentiating difference being the line width should obviously have a lower score for the one with wider lines than that with the narrower lines to reflect the relative probability of failure for each of the two situations. In fact the best way of coming by scores for different patterns and different ranges within pattern is to implement them in test structures and process them in a test chip and to repeat the structures within the test chip in such a way to give the results statistical significance, and then to assign the scores accordingly.

Next we consider layout representation.

For RPM, the layout is represented by a two-dimensional layout matrix $L_{N_1 \times N_2}$ where $L[i, j] = 0$ or 1 ($0 \leq i < N_1$ and $0 \leq j < N_2$). The conversion is as follows: If a rectangle overlaps a grid location, the value at that location is set to 1. Otherwise, the value of the grid is set to 0. Figure 3.32 illustrates the representation of a layout as a layout matrix.

3.11.4.2 Range Pattern Representation

If the range pattern specification is such that it only represents a small set of exact patterns then matrix representations for each individual pattern and existing algorithms such as ([70]) would suffice to find all the range pattern occurrences. But if such a set is extensive as would a real design usually have then such an algorithm will be too computationally expensive if one is to explicitly represent all patterns contained in a general range pattern. Here, we propose a new representation called the *cutting-slice* to efficiently represent all the flexibility inherent in a range pattern during RPM [69]. We begin with some basic definitions:

DEFINITION 3.1 A **horizontal(vertical) slice** is a 2D matrix in which all the rows(columns) are equal.

DEFINITION 3.2 A **fragment** of a horizontal or vertical slice is a sub-matrix in which all the matrix elements are equal.

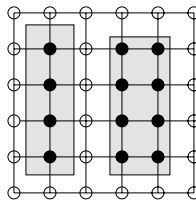


Figure 3.32. Representation of Layout as Layout Matrix

DEFINITION 3.3 A **cutting-slice** is a set of horizontal or vertical slices with the following specifications:

- 1 Adjacent slices are not equal.
- 2 If applicable, optimal values are specified for the fragments in each slice and for the slices themselves.
- 3 If applicable, ranges are specified for each slice and/or fragments within the slice.
- 4 If applicable, constraints between different fragments and/or slices are specified as linear functions.

The optimal values, ranges and constraints can be given on an absolute scale (i.e. in microns or nanometers) or in terms of the number of grids. Typically, the same grid will be used to translate the layout into a layout matrix and to generate the cutting-slice of a range pattern.

For example, the cutting-slice of range pattern Staircase (Figure 3.31) is shown in Figure 3.33. The range pattern can be cut into 5 slices denoted as S_0, S_1, \dots, S_4 . The fragments of slice i are denoted as $F_{i,j}$. It is possible to specify the variation range for the length of each fragment and the width of each slice. For example, based on the specification of the range pattern, the optimal width of S_1 is 90 nm and the allowable variation range is (90, 150) nm. In addition, it is also possible to specify constraints between different fragments. In this particular example, the overlap between rectangles 1 and 3 cannot exceed 50 nm. This translates to the following linear inequality: $F_{4,0} - F_{0,0} \geq -50$.

It should be noted that the number of cutting-slices required to fully capture all the patterns contained in a range pattern depends on the slicing direction, i.e. the direction used to generate the slices. The number of cutting-slices for a given slicing direction depends on the number and type of overlaps of different fragments caused by the ranges on their dimensions. Only ranges on dimensions that are orthogonal to the slicing direction need to be considered. Overlaps between two fragments can be classified into two categories:

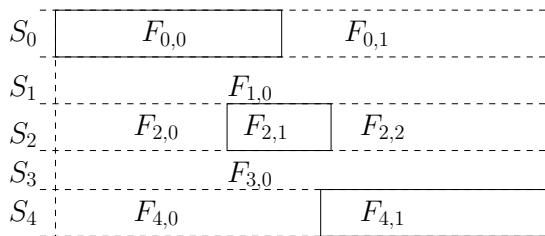


Figure 3.33. Cutting-slice of Range Pattern staircase

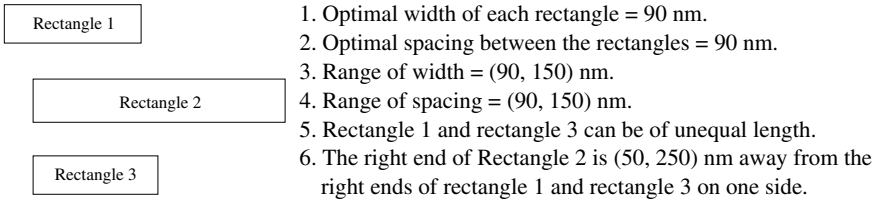


Figure 3.34. Range Pattern “rocket”

- 1 **Uni-directional overlap:** The two fragments extend in the same direction and their ranges may cause overlaps. Rectangles 1 and 3 of range pattern “rocket” in Figure 3.34 are an example of uni-directional overlap for a vertical slicing direction.
- 2 **Bi-directional overlap:** The two fragments extend in the opposite direction and their ranges may cause overlap. Rectangles 1 and 3 of range pattern “staircase” in Figure 3.31 present an example of bi-directional overlap for a vertical slicing direction.

For both uni-directional overlap between two fragments and bi-directional overlap between two fragments, three cutting-slices are needed. As an example for the range pattern rocket in Figure 3.34, three cutting-slices are required in the vertical slicing direction (Figure 3.35(a)-Figure 3.35(c)), whereas only one cutting-slice is required in the horizontal slicing direction (Figure 3.35(d)) to capture all the patterns contained in the range pattern. This is because the allowable length variations of rectangles 1 and 3 (Item 5 of the specification) allows three cases: (a) rectangle 1 is shorter than rectangle 3; (b) rectangle 1 is equal to rectangle 3; and (c) rectangle 1 is longer than rectangle 3. If a vertical slicing direction is used, three different cutting-slices will be needed to fully capture the flexibility. Figure 3.35(a-c) illustrates the scenario. On the other hand, a single cutting-slice will suffice when a horizontal slicing direction is used (Figure 3.35(d)), since neither uni-directional or bi-directional overlap occurs in this case. This analysis can be generalized for overlap between more than two fragments.

The total number of cutting-slices needed for a given range pattern can be calculated using the multiplication rule of combinatorics [71]. Typically, the slicing direction that results in the least number of cutting-slices is chosen.

3.11.5 Litho-Hotspot Detection System

3.11.5.1 Framing the solution

The **Range Pattern Matching (RPM)** problem boils down to the following: given the layout of a design and given a range pattern library for the technology

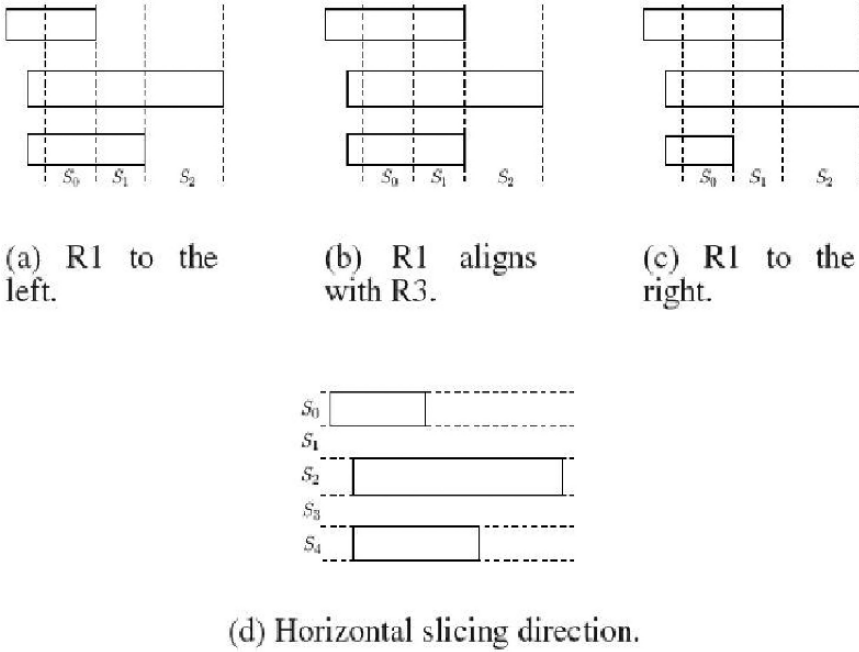


Figure 3.35. Horizontal and Vertical Cutting-slices of Range Pattern Rocket

in which the design is implemented determine all occurrences of the range pattern in the layout and score these occurrences. Then, applying the scoring mechanism pre-determined for the range pattern score the detected violating pattern. And then use this score to guide the router in optimizing the routes and in fixing those violations by assigning highest priorities to the most critical (highest scores) violators first, and so on.

3.11.5.2 Litho Hotspot Detection Algorithm

Here we present the details of the litho-hotspot detection system. The input for the system is the routed layout and a library of range patterns that describes litho-hotspots. The routed layout is processed one layer at a time. The flowchart in Figure 3.36 describes the litho-hotspot detection system with a single range pattern for one layer. This process can be easily extended to multiple range patterns.

The algorithm uses a hierarchical dual-grid scheme with matching done on two grid sizes (one coarse and the other much finer). The grid sizes are used to generate the layout matrices and the cutting-slices of a range pattern for each stage. Matching with the coarse grid identifies locations that are potential matches for the range pattern. At this stage, the entire layout is processed in a

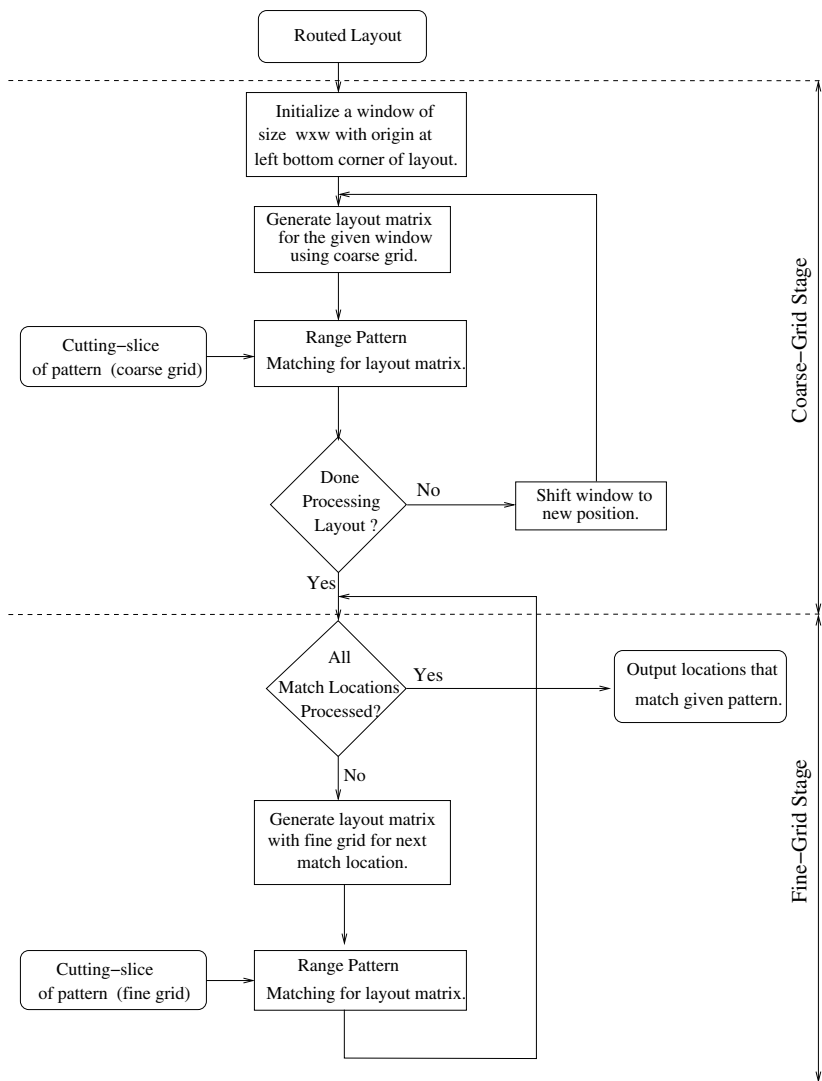


Figure 3.36. Flowchart of the Hotspot Detection System

window-by-window fashion and a range pattern matching problem is solved for each window. The windowing operation is necessary as it may not be feasible to represent the layout matrix for large layouts all at once. In the next stage, the layout matrix of the layout at each of the match locations and the cutting-slices of the range pattern are generated using a finer grid and the matching process is repeated. The match locations identified at this stage are the locations where a true match to the range pattern exists and hence are true litho-hotspots.

Typically, the fine grid size is equal to the manufacturing grid size. Thus, the coarse-grid stage helps to quickly identify potential match locations, whereas the fine-grid stage ensures that only true matches are returned. The algorithm is executed on both the original and a 90° -rotated layout.

3.11.5.3 Range Pattern Matching Sub-Problem

In this section, we discuss the solution for the RPM problem for a given range pattern and a given window of the layout, which is represented as a layout matrix. The matching problem is invoked both for the original range pattern and its 180° -rotated version. For ease of presentation, we discuss the solution for the original range pattern and also assume that a single cutting-slice in the vertical slicing direction can completely represent it.

The matching algorithm is performed block by block. Here a block refers to a sub-matrix of the layout matrix. The number of columns in the block is equal to the width of the layout matrix. The height of the block is equal to h , where $min_R \leq h \leq max_R$. Here, min_R and max_R denote the minimum and maximum possible number of rows of the range pattern, respectively (the height of the range pattern is not unique as the widths, lengths and spacings can vary). The first block starts from the left bottom corner of the layout matrix.

A ad hoc approach would look for potential matches at each location of a block. This would make the task computationally infeasible. Instead, a fast filtering operation is first performed at each block to efficiently filter out locations that can never be matched to the range pattern. The details of the filtering algorithm are provided in the next section. It can be proved that this operation never filters out locations that are true matches of the range pattern and hence does not result in the loss of any true matches of the range pattern in the window. All the locations that are not filtered out are examined more closely to determine if there is a match. To achieve this, the layout matrix near the match location is decomposed into slices and a thorough comparison is done between the slices of the layout matrix and the slices in the cutting-slice of the range pattern. This includes a check of the constraints on the fragments of each slice or between slices as well as constraints on the slices themselves. If the location passes the verification phase during the coarse-grid stage it is a potential match and is re-examined during the more refined fine-grid stage. If the location passes the verification during the fine-grid stage, a true match is recorded. In addition, a matching score is computed based on the cost function provided with the range pattern.

It is necessary to enumerate all the blocks whose heights are between min_R and max_R to find all the occurrences of the range pattern without loss of matches. However, these blocks share a lot of common information. In order to reuse work done in encoding the previous block, the blocks are processed

in a worm-like fashion such that only a few rows are changed each time. This enables incremental encoding of the block, thereby greatly improving runtime.

KMP-based Filter. The starting step of the filtering operation is to encode both the block \mathcal{B} and the cutting-slice \mathcal{C} of the range pattern as 1-D strings. Let the string representations of \mathcal{B} and \mathcal{C} be \mathcal{B}_E and \mathcal{C}_E , respectively. Given \mathcal{B}_E and \mathcal{C}_E , a KMP matching is done to find all potential matches of \mathcal{C}_E in \mathcal{B}_E . All locations that are not matches are filtered out. The locations that match are mapped back to locations in the block and are examined more closely to determine if they are true matches.

The block and cutting-slice encoding are done as follows:

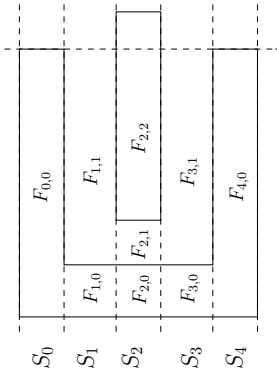
DEFINITION 3.4 *The run-length compression of a column $C[j][N]$ is equal to $\{b_0, b_1, \dots, b_{n-1}\}$, where*

- 1 $b_i \neq b_{i+1}$ ($0 \leq i < n - 1$);
- 2 $C[j][N]$ can be represented as a concatenation of n segments, i.e. b_0 repeated σ_0 times, b_1 repeated σ_1 times, and so on.
- 3 $\sum_{i=0}^{n-1} \sigma_i = N$.

For the range pattern, the run-length compression of each vertical slice (a vertical slice is uniquely represented by a single column) is generated. This is a string of alternating 0's and 1's. A "1" is appended at the top of each string generated after run-length compression to distinguish between strings "01" and "1". Each string is encoded into an integer value using binary encoding. Encoding each slice converts the cutting-slice of the range pattern into a string of numbers, where the length of the string is equal to the number of slices in the cutting-slice.

As an example, the slices in the cutting-slice of the range pattern Mountain (Figure 3.37) are encoded as follows: S0: "11" = 3; S1: "101" = 5; S2: "1101" = 13; S3: "101" = 5; S4: "11" = 3; The 1-D string representation of the range pattern is $\{3, 5, 13, 5, 3\}$.

The block is encoded in a similar fashion. First, the slices in a block are identified in one sweep starting from the left end of the block. The slices are created such that no two adjacent ones are equal. Then, the run-length compression of each slice is generated and each slice is encoded using the same method used for the slices in the cutting-slice of the range pattern. Using this method, the 1-D string representation of the layout in Figure 3.38 is the string $\{2, 10, 10, 2, 3, 5, 13, 5, 3, 2, 10, 10, 2\}$. It is easy to see that there is an exact match of the encoded range pattern $\{3, 5, 13, 5, 3\}$ in the encoded block. Hence, columns 5-14 of the block with the pattern in Figure 3.38 are examined more closely to see if it is a true match. The remaining locations can never be true matches and are therefore filtered out. This is reflected in the following Theorem.



1. Width of each rectangle = 90 nm.
2. Spacing between middle vertical rectangle and horizontal rectangle = 90 nm.
3. Range of width = (90, 150) nm.
4. Range of spacing between middle vertical and horizontal rectangles = (90, 150) nm.
5. Spacing range between vertical rectangles = (90, 120) nm.

Figure 3.37. Cutting-slice of Range Pattern Mountain

THEOREM 3.5 *The filtering algorithm satisfies the following conditions: Let C denote the cutting-slice of a range pattern P_R . For every occurrence of the original range pattern P_R in the original block B , there is an occurrence of the encoded cutting-slice C_E in the encoded block B_E .*

Proof Sketch: We will prove the theorem for the case when the range pattern P_R has a single cutting-slice C and for the case when the occurrences of P_R in B have the same orientation.

The block encoding has two steps: (1) block slicing, (2) run-length compression of each slice. The block slicing process moves horizontally from one end to the other identifying vertical slices such that no two adjacent slices are equal. By definition, a vertical slice is a 2D matrix where all the columns are

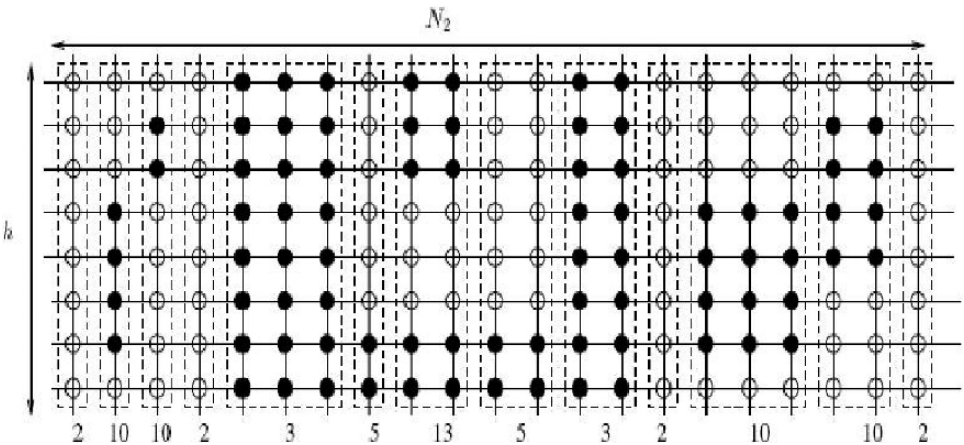


Figure 3.38. Layout Block Encoding

equal. Also by definition of a cutting-slice, the slices in C have the property that no two adjacent slices are equal. Since the range pattern P_R has a single cutting-slice C , the block slicing ensures that all occurrences of P_R in B will be replaced by slices that are identical to the slices in the cutting-slice C . Furthermore, since the same run-length compression is used for each slice of the block both occurrences of C in the sliced block will have the same encoding and will be represented by the same string in \mathcal{B}_E . In addition, this string is equal to \mathcal{C}_E since the same run-length compression is also used on the slices in C to generate \mathcal{C}_E . The same can be shown to hold if a range pattern P_R has multiple cutting-slices. Thus, no true matches are lost during the filtering operation. However, it is not necessarily true that each occurrence of the encoded range pattern in the encoded block implies a true match.

3.11.5.4 Scalability and Runtime Optimization

In most practical cases a direct translation of the entire layout into a layout matrix is impossible. Hence the hotspot detection system works on a window-by-window basis in an incremental fashion to cover the entire layout and an RPM algorithm is executed for each window. It is necessary to ensure that consecutive windows overlap to avoid loss of matches. The amount of overlap between adjacent windows depends on the maximum possible size of the range pattern. If the maximum possible numbers of rows and columns of the range pattern are m_1 and m_2 , respectively, the amount of vertical overlap between two consecutive windows should be $(m_1 + 1)$ and the amount of horizontal overlap should be $(m_2 + 1)$, respectively.

The grid size used for generating the layout matrix and the cutting-slices of a range pattern can greatly impact the runtime. One possible choice is to use the manufacturing grid, which is typically 5 nm in current processes. We are going to capture that choice in Theorem 3.6 stated here and then leave its proof to the reader.

THEOREM 3.6 *Let single-grid hotspot detection consist of overlapping window generation to cover the entire layout along with range pattern matching within each window for a given range pattern. If the layout matrix and the cutting-slices of a range pattern are generated using the manufacturing grid, then single-grid hotspot detection can determine all occurrences of the range pattern in the layout.*

Exercise: Prove Theorem 3.6.

The runtime for directly finding matches on the whole layout using a fine grid size is very slow. Hence, a hierarchical matching strategy is adopted to speed up the program. First matching is done on the coarse grid. During the translation of the layout to the layout matrix and the generation of the cutting-slice(s) using a coarse grid, it is not necessary that every rectangle in the layout aligns to the

coarse grid. This introduces the possibility of rounding errors. To counter this, the constraints in the range pattern are typically relaxed (i.e. a wider range is allowed) during this stage. Then, a second round of matching is carried out on the match locations found in the coarse-grid stage. This check is typically done using a much finer grid (usually equal to the manufacturing grid) to eliminate errors due to rounding issues or over-relaxation of constraints. It should be noted that the coarse grid size has to be less than the smaller of the two: the minimum width or the minimum spacing of the layer. Otherwise, neighboring features might merge resulting in an incorrect translation of the layout into a layout matrix.

Range patterns “staircase”, “rocket” and “mountain” are shown in Figure 3.31, Figure 3.34 and Figure 3.37, respectively. Range patterns Drill and Fly are shown in Figure 3.39.

3.11.6 Summary & Results

The outlined litho-hotspot detection system was tested on the metal 2 layer of a 65 nm design where the litho-hotspot library had 5 range patterns. The design size was a $1.8 \times 1.8 \text{mm}^2$ and had 774K rectangles. For the hierarchical matching strategy, the coarse grid size was set to be 50 nm and the fine grid size was equal to the manufacturing grid, namely 5 nm.

The results for this library are shown in Table 3.1. Column *Range Patterns* identifies the different range patterns in the library. The number of locations in the layout that match each range pattern are shown in Column *# of Matches*. Column *Score Range* shows the score range of the matches in the layout. These results confirm the assumption that many similar patterns can exist for a given layout.

To test if the hierarchical detection system is accounting for all the true matches a single-grid detection system was implemented using a grid size of 5 nm. The match locations were identical for the hierarchical and single-grid

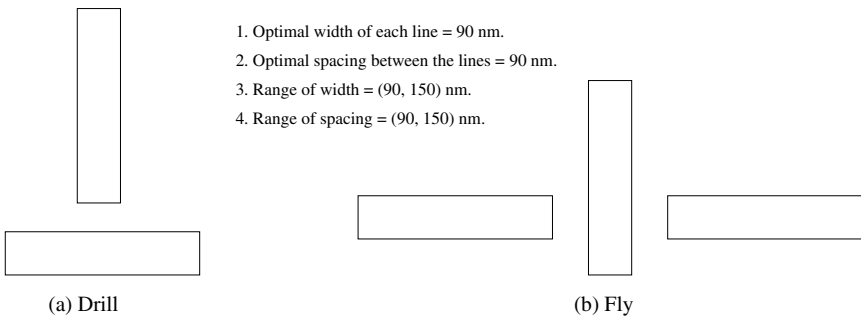


Figure 3.39. Drill and Fly

Table 3.1. Litho-Hotspot Detection Results

Range Patterns	# of Matches	Score Range	Runtime (s)	
			Hier.	Single-Grid
Rocket	4961	[91.75,91.75]	180.09	211432
Staircase	180	[91.75,91.75]	199.30	272532
Drill	172	[67.00,73.60]	140.08	71100
Fly	6	[75.25,76.90]	192.20	229260
Mountain	10	[71.71,76.43]	152.52	193215

methods. This proves that the hierarchical dual-grid scheme does not drop any matches. The columns under *Runtime* provide the runtime for each range pattern applying the hierarchical and single-grid schemes respectively on a Linux 2.4 System with a 2.8 GHz processor and 4 GB of RAM. The tabulated results show that the hierarchical scheme can find all the matches at a fraction of the time required for single-grid detection.

In conclusion this application of using an efficient algorithm for range pattern matching was described including a litho-hotspot detection system that guarantees no false positives. The algorithm is scalable and can work efficiently for large layouts.

3.12 DFM & DFY Centric Summary

The nano era of CMOS design is characterized by

- 1 Very high cost of ownership. Hardly any space for re-spins, especially multi-layers re-spins.
- 2 A paradigm shift in the understanding of DFM/DFY from being a manufacturing problem to becoming a design problem co-owned by all stakeholders.
- 3 Subwavelength manufacturing complexity requiring:
 - Detailed and early process information throughout the design-to-manufacturing flow and quick feed-back from design and manufacturing back to process
 - A new design software infrastructure to account for process, lithography mask manufacturability, and yield issues at every step of a design flow. Also, some new yield analysis, evaluation, and enhancement dedicated EDA tools
 - Advanced mask technology for analysis, inspection and repair as error free masks become prohibitive

3.13 Lithography Specific Summary

To sum up we will list the main challenges of lithography [11] as the ArF, $\lambda = 193\text{nm}$ source of illumination remains the main viable alternative for the 45 nm node and perhaps beyond with requirements of resolving critical dimensions less than a quarter of the light source wavelength:

- 1 Lack of linearity of low k_1 processes
 - Lenses with higher NA
 - Immersion technology
- 2 Low DOF due to the high NA needed
 - Significant difficulty of patterning small isolated features due to the high NA loss of DOF
- 3 High complexity of RET and of scanner illumination schemes needed to improve DOF
 - Model based OPC
 - Lithography rule checks
 - OPC aware routers
 - Complex illumination schemes that are highly technology specific (OAI and mask flavors)
- 4 New resist materials needed for better line edge roughness (LER is a leakage contributor)
- 5 Mask technologies
 - PSM varieties
 - Flatter masks
 - Mask preparation, inspection, and repair complexities
- 6 Huge database at all steps and the need for extensive computing power
- 7 Lithography friendly design (layout) methodologies
- 8 Enhanced metrology
- 9 Data-base size management
 - Smart selective OPC

Chapter 4

SYSTEMATIC YIELD - CHEMICAL MECHANICAL POLISHING (CMP)

4.1 Introduction

The classical IC manufacturing process is divided into what is referred to as “front end” processing and “backend” processing. The front end processing are the steps associated with building the devices themselves (gates) while backend processing refers to the interconnect steps that start at the level of contacting the transistor terminals and then progressing through a vertical stack of metal layers separated by layers of dielectric material. Wire segments in various metal layers are connected vertically to one another through vias that are etched in the dielectric layers for the purpose of such connectivity.

Aluminum interconnect was the standard metal used for IC manufacturing for all technology nodes 130nm and above. Limitations associated with the current carrying capability, high resistance, and metal migration of Aluminum prompted the search for a replacement. Gold (Au), Silver (Ag), and Copper (Cu) were the three contenders; and Cu emerged as the new standard on a combination of high current carrying capability, low resistance, and cost. But, dealing with Cu interconnect meant developing a totally different backend process namely the Damascene and then the Dual Damascene processes. Since Cu cannot be etched out using abrasive subtractive etching procedures as was used for Al, metal sputtering was not an option. A patterned trench filled with Cu through electroplating; and then etched in a columnar fashion are the basics of the modern Dual Damascene processes (Dual Damascene processes with Al fills were done first). Since this book is intended for the nano CMOS technology we will completely skip the Aluminum alloy metallurgy used in 130nm and older technology nodes and focus on Cu metallurgy currently used in all the nano scale processes.

In this chapter we will start with a brief description of the Dual Damascene process followed by a more detailed description of the electroplating and of the CMP processes. For each of those two processes we will build a physics based model. The main purpose of all this is to integrate the two models towards coming up with a way to optimize physical layout in order to minimize local ILD and metal thickness variability and thus improve depth of focus and improve manufacturability and yield.

4.2 The Dual Damascene Process

Figure 4.1 is a simplified illustration of what in Cu backend processing is referred to as a Damascene process. Single Damascene process was an evolution step towards the Dual Damascene which is widely used today. In a single Damascene, only a metal deposition or a via deposition is done at a time and each step (metal or via) is associated with its own dielectric layer. In a Dual Damascene process a single metal deposition step is used to simultaneously form the metal interconnect lines and the metal fill of the vias. While each of the via trench and the metal line trench needs its own mask and lithography step both of the trench for the metal line and for the via are shared in the same dielectric layer.

The Dual Damascene process is actually a significant advancement over the subtractive etching process as the difference in dimensions between the metal line trench and the via trench shrinks with every technology node and that is due to the fact that although the absolute alignment tolerance is shrinking, the alignment itself is performed before the metal film is deposited and is done through a transparent dielectric film rather than through an opaque shining metal deposit. This allows for higher packing densities [72].

A Dual Damascene process can be done in one of three well known fabrication sequences namely:

- Trench-first Dual-Damascene
- Via-first Dual-Damascene
- Self-aligned (buried via) Dual-Damascene [72]

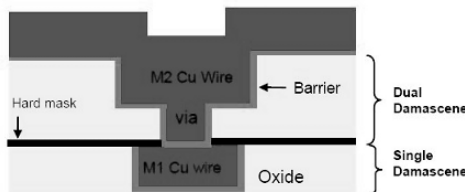


Figure 4.1. Simplified Cross Section of a Single and a Dual Damascene Process

There are other more sub-divided classifications such as partial via first [73] but we'll confine our discussion here to these three process sequences as most of the additional sub-divisions are for all practical purposes variations on those main three themes. Also, within the three mentioned sequences the via first is currently the most common approach and is predicted to continue to be the most common approach moving forward. The trench first remains in wide use as it was adopted first, but its significance will shrink with every new technology node because of the difficulty associated with defining a fine via pitch with a thick resist once the line trench is already etched out.

4.2.1 Via-first Dual-Damascene Process

In the via-first procedure the via mask is used to pattern the vias and the via trenches are fully etched through the whole dielectric stack except for the etch-stop, then resist is applied again and the trenches are patterned by a second mask. The etch process is then carried to the embedded etch-stop layer. There are several techniques available to make sure the etch stop layer at the bottom of the via is not affected in the process of the trench etching such as highly selective etching materials that are differential to the bottom via etch stop layer.

4.2.2 The Dielectric

In Figure 4.2 the ILD is drawn as a uniform layer. In reality, in the 90nm node for example the dielectric is a three layer sandwich with the top and bottom layers each about 5000A of S_iO_2 or of low k dielectric material, the middle layer of about 300A is usually a silicon nitride layer with the function of acting as an etch stop for the trenches. Needless to say, the lower dielectric is the one where vias are etched, the upper dielectric is where trenches are etched.

4.2.3 The Metal Barrier

Using Cu for metallization causes a serious problem related to the strong diffusivity of copper in silicon and to the relatively good diffusivity of copper

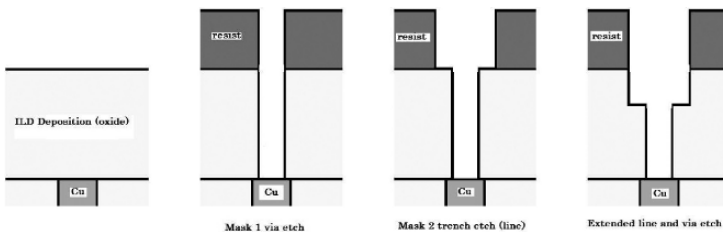


Figure 4.2. Lithography Steps of a Via-first Dual Damascene Process

in silicon oxide as well. Cu diffused in silicon forms deep level traps that degrades minority carrier lifetime and thus degrades the devices. Copper in silicon oxide creates leakage between metal layers of different bias. This problem of Cu contamination is dealt with in two manners. At the equipment level, equipment that come in contact with Cu are handled with special care to avoid contamination.

Cu interconnect itself is encapsulated to ensure zero diffusivity into the dielectric and further into silicon. This step of encapsulation is performed following the dielectric etch of wire trenches and vias alike. Barrier conducting material (very thin and highly resistive) lines the vias and trenches surfaces to fully encapsulate Cu. Barrier materials must exhibit several characteristics besides acting as a strong barrier to Cu diffusion including low contact resistance to copper, and good adhesion to oxide. Barrier films for Cu are evaluated in terms of their ability to block all Cu diffusion at 800 degrees C. Typical barrier materials are Ta and TaN.

We will not go into any further details about the conformal barrier process as it is pretty involved and as it does not directly impact the electroplating (ECP) and the CMP models we want to develop in order to address manufacturability and yield implications of the Cu metallurgy process.

4.3 Electroplating

There were several techniques that were explored for Cu deposition . What differentiates them besides economical aspects is their ability to achieve vias of high aspect ratios and to do that without forming any metal voids. A void is defined as a hole inside a Cu or a filling material. The main contenders were physical vapor deposition (PVD), chemical vapor deposition (CVD), electroplating, and electro-less plating [73]. PVD had good trench filling characteristics but was not void free. It required a complex annealing procedure and the thermal budget needed for that annealing put unnecessary burdens on the barrier film layer needed. CVD was a good contender but was quite expensive. Electroless plating was cheap but the resulting Cu film had poor electromigration characteristics. Electroplating, which is what we'll be discussing in this section emerged as the best cost effective solution to date and is now the standard for Cu metallurgy for ICs.

4.3.1 Procedure Description

Figure 4.3 shows a simplified drawing of a Cu ECP system [1]. A wafer coated with a thin electrically conductive layer of seed Cu is immersed in chemical solutions containing Cu ions. An external power source is then connected between the seed Cu on the wafer surface and the solid Cu, which act as a cathode and an anode respectively. The Cu ions in the solutions react with the electrons to form Cu on the wafer where the current passes through. This

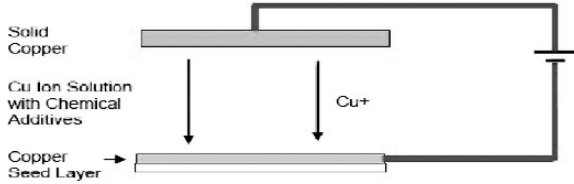


Figure 4.3. An Electroplating System [1]

can be described by the following Equation:



The Cu ions depleted from the chemical solution will be replenished from the solid Cu anode.

As we mentioned earlier when talking about various Cu metallization options a major challenge for the conventional ECP process is to fill up the high-aspect-ratio sub-micron trenches without causing any voids. It may cause an open circuit. The primary reason for void formation is a faster deposition rate at the neck of the trench than at its bottom. Therefore, void formation may be avoided by appropriately adjusting the local deposition rate. The current state of art Cu ECP process to prevent void formation is a bottom-up fill process where the deposition starts at the bottom of the trench and move upwards. To achieve such a bottom fill behavior, additive chemicals known as accelerators, suppressors, and levels are added to the plating solution. They are adsorbed on the wafer surface to either accelerate or suppress the local deposition rates.

There are various theories that try to explain the role and interactions of accelerators, suppressors, and levels in the bottom-up fill behavior. One of the most successful theories is an additive accumulation theory proposed by [2]. The illustration of additives behavior based on this theory is shown in Figure 4.4 for a single trench and can be described as follows: Once a wafer with a seed layer deposited is immersed in the plating solution, bath additives will be adsorbed on the Cu seed surface, and an equilibrium level of additives is on all surfaces of the wafer, including both the side walls and the top and bottom of the trench ($t=2\text{sec.}$ in Figure 4.4). Due to the equilibrium level of chemical additives, once the current is applied to the solution bath, a conformal plating process will start first ($t=10\text{sec.}$ in Figure 4.4). After a certain amount of time ($t=20\text{sec.}$ in Figure 4.4), the accelerators, which can neither be incorporated into the deposited Cu surface, nor be adsorbed into the plating solution, start to move to the bottom of the trench. The suppressors will be displaced by the accelerating species due to their weaker adsorbing ability. This leads to a high concentration of accelerators on the bottom of the trench. Therefore the deposition rate on bottom is faster than on the sidewall and neck, making the deposition void free.

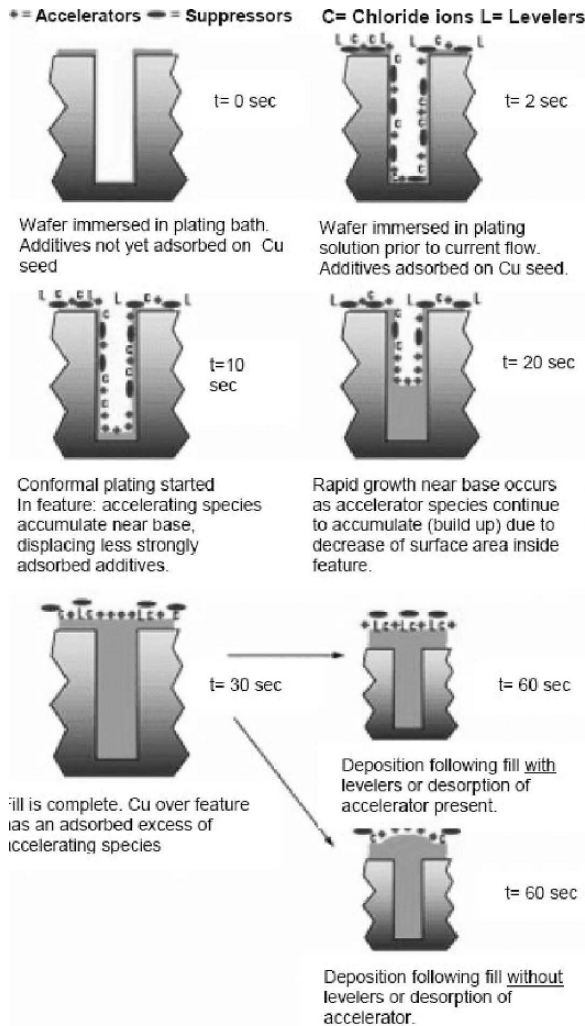


Figure 4.4. Additive Absorption Behavior During ECP [2]

This fundamental explanation of the Super-fill mechanism has been proven successful and is adopted by several more complicated numerical models [74–76].

One of the key ideas in the above model is that there is no consumption of accelerators during ECP. The deposition rate increases with the amount of the accelerators in the trenches, which is determined by not only the area of the trench bottom but also by the area of the trench sidewall. For finer trenches with the same sidewall area, a faster deposition rate is expected due to a higher concentration of accelerators. This idea will be applied in the formulation of the topography model we present in the next Section [77].

4.3.2 Electroplating Model

Cu and oxide thickness after a Damascene process is not uniform across the whole chip. Instead, systematic Cu and oxide thickness variations are observed. These systematic variations are found to be layout dependent. For example, when Cu wire width is changed from $0.9\mu\text{m}$ to $100\mu\text{m}$, a variation $> 100\text{nm}$ in Cu thickness is observed [78]. This thickness variation is around 20% for the nominal wire thickness of 550nm . As feature sizes scale down, these systematic variations are gaining more significance.

Modeling of the post ECP and post-CMP Cu and oxide thickness variation is critical for the following three reasons.

- First is the stringent depth of focus (DOF) requirements of the lithography process. The DOF budget of the lithography tools has been reduced to several hundred nanometers at best. The ITRS road map for the last several years states that the DOF requirements varies with each technology node and does not list a specific number, but a back of the envelop calculation using the DOF formula listed in Chapter 1 with a $k_2 = .5$ and two values of NA of $.65$ and 1.1 respectively (higher NA with every new node) indicates a drop in DOF from 250nm to 80nm . This stringent DOF requirement dictates that the CMP process generates a surface with thickness variation less than 100nm for all metal layers together. Thus it is crucial that one be able to predict oxide and metal thickness variation after CMP with topography modeling and simulation.
- Second is the need to compare and evaluate the impact of different yield improvement methods especially ones involving dummy fills to come up with an optimal solution for a minimal local variation.
- Third is the need to analyze the impact of the post-CMP thickness variations on timing. Cu and oxide thickness variations result in wire resistance and capacitance variations; which in turn impact the timing of a path in a chip [79, 80]. Topography modeling can help the designer in evaluating interconnect parasitic variations.

The post-ECP topography strongly depends on layout patterns, as shown in Figure 4.5. A physics-based layout dependent ECP topography model is presented here. The key idea of the model is that the volume of Cu deposited is proportional to the surface area, which is defined as the sum of the trench bottom area, the trench top area, and the trench sidewall area. The key advantages of this model are:

- Under a unified mechanism, the array height and step height can be obtained simultaneously. In addition, there are only four calibration parameters in the

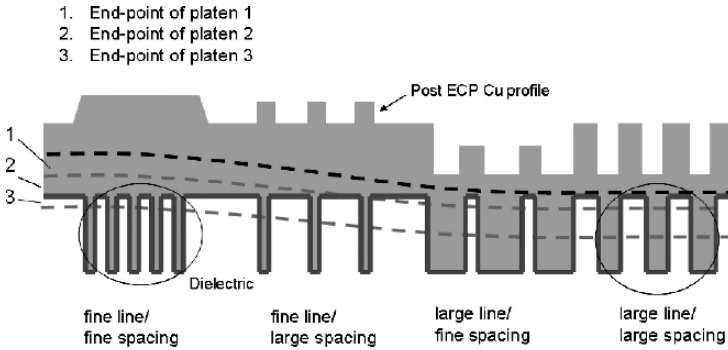


Figure 4.5. A Typical Topography After ECP Process

model, much fewer than the ten calibration parameters required in the empirical model in [1]. The physical significance of the calibration parameters in this model is clearer and therefore the risk of over-fitting is lower.

- The layout attributes, layout density, and perimeter sum - instead of the wire width and spacing - are used in the model to reflect the dependency of the topography on the layout. These layout attributes are applicable to any arbitrary layout pattern in a practical design.
- The whole chip is meshed into a number of small tiles. The topography model is directly built around the tile instead of around each small feature. The interaction length can be incorporated into the model easily to consider the long-range interactions in ECP processes.

4.3.2.1 Model Terminology

There are several terms that will be repeatedly used in presenting the ECP model formulation. They essentially represent the inputs and outputs of the model.

The two output variables that represent the final topography are the array height H , and the step height S . As shown in Figure 4.5 and Figure 4.7, the array height H is defined as the thickness of Cu above the oxide after deposition; the step height S is defined as the difference of Cu height between the Cu above the oxide and the Cu above the trench in the oxide. When the height of Cu above the oxide is larger than the height of Cu above the trench, the step height S is a positive value. Otherwise, it is a negative value.

Throughout this section “feature trenches” refers to trenches in the oxide. They will eventually be the wires and vias after the CMP process is completed. Therefore, their widths are the same as the wire widths. The depth of the feature trench is denoted as T in Figure 4.7. When the step height S in the Cu

topography is positive, a trench region is formed in the Cu above the feature trenches, as in Figure 4.7 (1). It is referred to as a copper trench. When the step height S is negative, a bump region is formed in the Cu above the feature trench, as in Figure 4.7 (2). It is referred to as a copper bump.

The proposed model relies on three layout parameters as its inputs. They are the perimeter sum L , the feature density ρ , and the topography density ρ_d . The perimeter sum L is defined as the sum of the perimeters of all the layout objects in a layout window. For the layout window shown in Figure 4.6,

$$L = 2(L_1 + L_2 + L_3 + L_4 + L_5 + L_6 + L_7 + L_8) + L_9 + L_{10} + 2L_{11} + L_{12} \quad (4.2)$$

Note that for the objects crossing the window boundaries, only the portion of the perimeter that is inside the window should be included. The reason that will be given in Section 4.3.2.2. The feature density ρ is defined as the area of all the layout objects (or feature trenches) divided by the total area of the design. It is also referred to as metal density or layout density. The topography density ρ_d is defined as the ratio of the area of the lower regions (the narrow part of the filled trench) of the deposited Cu to the overall Cu area after ECP. A more detailed definition of ρ_d for the three topography cases in Figure 4.7 will be presented in next section.

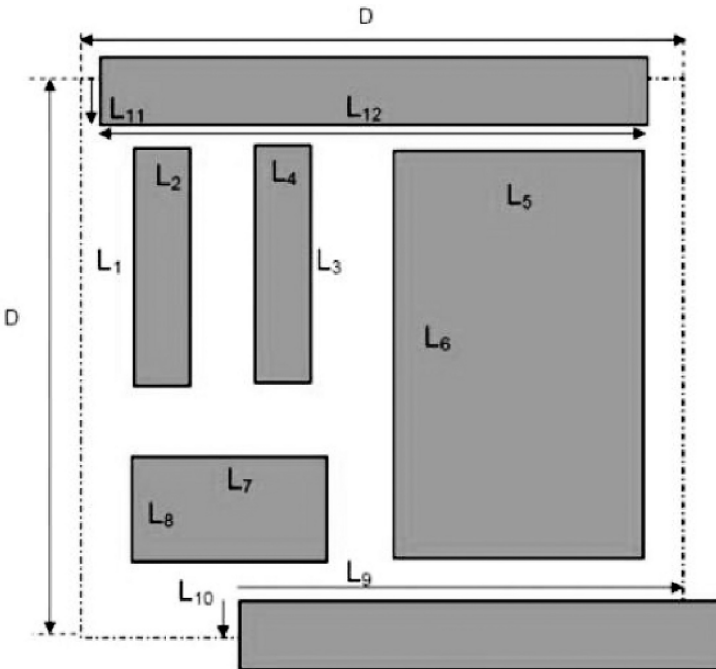


Figure 4.6. An Arbitrary Layout in Window with Size $D \times D$

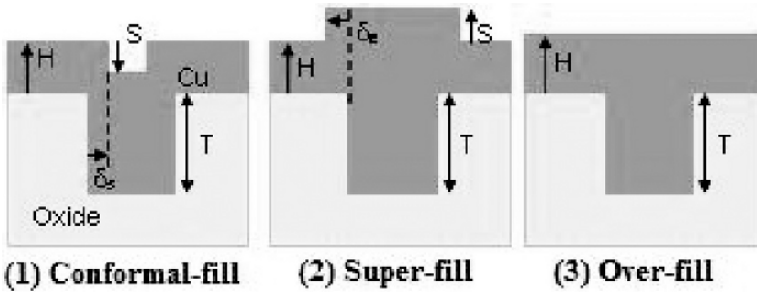


Figure 4.7. Three Kinds of Post-ECP Topographies of a Wire

Besides the above parameters, a process parameter: field copper thickness H_0 is introduced. It is referred to as the Cu thickness over a big empty area on the chip where there are no Cu wires.

4.3.2.2 Three Cases of Deposition Topographies

There are primarily three different topographies that result after an ECP process. For simplicity of the presentation, Figure 4.7(1)-(3) show the three topographies for a single wire only. However, the following discussion is applicable to multi-wires as well.

In case (1), the Cu above the oxide is higher than that above the trench. There is a positive step height S . In addition, the Cu trench width is smaller than the feature trench width in the oxide by amount δ_s , as shown in Figure 4.7(1). This case is called Conformal-fill. In case (2), the width of the Cu above the feature trench is wider than the feature trench width by amount δ_e . This is the differentiating property for case (2). The step height S can be either positive or negative in this case, as to be discussed later. Figure 4.7(2) only illustrates the case of a negative step height S for simplicity. This case is called Super-fill. In case (3), the Cu surface is flat after deposition. $S=0$ in this case. This case is called Over-fill.

The evaluation of topography density ρ_d for these three cases can be derived by definition as follows:

$$\left\{ \begin{array}{ll} \rho_d = \rho_s & \text{case(1)} \\ \rho_d = 1 - \rho_e & \text{case(2), } S < 0 \\ \rho_d = \rho_e & \text{case(2), } S > 0 \\ \rho_d = 1 & \text{case(3), } S = 0 \end{array} \right. \quad (4.3)$$

where ρ_s is referred to as the shrunk density for case (1), and can be calculated as the feature density after shrinking all the layout features by an amount of δ_s ; ρ_e is referred to as the expanded density for case (2), and can be calculated as the feature density after expanding all the layout features by an amount of δ_e .

These density variables are needed when we formulate the deposited copper volume in the next section.

4.3.2.3 Topography Modeling for the Three Cases

In this section, the topography as a function of layout variables is formulated. This is done through evaluating the volume of Cu after deposition, which can be evaluated from two different perspectives. One is from an additive physics perspective, the other one is from a topography geometry perspective.

First the deposited Cu volume based on the additive physics is formulated. One fundamental concept in the ECP topography model is that the volume of Cu deposited is proportional to the amount of accelerators on the wafer surface. Mathematically,

$$V = \alpha C \quad (4.4)$$

where V is the volume of Cu, α is a proportionality coefficient, and C is the amount of accelerators on the wafer surface. Based on the additive acceleration model the amount of the accelerators C is proportional to the surface area SA , which is defined as the sum of the oxide area, the trench bottom area, and the trench sidewall area. Therefore,

$$C = \beta SA \quad (4.5)$$

where β is a proportionality coefficient. For an arbitrary layout in a window with size $D \times D$ as shown in Figure 4.6, the surface area SA can be formulated as

$$SA = TL + D^2 \quad (4.6)$$

where T is the feature trench depth. Note that L is the perimeter sum including only the portion of the feature perimeters that are inside the window, because only this portion corresponds to the side walls falling in the window $D \times D$ (Equation 4.2). Considering that the original concentration of the accelerators absorbed on the sidewall may be smaller than that on the top and bottom of the trenches, an effective surface area SA_{eff} can be defined as

$$SA_{eff} = T_e L + D^2, \quad (4.7)$$

where T_e is the effective trench depth, and $T_e < T$. From Equations 4.4 to 4.7, an Equation for the deposited Cu volume V can be obtained as

$$V = \alpha \beta SA_{eff} = \alpha \beta (T_e L + D^2). \quad (4.8)$$

In order to evaluate the coefficients α and β , consider the case where there is no feature in a given window. Since $L=0$,

$$V = \alpha \beta D^2. \quad (4.9)$$

In addition, when there are no features in the window, the Cu surface after deposition is flat. The Cu thickness is equal to the field thickness H_0 , which can be measured directly from silicon. Therefore,

$$V = H_0 D^2. \quad (4.10)$$

Combining Equations 4.9 and 4.10 yields $\alpha\beta = H_0$, and Equation 4.8 can be rewritten as

$$V = H_0(T_e L + D^2). \quad (4.11)$$

Equation 4.11 formulates the Cu volume as a function of layout parameters L and D. This Equation applies to all three cases described in Figure 4.7. Now we will go through each of the three topographies to formulate the deposited Cu volume based on the geometry of each case.

Case (1): Conformal-fill For case (1), from a topography geometry perspective, the volume of Cu can be formulated as

$$V = HD^2 - SD^2\rho_s + TD^2\rho \quad (4.12)$$

where ρ and ρ_s are defined in Section 4.3.2.1. Combining the two Equation 4.11 and 4.12 for the deposited Cu volume, we have

$$H_0(T_e L + D^2) = HD^2 - SD^2\rho_s + TD^2\rho \quad (4.13)$$

There are two unknown variables in Equation 4.13, one is the step height S and the other is Cu array height H . Another equation is needed. From the mechanism of Cu evolution [2], since the accelerators in the trench are accumulated on the trench bottom and can not flow out of the trench the growth of the Cu on the oxide surface that shrinks the trench is solely due to the accelerators absorbed on the oxide, as shown in Figure 4.8. Therefore, the Cu volume on the oxide is formulated as

$$H_0 D^2(1 - \rho) = HD^2(1 - \rho_s). \quad (4.14)$$

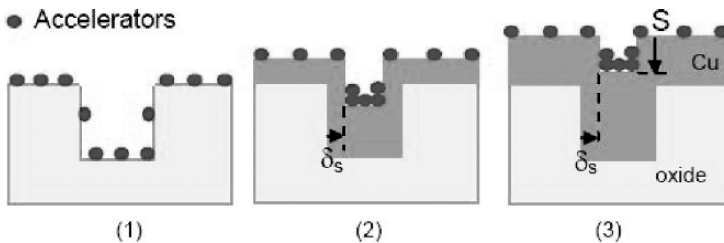


Figure 4.8. The Evolution of Topography in Case (1) Conformal-fill

The volume on the left side of the above equation is from the additive physics perspective and that on the right side is from the geometry perspective. Therefore, the array height H can be obtained as

$$H = H_0(1 - \rho)/(1 - \rho_s) \quad (4.15)$$

Substituting Equation 4.15 into Equation 4.13 yields the step height as

$$S = H_0(1 - \rho)/[(1 - \rho_s)\rho_s] + T\rho/\rho_s - H_0T_eL/(D^2\rho_s) - H_0/\rho_s \quad (4.16)$$

The topography density ρ_d is equal to ρ_s in this case.

Case (2): Super-fill For case (2), from the topography geometry perspective, the volume of the Cu can be formulated as

$$V = HD^2 - SD^2\rho_e + TD^2\rho \quad (4.17)$$

where ρ and ρ_e are as defined in Section 4.3.2.1 and Section 4.3.2.2 respectively. Combining the two Equation 4.11 and 4.17 for the deposited Cu volume, we obtain

$$H_0(T_eL + D^2) = HD^2 - SD^2\rho_e + TD^2\rho \quad (4.18)$$

Equation 4.18 has two unknown variables: array height H and step height S . We obtain the other equation from the topography evolution mechanism. In this case of Super-fill as shown in Figure 4.9, only the oxide in the range of expansion amount e is affected by the accelerators in the trench. For the oxide out of that range, the thickness of Cu deposited is not affected. Therefore it is the same as the Cu field thickness H_0 . This leads to the array height H as

$$H = H_0 \quad (4.19)$$

Substituting Equation 4.19 into Equation 4.18 yields the step height S as

$$S = T\rho/\rho_e - H_0T_eL/(D^2\rho_e) \quad (4.20)$$

Note that the step height S in this case could be either positive or negative. Positive step height S indicates that the Cu above the feature trench forms a trench with width larger than the width of the feature trench. On the other hand, a negative step height S indicates that the Cu above the feature trench forms a bump with a width larger than the width of the feature trench. The differentiating property of this case is that the trenches or bumps of Cu are wider than the wire. The expanded amount e is always observed as shown in Figure 4.7(2). Depending on the step height the topography density ρ_d is either ρ_e or $1 - \rho_e$ as shown in Equation 4.3.

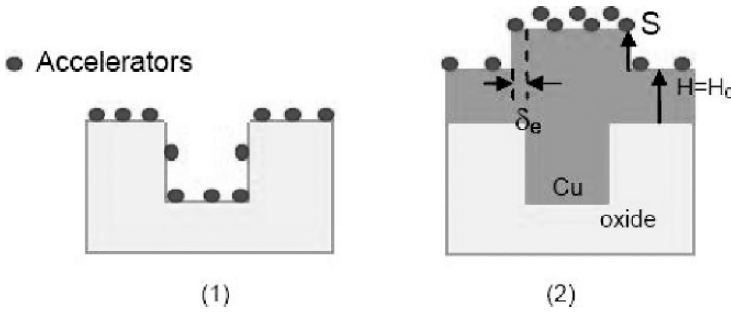


Figure 4.9. The Evolution of Topography in Case (2) Super-fill

When the step height $S = 0$, we have the special case of Super-fill as will be described in case (3). Case (3) implies the whole window is in the range of the expanded amount δ_e . Therefore the entire oxide surface is affected by the accelerators in the trench and H is not equal to H_0 any more. This implication will be used for the case selection in the next section.

Case (3): Over-fill For case (3), by definition, the step height

$$S = 0 \quad (4.21)$$

Since from a topography geometry perspective, the volume of deposited Cu is formulated as

$$V = HD^2 + TD^2\rho \quad (4.22)$$

Combining the two Equations 4.11 and 4.22 for the Cu volume, we therefore have the formula for the array height obtained by

$$H = H_0 + H_0(T_e L/D^2) - T\rho \quad (4.23)$$

Since the step height $S=0$, the topography density $\rho_d = 1$. Note that in the above formulations the term L/D^2 can be taken as the average perimeter of window $D \times D$. This term, similar to the layout density ρ , reflects the ‘density of perimeter’ in the window. The advantage of using this term is that the window size D does not explicitly show up in the formulation. We denote it by L_{avg} and will use it in later sections for convenience.

4.4 A Full Chip Simulation Algorithm

To evaluate the topography across a whole chip, the chip is divided into tiles. Each tile corresponds to a window of size $D \times D$ as shown in Figure 4.6. Assuming that the shrinking and expanding amounts δ_s and δ_e are obtained

by experimental calibration, the layout density ρ , the shrunk density ρ_s , the expanded density ρ_e , and the average feature perimeter L_{avg} in each tile can be extracted from the layout. These parameters can be substituted into the model formulations in Section 4.3's last subsection to obtain the chip topography. There are two remaining issues that need to be addressed for full chip simulation. One is the case selection algorithm based on layout patterns; the other is the extension of tile-scale modeling to chip-scale modeling by taking the interaction length into consideration.

4.4.1 Case Selection

Given the layout parameters of a design and the calibrated process parameters, an algorithm is needed to determine which of the three cases shown in Figure 4.7 should be applied to a particular tile to compute array height H and step height S .

Because of the evolution process of Cu topography, the accelerators in the trench do not affect the Cu growth on the oxide surface in the early stages. Therefore, case (1), the Conformal-fill case, should always occur first. The step height S calculated thereafter should be larger than 0. However, if for the given layout pattern the calculation of S from case (1) model turns out to be smaller than 0, it indicates that there are too many accelerators for this particular tile to stay in case (1). Therefore either case (2) or case (3) should occur. In that situation, the expanded topography density ρ_e should be used to determine whether case (2) or case (3) occurs. If $\rho_e < 1$, only part of the oxide in the tile is affected by the accelerators in the trenches. Therefore, case (2) occurs. If $\rho_e = 1$, the whole tile is affected by what we discussed earlier and then we have to resort to value of the shrunk amount δ_s -derived from the three expansion process parameter- to determine which case (case (2) or case (3)), a tile falls in. These three parameters are the fitting parameters for the model and needed to be calibrated from experimental data.

The framework of the case selection algorithm is shown in Figure 4.10. Note that the implementation of the algorithm should take into consideration the extreme cases as well. For example, when $\rho_s = 0$ or $\rho_e = 0$, it means that the topography after deposition is flat. Therefore it should directly lead us to case (3) in the case selection algorithm.

Before further discussion it is worthwhile to take a look at the dependency of the case selection on the layout patterns. We discuss the following four layout patterns: wide wire and wide spacing (WWWS), wide wire and fine spacing (WWFS), fine wire and wide spacing (FWWS, or isolated fine wire), fine wire and fine spacing (FWFS). Note that when fine or wide wire width and fine or wide spacing are referred to, it means that the width and spacing are far smaller or larger than the shrunk or expanded amounts in the topography.

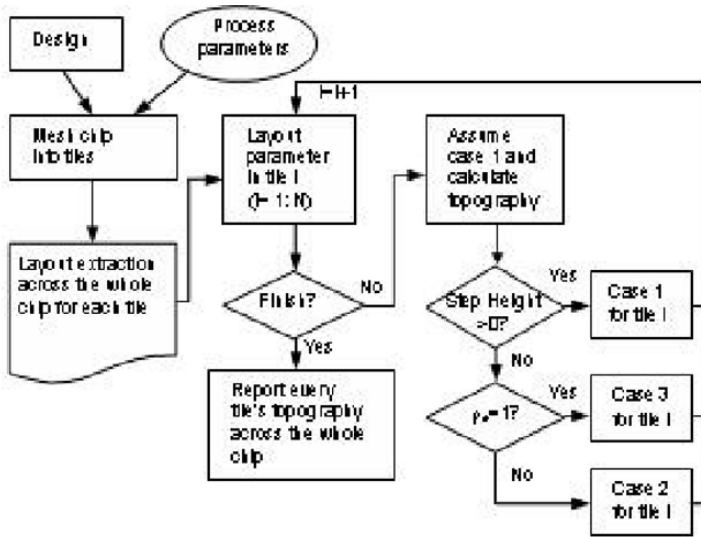


Figure 4.10. Framework of The Full-chip ECP Topography Simulator

4.4.1.1 Wide Wire and Wide Spacing (WWWS)

When the wire is wide, the average perimeter L_{avg} in $D \times D$ is small. Physically this means the contribution of the sidewall to the growth of the Cu in the trench is not significant and the growth of the Cu in the trench is mainly due to the additives on the trench bottom. Therefore the Cu thickness in the trench is approximately equal to the field Cu thickness. At the surface of the oxide, the additives contribute to the growth of both the Cu on the trench oxide surfaces and that shrinks (eats) into the trench. When the spacing is large, the amount of Cu shrinking into the trench is negligible (Figure 4.8). Hence, the additives contribute mainly to the growth of the Cu on the oxide, i.e., the Cu thickness on the oxide is approximately equal to the field Cu thickness as well. The step height S in this situation is approximately equal to the original feature trench depth T . This implies a Conformal-fill. Therefore, for wide wire and wide spacing Case (1) Conformal-fill (Figure 4.7) of the topography always occurs.

4.4.1.2 Wide Wire and Fine Spacing (WWFS)

When the spacing is fine, the shrunk amount of Cu into the trench is not negligible in comparison with the spacing (Figure 4.8). Therefore, the additives on the top of the oxide contribute to the growth of both Cu on the oxide and the Cu shrunk into the trench. This causes the trench Cu thickness to be smaller than the field Cu thickness. Since the thickness of Cu in the wide trench is approximately equal to the field Cu thickness as in the layout pattern WWWS,

the step height S is smaller than the original trench depth. However, the Cu in the trench will never grow higher than that on the top of the oxide. Once the height of Cu in the trench is equal to that on the oxide the additives in the trench will ‘spill’ over to the oxide and either case (2) Super-fill or (3) Over-fill of Figure 4.7 will occur. Because the spacing is fine, the whole oxide surface is covered by the additives from the trenches and therefore Over-fill occurs. In an extreme case where the spacing is equal to zero, Over-fill occurs from the beginning of deposition. Therefore, for a wide wire and fine spacing pattern, two cases may occur. When the spacing is very fine, case (3) occurs. When the fine spacing is relatively wider, Super-fill occurs.

4.4.1.3 Fine Wire and Wide Spacing (FWWS)

When the wire is fine, the average perimeter L_{avg} is large. The contribution of the additives on the side wall to the growth of Cu in the trench is significant compared to that on the trench bottom. Mathematically, the step height S calculated using Equation 4.20 is smaller than zero. Therefore, the additives will ‘spill’ out at some stage during the deposition. Since the spacing is large, the additives ‘spilled’ out can not cover the whole oxide surface. Hence Super Fill in Figure 4.7(2) occurs for the isolated fine wire.

4.4.1.4 Fine Wire and Fine Spacing (FWFS)

When the wire is fine, similar to that in FWWS, the additives will ‘spill’ out of the trench at some stage during the deposition. However, since spacing is fine, the whole oxide surface is covered by the additives ‘spilled’ out. Therefore Over-fill occurs, as shown in Figure 4.7(3). Figure 4.5 shows typical topographies corresponding to the above four layout patterns.

From the above discussion of the three post-ECP topographies it is clear that the final topography depends on layout patterns instead of simply on the layout density. For example, a layout pattern with fine wires and fine spacing and a layout pattern with wide wire and wide spacing can have the same layout density. But the former pattern leads to a conformal topography as in Conformal-fill and the latter one leads to a Super-fill or Over-fill. The perimeter plays an important role in ECP topography. This indicates that the final topography after CMP is not solely a function of the layout density. The density based dummy filling or slotting is not sufficient for Cu CMP. A pattern-driven dummy filling or slotting algorithm considering both the layout density and the layout feature perimeter is needed.

4.4.2 Tile Size and Interaction Length

Another issue for chip-scale simulation is the selection of the tile size. The size of the tile is primarily determined by the interaction length of the ECP

process. A tile size that is smaller than the interaction length is preferred for more accurate results. However, the whole chip simulation time is longer when the tile size is smaller. Based on experimental data from [1, 81, 82], it is estimated that the interaction length of the ECP process is in the range of several micrometers to $50\mu m$. For the examples in this chapter a tile size of $10\mu m$ is chosen. It is smaller than the tile size used in CMP simulation, which is usually around $20 \sim 40\mu m$ due to the relatively large interaction length of CMP ($100 \sim 200\mu m$ for Cu CMP, $500\mu m \sim 2mm$ for oxide CMP). The convolution of the layout density and feature perimeter sum in each tile with a pre-defined weight density function can be applied to incorporate the influences of neighboring tiles in the range of the interaction length, as shown in the CMP simulation of [83–85].

4.4.3 Model Verification

4.4.3.1 Experimental Verification from Test Structures

Experimental data from the test structures in [1] was used to verify the model proposed here. The field Cu deposition thickness H_0 is $1.55\mu m$ and the trench depth T is $0.55\mu m$. The Cu topographies over the structures with regular wire widths and spacings spanning from $0.25\mu m$ to $100\mu m$ are measured using high resolution profilers. Figure 4.11 shows the topographies measured with the field Cu thickness as a reference.

The GDSII file for these test structures was not available to us. However, once the line width L_w and spacing L_s are known, the layout parameters for these test structures can be derived as:

$$\rho = L_w / (L_w + L_s)$$

$$L_{avg} = 2 / (L_w + L_s)$$

$$\rho_e = \begin{cases} 1 & \text{when } \delta_e \geq L_s/2 \\ (L_w + 2\delta_e) / (L_w + L_s) & \text{when } \delta_e < L_s/2 \end{cases}$$

$$\rho_s = \begin{cases} 0 & \text{when } \delta_s \geq L_w/2 \\ (L_w - 2\delta_s) / (L_w + L_s) & \text{when } \delta_s < L_w/2 \end{cases}$$

Substituting these layout parameters into the model, we can simulate the array height H and step height S. In Figure 4.12 the triangle points show the correlation between experimental data and the simulation data from our model. The correlation clearly shows that the simulation results fit the experimental data well. The average error is 3.23% for the array height and 4.6% for the step height. Simulation data obtained by implementing the model in [1] is also plotted in Figure 4.12 for comparison. Its correlation with the experimental data is illustrated by the square points. The two subplots in Figure 4.12 clearly show

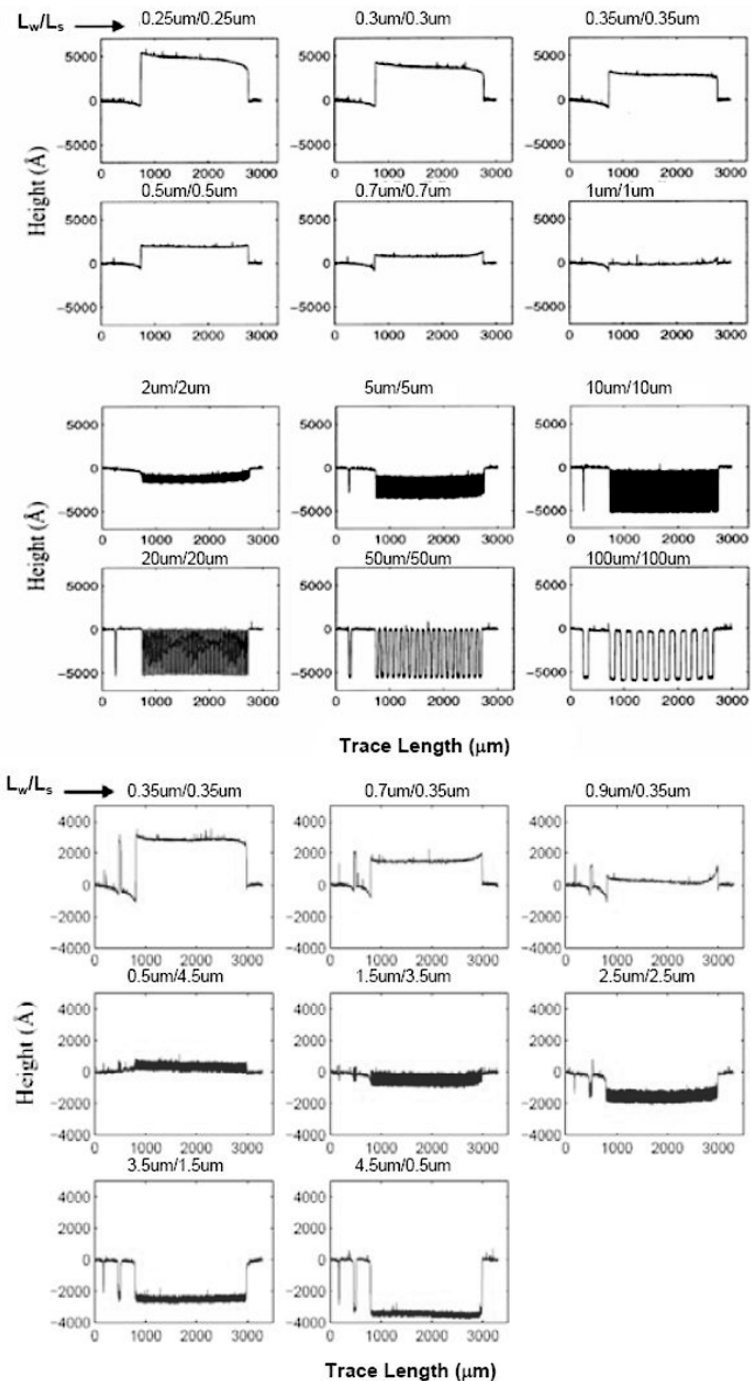


Figure 4.11. Experimental Post-ECP Cu Topography from [1]

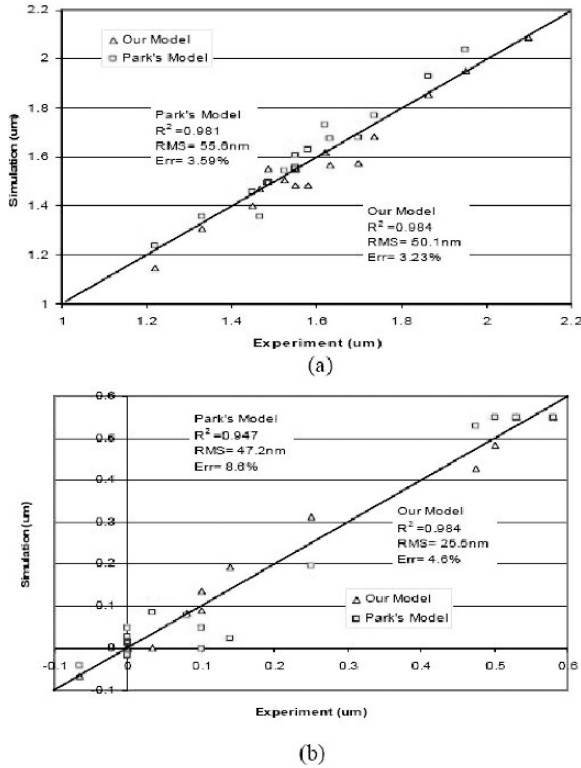


Figure 4.12. Experimental vs Simulation Results for (a) H and (b) S

that our model can fit the experimental data better than the empirical model in [1], especially for step height S , in Figure 4.12(b). The values of the three calibration parameters are: $\delta_e = 750\text{nm}$, $\delta_s = 133\text{nm}$, and $T_e = 130\text{nm}$. These values are quite reasonable considering their physical meanings. Comparison to the actual feature trench depth T of 550nm , $T_e = 130\text{nm}$ implies that the concentration of the accelerators on the side wall is $130/550 = 0.23 = 23\%$ of that on the top and bottom of the trench. $\delta_e = 750\text{nm}$ indicates that the accelerators in the trench spread 750nm from each side of the trench after they ‘spill’ out of the trench. $\delta_s = 133\text{nm}$ implies that the initial thickness increase on the side wall before accelerators moving from the wall to the trench bottom is 133nm . This small value makes sense considering the short time that the accelerators are absorbed on the walls.

The interaction length cannot be directly obtained from this set of experimental data simply because of the fact that in the above test structures the values of wire width and spacing are identical for a long range which is much larger than the actual interaction length. However, the interaction length range can be

estimated from the experimental results to be between $20\mu m$ and $50\mu m$. The reason is that if the interaction length is smaller than $20\mu m$, a Cu thickness equal to the field thickness should be observed at least on the center of the oxide. It is observed that for the $20\mu m/20\mu m$ wire width/spacing structure the Cu thickness on the oxide is smaller than the field Cu thickness (Figure 4.11). Hence, the interaction length should be larger than $20\mu m$. Similarly, the interaction length should be smaller than $50\mu m$ since the Cu thickness on the oxide of the $50\mu m/50\mu m$ test structures is equal to the field Cu thickness already (Figure 4.11). Therefore, for $50\mu m/50\mu m$ and $100\mu m/100\mu m$ structures, the wire width and spacing should be considered to be independent of each other. This indicates that in the simulation $\rho_e = 1$, $\rho_s = 1$, $\rho = 1$, $L_{avg} = 0$ should be applied to the tiles that are totally covered by the wide wires, and $\rho_e = 0$, $\rho_s = 0$, $\rho = 0$, $L_{avg} = 0$ should be applied to the tiles that are totally covered by the spacing. This yields a $1.55\mu m$ Cu thickness on the oxide spacing and a $1.55\mu m$ Cu thickness in the trench. The step height is $0.55\mu m$, which is the same as the trench depth, implying a Conformal-fill.

4.4.3.2 Simulation Results for a Real Design

One of the main advantages of the ECP model presented here is that it is not an empirical model built on regular test structures. Therefore, it can be applied directly to real designs and is not limited by any specific layout pattern.

Simulations on a real chip ($2.45\text{mm} \times 2.35\text{mm}$) with six metal layers were performed using calibration parameters obtained from the last section. The CPU (Linux, Intel XEON 2.20GHz, 2.06G) time including both layout extraction and topography simulation time is less than 2 minutes for each layer. We show the simulation results for metal three as one representative example. To avoid any confusion due to the negative step height in case (2) Super-fill (Figure 4.7), we introduce the surface height H_s and absolute step height S_a in the simulation. When the step height is positive, they are equal to the array height and step height respectively. The only difference is in case (2) of Figure 4.7 where the step height is negative. In this situation, the surface height H_s is equal to H_S and the absolute step height S_a is equal to $-S$. The S_a is always positive and H_s is always the highest height in the tile.

There are two purposes for these simulations, one is to test the applicability of the model to a real chip, the other is to test the sensitivity of the model to the interaction length. Figure 4.13 shows the simulation results of the surface heights H_s and absolute step heights S_a with three different interaction lengths $10\mu m$, $30\mu m$ and $50\mu m$. Figure 4.13 shows that reasonable simulation results were obtained. The H_s ranges from $1.0 \sim 2.4\mu m$, with $1.0\mu m$ corresponding to the skirt of the chip and $2.4\mu m$ corresponding to the center of the chip. This makes sense because the skirt is patterned with fine spacing and wide wires, whereas the center of the chip is patterned with fine spacing and fine wires.

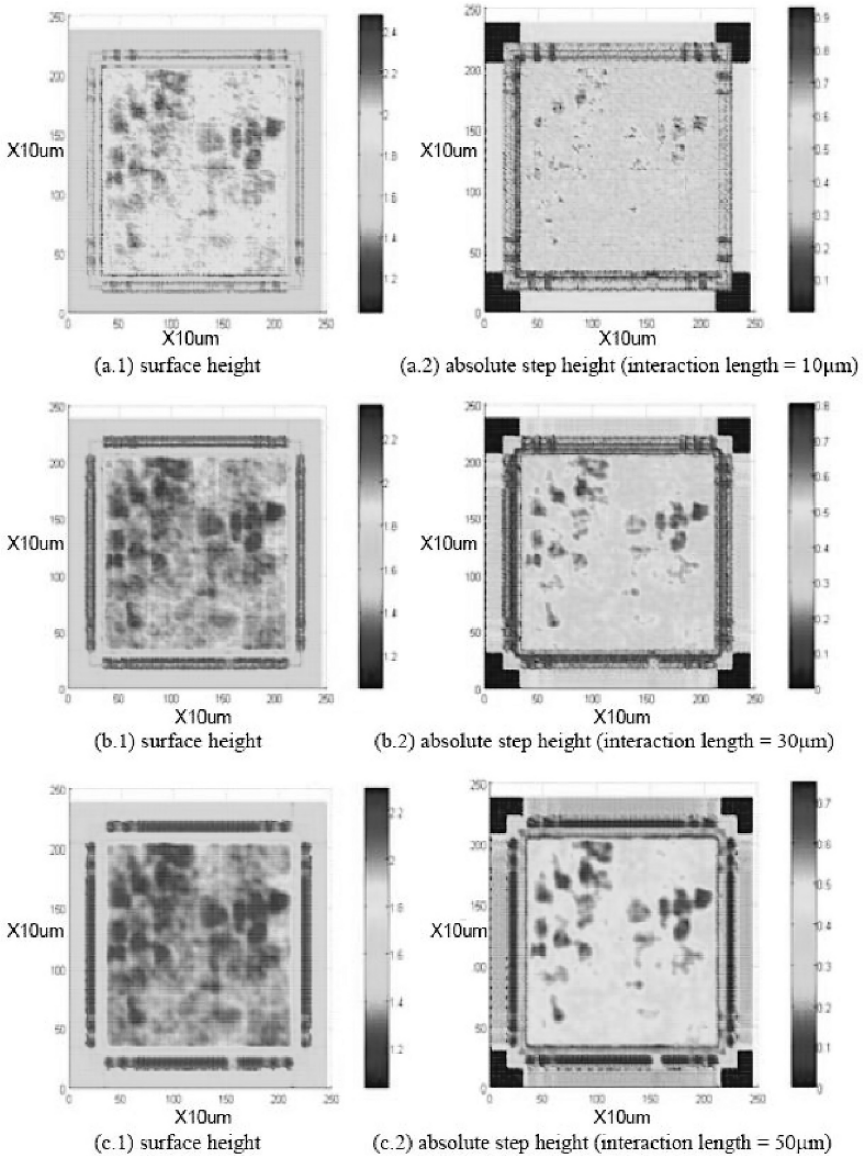


Figure 4.13. Simulation of Surface Height and Absolute Step Height Under Different Interaction Lengths

The S_a ranges from 0 to $0.9\mu\text{m}$, with $0\mu\text{m}$ corresponding to empty areas on the four corners of the chip and $0.9\mu\text{m}$ corresponding to the center of the chip. This is reasonable because on the empty area, a flat Cu surface with field Cu thickness H_0 is expected. For the layout patterns with fine spacing and wires

in the center of the chip, the absolute step height increases with array height, hence a larger step height is obtained.

The simulation results in Figure 4.13 also show the sensitivities of the topography to the change of interaction length. When the interaction length increases from $10\mu m$ to $50\mu m$, the surface height variation decreases from $1.4\mu m$ to $1.2\mu m$; the step height variation decreases from $0.9\mu m$ to $0.7\mu m$. Therefore, an accurate calibration of the interaction length is needed for accurate simulations.

4.4.4 Key Advantages of ECP Topography Model

In Sections 4.3 and 4.4 a full-chip ECP topography model was developed and tested. The key advantages of this ECP model over an empirical model are:

- It is built based on additive physics in the ECP deposition process with much fewer process parameters to calibrate.
- It is a unified model for the evaluation of array height and step height. The interaction between these two variables is preserved.
- It can be applied to arbitrary layout patterns in practical designs. It is not limited to just regular test structures.
- The incorporation of the interaction length into the model is easy and enables efficient full chip ECP simulation. This model can be used for full-chip ECP and CMP topography simulation to help evaluate a layout for catastrophic failure prevention, yield-aware design, and variation aware timing analysis. It can also be applied for the pattern-driven model-based dummy fillings and slotting

4.5 CMP

In Figure 4.5 of Section 4.3.2 we illustrated the topography of a silicon wafer after an ECP process. Also, in the same section we mentioned three main reasons why the surface of the wafer (post ECP) need to be planarized. Topping that list of reasons is the depth of focus (DOF) budget issue that need to be addressed in order for subsequent lithography steps to be carried successfully. Achieving planarity at the nano scale over a radial range of several millimeters is a very difficult task. After considering several alternatives the semiconductor industry has settled on chemical mechanical polishing for this purpose. Chemical-mechanical polishing (CMP) is a process used to remove surface irregularities and to obtain a uniform (planar) wafer surface. CMP is not totally new. It has its roots in the glass polishing industry, but obviously, the tolerances needed for the semiconductor application are more stringent causing CMP to be a heavily studied and researched process. Before moving to the

next section describing the CMP process it is worth mentioning that the use of CMP is not restricted to Cu but is equally used for silicon dioxide, polysilicon, titanium alloys (nitrides), and low-k dielectrics.

4.5.1 CMP Process Description

Figure 4.14 shows a picture of a real CMP station, Figures 4.15 and Figure 4.16 show a more detailed breakdown of the components and a schematic illustration of how a CMP station operates.

Mechanically, a wafer is held in an upside down position by the rotating wafer holder and is pressed against the pad as shown in Figure 4.16. At the same time this is being done an active chemical referred to as the slurry is constantly applied to the pad. The slurry contains a suspension of abrasive particles of alumina and silica as well as other chemicals. The chemicals interact with the surface of the layer to be polished rendering that surface softer. The surface of the pad itself is not a smooth surface but is rather a surface with indentations (small bumps) such that when the rotating wafer holder touches the pad under some pressure, the bumps spread the slurry on the surface of the wafer as well as do their own abrasive function in polishing the wafer. It is important to know that it is the combination of the chemical applied (the slurry) and the roughness of the pad surface together that do the polishing simultaneously and not one or the other alone; thus the name chemical-mechanical polishing.

In reality the Cu CMP process is a bit more complex. It is usually carried sequentially in three steps using three polishing platens, each with its own

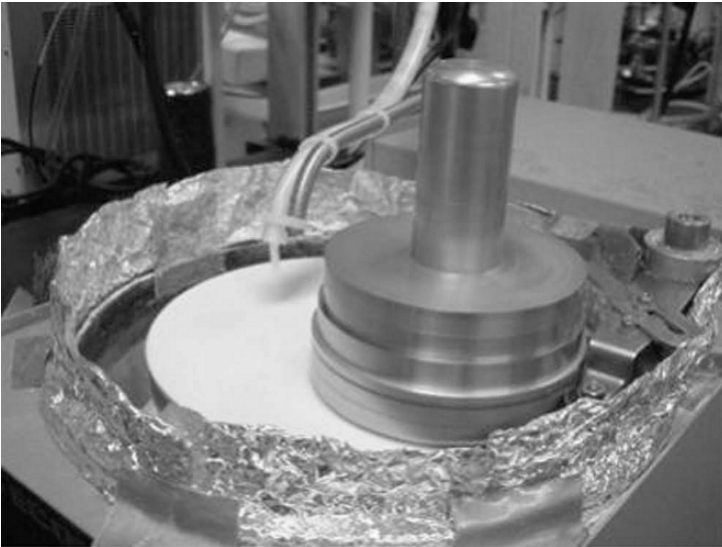


Figure 4.14. Polish Table: A Picture of One Sector of A Polishing Table

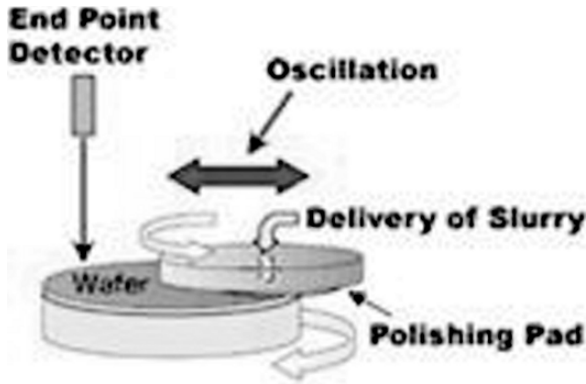


Figure 4.15. A Break-down of the Details of A Polishing Station

consumable mixture. Typically, bulk copper is removed in the first step, the barrier layer is removed during the second step and a dielectric-buffing¹ step is carried out in the third step. In Cu CMP, in-situ endpoint-detection of the desired remaining thickness is applied in polishing steps 1 and 2 to control the completion of the polishing. Polishing time is often used to control the completion of step 3.

As with many processes the use of CMP has been ahead of the full understanding and modeling of the process. In this section we will cover some basic models that describe and explain various aspects of CMP.

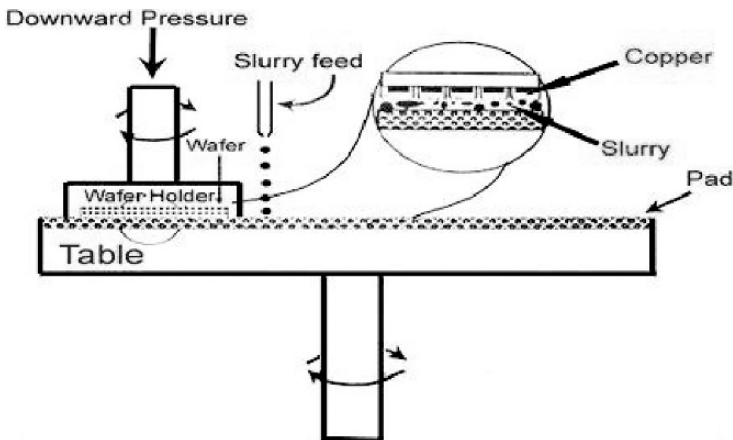


Figure 4.16. Schema: A Schematic Representation of A Polishing Station

¹Dielectric buffing is a step used to ensure all barrier materials are cleared from the dielectric surface.

4.5.1.1 Material Removal Rate

The most fundamental Preston's Equation describing the rate of removal of material is

$$R = KP V \quad (4.24)$$

Where R is the removal rate; K is a proportionality constant referred to as the Preston coefficient (function of the slurry used), P is the downward applied pressure, and V is the linear velocity of the polishing pad. The basic Preston Equation 4.24 predicts a zero removal rate for either of zero velocity (no rotation) or zero pressure. This is contrary to the experimental results which show a non-zero removal rate for zero P and zero V . This is obviously due to the chemical removal rate, and thus Equation 4.24 should be modified to account for that:

$$R = (KP + B) \times V + R_c \quad (4.25)$$

Where B is a proportionality constant and R_c is the chemical removal rate.

Another simple and useful way of expressing Preston's Equation for evaluating the removal rate [72] is expressed as

$$\frac{\Delta height}{\Delta t} \propto v P \quad (4.26)$$

Where v is the relative sliding velocity and P is the nominal contact pressure. The proportionality constant can be determined either from experimental data or approximated by $1/2E$ where E is Young's modulus.

4.6 Dummy Filling

We have covered in earlier sections the topics of ECP and CMP and have established that the final topography is a function of layout and of patterns. Another crude way of putting it is to add that it is also a function of pattern density which is just partially true. It is intuitively obvious that a sparse metal pattern is liable to be over-etched along the pattern edges next to empty areas. Empirical data can easily support such an intuitive assumption. Driven by that observation all fabrication facilities has long established minimum density rules for all metal layers and few non-metal layer in an effort to improve the planar integrity of their Damascene processes. Such rules are usually expressed by a minimum and maximum percentage of the metal in a specified window size for a certain layer. An example would be metal 2 layer for metal density to be no less than 20 or 30% of the total area of metal in predefined window. However no restriction or recommendation is issued regarding the manner in which this fill takes place as long as the final resulting density is achieved. The process of populating the empty areas of a particular layer with geometries of that layer to bring up the density of fill of that layer to the required minimum level or higher is referred to as "dummy fills".

However, with more research applied to this area a more sophisticated and more accurate approach to the metal (or any layer for that matter) fill problem

is arrived at. It is a model based fill where the impact of a particular fill pattern, its location and its density, are simulated using a CMP model to optimize the planarization of the final layer topology.

There are mainly two major approaches to metal fills:

4.6.1 Rule Based

The objective of rule based metal filling was to achieve better density uniformity. It worked with good results for Al metallization. Rule-based solutions, which are widely used in current EDA commercial tools, use guidelines from the fabs to insert metal fills such that the minimum and maximum density of the layout are within certain bounds and the density of a set of windows in the layout is within certain bounds. The layout is typically divided into windows and two adjacent windows overlap with each other by a pre-determined amount (usually equal to half the window size) to have a greater control on the density. Same pattern is repeated in the empty areas to bring the overall density of the metal in line with the recommended density. It has very basic rules and restrictions having to do with the minimum spacing of the fills to active lines to minimize parasitic interaction. The fills are basic, simple, and easy to array, aimed at maximizing the density.

4.6.2 Model Based

Model based dummy fills are driven by either an ILD thickness model that is effective density driven or a Cu model based on a combination of both effective

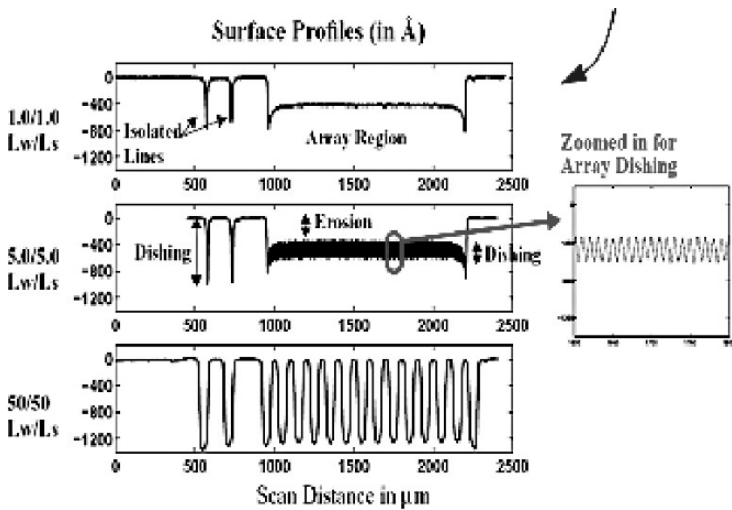


Figure 4.17. Surface Topography Profiles for Pitch Structures

density and perimeter of metal. We will be covering both approaches in this chapter.

Model-based solutions use an ILD thickness model to guide the metal filling process. The ILD thickness model that is typically used can be represented as follows [86]:

$$z = \begin{cases} z_0 - \left[\frac{K_i t}{\rho_i(x,y)} \right] & t < (\rho_i z_1) / K_i \\ z_0 - Z_1 - K_i t + \rho_i(x,y) z_1 & t > (\rho_i z_1) / K_i \end{cases} \quad (4.27)$$

where K_i is the blanket polishing rate, z_0 is the thickness of dielectric deposition, z_1 is the thickness of the existing feature, t is the polishing time and $\rho_i(x,y)$ is the convolution of the metal density and a weighting function which considers the deformation of the polishing pad during polish. All model based solutions seek to minimize $(\rho_{max} - \rho_{min})$, since thickness is proportional to ρ in the steady state. Some of the encountered solutions formulate the above problem as an linear programming solution [86, 87], whereas others use heuristic based solutions [88–90]. If the primary goal is to reduce the density difference between the different regions in the layout, rule-based solutions are known to suffice and are the most commonly used solutions.

Figure 4.18 is a side by side illustration of rule based metal fill and of an algorithmic simulation based metal fill. It is obvious that the traditional rule based metal fill is easy to apply and does not need much of computational bandwidth but will not necessarily result in minimizing ILD and metal thickness variability. Furthermore, achieving the overall fill density might still leave a

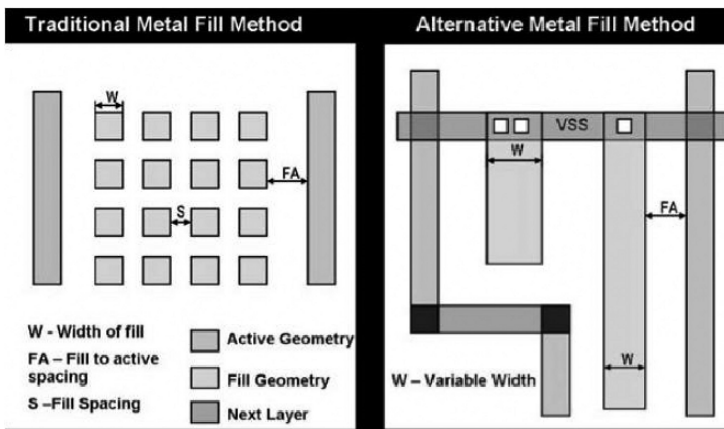


Figure 4.18. Metal fill Illustrates the Rule Based (Traditional) vs Algorithmic (Alternative) Approach

small active region un-evenly protected and thus a yield hot spot candidate. On the other hand a model based fill is computationally more expensive and slows down the router, but the resulting metal fill is superior in every aspect.

4.7 Application: ILD CMP Model Based Dummy Filling

4.7.1 Introduction

In Nano-CMOS regimes post-CMP wafer topography variation is a major cause of many yield and circuit performance variation rooted problems. Recent studies show post-CMP topography strongly depends on the features density in ILD CMP process [91]. Improving the density uniformity through dummy feature filling often leads to a better CMP planarization quality [92, 86]. Both oxide CMP [86] and copper CMP processes [93] have benefited from dummy filling. Major foundries have also set foundry rules requiring filling dummy features to improve the quality of CMP. However, the simple rule-based filling are not efficient [86]; it is not even effective in some cases. Smart dummy filling methods may significantly improve the filling quality by guiding the filling using an accurate CMP process model [88, 89, 92, 94, 95]. Results show that the smart dummy filling approaches can achieve much better post-CMP topography uniformity than “no fill” or rule-based filling [86].

Smart dummy filling is a complicated process that usually includes CMP process modeling, layout density acquisition, dummy feature density assignment, and dummy feature placement. Applying a fast dummy feature density assignment algorithm in combination with the right CMP model is the key to efficiently solving the smart dummy-filling problem. An accurate 2-D low-pass filter CMP model has already been developed and tested [96–98]; it is computationally inexpensive and easy to calibrate. Various smart dummy density assignment algorithms have been reported [88, 89, 92, 94, 95]. The linear programming method produces an optimal solution but it is also the most computationally time-consuming method. The Greedy method and the random Monte Carlo method [89] have been shown to be much faster. The Monte Carlo method randomly selects a panel for the filling in each step; the Greedy method searches for the panel with the highest priority in each step and fills it with the maximum possible amount of dummy features [89]. In this section we present a new iterative method that seamlessly couples with the 2-D CMP filter model. Instead of randomly selecting (Monte Carlo), or searching and filling one panel at a time (Greedy), this method guides the simultaneous filling of many panels using a variance minimizing heuristic. It iteratively fills in the low-density areas and nearby areas (or removes dummy fills from the overfilled areas) to achieve a result very close to the optimal solution. The new method has a low computational cost of $O(n\log(n))$. ILD CMP dummy filling is a linear problem that is perfect for illustrating the filling algorithms, so we

discuss dummy filling methods for single-layer oxide CMP with a min-variation [3] target in this section.

4.7.2 The 2-D Low-pass-filter CMP Model

A detailed CMP process model, which takes process parameters such as slurry contents, down pressure, pad material, and pad speed into consideration, is usually complicated. However, an abstract-level model may be simple since the CMP process that is designed to polish uneven surfaces is analogous to a low-pass “filter”. A 2-D low-pass-filter CMP model is found to be both efficient and easy to calibrate [97, 98]. According to the 2-D low-pass-filter model, the inter-level dielectric (ILD) thickness z [97] in the oxide CMP process is a function of the effective pattern density in Equation 4.27. After the layout is discretized using rectangle panels, the effective pattern density at the centroid of panel (i, j) is a 2-D convolution of the pattern density with the filter function. The effective pattern density can be calculated using [86]:

$$\rho_0(i, j) = IFFT[FTT[d(i, j)] \times FFT[f(i, j)]] \quad (4.28)$$

where $\rho_0(i, j)$ is the effective pattern density at the centroid of panel (i, j) , $d(i, j)$ is the pattern density, and $f(i, j)$ is the 2-D low pass filter function extracted from experimental data. The authors of [97] suggested that an elliptic filter function is a good approximation. In this section, we adopt the filter function used in [86]:

$$f(x, y) = c_0 \exp[c_1(x^2 + y^2)^{c_2}] \quad (4.29)$$

4.7.3 The Dummy Filling Problem

Only the single-layer metal dummy-filling problem of oxide CMP is discussed in this section. Assuming the wafer surface is perfectly flat before the metal layer is deposited, we minimize the effective density variation by adding dummy metal density in empty areas and removing dummy density from over-filled areas. According to the second Equation in 4.27, minimizing the effective density variation is equivalent to minimizing the ILD thickness variation $z = z_0 - z_1 - K_{it} + \rho_0(x, y)z_1$. The min-variation problem for single-layer dummy filling was presented in [86]. Here we modify the Equations slightly:
Minimize

$$\rho^H - \rho^L \quad (4.30)$$

Subject to

$$\begin{aligned} 0 &\leq \rho^L && \leq \rho_0(i, j) \leq \rho^H \leq 1 \\ 0 &\leq d_j(i, j) && \leq S(i, j) \\ d(i, j) &= d_0(i, j) + d_1(i, j) \end{aligned} \quad (4.31)$$

where ρ^H and ρ^L are the maximal and minimal effective density of the layout, $d_1(i, j)$ is the filled dummy feature density on panel (i, j) , and $S(i, j)$ is the slack density or the allowed maximal dummy feature density according to the foundry rules.

4.7.4 The Linear Programming Method

The linear programming (LP) method was presented in [86, 92]. Although this method produces the minimal, it suffers several drawbacks. The first drawback is its expensive computational cost, which is $O(n^3)$ [88]. When the discretization size is large and the problem has lots of unknowns and constraints, LP is a time-consuming method. A second drawback is that the LP solution may need to be rounded to an integer number of fill features. The rounding error could make the LP solution not optimal. We implemented the LP method by formulating the filling problem using the standard LP format [86], and solving it using `lp_solve 4.0`.

4.7.5 The Min-variance Interactive Method

To improve the computational efficiency and the dummy filling quality, we developed the min-variance iterative method that integrates seamlessly with the effective density model. This method guides the filling using a variance-minimizing heuristic.

Our goal is to reduce the effective density non-uniformity. The new iterative method first calculates the effective density of the layout by applying the filter model in Equation 4.28 at each step. It then calculates a target effective density as the mean of the effective density. Based on the difference between the local effective density value and the target effective density value, panels are prioritized and many panels are selected simultaneously for filling. The new method then assigns dummy features in low-effective-density areas or removes the already filled dummy features from high-effective-density areas. The above process is repeated until the uniformity of the effective density cannot be further improved, or until the maximum number of iterations is reached. Assuming no prioritization process is applied and the target effective density value is the mean value of the effective density of the entire layout, the basic min-variance iterative algorithm may be described by the following pseudo code:

Algorithm Min-variance Iterative

- 1 Evenly discretize the layout into panels (tiles).
- 2 Calculate the existing feature density $d_0(i, j)$ and the slack density $S(i, j)$.
- 3 Normalize the filter function, e.g., $f(i, j) = f(i, j) / \sum f(i, j)$

- 4 While(maximal number of iterations is not reached) {
- (a) Calculate the effective density using Equation 4.28;
 - (b) Calculate the filling amount $\Delta(i, j) = coef \times (mean(\rho_0) - \rho_0(i, j))$;
 - (c) Adjust $\Delta(i, j)$ such that

$$\begin{cases} \Delta(i, j) = \min(\Delta(i, j), S(i, j)) & \text{if } \Delta(i, j) > 0 \\ \Delta(i, j) = \max(-d_1(i, j), \Delta(i, j)) & \text{if } \Delta(i, j) < 0 \end{cases}$$
 - (d) Add dummy density $d_1(i, j) = d_1(i, j) + \Delta(i, j)$;
 - (e) Update slack density $S(i, j) = S(i, j) - \Delta(i, j)$;
 - (f) Terminate the iteration if the solution of $d_1(i, j)$ converges or $\Delta(i, j)$ becomes too small.
- 5 }

Note that discretization is the first step and is an important step. The panel size should be small enough to avoid significant discretization errors. Using panel size smaller than 1/10 of the filter characteristic length is recommended. In the second step, foundry rules should be satisfied. For example, $d_0(i, j)$ should be adjusted if it violates the minimal density rule; $S(i, j)$ should be reduced if $d_0(i, j) + S(i, j)$ is above the upper density limit. To avoid numerical stability problems and confusions, the filter function is normalized in the third step so that a perfectly smooth layout with $d(i, j) = \text{constant}$ everywhere also has the same effective density everywhere. The coefficient “coef” in step 4 of Algorithm Min-variance Interactive is a damping factor that adjusts the filling speed. Compared with the existing methods, the Min-variance Iterative method is more efficient and flexible:

- 1 Compared with the LP method, the iterative method has a very low computational cost dominated by the 2-D FFT operation, which costs $O(n \log(n))$. The total computational cost of the new method is approximately $O(n \log(n))$ if no more than a constant number of iterations are needed to achieve a satisfying result.
- 2 If the user decides to apply a pre-defined dummy pattern to the layout, such as a dummy pattern with evenly-spaced floating dummy squares, the final LP solution may need to be rounded so that an integer number of dummy features can be used. The rounding error could make LP solution non-optimal [95]. The iterative method can handle this rounding issue at each step and its final solution is still close to optimal.

- 3 Compared with the Monte Carlo and Greedy methods [89] the new method uses a variance-minimizing heuristic to guide the selection of multiple panels instead of selecting randomly or selecting one panel at a time. The above pseudo-code of a basic implementation shows that multiple low-effective density areas can be selected and filled simultaneously. And the filling amount of a panel in one iteration is not limited to the maximal possible amount. If desired, a more complicated function can be applied to adjust $\Delta(i, j)$ in step 4 of Algorithm Min-variance Iterative; and a prioritization function can be applied to reject certain selected panels. So the new method is much more efficient and flexible. After the first step the new iterative method may remove dummy features from the over-filled areas.
- 4 If we apply a prioritization function to select the panel with the highest priority in each iteration and let $\text{coef} = \infty$ in step 4, the new method becomes the Greedy method presented in [89]. So the Greedy method may be considered as a special case of the new iterative method. Some improvements that are applicable to the Greedy method may also be applicable to the new method.
- 5 The iterative method could produce a smoother effective density profile. As illustrated in Figure 4.19, the effective density solution of the new method does not have the second large bump marked by the magenta circle. This bump is the result of the LP method that tries to achieve the smallest peak-peak value by adding too many dummy fills in this region resulting in a high density. The peak-peak value of a function f is defined as $\max(f) - \min(f)$.
- 6 This iterative method is flexible. If a min-fill (minimizing dummy fills) target is desired instead of the min-variation target, the above algorithm may be modified to solve this problem.
- 7 Several heuristics can be applied to make this iterative method achieve high quality of results more efficiently, such as not filling panels close to the maximal effective density areas or those defined as locked according to [89].

Exercise: Please find at least one heuristic that can make the iterative method achieve high quality results more efficiently.

The efficiency of the new method is straightforwardly illustrated by the 1-D example shown in Figure 4.19. We discretize the “1-D” layout using 50 evenly divided segments. Figure 4.19 shows the effective density at the centers of the segments. The curve labeled “No fill” is the effective density of the single-layer layout without dummy filling. The curve labeled “Rule-based solution” is the effective density when all empty areas are filled [86]. The “LP solution” is the effective density solution of the LP method. The peak-peak value and the standard deviation of those solutions are given in Table 4.1. The peak-peak

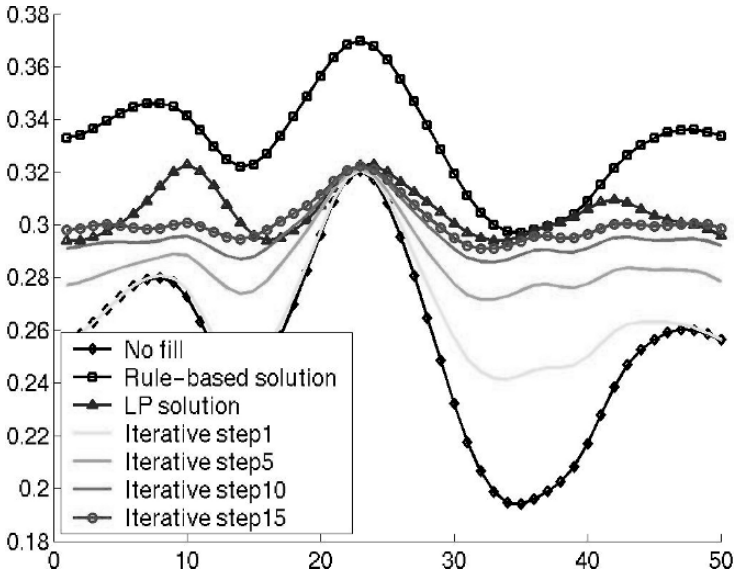


Figure 4.19. Solutions of a Simple 1-D Problem

value of the LP solution is the smallest since the rounding issue mentioned previously is not considered here. Figure 4.19 and Table 4.1 also shows that the new Min-variance Iterative method quickly converges to a solution that is very close to the optimal. The curves labeled with “Iterative step n” are the effective density solutions after n iterations. A result very close to the optimal solution is achieved with 15 iterations. Results also show that the iterative method solution has the smallest standard deviation.

4.7.6 Improving the Detection Capability of the 2-D Low-pass Filter

The CMP model guides the filling by selecting low/high effective density areas. However, the 2-D low-pass filter models the planarization effect of the CMP process. It is good at “averaging” but not very good at “selecting” where to fill so that the effective density variations can be minimized. In other words,

Table 4.1. Peak-peak Value and the Standard Deviation of Effective Density

Solutions	Peak-peak	Standard deviation
No-fill	0.1264	0.0337
Rule-based solution	0.0729	0.0196
LP solution	0.0287	0.0090
Iterative step15	0.0312	0.0076

the low-pass filter removes high frequency components, which could be the information needed for determining the filling. Bad detection happens more often in 2-D low-pass filters with larger characteristic lengths because those filters remove more high frequency components. This problem is illustrated in Figure 4.20. The first subplot in Figure 4.20 shows a filter function f that takes the average value of seven neighboring points. The second subplot shows the density d and the third subplot shows the effective density (the density convolved with the filter function). Interestingly, the effective density has the maximal value at position zero even though the density has the minimal value at this point. Apparently, the 2-D low-pass filter is misleading. If we do filling based on the above result, we should fill in high-density areas that may have zero slack density to fill instead of low-density areas.

The problem is caused by the width of the filter. Given the waveform in the second subplot, every point with the maximal value has 4 zero neighbors and another two with the maximal values. But every point with the minimal value has 4 neighbors with the maximal values among the 6 closest neighbors. So after convolving with the filter, the effective density trend does not match with that of the density. However, there is an easy solution: we can simply reduce the filter width to avoid it. Subplot four in Figure 4.20 shows a new filter with a shorter width, and Subplot five shows the new effective density that can be used to locate the low-density area. This observation also answers the question of why using a filter with a shorter characteristic length to do the

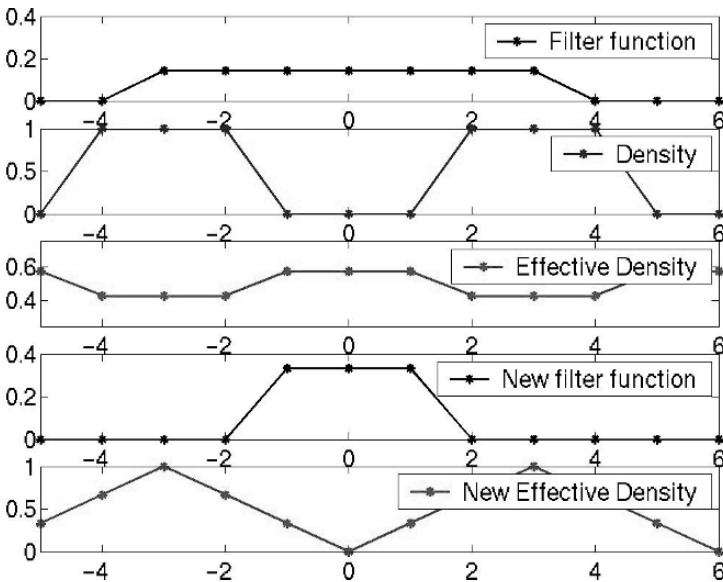


Figure 4.20. A Specific Case

dummy filling may produce even better results than using the given filter. Filters with shorter characteristic lengths can effectively locate local low-density areas. Based on the above observation, we modified the fourth step of the Algorithm Min-Variance Iteration described in Section 4.7.5 by adding an outer iteration loop. This iteration adjusts the filter characteristic length. We first use a filter with a shorter characteristic length (e.g. 20% of the given one) to do the filling, and then gradually increase the filter characteristic length until the given one is reached. The fourth step of the Algorithm Min-Variance Iteration is modified as follows:

Step 4 of Algorithm Min-variance Interactive

- 1 for (filter_length = 0.2 * original_filter_length; filter_length != original_filter_length; filter_length = filter_length + 0.2 * original_filter_length) {
 - (a) (Keep on using $d_1(i, j)$ and $S(i, j)$ in the previous iteration.)
 - (b) While (the maximal number of iteration is not reached) do {
 - (c) Calculate the effective density using Equation 4.28;
 - (d) Calculate the filling amount $\Delta(i, j) = coef \times (mean(\rho_0) - \rho_0(i, j))$;
 - (e) Adjust $\Delta(i, j)$ such that

$$\begin{cases} \Delta(i, j) = \min(\Delta(i, j), S(i, j)) & \text{if } \Delta(i, j) > 0 \\ \Delta(i, j) = \max(-d_1(i, j), \Delta(i, j)) & \text{if } \Delta(i, j) < 0 \end{cases}$$
 - (f) Add dummy density $d_1(i, j) = d_1(i, j) + \Delta(i, j)$;
 - (g) Update slack density $S(i, j) = S(i, j) - \Delta(i, j)$;
 - (h) Terminate the iteration if the solution of $d_1(i, j)$ converges or $\Delta(i, j)$ becomes too small.
 - (i) }
- 2 }

4.7.7 Simulation Results

All simulations given in this section were performed on a 400MHz Sun Ultra-4 workstation with 4 GB RAM. We used lp_solve 4.0 to solve LP problems. The FFT operations were performed using FFTW 3.0. The maximal number of iterations used in the min-variance iterative method is 120. However, as described in the previous sections, the iterative solver stops when the convergence criteria are satisfied.

4.7.7.1 Test I: Accuracy

To test the performance of the new min-variance method, we did an exhaustive test using 1000 randomly generated cases. In each case the layout

is assumed to be 10mm*10mm and it is evenly discretized into 20*20 panels. We simply assume the layout is filled with metal wires separated by the minimal spacing, and the dummy features are even-spaced square blocks. So the maximal metal wire density is 50% and the maximal dummy feature density is 25%. We assume the metal wire density $d(i,j)$ on each panel is a random number uniformly distributed between (0, 0.5). The slack density on the panel is assumed to be

$$S(i, j) = \max(0, 0.5(0.5 - d(i, j)) - \text{slack_reduction}) \quad (4.32)$$

When calculating the slack areas, foundry dummy rules have to be satisfied. This makes the fillable areas smaller than or equal to the vacancy areas. We model this using a parameter “slack_reduction” that reduces the fillable area density. slack_reduction is a single random number between $0 \sim 0.1$; it is applied to every panel on the layout. The goal of the dummy filling approach is to reduce the non-uniformity of the post-CMP profile. So it is important to compare with the no_fill solution to show the improvement. We ignore the rounding problem so that we can have a fair comparison with the optimal LP solution. We define the relative error as:

$$\text{rel_err} = \frac{\text{abs}(\text{peak_peak}(\text{iterative}) - \text{peak_peak}(\text{LP}))}{\text{peak_peak}(\text{no_fill})} \quad (4.33)$$

where abs() is the absolute value function; and the peak-peak value of a function f is defined as max(f)-min(f).

Based on the above definition, the average value of the relative error of the min-variance iterative method is 2.38%, and the standard deviation of the relative error is 1.68% for the 1000 test cases. Clearly, this exhaustive test shows that the solution of the new approach is very close to the optimal LP solution.

4.7.7.2 Test II: Discretization Error

Fast speed is a significant advantage of the new min-variance method over the LP method. Although LP could produce a quick solution if a coarser discretization is used, large discretization errors often make this “trick” impractical. We recommend using the filter characteristic length to determine the discretization size. Only the LP method is used in this discretization-error test so that the error is 100% from the discretization. We used Metal-4 layer of a real design. The panels are all square panels. The finest discretization uses 30*30 panels, while the other coarser discretization use 6*6, 10*10, 12*12, and 20*20 panels respectively. Figure 4.21 shows the peak-peak value of the effective density of the LP solution vs. the normalized panel size, which is defined as

$$\text{normalized_panel_size} = \frac{\text{panel_size}}{\text{filter_characteristic_length}} \quad (4.34)$$

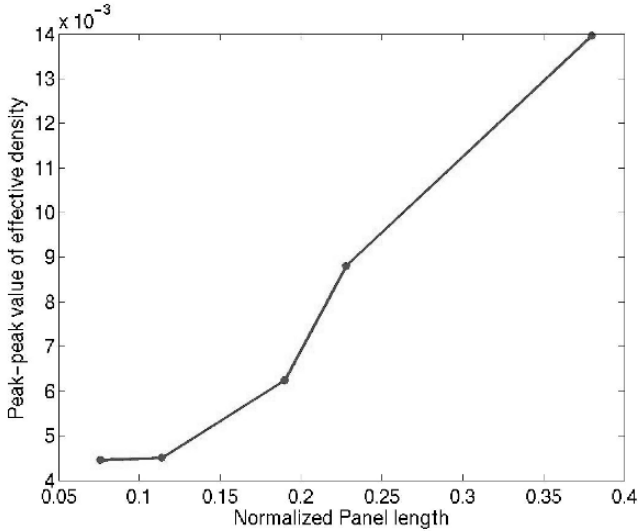


Figure 4.21. The Discretization Error of LP

The definition of the filter characteristic length is the same as that of [97]. In this test, LP is applied to assign dummy feature density to each panel. If the discretization is not the finest discretization, the layout is rediscritized into the finest discretization using 30×30 panels after the dummy feature density has been assigned, and the effective density is recalculated using the finest discretization. Figure 4.21 shows that the peak-peak value of the effective density solution converges when the discretization gets finer. As expected, the discretization error is negligible when the panel size is less than 10% of the filter characteristic length.

4.7.7.3 Test III: Speed

We also used the previous example to test the speed of the new iterative method. CPU time (in seconds) is given in Figure 4.22. The horizontal coordinate is the number of unknowns. When the entire layout is discretized into 30×30 panels, the total number of unknowns is 900. As shown in Figure 4.22, the min-variance iterative method is much faster than the LP method.

Figure 4.23 and Figure 4.24 show the effective density solution of the LP method and the min-variance iterative method, respectively. The rel_err of the min-variance iterative method is 2.29%. Table 4.2 shows the effective density solutions of the 5 filling approaches: no fill, the rule-based method, the LP method, the min-variance iterative method, and our implementation of the Greedy method. The finest discretization with 30×30 panels is used. As

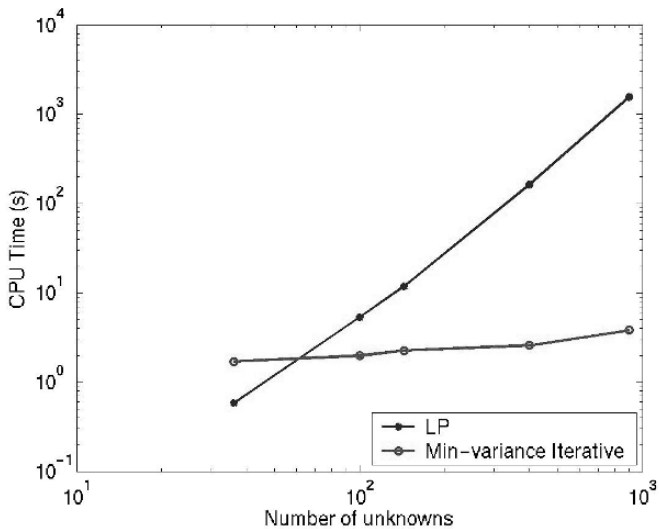


Figure 4.22. The CPU Time Comparison

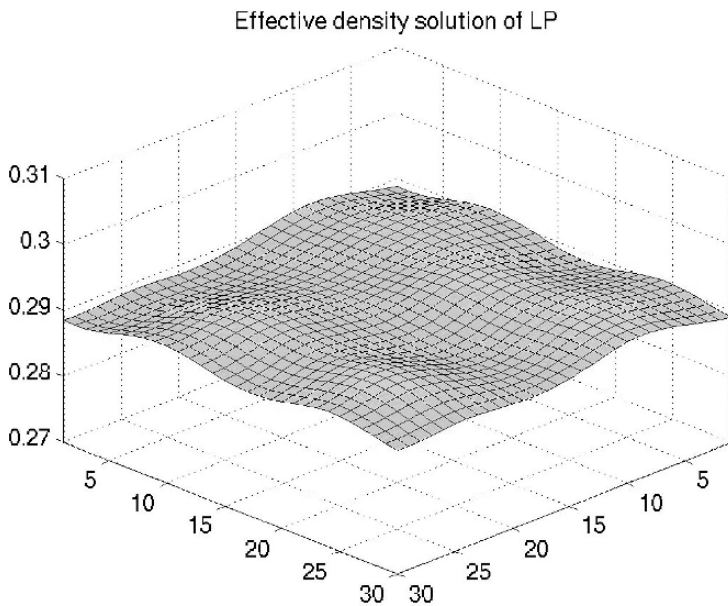


Figure 4.23. The Effective Density of the LP Method

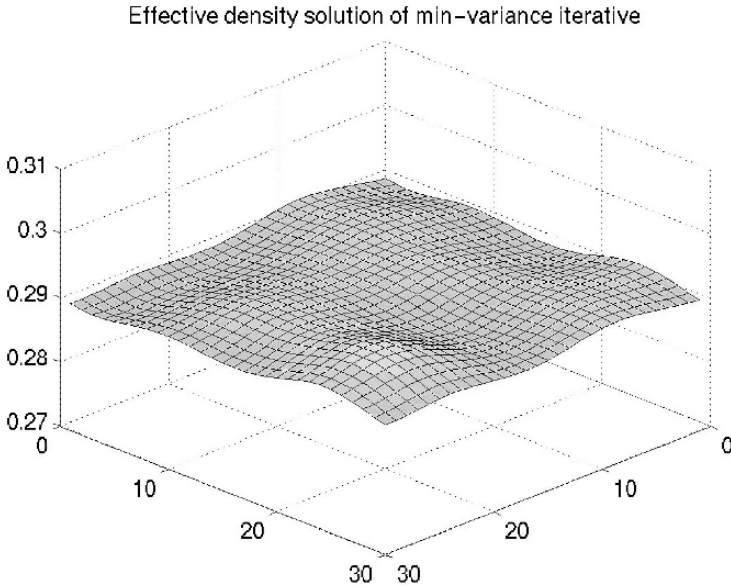


Figure 4.24. The Effective Density of the New Min-variance Iterative Method

expected, the effective density peak-peak value solution of the min-variance method is very close to that of the optimal LP method; and it is about 1/10 of the peak-peak value of the no-fill solution. The computational cost of the new method is almost negligible compared with the cost of LP. We have also implemented the Greedy method. The results of the Greedy method are also close to that of the LP method. However, due to our slow searching implementation of search, its speed was slow. The new iterative method has achieved a significant non-uniformity reduction. Although it cannot achieve the optimal solution because it uses the 2-D low-pass filter that does not have a perfect detection capability, we found its solution good enough for the purpose of dummy filling.

Exercise: Extend the method in Section 4.7 from one layer to multi-layers.

Table 4.2. Peak-peak Value and the Standard Deviation of Effective Density

Solutions	Peak-peak	Standard deviation	CPU time (s)
No-fill	0.0567	0.0184	N/A
Rule-based solution	0.0525	0.0163	N/A
LP solution	0.0039	0.0010	1,566
Iterative	0.0052	0.0010	5.67
Our Greedy implementation	0.0055	0.0013	N/A

4.8 Application: Cu CMP Model Based Dummy Filling

In this section we describe an algorithm aimed at minimizing the thickness range (the difference between the highest point and the lowest point of the chip surface) of a chip through the use of an optimized metal fill [99, 100].

4.8.1 Why Model Based Metal Filling?

For Cu metallurgy processes a variety of layout parameters (besides density) can affect the final after CMP topography. Figure 4.5 shows an example where two regions with the same density (highlighted by the two circled regions) can end up with very different topographies. Hence, it is no longer sufficient to only reduce the density differences between the different regions in the layout during metal filling. In fact, pure density-driven metal filling can often increase the final thickness range, a claim that has been supported by experimental results. The algorithm takes in to account the physical mechanisms of the Damascene process, namely ECP and CMP. The algorithm outputs three key predictors of the final thickness range that are computed efficiently and are used to drive the metal filling process. The primary features of this algorithm are as follows:

- 1 Key reliable predictors of the final thickness range based on the physical mechanisms of Cu ECP and CMP are identified and used to guide the metal filling process. These predictors can be efficiently computed, while reliably predicting the final thickness range of the chip surface. This makes it possible to have a high quality and yet practically feasible metal filling solution.
- 2 Use of smooth ECP topography as an objective allows parameters besides density to be considered during metal filling. In particular, it allows accounting for perimeter effects during metal filling, thereby making the proposed solution strongly layout pattern dependent. The proposed solution is a truly comprehensive solution in that it considers ECP effects during metal filling.
- 3 Experimental results indicate that the reduction in thickness range obtained using the proposed scheme (as measured by Synopsys CMP simulator) is significantly better than that obtained using the standard available density-driven solutions. In addition, the density-driven solutions can often increase the thickness range after metal filling, a scenario that is not desirable and that this proposed method successfully avoids. solution.
- 4 The proposed filling algorithm can be easily incorporated into current place & route and/or verification tools making on-the-fly optimal metal fills possible.

To simulate the layout dependency of Cu thickness variation after CMP, a CMP simulator was developed (Synopsys). The simulator includes four components: an ECP topography model, platen 1 polishing model, platen 2

polishing model and platen 3 polishing model. Typical process parameters from a fab were inputted to the simulator. The simulator is quite comprehensive in its modeling and can capture both typical CMP non-uniformities such as dishing, erosion and multi-layer accumulative effects and atypical CMP non-uniformities such as edge erosion and isolated line dishing.

The inadequacy of density in faithfully predicting Cu CMP topography is illustrated by two examples. Figure 4.17 shows the measured surface profiles of three structures with the same density (50%) but different line widths and spacings after Cu ECP and CMP [85]. As can be seen, the surface profiles are quite different with increased dishing for the larger line widths. To test this more exhaustively, we also ran the Synopsys in-house CMP simulator on a test-chip which had patterns with different density and perimeter combinations. The test-chip includes patterns with the same density and different perimeters as well as patterns with different densities and perimeters.

Figure 4.25 shows the density map and the thickness map for the test-chip. It can be seen that different regions with the same density have different final thickness values after Cu ECP&CMP. Based on the above data, it can be concluded that it is not sufficient to only consider density during metal filling for copper processes.

4.8.2 Predictors of the Final (Post-CMP) Thickness Range

In this section the range of the final metal thickness that could be used to drive the metal filling. The goal is to have predictors that can be efficiently calculated while being fairly representative of the final thickness range. From

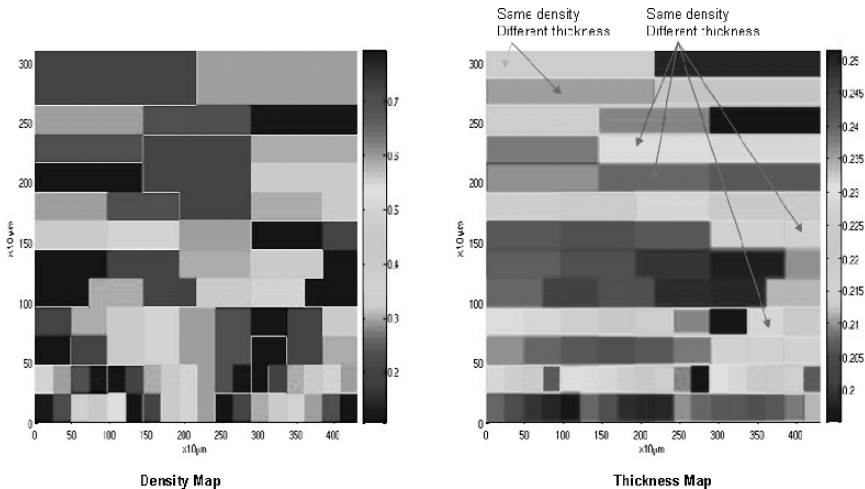


Figure 4.25. Topography Results using CMP Simulator

this point on in this chapter, Cu ECP and CMP are simply referred to as ECP and CMP, respectively.

4.8.3 ECP Thickness Versus Final Thickness

We noted in a previous section that surface non-uniformities after ECP can propagate through the CMP platens and result in a non-uniform final topography. This suggests that a smaller ECP thickness range (i.e. a more flat ECP topography) for a given design would result in a smaller final thickness range.

To experimentally test this thesis², we modified the ECP topography model in our in-house simulator to produce progressively smoother ECP topography without changing the subsequent CMP platens. The ECP model was run with five different settings to produce ECP profiles with the following ranges for a given design: original range (which is the ECP thickness range with no change to the ECP model), range = 75% of original ECP range, range = 50% of original ECP range, range = 25% of original ECP range and range = 0% of original ECP range (i.e. flat profile after ECP). For each setting, the ECP thickness value of each tile was scaled equally by the same ratio. The results of running the CMP simulator with five different settings for the ECP model on a set of 65nm and 90nm designs are presented in Figure 4.26. It can be seen that for the same layout as the ECP thickness range is reduced, the final thickness range was monotonically reduced by a substantial amount. The above results clearly indicate that the range of the incoming ECP profile does have a strong impact on the final thickness range; and a smaller ECP thickness range results in a smaller final thickness range.

Thus, using ECP thickness range minimization as an objective during metal filling has a very high likelihood of resulting in a smaller final thickness range for the metal filled design than the original. Most metal filling solutions available today fail to consider the dependency between ECP thickness and final thickness during metal filling.

4.8.4 Effective Density Versus Final Thickness

For more uniform ECP profiles, there is a dependence between the final thickness and density [84]. Typically, thickness in such cases is inversely proportional to the *effective density*, which is a function of the density. The effective density denoted by ρ is equal to the convolution of the density and a weighting function and is computed as follows: $\rho = d \otimes w$ where d is the metal density and w is the weighting function that accounts for the deformation of the polishing

²The absence of a closed-form analytical equation for final thickness makes it very hard to mathematically derive the relationship between ECP thickness range and final thickness range.

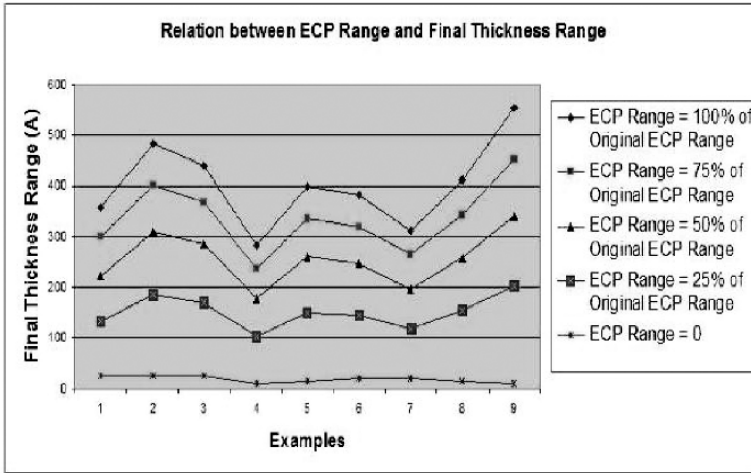


Figure 4.26. Impact of ECP Thickness Range on Final Thickness Range

pad [83]. The weighting function that we use is from [83] and is given by the following equation:

$$w(r) = (4(1 - \nu^2)qa^{\pi/2}/\pi E) \int_0^{\pi/2} \sqrt{1 - r^2/a^2 \sin^2(\theta)} d\theta, \quad (4.35)$$

where r is the distance, a is the radius of the interaction region, q is the down pressure, ν and E are the Poisson ratio and the Young's modulus of the polishing pad, respectively. Typical values of a for Cu CMP range between 40-120 microns [101] and is henceforth referred to as the *CMP radius of influence*.

A smaller effective density range translates to a smaller thickness range if the incoming ECP profile is quite uniform. *Thus a smaller effective density range for the same ECP thickness range and same maximum ECP thickness after metal filling will result in a smaller final thickness range.*

It should be noted that both the ECP thickness values and the effective density values can be calculated very efficiently since both these values can be analytically computed in a single step. Thus, it is computationally feasible to develop a high quality metal filling solution that is guided by these predictors. On the other hand, using the CMP simulator directly to drive metal filling is not a feasible solution since the simulator performs a series of repeated iterative evaluations of equations until a steady-state is reached.

4.8.5 Details of the Proposed Metal Filling Algorithm

The details of the featured metal filling algorithm based on the predictors outlined in the previous section are discussed here. The key objective of the

algorithm is to minimize the final thickness range of the chip surface. The algorithm uses an ECP model, among other things, to guide the filling process. The ECP thickness at a location depends on both the density and perimeter of the layout features in the areas surrounding it and hence is pattern dependent [102, 77] (for instance, it is necessary to distinguish between fine line/fine spacing and wide line/wide spacing even if they have the same density). Hence, we will refer to the proposed algorithm as the *model-based layout pattern dependent (MBLPD)* algorithm. The *MBLPD* algorithm has to manipulate both the density and the perimeter of the layout to achieve the best possible final thickness range reduction.

The *MBLPD* algorithm is divided into two main steps: *parameter assignment* and *fill placement*. The key objective of the *parameter assignment* step is to determine the best density and perimeter targets for all the tiles of the layout such that the final thickness range is minimized. The size of the tile is set to be the same as the tile size for the ECP model being used. The parameter assignment step accounts for both the ECP profile and the effective density and performs the following in a sequential fashion: meshes the layout into tiles, minimizes the ECP thickness range between the tiles and then as a post-processing step minimizes the effective density range (i.e. the difference between the largest effective density and the smallest effective density) between the tiles while ensuring no increase in the ECP thickness range. In both minimization steps, the maximum ECP thickness after parameter assignment is kept the same as the maximum ECP thickness of the original design. As mentioned earlier, this ensures a ‘good’ distribution of the ECP thickness values of the tiles with a larger number of tiles with ECP thickness above the transition point. During *fill placement*, the fills are inserted in the layout. The fills are selected to best match the density and perimeter targets computed in the assignment step for each tile.

In the *MBLPD* algorithm, parameter assignment and fill placement are decoupled for runtime efficiency. However, to increase the likelihood that fill placement can find the fills necessary to satisfy the targets assigned by parameter assignment, both steps use the same input information about the different types and configurations of fills that can be used. This ensures that the parameter assignment step only assigns density and perimeter targets that are realistic and based on actual fill patterns that can be inserted during the fill placement step. Information related to the types and configurations of the fills is stored in a library of fill patterns. Each element of the library represents a particular pattern of fills and is denoted as (l, w, x_s, y_s) . Here l denotes the length of the fill element, w denotes the width of the fill element, x_s and y_s denote the the spacing between fill elements in the horizontal and vertical directions respectively. The library used in our experiments has ~ 2000 unique fill elements. Note that the fill pattern can contain multiple instances of a fill element. The values of l , w , x_s and y_s are chosen such that the DRC rules and grid restrictions are satisfied.

This ensures that the fill placement step only has to focus on achieving DRC correctness between signal wires and fills.

4.8.5.1 Parameter Assignment

The key layout parameters that are considered in this step are density and perimeter since ECP thickness profile primarily depends on both these parameters and the effective density depends only on density. As mentioned earlier, the parameter assignment step has two main steps.

In the first step, the objective is to minimize the thickness difference between the highest tile and lowest tile at the end of the ECP process. The only constraint during this step is to make sure that maximum ECP thickness for the layout after this step be the same as the maximum ECP thickness of the original layout. As described earlier, the relationship between the layout parameters and the ECP thickness of a tile depends on the particular case (Conformal/Super/Over -fill) it falls under. This makes it hard to perform ECP thickness minimization as the tile thickness values may oscillate depending on their respective cases. In our solution, we tackle this issue by pushing all the tiles into the Over-fill case before starting the minimization problem. A few key observations can justify this simplification. First, the ECP thickness within a tile is smooth in the Over-fill case. Second, most of the tiles in typical industrial layouts fall into the (Super/Over)-fill cases and the Super-fill tiles can be very easily converted to the Over-fill case by inserting a small number of fills. Thus, the original design is perturbed very slightly during this conversion. Finally, an Over-fill tile has a very high likelihood of remaining an Over-fill tile if the only allowable layout modification is the insertion of fill patterns. Simple checks can be performed during the insertion process to ensure that an Over-fill tile never moves to any other case. In fact, in all our examples, a tile never moved from the Over-fill case to any other case. Thus, the likelihood of oscillation in the cases is significantly reduced once the tiles are all Over-fill tiles. At this point, there is a unique dependence of the ECP thickness on density and perimeter and the thickness difference between the different tiles can be more easily minimized.

The second step of the assignment algorithm seeks to reduce the effective density range between the tiles without increasing the ECP thickness range between the tiles. This step is necessary since the dependence of the final thickness on effective density increases as the ECP topography gets more uniform after the first step of parameter assignment. The details of the parameter assignment step is given below.

1 Layout Preparation:

- (a) Mesh the layout into non-overlapping tiles. Denote the i th tile as T_i .
- (b) Determine the amount of available space, henceforth referred to as the *fill-able area*, in each tile for inserting fills based of DRC/routing rules.

The ratio of *fill-able area* and total tile area multiplied with a weighting factor³ gives the *fill-able density*. The *fill-able density* of the tile T_i is denoted as d_i^F .

- (c) Based on the input fill pattern library, enumerate valid (density, perimeter) combinations that can be assigned to the tiles. The set of combinations is denoted as CS .

2 Reduce ECP Thickness Range:

- (a) Let the maximum ECP thickness of the design be H_{max} .
- (b) Determine case of each tile using an ECP model. In this work, the ECP model proposed by Luo et al. [77] was used.
- (c) For each tile T_i in the layout:
- i If T_i is in Over-fill case, continue.
 - ii Pick $c = (d_k^c, p_k^c) \in CS$ such that $d_k < d_i^F$ and the density and perimeter of T_i incremented by (d_k^c, p_k^c) satisfies the conditions for the Over-fill case. Typically, the element c with the smallest value of d_k^c that satisfies the above condition is picked. If no such element c exists, then go to Step 3⁴.
 - iii Update $d_i^F = d_i^F - d_k^c$.
- (d) For each tile T_i , unlock it and compute its priority as a function of the difference of its ECP thickness and the maximum ECP thickness.
- Typically, a tile with a small ECP thickness or a tile which has a large number of neighbors with small ECP thickness has a higher priority. Tiles whose ECP thickness are equal to or within a certain range of H_{max} are assigned zero priority and are left untouched in this iteration.
- (e) Until (some tiles remain unlocked)
- i Initialize $DT \leftarrow \phi; TS \leftarrow \phi$.
 - ii Sort the tiles according to the priority function.
 - iii Until (all unlocked tiles are processed)
 - Pick next tile in the priority order. If the tile belongs to DT , continue. Else insert it in TS and add all the tiles within its *ECP radius of influence* into DT .
 - iv For each tile $T_i \in TS$, do

³The weighting factor is less than 1 to account for the fact that the sum of areas of the inserted metal fills is usually less than the fill-able area due to spacing rules between fills.

⁴It should be noted that in all the examples we tried we were always able to convert all Conformal/Super-fill tiles to Over-fill tiles.

- Pick $c = (d_k^c, p_k^c) \in CS$ such that $d_k < d_i^F$ and the following conditions are satisfied: (1) Difference between H_{max} and ECP thickness of T_i after incrementing the density and perimeter of T_i by d_k^c and p_k^c , respectively, is minimized. (2) New ECP thickness values of T_i and the tiles in its *ECP radius of influence* are \geq their original thickness values⁵ and $\leq H_{max}$.
 - Update $d_i^F = d_i^F - d_k^c$ and lock T_i .
- v Re-compute priorities of remaining unlocked tiles and go to Step 2(e).

3 Minimize Effective Density Range:

- (a) For each tile T_i , unlock tile and compute its priority as a function of the difference of its effective density and the maximum effective density.
- Typically, a tile with a smaller effective density or a tile surrounded with tiles with lower effective density has a higher priority. Tiles whose effective densities are equal to or within a certain range of the maximum effective density are assigned zero priority and typically left untouched.
- (b) Until (some tiles remain unlocked)
- i Initialize $DT \leftarrow \phi; TS \leftarrow \phi$.
 - ii Sort the tiles according to the priority function.
 - iii Until (all unlocked tiles are processed)
 - Pick next tile in the priority order. If the tile belongs to DT , continue. Else insert it in TS and add all the tiles within its *CMP radius of influence* into DT .
 - iv For each tile T_i in TS , do
 - Pick $c = (d_k^c, p_k^c) \in CS$ such that $d_k < d_i^F$ and the following conditions are satisfied: (1) Difference between effective density of T_i after incrementing the density of T_i by d_k^c and maximum effective density is minimized. (2) New ECP thickness values of T_i and all tiles in its *ECP radius of influence* \geq original thickness values and $\leq H_{max}$.
 - Update $d_i^F = d_i^F - d_k^c$ and lock T_i .
- (c) Re-compute priorities of remaining unlocked tiles and go to Step 3(b).

The *fill-able* area computation in Step 1 can incorporate additional rules like fill to metal spacing, etc. In our algorithm, we require that all fills should be

⁵In most cases, this check is redundant as the ECP thickness of an Over-fill tile rarely decreases after filling. This is another benefit of converting all tiles to Over-fill.

separated from the signal lines by at least $2\times$ minimum spacing to reduce the impact of RC coupling. In Step 2, tiles whose ECP thickness values are less than H_{max} are aggressively filled to bring their ECP thickness values as close to H_{max} as possible. This combined with the fact that the maximum ECP thickness after parameter assignment is never greater than H_{max} ensures that the ECP thickness range is reduced and the distribution of ECP thickness values is ‘good’ (as discussed in Section 4.8.2). This ensures that the final thickness range is always reduced after the above parameter assignment step. In Step 3(b)(iv), after each set of tiles is assigned new density and perimeter values, it is possible that the effective density range might increase. Thus, an additional check is done after each such step and the density and perimeter values of the layout features of all the tiles are temporarily saved only if the effective density range after assignment to this set of tiles is smaller than the effective density range before the assignment. The final solution at the end of Step 3 is the best solution saved in the temporary storage.

The above parameter assignment algorithm is based on the ECP model described in [77] which uses analytical equations for computing ECP thickness values of the tiles. However, a look-up table based ECP model could also be used to determine the cases and/or the thickness values of the tiles in the layout.

4.8.5.2 Fill Placement

The main objective in this step is to pick one or more fill patterns for each tile to ensure that the density and perimeter targets for each tile are simultaneously satisfied as closely as possible. The fill placement step is very flexible and can insert fills either on the manufacturing grid or routing grid. Thus, the proposed algorithm can be used either in traditional place&route tools or in subsequent verification tools.

In order to match each tile’s density and perimeter target with as much accuracy as possible, each tile T_i ’s *fill-able* area F_i is decomposed into non-overlapping rectangles R_{ij} , where $\sum_j R_{ij} = F_i$. For each rectangle R_{ij} , a density and perimeter budget is computed: the density budget is simply equal to the $\{(\text{target density} - \text{original density}) \times (\text{area}(T_i) / \text{area}(F_i))\}$; the perimeter budget is equal to the $\{(\text{target perimeter} - \text{original perimeter}) \times \text{area}(R_{ij}) / \text{area}(F_i)\}$. Then, for each R_{ij} , the library element that matches its density and perimeter budget with the smallest possible error is determined and placed in the appropriate grids (for instance, the routing grid). The number of instances of the library element that produces the best match for the density and perimeter budgets is inserted.

The budgets are computed such that if the density and perimeter budgets of each R_{ij} is satisfied, the density and perimeter of the tile is equal to the target density and target perimeter, respectively. It can be shown that the density budget of each R_{ij} is always less than 1. This is because the difference between target density and original density is always less than $\text{area}(F_i) / \text{area}(T_i)$,

since the additional assigned density of each tile is never greater than the tile's *fill-able density*.

4.8.6 Experimental Results

In this section, we present experimental results to validate the proposed *MBLPD* algorithm. It is compared with a commercially available density driven metal filling solution from an EDA vendor. The metrics used to compare the two metal filling solutions are the final thickness range (i.e. the difference between the highest point and the lowest point on the chip surface after CMP) and the percentage of fills inserted. A Synopsys internal CMP simulator is used to simulate the topography of each layer of the chip and the thickness range is computed. The percentage of metal fill is equal to the inserted fill area divided by the total area of the chip. We present data for seven layers for two industrial chips. The first one (henceforth referred to as D1) is $0.7 \times 0.7 \text{ mm}^2$ and the second one (henceforth referred to as D2) is $1.78 \times 1.78 \text{ mm}^2$.

Table 4.3 provides a comparison between the different metal filling schemes. Columns *Design* and *Layer No.* specify the design and the layer number of the design, respectively. Column *Original* gives the final thickness range of the layer for the original design. The final thickness range for that layer after density-driven metal filling and the proposed model-based layout parameter-driven metal filling are given in Columns *Post_DD_MF* and *Post_MBLPD_MF*, respectively. All thickness ranges are reported in angstroms. Columns *FillArea_DD* and *FillArea_MBLPD* present the percentage of total area that is occupied by metal fills for the density-driven and the proposed algorithm, respectively. Columns *ED_Org*, *ED_MBLPD* and *ED_DD* report the effective density range for the original layer, the layer after the *MBLPD* algorithm and the layer after the density-driven algorithm, respectively. The typical run-times for the *MBLPD* algorithm range between 150 – 200 seconds per layer for the smaller design and 600 – 700 seconds per layer for the larger design. These numbers are a very small fraction of the typical routing times. Hence, we believe that runtime should not be a factor limiting this application.

4.8.7 Discussion of Results

The results show that the proposed algorithm always reduces the final thickness range after metal filling whereas the density-driven approach can often increase the final thickness range after metal filling. On average, the range reduction using the density-driven algorithm is -7.8%, where as the range reduction with our approach is 22.1%. It should be noted that the density-driven algorithm is quite proficient in reducing the effective density range as per its original intention. It achieves an average effective density range reduction of 60.5%. In spite of this, the poor thickness range reduction by the density-driven

Table 4.3. Comparison of Different Metal Filling Results

Design	Layer Num	Original (A°)	Post_DD_MF (A°)	Post_MBLPD_MF (A°)	FillArea_DD	FillArea_MBLPD	ED_Org	ED_MBLPD	ED_DD
D1	L1	96.00	105.51	71.77	2.59	1.62	0.25	0.17	0.05
D1	L2	258.93	349.45	219.76	13.63	4.94	0.10	0.08	0.08
D1	L3	374.88	340.03	311.98	15.38	10.53	0.17	0.10	0.07
D1	L4	357.91	362.27	324.50	15.62	7.95	0.21	0.16	0.06
D1	L5	289.04	297.68	237.78	13.49	10.55	0.22	0.12	0.06
D1	L6	409.94	293.12	306.92	8.80	8.07	0.26	0.18	0.08
D1	L7	551.22	397.08	334.55	12.57	15.30	0.26	0.12	0.06
D2	L1	555.12	215.13	361.46	17.07	11.57	0.10	0.06	0.08
D2	L2	281.52	294.80	183.83	11.62	10.88	0.22	0.11	0.06
D2	L3	252.95	275.42	155.69	11.21	9.35	0.24	0.09	0.06
D2	L4	274.32	311.61	201.20	3.60	3.32	0.28	0.17	0.09
D2	L5	729.77	626.00	628.76	5.58	4.89	0.25	0.11	0.10
D2	L6	528.53	1288.79	519.03	13.95	5.22	0.21	0.20	0.11
D2	L7	1198.04	1565.70	1070.00	7.76	7.59	0.24	0.11	0.11
Avg Imprv	-	-	-7.8%	22.1%	-	-	-	39.5%	60.5%

algorithm in a majority of the cases can be attributed to two factors: (1) significant increase in ECP thickness range⁶ after filling (for cases (D1:L2), (D2:L6) and (D2:L7)), (2) change in distribution of tiles above and below the transition point with a very few tiles with large ECP thickness (for the remaining cases). The results indicate that there is much greater degradation in the final thickness range for the cases mentioned in (1). The *MBLPD* algorithm, on the other hand, always reduces the ECP thickness range and ensures a 'good' distribution by having more tiles above the transition point. For the case in which the density-driven algorithm does significantly better than the *MBLPD* algorithm (D2:L1), the density-driven approach obtains a better ECP thickness range reduction than the *MBLPD* algorithm while still maintaining a 'good' distribution⁷. Based on these results, it can be concluded that the dependence of final thickness range on the ECP thickness range is definitely a first order effect, whereas the impact of ECP thickness distribution on the final thickness is a second order effect. However, both need to be considered to ensure predictable final thickness range reductions after metal filling. It has also been observed that the minimum and maximum values of the final thickness after metal filling using the *MBLPD* algorithm do not exceed the minimum and maximum thickness values of the original design. This is noteworthy since some manufacturers prefer the minimum and maximum thickness values to be within pre-specified bounds. Hence for the proposed scheme, the metal filled design is never worse (usually it is much better) than the original design in this regard. This is not true for the designs after density-driven approaches.

In addition, in almost all the cases (all but one) the proposed algorithm introduces a smaller amount of fill when compared with the density-driven approach. The proposed algorithm only introduces 7.9% fill, whereas the density-driven algorithm introduces 10.9% fill. Since metal fills can introduce undesirable coupling effects, it is likely that the proposed metal filling will have significantly less timing impact compared to the density-driven approach. However, a more thorough investigation is necessary before a solid conclusion is drawn in this regard.

To summarize, the density-driven approach usually increases the final thickness range after metal filling and inserts more fill on average compared to the proposed *MBLPD* approach. For the results presented earlier, the fills are inserted on the routing grid. This is done to ensure a fair comparison between our approach and the density-driven approach since the density-driven approach currently being used works at the routing stage. It is likely that greater thickness range reductions can be obtained if the fill insertion is done on the manufacturing grid due to the added flexibility.

⁶There was an average ECP thickness range increase of 22% for these examples. Due to lack of space, the detailed ECP data could not be presented.

⁷It should be noted that since *MBLPD* algorithm is heuristic in nature, it is not guaranteed to always obtain the optimum ECP range reductions.

Chapter 5

VARIABILITY & PARAMETRIC YIELD

5.1 Introduction to Variability and Parametric Yield

As it is the case with any manufacturing process there is a certain degree of variability around the targeted “center” of the product specifications and it is accounted for in the product specifications in the form of a “window” of acceptable variation for each of the critical parameters of a product. It has several sources: machine absolute tolerances, machine to machine variations tolerances, operator (human) error, and environmental tolerances. All this equally applies to the IC manufacturing process as we’ll cover in this chapter. However, as has been repeated perhaps in every chapter of this book a major source of excessive intra-die variability presented itself in the lithography part of the IC manufacturing due to the limitations of the optically-based manufacturing process with an illumination source stuck at a wavelength of $\lambda = 193\text{nm}$ attempting to resolve tolerances a quarter the size of that wavelength perhaps finer. This creates a big challenge towards containing the intra-die variability of critical parameters of the IC manufacturing process to within acceptable limits in such a way that designers can still meet their design targets without having to guard-band their designs in an excessive fashion and at a high cost.

5.2 Nature of Variability

The main purpose of classification of the sources of variability into systematic and random, correlated and uncorrelated, and if correlated the nature of this correlation and to what extent are the sources of variability spatially correlated is to be able to model variability as accurately as possible in order to design taking variability into account and to maximize yield without having to over-design. In fact the timing and power budgets of current systems do not have that much margin for any over design in the first place and an over design with

ample slack is not an option. Also, leaving performance potential on the table for the sake of maximizing yield might not be any better financially than having a higher performance system and taking a pre-determined and quantified hit on yield.

Therefore the first step is to categorize variance. One such good categorization is on the following basis:

- (I) Random vs. Systematic
- (II) Correlated vs. Uncorrelated
- (III) Spatially correlated vs. temporal in nature

It is important to have a good understanding of these classifications. Randomness does not mean uncorrelated. Randomness could be uncorrelated such as atomistic variability and LER and the main statistics associated with such randomness is its standard deviation σ , or could be correlated such as variability in VDD and temperature within a die or in R & C. A correlated random process indicates it is distance dependent and monotone in its nature but the full nature of its variation is not a defined function. Thus it can be defined by a max, a min, and a mean; it can also be defined by a local slope, etc. but not by an exact shape; thus its classification as random rather than systematic.

Systematic indicates an ability to model the spatial (or any other relation such as time, T, etc. but here spatial is the most important) relationship in the variable indicated as systematic. Associated with that understanding is usually an understanding of the causal effects and the ability to mitigate some or all of those effects if so desired (at a cost).

As mentioned repeatedly it is important to stress that certain sources of variability has both systematic and random components to them and the task of filtering out the systematic part before modeling the random part is not an easy task.

We will revisit spatial correlation in the next section under local variability after we cover sources of variability as it makes visualizing local variability more plausible.

5.3 Source of Variability

There are as many sources of variability in the IC design and manufacturing process as there are steps carried out in the design, manufacturing, and usage of a finished IC product. There is no unique way of breaking down the sources of variability. For the purpose of this chapter we are going to break them down in the following fashion for a specific reason: category (I) wafer level variability along with (V) Environmental and (VI) aging practically fully captures the old 3-corner simulation model of designing with variability in mind.

- (I) Wafer level variability
- (II) Materials based variability
- (III) Lithography based variability
- (IV) Local (layout, location, and density)
- (V) Environmental
- (VI) Aging

However, at all times one needs to keep variability in perspective and focus on what type of variability matters and why? What type of variability is random and what type is systematic? What variability is deterministic, and what can be accounted for in a statistical fashion only. The goal after all is to be able to get a working design while maximizing yield and performance simultaneously. Thus the focus is on the parameters that most impact I_{on} and I_{off} for the active device, and R and C for interconnect. In this Section we will concentrate on the most critical parameters of a device, namely device width (W), channel length (L), gate oxide thickness (T_{ox}), and device threshold voltage (V_{th}); and of the metal interconnect structure, namely metal line length (L), width (W), thickness (h), and interconnect thickness (t); and of the intra-metal oxide (ILD) thickness (h1); and the environmental variables within and surrounding the IC, namely voltage (V) and temperature (T).

Figures 5.1, 5.2, and 5.3 are simultaneously an illustration of the cross section of an IC built using a dual Damascene process with its full metallization structure, the device itself, and two adjacent layers of metallization. Note that V_{th} is not shown in the drawings as it is not a physical parameter but a derivative device parameter highly dependent on doping and on oxide thickness (as a direct proxy for gate oxide capacitance C_{ox}).

5.3.1 Wafer Level Variability

By wafer level variability we are referring to fab-fab, lot-lot, wafer-wafer within a lot, and intra-wafer variability. Intra-die variability is not discussed at all in this subsection. Fab-fab variability is due to several factors. Different fabrication facilities use different versions (new vs. old) of the same piece of equipment, maintenance and process control procedures might vary from fab to fab, any particular piece of equipment might be drifting out of calibration at any particular fab and still be within specs. The nature of this variance is totally random.

Lot-lot variance is another totally random variance caused by slight drift in equipment from lot to lot and in human operating procedures (to the extent that there is any human interaction). Again, a lot is acceptable as long as each

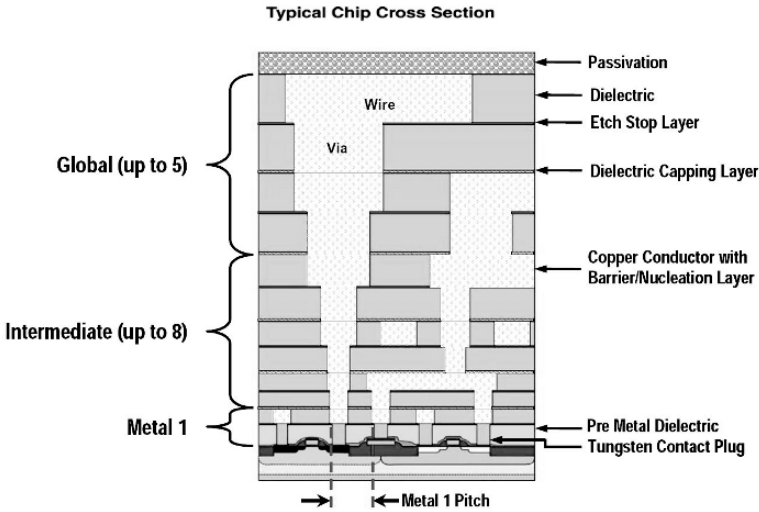


Figure 5.1. Illustrative Cross Section of a CMOS IC with Metallization

critical parameter is within the acceptable window of a mean value and a 3σ from that mean.

Wafer-wafer variance within a lot is mainly systematic. It is caused by the location of a wafer within a lot and the gradient of a gas flow in the lot as an example. It could be linear or quadratic in nature. But, the bottom line is that it is systematic within a lot and can be modeled properly.

Intra-wafer variance (we avoided calling it die-die as we do not want at this point to get into the reticle field issues and want to focus on the simple radial variance within a wafer) is mostly systematic and radial in nature due to a combination of thermal and centripetal forces when spinning of photoresist

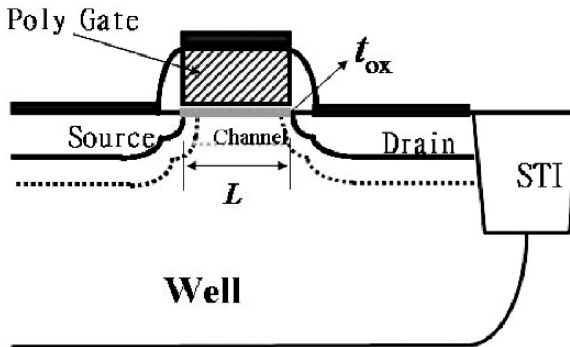


Figure 5.2. Planar Cross Section of a CMOS Device Showing Main Physical Parameters

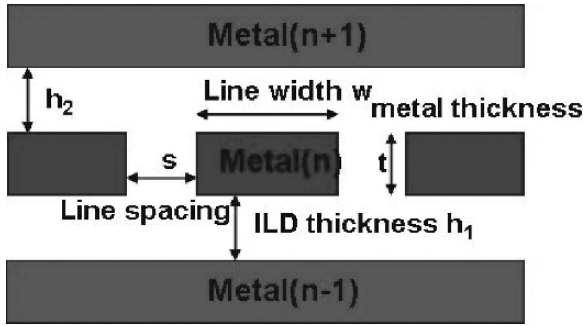


Figure 5.3. Illustration of Interconnect Parameters for 2 Layers of Metal

on wafers. Again it could be modeled and it is captured within the 3σ spread around nominal values of parameters.

5.3.2 Materials Based Variability

The contribution of materials to variability is a rather difficult thing to quantify in the nano regiment of CMOS processing because of the high interaction of materials and lithography combined in shaping the variances encountered.

One of the most significant examples of material based variances (heavily biased by layout and lithography) is line edge roughness (LER) and line edge erosion (LEE) for metal lines and gates at 65nm and 45 nm technologies.

Figure 5.4 is an example of metal LER. As it is obviously true every metal line has two edges and the two edges can experience different LER. If the LER was uniform on both edges of a line in amplitude and frequency, the CD of the line will be intact although such a behavior will impact cross talk coupling

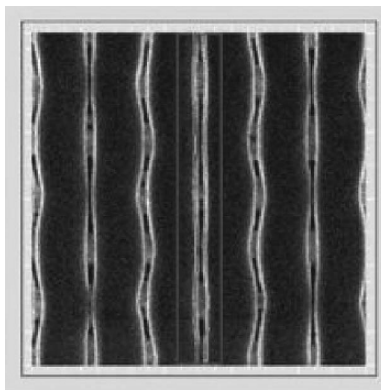


Figure 5.4. Example of Metal LER

to neighboring lines and will impact performance. Also, LER could manifest itself in the form of total line breakage due to insufficient resist during the etch process (this is usually pattern and location dependent). An even more critical form of LER is associated with gate etching at 90nm and below. In addition to the problems associated with the photoresist materials the high aspect ratio of gates makes cantilever stress induced line deformations more pronounced as the deflection of the top of the gate is a cubic function of the aspect ratio of the gate (Figure 5.5).

$$W \propto (A^3) \times F \quad (5.1)$$

Where F is the force experienced at the tip of the gate structure.

Thus the problem will only get worse with each new generation of devices. Gate LER makes achieving a V_t uniformity for a device very difficult and increases V_t variability significantly.

One important note to make is that although we tried here to separate materials based variability from lithography based variability, in most cases it is the interaction of the two that is the cause of the variability. LER and CMP are both excellent examples of that.

Since we covered CMP in great detail in previous chapters we will not discuss it here in this section beyond mentioning it and mentioning that the chemical over-etching of isolated features is a point in case of material based sensitivity and that is why adding smart fills to avoid having such isolated patterns is so important. We'll leave it at that for CMP.

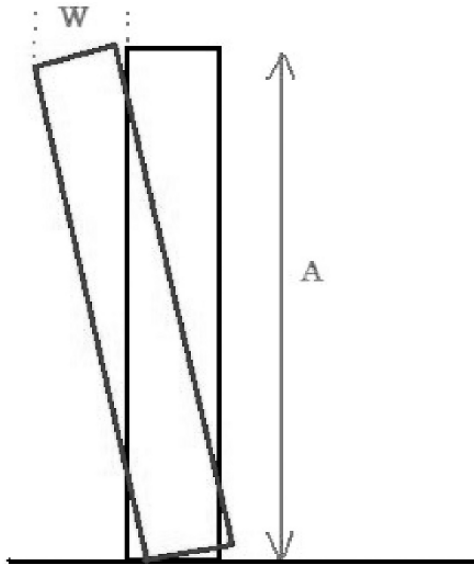


Figure 5.5. LER for Device Gate

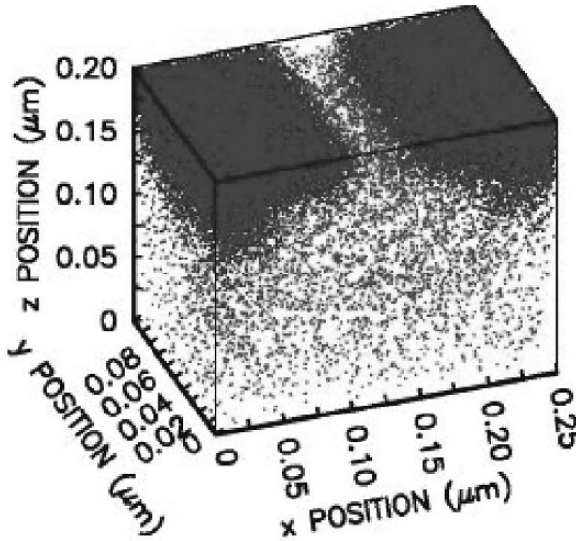


Figure 5.6. Doping Fluctuations Are Pronounced at 45nm and Beyond

5.3.3 Atomistic Variability

Gate oxide thermal growth (deposition) is a well controlled procedure, but with oxide thickness becoming a stack of 3 atomic layers controllability of local oxide thickness is very difficult. This results in a random variance of the oxide thickness of about 2 to 3 Å (corresponding to one atomic layer height) and a corresponding random variance in the threshold voltage V_t .

Another random atomistic variance with a large impact on V_t is the doping profile. With the number of dopant atoms scaling down with device channel length and with the difficulty in controlling doping profiles at that technology level random variances in V_t are the result.

5.3.4 Lithography Based Variability

The lithography steps are a major source of both random and systematic variability. The random portion of variability in the lithography steps is associated with:

- (I) fab to fab and machine to machine variability. This includes lens aberrations.
- (II) misalignment of one processing step to the other: example is via alignment that will result in a random distribution of via resistance values.
- (III) lens defocus.

(IV) resist control. This includes local unevenness of the thickness due to planar non-uniformity but does not include the radial thickness gradient due to photoresist spin which is systematic.

The systematic portion of the lithography process is mainly pattern density dependent and layout dependent resulting in the proximity effects discussed in chapter three (which for most part can be corrected for to some extent); and the orthogonal movement of the scanner with respect to the slit discussed in the next paragraph (cannot be corrected for).

Figure 5.7 is a representative diagram of what is called step and scan lithography. The optics involved are simplified for clarity of the correlation argument being discussed. In reality the optical system involves a light source, a condenser lens on one side of the mask (reticle) and a projection lens between the reticle and the wafer. Another important thing to establish is the orientation of the die with respect to the scan movement and to the slit orientation as it has been established experimentally that measured CD in the slit direction have a higher degree of correlation than those same measurements when the features are oriented along the scan direction.

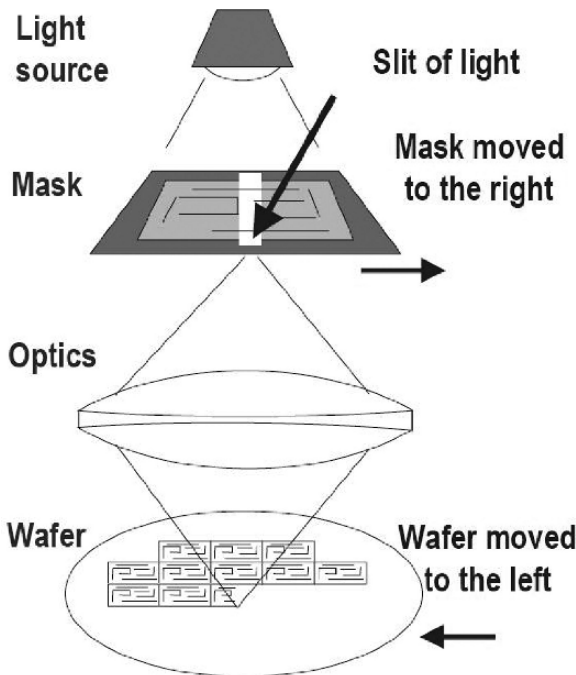


Figure 5.7. A Scan and Step Lithography System Representation

5.3.5 Local Variability

Local variability discussion is complementary to the discussion on the nature of variability covered in section 5.2. However we delayed covering it until we covered several sources of variability especially lithography related sources as it allows the reader to have a better comprehension of local variability.

Local variability is very hard to model mathematically because it is a combination of systematic and random variability. Also, it is highly spatially dependent. So, finding out the distance of interaction is critical for proper modeling of variances.

The work of [103] is an excellent experimental and analytical snapshot of the nature of local variability of critical parameters.

Our collective knowledge and experience in fab-fab, lot-lot, and wafer-wafer variances is extensive and we know how to capture the random as well as the systematic (radial, linear) nature of such variances. So, probing into die-die and intra-die variability for nano-scale CDs is important.

Figure 5.8 clearly shows that there is no systematic correlation from die to die within a wafer [103].

On the other hand Figures 5.9 and 5.10 show strong short distance spatial correlation for each of V_{th} and I_{ds} which are good proxies for T_{ox} , L, W, etc. So, the critical question to understand here is the length of this spatial correlation. Figure 5.11 provides that answer as 1 to 3 mm dropping exponentially with distance.

5.3.6 Environmental Variability & Aging

In this Section we are not talking about the variance in the nominal operating conditions of voltage and temperature as these are part of the operating specifications of a chip or of a system but are rather talking about the intra-die

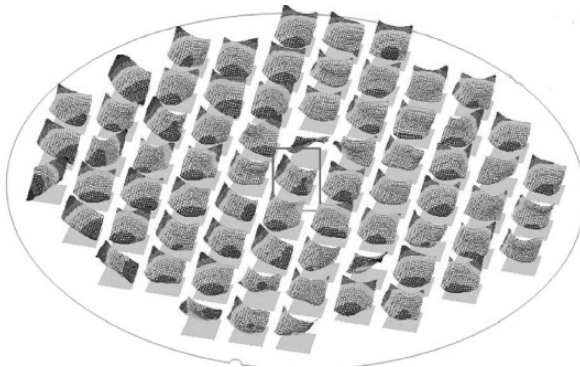


Figure 5.8. Die to Die Variability

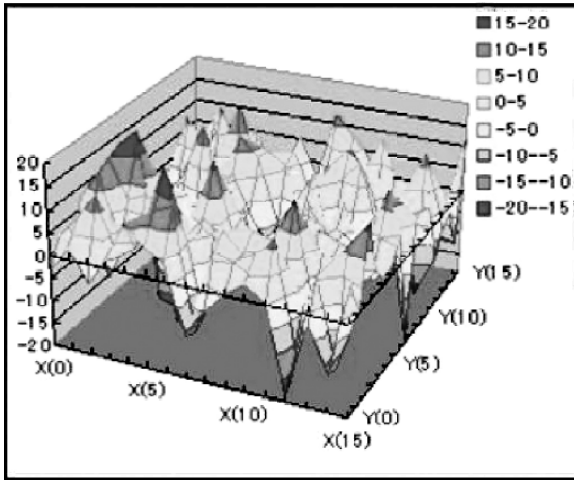


Figure 5.9. I_{ds} within Die Variability

variability in temperature, voltage ($I * R$ drop) and their impact on performance and on reliability especially given the fact that due to the combination of materials and lithography effects there is a wider intra-die distribution of device and interconnect CDs and that there are few “marginal” devices and interconnects that do not require much in terms of the migration in their characteristics to fail.

The landscape of most chips consists of a large area of cache (usually distributed), some processors, DSP, and few blocks of glue logic. Various schemes

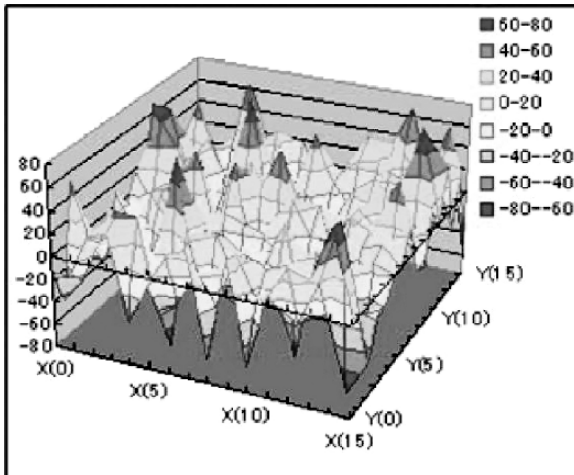


Figure 5.10. V_{th} within Die Variability

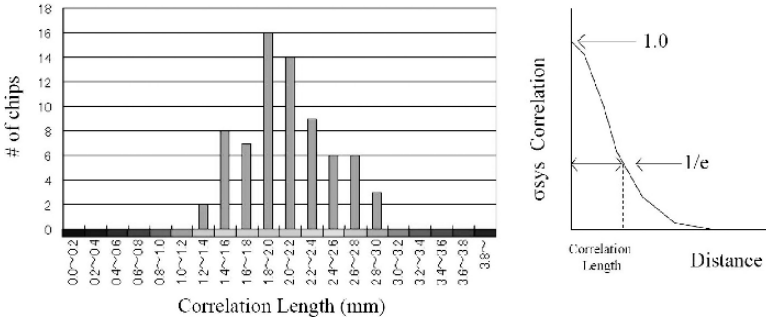


Figure 5.11. Correlation Length

of clock gating are used to manage dynamic power. Figure 5.12 shows the temperature distribution in the substrate of a typical chip. Notice the rather large variance between the relatively cold cache and the few spots of high temperatures (think processors). Calculating local power densities at various locations reveals non-uniform thermal gradients. Clock gating schemes also significantly contributes to thermal gradients between blocks.

From a dynamic power perspective higher temperature translates to slower devices, but the total power consumed at a particular clock frequency is practically the same ($C \times V^2 \times f$). However, leakage power grows exponentially

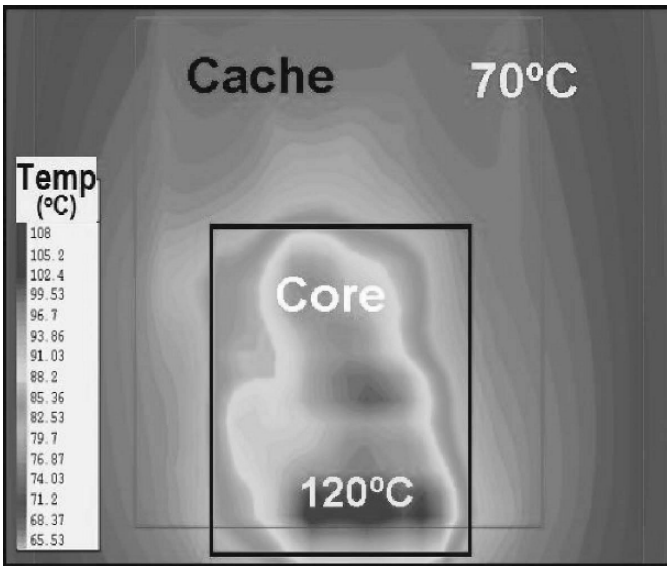


Figure 5.12. A Temperature Distribution Map of a Typical Chip with a Core and Cache

making the $I \cdot R$ drop accelerate. Thus it is fair to claim that voltage-drop increases with the increase in the magnitude of hot-spot thermal gradient.

The other and perhaps more interesting and critical aspect of thermal distribution is the local temperature profiles in devices and in interconnects. Figure 5.13 shows a temperature distribution in and near the junction of a device. The implications of elevated temperature in the device are twofold. One is the increase in leakage power dissipation with temperature. Couple that with the random distribution of leakage within a chip due to random variances of L and doping and we have candidates for thermal runaway and for device damage.

A similar situation applies to interconnect in general and to individual vias in particular. Again the result is a reliability problem and often failures.

We will finally touch briefly on aging as an added source of variability. Most of the time aging is very closely related to thermal variability and to gradients in current densities. Thermal variability can result in dopant re-distribution altering the doping profile of devices and resulting in a V_t shift with time.

5.3.7 Device and Interconnect Parameters Variability

We have already covered but in no particular order the impact of variance in doping, oxide thickness, etching, lithography, and other factors on critical device and interconnect parameters. In this Section we will focus on the most critical device and interconnect parameters as our point of reference (since the performance of circuits is modeled in terms of these parameters), list, and briefly discuss the most critical variances impacting them. The parameters we shall focus on are: V_t , T_{ox} , μ , L , W , R , and C . The implied targets are I_{on} and I_{of} and the corresponding delay and power dissipation associated with them.

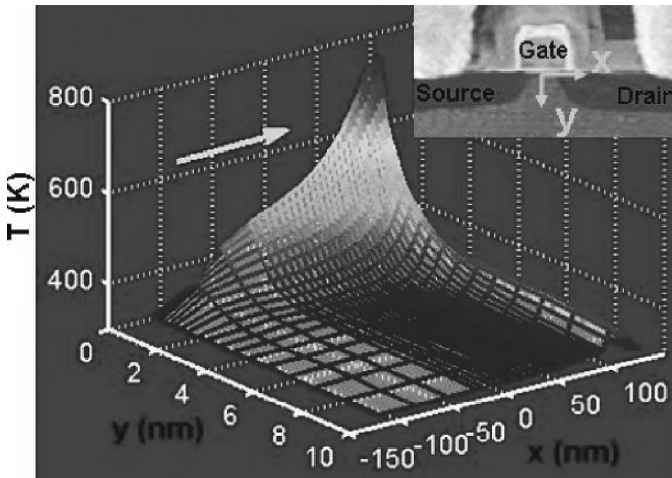


Figure 5.13. Junction Temperature Distribution of a CMOS Device

V_{th} : The two major parameters impacting V_{th} are the dopant profile and the oxide thickness. There are also second and third order effects related to channel width 3D field effects, stress (both STI and SiGe engineered stress), and the dopant concentration due to the poly depletion related to the use of metal gate (for high K gate oxide).

$$Vt\alpha(N_a/C_{ox})^{\frac{1}{2}} \tag{5.2}$$

The variance in dopant profile is itself a function of the implant tilt, dose, and energy. It is also impacted by well proximity effects, anneal temperature and time, and by stress profile (impacts dopant diffusivity).

T_{ox} : another main factor, is more uniform but is nonetheless subject to a variance that is a function of interface roughness (random component) as well as growth uniformity which is a function of growth temperature and time.

μ : mobility's main source of variability is dopant variability already discussed. The other main source is stress, intrinsic (STI) and engineered. Another important factor is layout itself. Mobility is dependent on the poly to poly spacing, on the number of contacts, and on the spacing of the gate from the diffusion edge.

Device L and W: the most important factors contributing to L and W variance are pattern density, etching, location, and pattern proximity.

The upper part of Figure 5.14 captures the variance in interconnect due to the random lot to lot and process variation (3 corners) while the lower part shows the combined systematic and random variances associated with lithography, materials (etching), layout, and pattern.

R and C: Interlayer interaction is cumulative for metal and dielectric layers, and thus surface topography is a very critical variable in determining metal

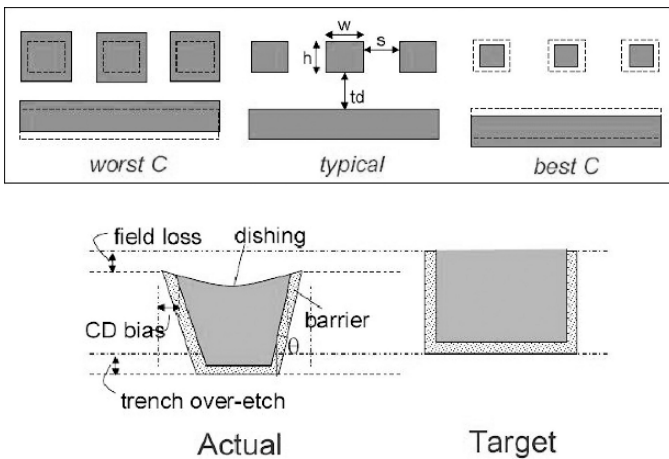


Figure 5.14. Interconnect Cross Section

and dielectric thickness. The other critical variable is etching which is very dependent on pattern and on pattern density. A wide, non-slotted metal is more susceptible to dishing than a thin metal. An isolated feature will most likely be over etched than a dense pattern. That is where model based metal fills play an important role in reducing the variability in the R and C parameters.

It is important to note that R and C variations are strongly cross-correlated. A fatter metal will increase C (smaller metal to metal spacing) but will reduce R (larger cross sectional area) and vice versa. Also, R and C tend to be strongly spatially correlated. There are no “abrupt” changes in R and C along an individual wire.

5.4 Yield Loss Sources & Mechanisms

Before discussing sources of yield loss we will briefly comment on the trend in the type of yield impacting defects as a function of technology node. Figure 5.15 shows a relative split between random and systematic yield and further within the systematic yield between lithography and material systematic loss versus the design related loss as a function of the technology node. Although the data stops at 90 nm the trend is established and is even more pronounced at 65nm and beyond given the limited data available from 65nm and 45nm at this time. Few trends are obvious, mainly that systematic yield loss as a percentage of total yield is steadily increasing at a faster rate than random yield loss to where it is by far the dominant source. And furthermore, within the systematic part of yield loss we find that design-based yield loss is becoming the most significant source of systematic yield loss. Since systematic yield loss is the type of yield loss that can be mitigated, especially the design related part, it is obvious that a lot of work can and should be done to reduce this \$30B/year estimated loss.

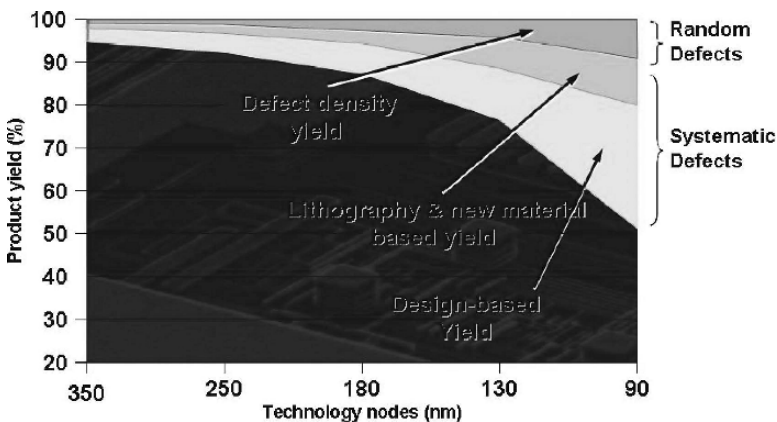


Figure 5.15. Defect Categories Distribution Trend as a Function of Technology Node

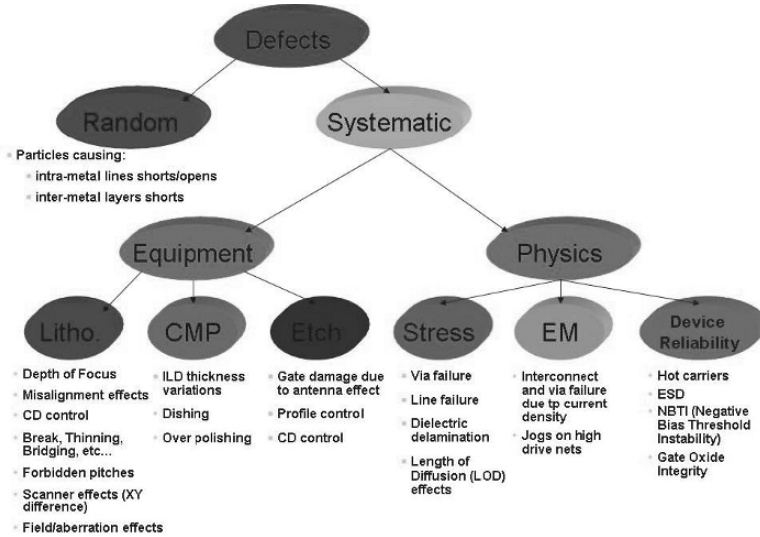


Figure 5.16. A Comprehensive Chart of the Sources of Yield Loss

Figure 5.16 is a chart covering sources of yield loss. Yet, except for the random defects component and the physics component (stress, EM, and reliability) it could have easily been used as a map of the sources of variability. We have covered most of the items mentioned in the equipment section of the sources of yield loss so we will not repeat them here. We will simply innumerate the most significant elements of yield loss covered in variability.

- Depth of focus
- Misalignment effects
- Forbidden pitches
- Scanner X-Y field difference
- Field effects
- ILD thickness variation
- Dishing
- Over polishing
- Gate damage, antenna effects
- Profile control

- CD control
- Via failure
- Line failure
- Dielectric delamination
- Scanner motion dependency
- ILD thickness variation
- Dishing
- Antenna effects
- Via EM failure
- Corner (jogs) EM failures
- Hot carrier
- ESD
- Gate oxide integrity
- And more...

We will limit ourselves to listing those sources in this section.

5.5 Parametric Yield

Historically parametric yield was associated mainly with the drift of the process parameters across a wafer to where it is out of specs or where it causes significant mismatches for sensitive analog and high speed digital devices. It essentially focused on the random variation of process parameter especially at the early stages of a process development. Die size had a significant impact also on parametric variability and yield. These considerations now take a back seat to systematic and random intra-die variability associated with nano-CMOS processing.

Parametric yield loss as we are dealing with it here refers to the yield loss associated with any of a device's parameters that falls out of specifications or that results in unacceptable functional performance. The sources of parametric yield loss are as diverse as all the sources of variability listed in this chapter. However, instead of looking at the particular phenomena causing that variability we are more concerned with the impacted parameter and its own impact on performance. Sometimes a combination of phenomena could impact a particular parameter. A good example of that is V_t and I_{off} . V_t is impacted by channel

length, doping profile, narrow W effects and so on, yet what matters to us is the variability in V_t and its corresponding impact on leakage and on performance. Poly density patterns discussed earlier impacts poly length (lithography) and impacts mobility (tensile stress pattern), and metal dummy fill patterns impact metal lines width and resistivity. Same pattern dependencies apply to via patterns and their impact on via resistivity.

Chapter 6 will deal with yield modeling for random, systematic, correlated, and uncorrelated yield loss mechanisms. However, one thing worth mentioning here is that modeling as well as testing individual causes of variability is much easier than modeling a parametric variability due to multi-causes of variability. Therefore test structures and experimental data are the best sources of gauging parametric variability and yield.

5.6 Parametric Yield Test Structures

Designing test chips and test structures for evaluating parametric yield and most importantly evaluating critical patterns and critical parameters within patterns is a powerful tool in yield improvement in general, and parametric yield improvement in particular. A well thought and implemented test chip attends to what parameters and patterns are to be tested for, how are the measurements going to be done, testing automation with minimal manual intervention, and finally designing the individual tests to generate clear unambiguous results and trends.

Lithography effects are easy to observe. One can design patterns to check for:

- corner rounding
- end of line pull back
- density and pattern dependent line width
- density and pattern via opening
- SRAF impact on printability of isolated features
- OPC impact on digitized features

However, most parameters can be deduced through electric measurements such as via chain resistance. Special care should be done in designing the experiments to minimize noise in the measurements.

Figure 5.17 is an example of a well studied test pattern for evaluating the CMP effects on a dense versus an isolated pattern. A similar pattern with various dummy fills could be experimented with for impact of dummy fill on width of isolated features can be implemented.

A well planned and implemented test chip can be a great vehicle for yield improvement especially for the early stages of a process.

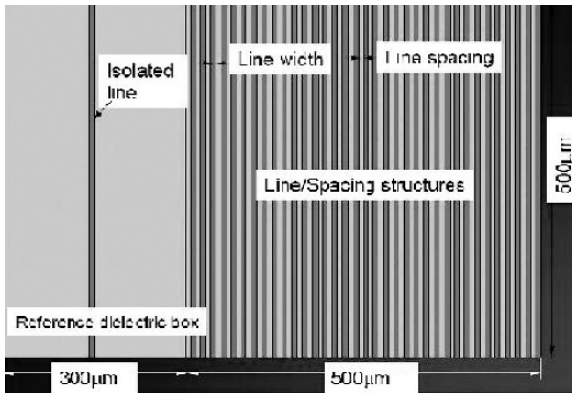


Figure 5.17. A Well Designed Pattern for CMP Evaluation

5.7 Variability & Parametric Yield Summary & Conclusions

It is a forgone conclusion that with continued scaling lithography induced intra-die variations are growing in significance to the point where they are dominant. Of the device parameters variability in I_{off} and in V_{th} is most pronounced; T_{ox} and LER are also affected but to a lesser degree. Statistical analysis of experimental data [103] indicates that there is a 30% intra-die variation of I_{on} in the 3σ variation of that parameter. Intra-die variations are both random and systematic. It is important to determine the systematic part of variability which can be mitigated to a certain degree most of the time. There is not much that can be done to impact the random part of variation but there are ways to account for that random variation using statistical approaches as shall be discussed in Chapter 6.

It is important to understand and model individual causes of variability. It is also equally important to understand and statistically model their cumulative impact on the most sensitive design parameters in order to optimize performance and yield. Chapter 7 will deal thoroughly with yield modeling.

Chapter 6

DESIGN FOR YIELD

6.1 Introduction - Variability and Yield - the Two Drivers of Statistical Design

Yield (profitability) has always been the primary driver in the IC industry. That has not changed. What changed is the complexity of the yield problem in the form of:

- Tighter timing budgets dictated by the quest for ever higher performance requirements expected from technology scaling, yet met with lower supply voltages, dictated in turn by power limitations; especially leakage power limitations.
- Higher number of issues that can derail yield exacerbated by optical lithography limitations and manifested in wider and more complex modes of variability, especially intra-die variability. Intra-die variability alone, as we shall see shortly, has put an end to the old style of design and dictated a statistical approach.
- Shorter product life cycle leaving little room for minor fixes and hardly any room for costly re-spins.
- An ever escalating level of non-recurring expenses (NRE) to first silicon at every stage of the product introduction. The design and verification cycle is more complex, tooling is significantly more expensive. So is processing, packaging, and testing.

In this chapter we focus on the timing and power issues in the context of statistical timing and power analysis and statistical design optimization.

6.2 Static Timing and Power Analysis

6.2.1 Overview

Before starting to talk about timing analysis we are assuming that the reader is at least familiar with the concepts of synchronized systems, set-up and hold times, arrival time of a signal, and the concept of slack. If not the reader should look them up in any standard engineering textbook.

Traditional timing analysis - better known as static timing analysis (STA) - is a full chip, input independent, timing verification approach and it has two components that need accurate modeling: gate timing modeling and interconnect timing modeling. Static timing analysis deals with “design corners” that lump a “worst case”, or a “typical”, or a “best case”, or simply a “specific condition” scenario for a particular design parameter or a particular design condition into one case file for the purpose of evaluation or analysis of a design. Thus the name of case or corner analysis used with STA. At the heart of STA is the assumption of full correlation of process parameters within a die. That is, all devices and interconnect on a chip are slower or faster in tandem, a situation which is relatively true if there is absolutely no intra-die variation and if all the variability is the random die-to-die, wafer-to-wafer, and lot-to-lot type. We use the term “relatively true” very loosely here because even under these conditions of random variability dominance the sensitivities of devices and of interconnect to process corners are not ideal and do sometimes move in opposite directions and thus do not track; yet STA has no means of dealing with that. From a computational consideration, STA is linear in time with the number of paths analyzed and furthermore it is input independent and is thus very tractable and manageable.

Figure 6.1 is an illustration of the basics of static timing analysis. G1 and G2 are typical gates while the net including segment AB plus all nets driven by gate G1 and connected to AB would be an example of an interconnect load.

Case file based static timing analysis worked (relatively) well when the variability was dominated by lot-to-lot, wafer-to-wafer, and die-to die sources of variability, when the effect of the 3σ variability of any parameter as a percentage of its total contribution to timing or power budget was reasonable, and when the total number of corners to be evaluated were limited and manageable.

But, with every step of scaling in the technology roadmap, more “cases” or “corners” had to be considered or analyzed to saturate the sensitivity of all relevant design parameters to the variability of the process parameters and to take care of the fact that what is relevant to a specific design or a critical path in a design does not necessarily always take place at process parameters extremes but at certain particular combinations. Furthermore the effect of a 3σ variance in some dominant parameters accounted for a significantly larger percent of the overall timing or power budget, and as such designing based on a worst case

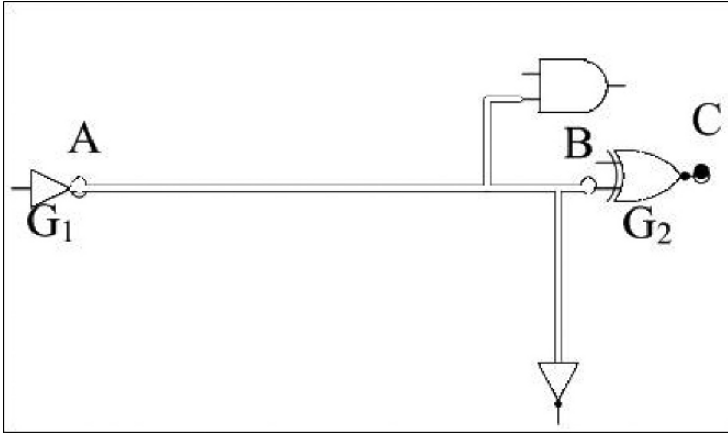


Figure 6.1. Illustration of Gate Timing and Interconnect Timing

“corner” environment translated into excessive conservatism and into throwing away a significant amount of good die (yield) for the sake of design robustness. For this reason it is clear that a different, more realistic approach is needed to deal with timing analysis that will still maintain a high level of confidence in the fidelity of a design without the ultra-conservative and wasteful nature of STA. But all that reasoning is dwarfed by a single factor, namely intra-die variability. Assuming intra-die process correlation is outright wrong. Thus the need for a statistical static timing analysis (SSTA) that we cover in this chapter is more than a convenience. It is a must.

6.2.2 Critical Path Method (CPM)

The most common STA approach is the critical path method (CPM) also referred to (erroneously) as the PERT approach (stands for program evaluation and review technique). It is a technique used for managing circuit graphs. A circuit graph is:

- 1 a set of internal vertices that corresponds to gate inputs and outputs
- 2 a set of vertices corresponding to primary inputs and outputs
- 3 a set of connections that connect the primary inputs to gates inputs, gates to each other, and finally gates outputs to primary outputs.

Figure 6.2 is an illustration of a typical circuit graph for an “In” to “out” path. The CPM is concerned with calculating the path delay from an input to an output. It proceeds from a primary input to the primary output in topological order. It computes the worst-case rise and fall arrival times at each intermediate node, and eventually at the output of the path. The arrival time at each node is

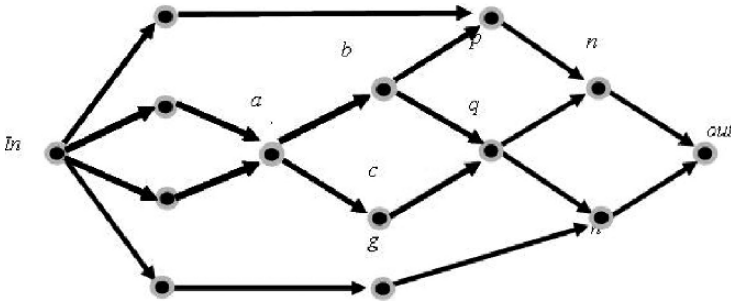


Figure 6.2. Illustration of CPM Method for Path In->out

calculated from pre-characterized timing specifications of individual gates and their corresponding driven interconnects usually stored in a pre-characterized library in the form of look-up tables or expressions. As Figure 6.2 shows a path can have many trajectories. Thus the path delay is arrived at by first performing a summation operation for various trajectories forming the path. A “max” operation is performed to arrive at worst delay among all possible trajectories. The calculated path delay is compared to a target delay for that path and the difference between the target and the calculated number is the slack for that path which can be a positive or a negative number. A positive slack indicates a path that meets the target time with time to spare. A negative slack indicated the failure of the path to meet the target. Therefore the CPM method could be summed up in two operations, a “sum” and a “max”. In the “sum” operation it is assumed that all the arrival times (or rise and fall times) at the input of a gate being processed are known. The gate delay is added to arrive at all the potential delays from input to output. Then a “max” operation is performed on all the candidate delays to compute the worst case (maximum) arrival time at the output. This is carried for all the gates comprising a path to calculate the maximum delay of a path.

The second most prominent approach in STA is the depth-first approach. We leave researching this approach in detail to the interested reader.

6.3 Design in the Presence of Variability

In Chapter 5 we covered the main sources of variability and we summarize them here for the sake of completeness of this chapter in terms of the most critical factors:

(I) Process, Material, and Lithography based variations. Impacted parameters are:

- 1 effective channel length (L_{eff})
- 2 oxide thickness (t_{ox})

- 3 dopant concentration (N_a)
 - 4 threshold voltage (V_t)
 - 5 device width (w)
 - 6 inter-layer dielectric (ILD) thickness (t_{ILD})
 - 7 interconnect height (h_{int})
 - 8 interconnect width (w_{int})
- (II) Environmental Variations: changes in the operating environment and conditions of the circuit
- 1 variations in the external supply voltage (V_{dd} and ground) levels
 - 2 variations in internal supply voltages within chip ($I * R$ drop and dynamic $L * \frac{d_i}{d_t}$ or surge)
 - 3 variations in the ambient temperature
 - 4 variations in local temperatures (device junctions and interconnect) and local thermal profiles that are a function of switching behavior and local current densities.

We also discussed Fab-fab, wafer-wafer, die-die, and intra-die variability and the differentiation between random vs. systematic variability. Random variations depict random behavior that can be characterized in terms of a distribution with a known mean and standard deviation. Systematic variations on the other hand, while spatially correlated, do not in general follow a specific distribution with a known mean and standard deviation.

6.4 Statistical Timing Analysis

6.4.1 Overview

Before getting into the various methods used in SSTA we want to further illustrate and outright build the case for the statistical design approach by revisiting Table 6.1 first mentioned in Chapter 1, and Figures 6.3 and 6.4 respectively.

Table 6.1 clearly indicates that while the nominal value of V_t is shrinking with technology scaling the standard deviation in that parameter is increasing. Thus, the percentage variation has almost doubled in scaling from 90nm to 45nm.

Table 6.1. Absolute and Relative Variability of V_t for Successive Technology Nodes

L(nm)	250	180	130	90	65	45
V_t (mV)	450	400	330	300	280	200
σ - V_t (mV)	21	23	27	28	30	32
σ - v_t/V_t	4.7%	5.8%	8.2%	9.3%	10.7%	16%

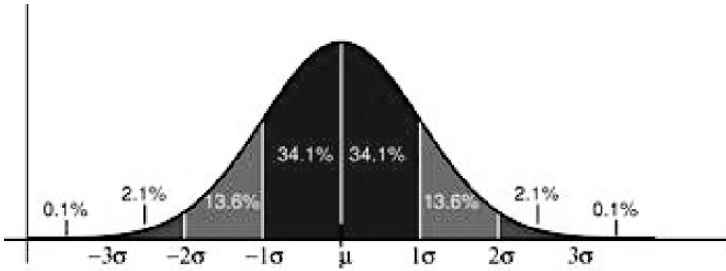


Figure 6.3. Confidence Levels for 1σ , 2σ , and 3σ for a Normal Distribution

Figure 6.3 indicates that roughly 68% of the population is included within $\pm 1\sigma$ of the mean, and that 95% of the population is included within 2σ , and 99.5% of the population are included within 3σ . This tells us that the “corners” design approach, while conservative, gives us a 99.5% confidence that our design meets the target timing that we are targeting.

Now, let's look at the same problem from a different angle, that of a probability density function (pdf) distribution as a function of a variable (this could be timing slack or leakage power for example) for various values of σ . What we clearly see is that for a small value of σ , a ± 1 delta on the variable distribution corresponds to more than 90% confidence level (see brown curve with $\sigma^2 = 0.2$). That same delta in the variable does not account for more than 18% confidence

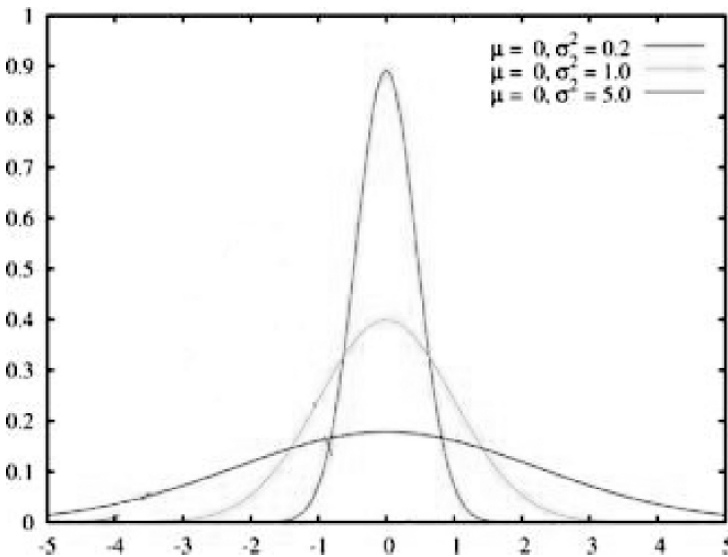


Figure 6.4. Probability Density Function for a Normal Distribution Function of a Variable x with $\mu = 0$ for Various Values of σ

for a σ^2 of 5. This is precisely what is happening with timing and power, and other relevant variables such as VIH/VIL. If one is to design to 3σ variances to capture over 99% confidence that all die meet the timing and power constraints given that intra-die variability is not captured in such distribution, then a lot of design margin is left behind. In fact, the overall timing target of such a design might not be met at all and a lower standard need to be adopted as the best one can do. On the other hand a probabilistic approach (given the significant random intra-die variability component that lends support to the anti-corner argument) allows a much tighter design with a finite probability of yield loss that can be modeled with an accuracy based on available process based yield models.

6.4.2 SSTA: Issues, Concerns, and Approaches

We have established the necessity of using SSTA as a more realistic approach for timing analysis yet STA (and especially the critical path method - CPM-) has survived practically unchallenged all these years for good reasons:

- simplicity (delay and power are discrete numbers)
- tractability; easy to manage in that STA is really managing a timing graph
- input independent
- linear run time with number of gates, interconnect, and paths
- conservatism (that virtue became a vice at 90nm and beyond) as a guarantee measure
- relative accuracy (again, the accuracy started deteriorating around 90nm and polynomials needing evaluation started replacing look-up tables)

SSTA on the other hand had several challenges stemming from replacing the delay and power numbers of STA with a probability density function (pdf):

- Accuracy vs. runtime.
- Continuous closed form vs. discrete (exact continuous - exponential order N)
- Assumptions on the distribution form of the pdf (Gaussian vs. other)
- Assumptions about the linearity of delay times
- Number of dominant process parameters to deal with
- Complexities associated with randomness (intra-die) and with spatial correlations
- Correlation of re-convergent paths

As a result an incredible amount of research has been done (and continues to be done) in the area of SSTA all aimed at dealing with one or more of the issues we just listed and more importantly, at simplifying the SSTA approach to where it becomes almost an extension of the deterministic, linear, and easy to deal with STA. The simplification takes the form of finding accurate enough techniques to de-correlate the correlation of the associated variables' pdfs to where STA like approaches of summation and of taking the maximum of a set of numbers is applicable. These works could be generically lumped in to two main categories:

- Block based approaches (tend to be more runtime efficient)
- Path based approaches (tend to be more accurate but less efficient)

Path-based approaches (depth-first timing graph) handle one full path at a time. They are accurate and can accurately capture the associated correlations, but the propagation of the pdfs of the path components tend to be computationally expensive, especially if the approach uses discrete pdf functions. These approaches are useful for small circuits where the number of critical paths is small and thus the computational task of propagating a delay pdf for each path and then performing a max operation is manageable. Also, path based approach are useful in accounting for global correlations.

Block-based approaches on the other hand perform a "breadth-first" topological CPM-like traversal processing each gate once. However, the simplification in the data processing rendered by this block-division comes at some cost in accuracy caused by only partial capture of the extent of correlation between components. In block based approaches path sharing is totally ignored.

Before moving on to pdf modeling issues it is worth mentioning few differentiators between using continuous vs. discrete pdfs in SSTA. While continuous pdfs are compact and thus lend themselves to closed form solutions they are limited by assumptions that have to be made about the nature of the pdfs (Gaussian vs. other) limiting its flexibility and its accuracy as well. Discrete pdfs on the other hand are data intensive particularly as the number of terms can increase exponentially after repeated convolution operations (for discrete the output pdf is the convolution of the input pdf and the gate delay pdf). But discrete approaches are more versatile in their ability to handle any type of distribution function and not be limited to normal distributions or to linear relations only. Furthermore, the data explosion can be limited by clever data manipulation techniques that exploit special features of spatial correlation to keep the data size manageable.

In the next two subsections we address the issues of pdf modeling for delay and for associated process parameters that impact SSTA. We also discuss spatial correlation issues.

6.4.3 Parametric and Delay Modeling PDFs

Figure 6.5 illustrates using a simple timing graph with discrete gates and the concept of using a pdf function rather than a discrete number to represent the delay of gates and of interconnects. Given that gate delays and interconnect delays are each a function of the underlying parameters it is obvious that we need to model delay pdf as a function of the underlying parametric distribution functions of the parameters impacting the delay.

For that we consider an delay function $d = f(P)$, which operates on a set of circuit parameters P , where each $p_i \in P$ is a random variable with a normal distribution given by $p_i \sim 2N(\mu_{p_i}, \sigma_{p_i})$ (Figure 6.5). Since die-to-die variations (overwhelmingly random) can be solved by traditional STA, only within-die variations will be considered here. We can approximate delay linearly using a first order Taylor expansion:

$$d = d_0 + \sum_{\forall \text{parameters } p_i} \left[\frac{\partial f}{\partial p_i} \right]_0 \Delta P_i \tag{6.1}$$

where d_0 is the nominal value of d , calculated at the nominal values of parameters in the set P . $\left[\frac{\partial f}{\partial p_i} \right]_0$ is computed at the nominal values of p_i [104] $\Delta p_i = p_i - \mu_{p_i}$ is assumed to be normally distributed random variable, and $\Delta P_i \sim 2N(0, \mu_{p_i})$. Since we assumed a Gaussian distribution for all of the parameters then we have a linear combination of Gaussians, which is itself Gaussian with a mean μ_d and variance σ_d^2 :

$$\mu_d = d_0 \tag{6.2}$$

$$\sigma_d^2 = \sum_{\forall i} \left[\frac{\partial f}{\partial p_i} \right]_0^2 \sigma_{p_i}^2 + 2 \sum_{\forall i \neq j} cov(P_i, P_j) \tag{6.3}$$

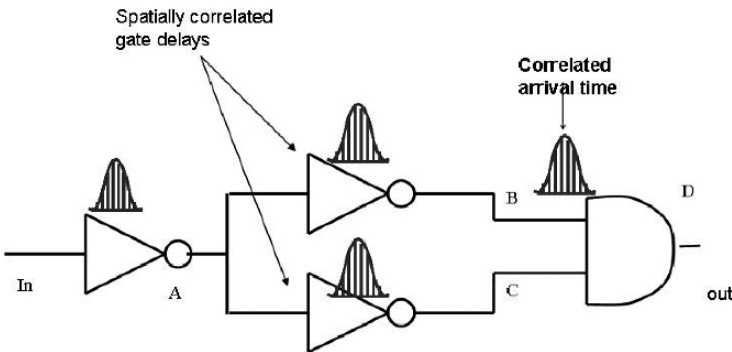


Figure 6.5. Gate and Interconnect Delays Are Represented as PDFs in SSTA

6.4.3.1 PDF of Gate Delay for Multi-input Gates

For a multiple-input gate, the pin-to-pin delay of a gate differs for different input pins. Let d_{gate}^{pin} be the delay of the gate from the i^{th} input to the output. In general, d_{gate}^{pin} can be written as a function of the process parameters P of the gate, the load capacitance of the driven interconnect tree C_w and the succeeding driven gates input capacitance C_g , and the input signal transition time S_{in} at this i^{th} input pin of the gate:

$$d_{gate}^{pin} = d(P, C_w, C_g, S_{in}) \quad (6.4)$$

Now we consider the calculation of a gate's S_{out} , which denotes the longest path delay from any input pin of the gate to its output. In statistical static timing analysis, each of the paths through different gate input pins has a certain probability to be the longest path. Therefore, S_{out} should be computed as a weighted sum of the distributions of the gate delays d_{gate}^{pin} , where the weight equals the probability that the i^{th} path through the pin is the longest among all others:

$$S_{out} = \sum_{\forall input-pins_i} \{Prob \left[d_{path_i} > \left(\max_{\forall j \neq i} d_{path_j} \right) \right] \times d_{gate}^{pin_i} \} \quad (6.5)$$

where d_{path_i} is the distribution of path delay at the gate output through the i^{th} input pin. The calculation of d_{path_i} and $\left(\max_{\forall j \neq i} d_{path_j} \right)$ can be achieved by combinations of "SUM" and the "MAX" operators.

6.4.4 Correlation Issues

The variation in p_i (Equation 6.1) includes both systematic and random variations. Since spatial correlations exists only among systematic variations while random variations are by their nature independent of each other we can divide the second term of Equation 6.1 into two terms to separately account for these two different kinds of variations respectively [104].

6.4.4.1 Spatial Correlation

It is common sense to assume that intra-die variability is highly spatially correlated. Yet mainly due to the increasing complexities of the lithography system there is an increasing intra-die random component of this variability. It shows in varying degrees for different parameters. For example, while there is hardly a random component for intra-die variation in T_{ox} , V_t shows a significant random component to its intra-die variability [105]. Yet Intra-die random variations (RV) for most process and for some environmental parameters (such as those in the temperature, supply voltage, or L_{eff}) while random in nature

still show a measurable degree of local spatial correlation, whereby localized variations for devices within a section of the die are remarkably similar in nature to those in spatially neighboring devices, but may differ significantly from those that are far away. We have illustrated that in Figures 5.9 and 5.10 of chapter 5 for I_{ds} and V_{th} .

To model the intra-die spatial correlations of parameters, [106] suggested a method that the die region may be partitioned into $n_{row} \times n_{col} = n$ grids which is illustrated in Figure 6.6. Since devices or wires close to each other are more likely to have similar characteristics than those placed far away, it is reasonable to assume perfect correlations among the devices [wires] in the same grid, high correlations among those in close grids and low or zero correlations in far-away grids.

Under this model, a parameter's variation in a single grid at location (x,y) can be modeled using a single random variable $p(x,y)$. For each type of parameter, random variables are needed, each representing the value of a parameter in one of the grids.

An alternative model for spatial correlations was proposed in [107, 108] as shown in Figure 6.7. The chip area is divided into several regions using multiple quad-tree partitioning, where at level l , the die area is partitioned into $2^l \times 2^l$ squares; therefore, the uppermost level has just one region, while the lowermost level for a quad-tree of depth k has 4^k regions. An independent random variable $\Delta p_{i,r}$ is associated with each region (i,r) to represent the variations in parameter p in the region at level r . The total variation at the lowest level is then taken to be the sum of the variations of all squares that

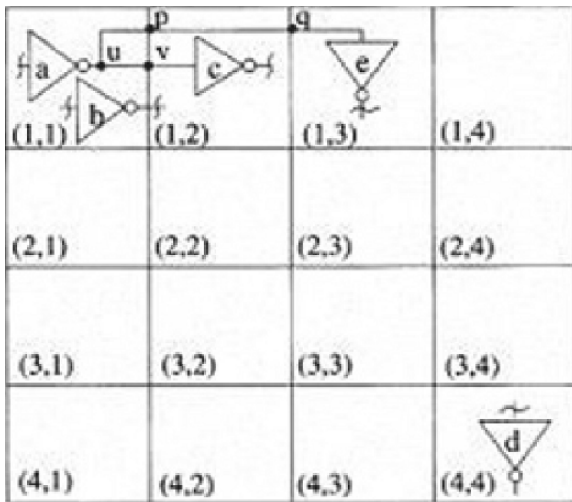


Figure 6.6. Grid Model of Spatial Correlation

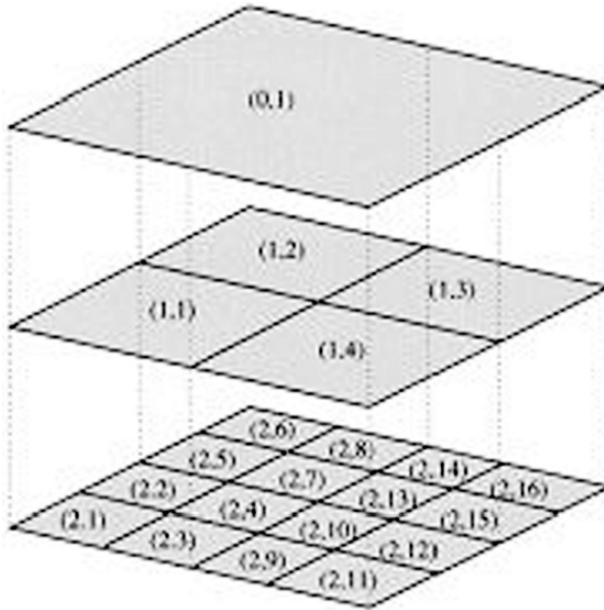


Figure 6.7. The Quad-tree Model for Spatially Correlated Variations

cover a region. It can be shown that this model has the advantage of having fewer characterization parameters than the model by [106].

6.5 A Plurality of SSTA Methodologies

As we mentioned earlier the area of SSTA has been an active area of research and thus the literature is full of solid approaches that in many ways built on each other where each new approach vies to improve on a limitation or a short-coming of a previous approach. In this section we will briefly go over several approaches and highlight the major issues they are addressing. The reader can go to the original work in each case for full details of the specific approach cited.

6.5.1 Early SSTA Approach: Using Continuous PDFs

One of the earliest approaches to SSTA proposed by [109] treats gate delays and arrival times as Gaussians. Thus the total delay using a “SUM” operation is also Gaussian. This is obviously inaccurate but highly practical. However, the computation of the “MAX” function is problematic since the “MAX” of two Gaussian distribution is in general not a Gaussian. Thus the result of the “MAX” operation is an approximation at best. Given the nature of the delay functions at that time that were highly uncorrelated such a shortcoming was not

critical. Then [110] dealt with this limitation in their work on a block-based approach by using pdfs for delays and cdfs (cumulative density function) for arrival times, then utilize the familiar “SUM” and “MAX” operations.

6.5.1.1 Using CDFs for “MAX” Operation

In the previous section we mentioned using CDFs for calculating delay as a solution to the limitation of assuming a Gaussian for the “MAX” operation [110]. In this subsection we will briefly address this approach. For multi-input gates, a “MAX” operation must be carried out: for a k -input gate with arrival times m_i , $i = 1, \dots, k$, and input-to-output delays d_i , $i = 1, \dots, k$, the arrival time at the output is found as the PDF of:

$$m_{out} = \max_{i=1tok}(m_i + d_i) \quad (6.6)$$

Instead of a discrete PDF, this method uses a piece-wise constant PDF, which translates to a piecewise-linear cumulative density function (CDF). It is worthwhile to recall that the CDF is simply an integral of the PDF. The CDF of m_{out} is easily computed given the PDFs of the m_i s and d_i s. The PDF of $m_i + d_i$ can be obtained by convoluting their respective PDFs, i.e.,

$$PDF(m_i + d_i) = PDF(m_i) \otimes PDF(d_i) \quad (6.7)$$

It can be shown that the CDF of this sum is given by:

$$CDF(M_i + d_i) = CDF(m_i) \otimes PDF(d_i) = PDF(m_i) \otimes CDF(d_i) \quad (6.8)$$

The CDF of the maximum of a set of independent random variables is easily verified to be simply the product of the CDFs, so that we obtain

$$CDF(\max_{i=1tok}(m_i + d_i)) = \prod_{i=1tok} (CDF(m_i) \otimes PDF(d_i)) \quad (6.9)$$

The term in the inner parentheses is the product of a piecewise linear CDF with a piecewise constant PDF, which is piecewise linear and therefore the CDF is found by multiplying a set of piecewise linear terms which yields a piecewise quadratic. The resulting quadratic is approximated by a piecewise linear CDF, and the process continues as blocks are processed in CPM-like order. The technique also has some mechanisms for considering the effects of structural correlations and thus broadening the scope of its usefulness and accuracy.

6.5.2 Four Block-based Approaches with Spatial Correlation Considerations

First we describe a PCA based approach. The authors in [106] proposed an algorithm for SSTA that computes the distribution of circuit delays while

considering spatial correlations. In their approach they treat delay as a correlated multi-variate normal distribution considering both gate and wire delay variations then apply the Principal Component Analysis (PCA) to transform the sets of correlated parameters into sets of uncorrelated ones. That transforms the algorithm's complexity to a linear one - $pn(N_g \& N_i)$ where p is a varying parameter associated with finding the principal components, and n is the number of grid squares (see Figure 6.6 for example). That puts the upper cost for this algorithm compared to STA at $p*n*STAcost$. The PCA step can be performed as a preprocessing step for a design.

6.5.2.1 A PCA Based Method

Given a set of correlated random variables X with a covariance matrix \sum , the PCA method transforms the set X into a set of mutually orthogonal random variables X' , such that each member of X' has a zero mean and a unit variance. The elements of the set X' are called principal components in PCA and the size of X' is no larger than the size of X . Any variable $x_i \in X$ can then be expressed in terms of the principal components X' as follows:

$$x_i = \left(\sum \sqrt{\lambda_i} v_{ij} x'_j \right) \sigma_i + \mu_i \quad (6.10)$$

where x'_j is a principal component in set X' , λ_i is the i_{th} eigenvalue of the covariance matrix \sum , v_{ij} is the i_{th} element of the j_{th} eigenvector of \sum , and σ_i and μ_i are the mean and standard deviation of x_i , respectively.

For either of gate or interconnect delay as described in Equation 6.1, the delay may then be written as a linear combination of the principal components

$$d = d_0 + K_i \times p'_1 + \dots + k_m \times p'_m \quad (6.11)$$

where $p'_i \in P'$ and $P' = L'_g \cup W'_g \cup T'_{ox} \cup N'_a \cup W'_{int_i} \cup T'_{int_j} \cup H'_{ILD_l}$ and m is the size of P' . Since all of the principal components that appear in Equation 6.11 are independent, the following properties ensue:

(a) The variance of d is given by

$$\sigma_d^2 = \sum_{i=1}^m k_i^2 \quad (6.12)$$

(b) The covariance between d and any principal component p'_i is given by:

$$cov(d, p'_i) = k_i \sigma_{p'_i}^2 = K_i \quad (6.13)$$

(c) For two random variables, d_i and d_j given by

$$d_i = d_i^0 + k_{i1} \times p'_1 + \cdots + k_{im} \times p'_m \quad (6.14)$$

$$d_j = d_j^0 + k_{j1} \times p'_1 + \cdots + k_{jm} \times p'_m \quad (6.15)$$

Furthermore, the covariance of d_i and d_j , $cov(d_i, d_j)$ can be computed as

$$cov(d_i, d_j) = \sum_{r=1}^m k_{ir} k_{jr} \quad (6.16)$$

In other words, the number of multiplications is linear in the dimension of the space, since the orthogonal nature of the principal components implies that the products of terms k_{ir} and k_{jr} for $r \neq s$ need not be considered.

The above SSTA approach [106] assumes that the fundamental process parameters are in the form of correlated Gaussians, so that the delay, given by Equation 6.11 is a weighted sum of Gaussians, which is therefore Gaussian.

The computation of the distribution of the sum function $d_{sum} = \sum_{i=1}^n d_i$, is simple. Since this function is a linear combination of normally distributed random variables, d_{sum} is a normal distribution whose mean, $\mu_{d_{sum}}$ and variance $\sigma_{d_{sum}}^2$ are given by

$$\mu_{d_{sum}} = \sum_{i=1}^n d_i^0 \quad (6.17)$$

$$\sigma_{d_{sum}}^2 = \sum_{j=1}^m \sum_{i=1}^n k_{ij}^2 \quad (6.18)$$

Strictly speaking the max function of n normally distributed random variables, $d_{max} = \max(d_1, \dots, d_n)$, is not Gaussian; however, like [109], it is approximated as one. The approximation here is in the form of a correlated Gaussian and the procedure reference from [111] is employed. The result is characterized in terms of its principal components, so that it is enough to find the mean of the max function and the coefficients associated with the principal components.

Back to the approach covered above [106] the approach also assumes that the process parameters are normally distributed variables; and it further assumes that the intra-die parametric variation can be decomposed into:

- A deterministic global component
- A deterministic local component
- A totally random component

For modeling intra-die spatial correlations of parameters the region of a die is divided into n -rows \times n -columns; therefore into n grids. Perfect correlation is assumed within a grid, high correlation in direct neighbors, and zero away from direct neighbors. Furthermore grid to grid correlation is only considered for one process parameter at a time with no cross-correlation across parameters.

To sum up the approach the following is the overall step by step flow of the PCA-based statistical timing analysis method.

- (i) Input: Process parameter variations (and obviously the relation between those parameters and delay)
- (ii) Output: circuit delay distribution function
 - 1 Partition the chip into $n = nrow \times ncol$ grids, each modeled by spatially correlated variables.
 - 2 For each type of parameter, determine the n jointly -normally distributed-random variables and the corresponding covariance matrix.
 - 3 Perform an orthogonal transformation to represent each random variable with a set of principal components.
 - 4 For each gate and net connection, model the gate delay and the net delay as a linear combination of the principal components generated in Step 3.
 - 5 Using the operators of “SUM” and “MAX” functions on Gaussian random variables, perform a CPM-like traversal on the graph to find the distribution of the statistical longest path. The distribution achieved is the circuit delay distribution.

Correlation due to re-convergent paths is a problem Adding to that the fact that process parameters are in reality correlated and the assumption that they are not is not entirely accurate. That adds to the complexity of the problem.

An approach proposed by [112] takes the work in [106] and adds to it a methodology to account for process parameters’ correlation and re-convergence in paths. It further accommodates dominant interconnect coupling effects. However, the base of [112] is nonetheless rooted in the block-based PCA techniques of [106] to compute the statistical distribution of Min and Max.

A third approach is a first order incremental block-based approach proposed by [113]. It uses the concept of tightness probability of two variables X and Y which is computed as conditional probability of X dominating Y . We will not go into the details of this approach which we encourage the reader to look up, but what makes this approach so valuable is its ability to do a tightness probability of delays for each node as a post processing step allowing it to be used for sensitivity analysis in the inner loop of a synthesis engine. Thus it

allows the use of “dominant-timing” reducing the overall computational time for the timing analysis of a design.

A fourth block-base approach also using the PCA approach is proposed by [114]. It uses a technique based on Polynomial Chaos for dimensionality reduction for computing the maximum of two delay functions.

The steps of this approach can be summarized as:

- 1 intra-die correlations are captured
- 2 PCA method is used to de-correlate the random variables
- 3 Charles approximation [114] to do a MAX on the delay expressions

6.6 Bounding Approaches

One approach we find particularly interesting in its practicality is the concept of using statistical bounding for delays. The most advanced work in the statistical bounding area is in [3, 4]. This work uses bounding techniques to arrive at the delay distribution of a circuit. The method is applicable to either continuous or discrete PDFs, and at its core, it is based on reduction of the circuit to easily computable forms. Using a bounding technique preserves the simplicity of STA in its linearity of runtime. Bounds can determine the percentage probability error one is willing to tolerate for the sake of keeping a linear runtime for the SSTA.

The steps of this approach are summarized as follows:

- 1 Using timing graphs the pdfs for series-connected edges with a single fan-in (defining the dependent arrival time nodes) are processed by a convolution.
- 2 For parallel-connected edges the CDF are computed by taking the product of the cdfs of the incoming edges (assuming these edges are statistically independent). Key steps of this method are illustrated in Figure 6.3 and further expanded in Figure 6.8.
- 3 For re-convergent sub-graphs that are not in either of these forms the computation is carried out by a path enumeration over the sub-graph followed by computing the final arrival time by summing up the conditional arrival time pdfs weighted by the product of their conditional probabilities.

The next step is finding upper and lower statistical bounds. The bounding function (Figure 6.9): cdf $GU(t)$ is an upper bound on the cdf $GL(t)$ if for all t : $GU(t) \leq GL(t)$

The operation: $Max(x + y, x + z)$ is used as a special form of correlation in reconvergent paths. The following theorems is used to arrive at the bounds. $Max(x_1 + y, x_2 + z) > Max(x + y, x + z)$, where x_1 and x_2 have same PDF as x . $Max(a + b, x + y) \leq Max(a, x) + Max(b, y)$. Figure 6.9 graphically explains the physical relevance of the upper and lower bounds. The cdf function $P(t)$ is

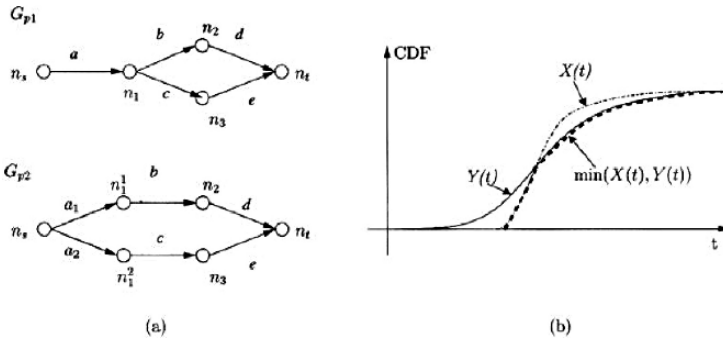


Figure 6.8. Illustration of the Computation of (a) Upper and (b) Lower Bounds for the CDF $X(t)$ for Paths a-b-d and a-c-e [3, 4]

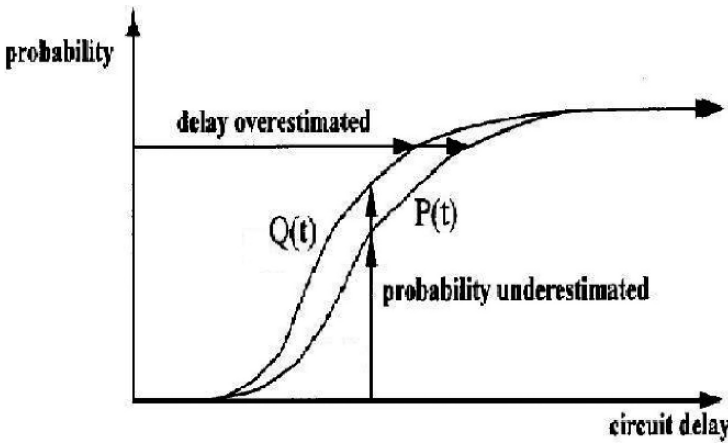


Figure 6.9. Illustration of Upper and Lower Bound Functions

an upper bound on the cdf function $Q(t)$ and thus $Q(t)$ is the more conservative for both delay and probability (yield). In other words for the same probability (yield) $P(t)$ gives a more conservative delay; or for a fixed delay, $P(t)$ gives lower yield (again, conservative).

6.7 Statistical Design Optimization

Statistical design optimization needs a whole chapter by itself if it is to be addressed properly. However, we are going to mention it briefly here as an area the reader interested in design for yield must look up and study.

Deterministic design optimization does not take into consideration the increasing intra-die variability and its highly random nature. Furthermore, the uncertainty in some variables is itself sometimes a function of the variability in others. A good example of that would be device threshold voltage V_t whose variability is significantly impacted by the device sizes (W). Worst case corner

based optimization does not account for that and as such does not allow optimization based on the intersection of “co-variant sets” of variables allowing for a certain yield target as the optimization metric for a design.

Another important point to make since we have addressed SSTA in this chapter is to make it very clear that statistical design optimization is different from SSTA. Granted there is a significant gain in yield obtained by using SSTA compared to the “corners” technique, but that does not mean the circuit under consideration is optimal. The circuit’s performance is still ruled by the worst path with the worst slack as a performance limiting factor.

Statistical design is the approach of doing sensitivity analysis for each path around parametric variability to arrive at the optimal performance, or what [115] calls a well tuned circuit in which a majority of paths are clustered in a narrow “performance wall” and are critical.

Statistically based optimization techniques using utility theory is being increasingly utilized in design optimization for yield [115]. The idea is to define a disutility function U_p of a path which is a function of the path’s delay. Each path is then assigned an expected value of its disutility function $E(U_p)$ and the path that corresponds to maximum expected disutility is the path responsible for maximum yield loss and is thus a candidate for fixing. Statistical design can be carried for timing or leakage power just to mention two critical yield killers. Sizing techniques for simultaneous optimization of parameters for yield is an area of active research. Figure 6.10 is a graphical representation of the expected gain from the use of statistical design approaches for leakage.

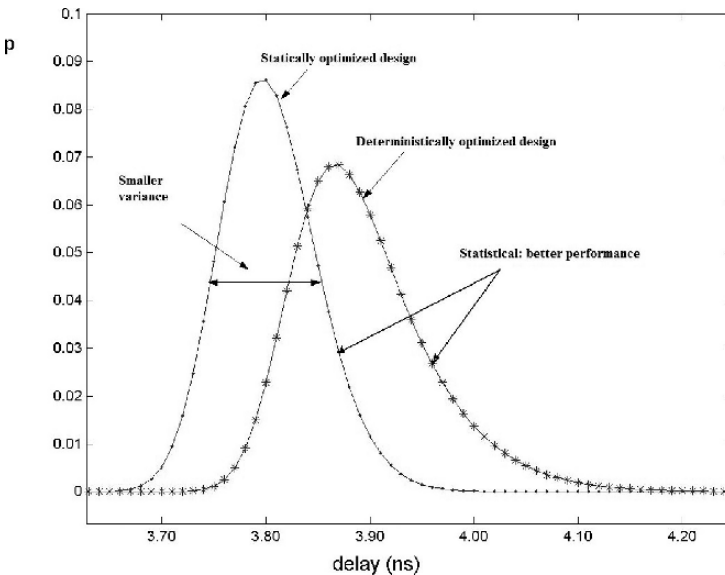


Figure 6.10. Statistical Optimization Results for Static Power

6.8 On Chip Optimization Techniques

In conjunction with the use of statistical design optimization which as shown in Figure 6.11 is superior to the use of deterministic design techniques there are two additional circuit design techniques that can add to the optimal performance of a chip in the three areas of speed, static power and dynamic power. These two techniques are body biasing and adaptive voltage scaling. They can be used separately or together.

We will not go into the device physics associated with body biasing but we will simply mention few facts which are all what we need to know in order to cover the value of these techniques. The literature is full of circuit implementations which can be used for that purpose and therefore again we will not get into specific circuit implementations and limit our coverage to block diagrams. More recent optimization techniques in that area are found in [5, 116, 117]. Also, it is worth mentioning that the use of body biasing for enhanced circuit performance is very old and has been especially used for enhanced memory performance since the early eighties.

We will start by listing four basic equations involving active and inactive current, as well as static and dynamic power that will make all subsequent discussions in this section very simple to follow.

Equation 6.19 is the basic Id expression for a transistor. All what we need from it is the relation between V_t and I_{don} . Lower V_t translates to higher “on” current and higher V_t has the opposite effect. Also, higher V_{ds} (higher V_{DD})

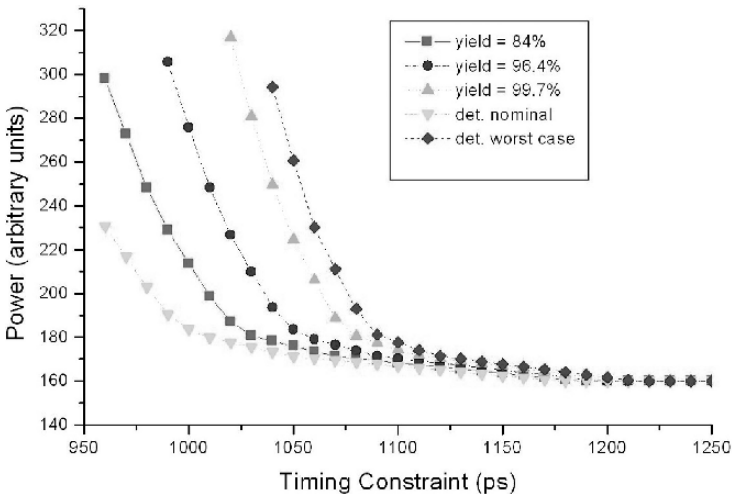


Figure 6.11. Statistical Design Optimization Always Superior to Worst Case

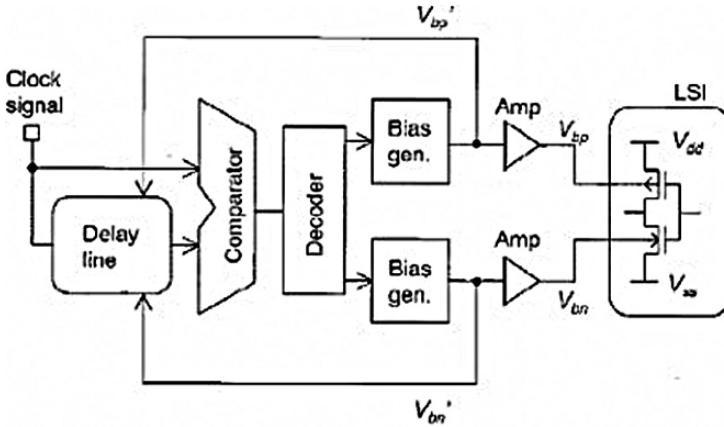


Figure 6.12. Block Diagram of Body-bias Implementation in [5]

translates to higher I_{on} but as we'll see later also translates to higher power.

$$I_{don} = (\mu \times C_{ox} \times W/L)(V_{gs} - V_t)V_{ds} \quad (6.19)$$

Equation 6.20 covers the I_{off} or the sub-threshold current I_{sub} . Again, we are interested here in the exponential to the minus V_t . A higher V_t translated to lower off current and a lower V_t translated to a higher sub-threshold current. The relation is exponential; roughly 80 mV change in V_t translated to an order of magnitude of I_{off} . Also, I_{off} is directly proportional to V_{ds} (V_{DD}).

$$\begin{aligned} I_{sub} &= I_0 \times W/L \times e^{(V_{gs}-V_t)/V_c} \times 1 - e^{q \times V_{ds}/kT} \\ V_c &= k \times T/q \times [1 + a \times \sqrt{N_a} \times t_{ox}] \end{aligned} \quad (6.20)$$

From Equations 6.19 and 6.20 it is obvious that ideally you would want to lower V_t when the device is operating and raise V_t when the device is idle. Also, higher V_{DD} translates to higher I_{don} (faster) but also higher I_{off} (more leaky).

Equation 6.21 is the most generic equation for power, both static and dynamic. It is obvious that a lower V_{dd} lowers both static (including leakage or sub-threshold) power and dynamic power. Equation 6.22 stresses the square ratio of dynamic power to voltage since V_{swing} is equal to V_{dd} for static CMOS and thus dynamic power directly related to V_{DD}^2

$$P \sim \alpha \times (C_L \times V_{swing} + \overline{I_{SC}} \times \Delta t_{SC}) \times V_{DD} \times f + (I_{DC} + I_{Leak})V_{DD} \quad (6.21)$$

$$P \sim \alpha \times C_L \times V_{swing} \times V_{DD} \times f \quad (6.22)$$

So, there are two variables to work with V_t and V_{DD} . Each of them have a speed and a power implication on the performance of a circuit.

At the heart of both adaptive body-biasing and adaptive voltage-scaling is an on-chip sensor circuitry that can monitor performance or power (or both). A typical performance sensor compares the speed generated from a long chain ring oscillator that essentially reflects a spatial sampling of the devices of a die to a reference frequency and the output of the comparator drives body-biasing circuitry or a DC-DC converter regulator for adaptive voltage scaling. Similarly a power sensor (voltage divider or other circuitry) can drive another comparator which again can control adaptive body biasing or adaptive voltage scaling circuitry.

6.8.1 Adaptive Body-biasing

Figure 6.12 illustrates adaptive body biasing at a block level while Figure 6.13 zooms in on the device level to illustrate body biasing for individual P and N devices which in reality takes place through biasing the corresponding N or P well in which those devices reside. This technique can be used for performance enhancement through forward biasing device bodies resulting in lower V_t and thus higher drive currents, and, it can be used to reverse bias the device bodies during idle resulting in higher device V_t and thus significantly lower leakage power. This technique is especially important given that with technology scaling V_t control is very difficult and I_{off} intra-die distribution is very hard to model.

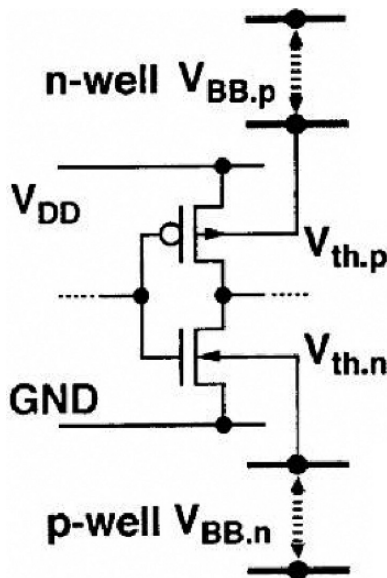


Figure 6.13. Basic Illustration of Body Bias for P and N Devices

Thus the leakage power budget could be easily exceeded and some help from adaptive body biasing in the off state can go a long way.

6.8.2 Adaptive Voltage Scaling

Adaptive voltage scaling on the other hand is more significant for fine tuning performance and dynamic power consumption. It is useful in leakage power management but is not as effective in that regard as adaptive body-biasing. Again, a higher V_{DD} translated to higher current and thus higher performance (provided one does not hit carrier saturation velocities where higher voltage translates to just higher power consumption) when needed and a slightly lower V_{DD} will save on dynamic power in a quadratic fashion when performance is exceeded and a lower V_{DD} would do.

6.8.3 A Combination of Adaptive Body Biasing and Adaptive Voltage Scaling

The best of both worlds is a combination of both adaptive body-biasing and adaptive voltage scaling. Figure 6.14 shows the block diagram for such a combination approach [5]. Since each of those techniques could enhance speed but also has power consequences there is space for an optimization in the choice of the extent of the use of each technique for optimal power consumption as shown in Figure 6.15.

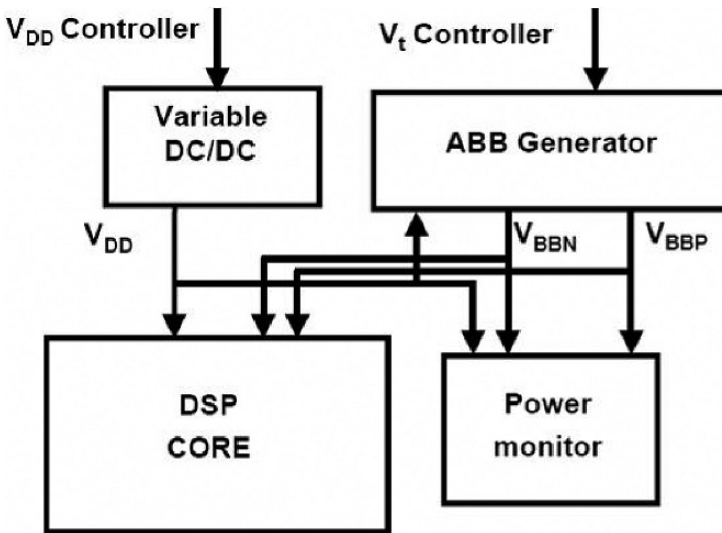


Figure 6.14. Block Diagram of a Combination of Adaptive Body Biasing and Adaptive Voltage Scaling

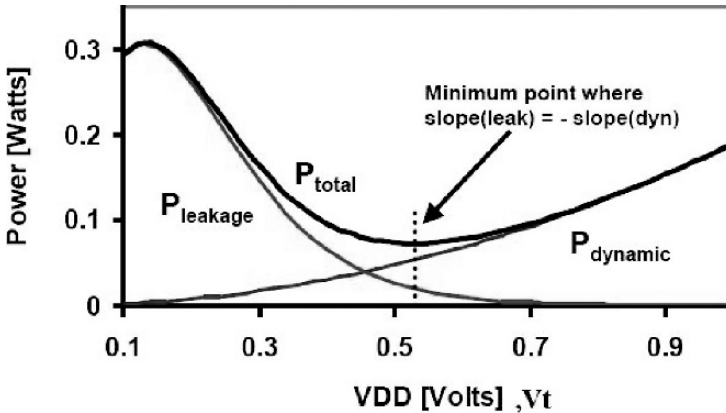


Figure 6.15. Optimization of Speed and Power Using Both Adaptive Voltage Scaling and Body Bias [5]

6.9 Summary: Design for Yield

It is very important to keep in mind that SSTA and statistical design optimization, while using similar approaches are quite different and should be treated separately. Therefore we are dividing the summary section to two sub-sections to stress this differentiation.

6.9.1 Summary for SSTA

- 1 Most research work is on gate delay calculation. Statistical interconnect modeling is lagging behind significantly. Also, the treatment of other critical performance metrics such as clock slew and set-up and hold times is also missing.
- 2 Most SSTA works assume linear delay models dependency on process parameters and so far such an assumption has not been proven lacking. However this can change with further process scaling that keeps pushing in the lithography capabilities of the processing equipment.
- 3 Most of the work on SSTA has been done at the timing analysis level. Statistical Spice models backed with solid statistical data from foundries is still lagging behind. That leaves a lot of uncertainty in SSTA especially in the area of intra-die correlation assumptions of various models.

6.9.2 Summary for Statistical Design Optimization

- 1 Traditional case files (corners) are no longer sufficient for design optimization. The robustness they guarantee comes at a very high cost in yield and

in number of corners to be considered. Furthermore it leads to settling for sub-standard performance metrics when higher targets can be achieved.

- 2 SSTA does not give alternatives for what is statistically optimal for a design, and while it is an essential procedure for timing verification it is not for design optimization.
- 3 Timing and leakage joint co-optimization using a statistical approach is key. Leakage variability grows with every technology node scaling and the need for statistical treatment of leakage variability grows steadily.
- 4 Post-silicon (built in circuitry) tuning for performance and leakage holds a key place perhaps as important as statistical optimization.

Chapter 7

YIELD PREDICTION

7.1 Introduction

Being able to predict the yield of a design at the onset of a design or before tape out is very useful in determining what your profit margin will be. A yield predicting tool for that purpose is very useful. But, what is more powerful is a tool that can analyze the sources of yield loss and allows the designer to do a sensitivity analysis to determine the cost or benefits of dealing with every yield determining parameter and thus to optimize yield. In this chapter we comprehensively cover yield analysis, prediction, and enhancement.

We start with a very basic and general definition of yield for an IC: yield is the ratio of the number of good units of a manufactured product (IC) that meets all the performance, power, functionality, and quality specifications of the product to the total number of manufactured units. Yield (otherwise read as profitability) is the main driver in the IC manufacturing process. Thus all the steps of a product are optimized towards an outcome that maximizes yield. Also, all subsequent steps of fine-tuning individual process modules as well as procedures after the introduction of a product are geared towards increasing that yield in a consistent fashion.

Table 7.1 shows the desired 3σ budget for each of the device critical parameters for technology nodes 80 nm to 22 nm. A white color indicates an achievable target, a yellow highlight indicates that it is a challenge but that technical solutions are known, and a red highlight indicates that manufacturable solutions are not known yet. The table is self-explaining in terms of the challenges that need to be addressed to achieve such 3σ budgets. But, given that there are no known solutions for the time being and for the foreseeable future we need to address these parameters in a statistical way in an effort to essentially live with what we have, quantify the variability, and design with that knowledge on hand.

Table 7.1. CD Variability Budget as a Function of Technology Node

Year	2005	2007	2010	2013	2016
DRAM $\frac{1}{2}$ pitch (nm)	80	65	45	32	22
Total gate 3σ (nm)	3.15	2.5	1.9	1.3	0.9
Lithography 3σ (nm)	2.8	2.2	1.4	1.1	0.8
LER 3σ (nm)	2.6	2.0	1.4	1.0	0.7
Gate Etch 3σ (nm)	1.4	1.1	0.8	0.6	0.4

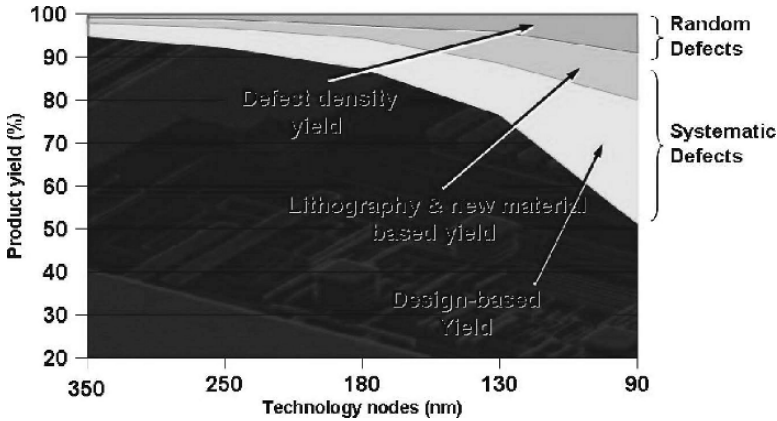


Figure 7.1. Defect Categories Distribution Trend as a Function of Technology Node

In fact it is worth mentioning that while Table 7.1 shows a tighter 3σ budget with every node the impact of lithographic interactions is making the 3σ of parameters such as V_t go in the opposite direction to the desired trend. The absolute value of the 3σ for V_t is increasing with every node.

7.2 Yield Loss Sources & Mechanisms

We covered the sources of yield loss in detail in Section 5.4 of Chapter 5. The reader is encouraged to revisit that section. We just reiterate the two facts that systematic yield loss is becoming dominant and that it is very difficult to separate the systematic from the random components of parametric yield.

7.3 Yield Modeling

7.3.1 Early Work in Yield Modeling

Early work in IC manufacturing yield done in 1964 [118] and 1978 [119] dealt with yield models centered around random defects. Random defects were mainly particle defects leading to opens and shorts and crystal defects resulting in V_t shift or in μ degradation [120].

The starting point in yield prediction was:

$$Y = f(\lambda)\lambda = A \times D \times \Phi \quad (7.1)$$

where, A = chip area, λ was the average number of fatal defects, D = defect density, and Φ = average probability that defect is fatal

The question associated with that function was: what are the spatial distribution statistics governing the faults distribution?

The most common early days yield distribution function was the Poisson equation

$$\begin{aligned} Y &= Y0 \times e^{-\lambda} \\ &= Y0 \times e^{-(A \times D0)} \end{aligned} \quad (7.2)$$

Where D0 is the mean defect density

The constant Y0 is an adjustment factor to account for the non-random defects (lumping all systematic defects into that factor).

And Seed's equation

$$Y = (1 + \lambda)^{(-1)} \quad (7.3)$$

Both Poisson's equation and Seed's equation had a major flaw associated with their inability to account for clustering effects when all empirical evidence suggests that fault clustering is a real life phenomenon prevalent in IC manufacturing; thus the emergence of the use of the Negative Binomial distribution function:

$$Y = (1 + \beta \times \lambda)^{(-1/\beta)} \quad (7.4)$$

β is a measure of clustering.

In reality Seed's and Poisson's equations are special cases of negative binomial (NB) subject to special conditions. By setting β to 1 (i.e. no clustering) NB becomes Seed's equation.

Later, D0 in Equation 7.2 was replaced with a distribution function $f(D)$ and thus the yield equation was transformed to:

$$\begin{aligned} Y &= \int f(D) \exp(-A * D) * dD \\ Y &= Y0 \int f(d) \exp(-A) * dD \end{aligned} \quad (7.5)$$

7.3.1.1 Nano-scale IC Yield Modeling

There are many ways of expressing a yield model that incorporates systematic and parametric aspects of yield in addition to the random aspects. In Section 7.6 we will go through a comprehensive yield modeling exercise that takes into account intra-die variations in detail. For this section we will keep the representation very simple and at a high level to demonstrate the basic principle.

For simplicity and ease of manipulation purposes we are going to start with the Poisson yield model for random yield [121].

$$Y = e^{-\lambda_0} \text{ with } \lambda_0 = D_0 * A \tag{7.6}$$

Where, Y = die yield, λ_0 = mean number of defects per die, D_0 = mean defects per square centimeters, and A = die area in square centimeters

Note that λ_0 here combines the characterized defect size distribution per process step (module) and the critical area of the product design by layer as a function of defect size [121].

$$\lambda_i = \int_0^\infty A(x) * D(x) * dx \tag{7.7}$$

where, x = defect size, A(x) = critical area as a function of defect size, D(x) = defect size distribution function, and i = individual process step or module from there total random yield Y_r becomes:

$$Y_r = \prod_1^n e^{-\lambda_i} \tag{7.8}$$

This formulation is then expanded to generate the full chip yield Y_{fc} as a function of the random yield Y_r , the systematic yield Y_s , and the parametric yield Y_p as:

$$Y_{fc} = Y_r * Y_s * Y_p \tag{7.9}$$

Although this model is developed for a full chip it can equally be used in a hierarchical fashion for any level or stage of chip development. So for the design flow in Figure 7.2 the total chip yield will be

$$Y_{fc} = Y_{ip} * Y_{dc} * Y_{fp} * Y_{pl} * Y_{rt} \tag{7.10}$$



Figure 7.2. A Simplified Design Flow for Illustration Purposes

And where each of the individual modules' yield equation will follow Equation 7.9 above. Example:

$$Y_{ip} = Y_{ipr} * Y_{ips} * Y_{ipp} \dots \quad (7.11)$$

Again, for a comprehensive development of a rather involved yield model development see Section 7.6.

7.4 Yield Enhancement Mechanisms

Random and systematic yield enhancement techniques have been thoroughly covered in Chapters 2 through 4. In this section we will simply go over most of them very briefly, mention the technique and the corresponding desired effect. We will follow the simplified design flow of Figure 7.2 as a rough guide.

7.4.1 IP Development

In the area of IP development we can generate multi-versions of each cell with various yield grades and a corresponding area, static power, and timing arcs. We know that poly to poly spacing impacts shorts critical area for poly, it also impacts mobility (stress effects). Also, poly spacing from diffusion edge (STI) impacts mobility as well. We can create test chips with various implementations of each element of a cell library and generate a yield grade for each cell accordingly. We can also make sure that placing any one cell next to another will not create forbidden pitches for poly or any non-OPC'ible situation.

7.4.2 Synthesis

There is nothing physical to be done at this stage. Using cell graded libraries will give the designer an optimization matrix of yield, performance, area, and static power.

7.4.3 Placement and Routing

This is the richest area of possible manipulation for the purpose of improving yield and a lot of the steps could be carried in an opportunistic fashion resulting in very little or no area cost. Steps include :

- (I) RET at large (OPC, PSM, SRAFs). This leads to better resolution and printability.
- (II) Wire spreading. This leads to improved shorts CA yield.
- (III) Wire widening. This improves the open CA yield. Care has to be taken that shorts CA yield is not compromised
- (IV) Via doubling. This improves via yield.

- (V) Smart metal fill. This improves the whole CMP process. It improves yield of each layer to which it is applied and all the layers following it since planarity effects are cumulative.

Again, we will refer the reader to Chapters 2, 3, and 4 for a comprehensive coverage of yield improvement techniques through better printability, resolution, and planarity.

7.5 EDA Application I: A Yield Prediction Model with a Consideration of Correlations

7.5.1 Preliminary Definitions & the cdf Approach

The focus of this application is the evaluation of the increasingly dominant systematic and parametric yield components although its scope can be easily extended to encompass random yield as well for a total and comprehensive yield prediction solution. Examples of such systematic yield components are the CMP induced yield and lithography printability induced yield. There are no mature yield predictability routines in the EDA industry dealing with systematic and parametric yield.

By definition, yield for a measured variable is the probability of the yield measuring variables falling inside the manufacturing specs/bounds at all locations within a chip. Hence for a CMP process Cu and oxide thicknesses are examples of the measured variables for CMP yield. Similarly CDs and NILS (normalized image log-slope) values are examples of measured variables for litho based printability yield. Ideally, if the distribution of the yield measuring variables on all locations and their correlations are precisely known, then a joint cdf (cumulative distribution function) can be derived for each variable; and hence the total chip yield can be calculated. This is known as the cdf approach. A typical flow for the cdf approach is shown in Figure 7.3.

The cdf approach is quite simple, however it is very hard to accurately predict yield using the cdf approach for several reasons:

- 1 Precise process parameters distributions are very hard to obtain, due to both technical difficulties and confidentiality and competitiveness reasons associated with fabrication facilities wanting to protect their real yield figures.
- 2 Different layout patterns impact the yield measuring variables in a very complicated way. Therefore, the process parameters distributions become design dependent. Also, even if the process parameters have Gaussian distributions, their corresponding yield measuring variables are usually non-Gaussian. Furthermore, the yield measuring variables at different locations of a die do not have the same distributions; adding to the complexity of the problem.

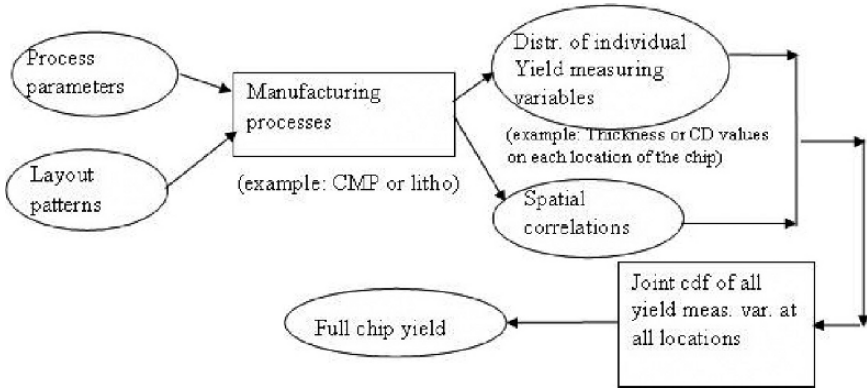


Figure 7.3. The Yield Prediction Flow in cdf Approach

Therefore for a cdf based approach to be adopted many assumptions have to be made and the errors associated with these assumptions are pretty significant and unpredictable.

7.5.2 Our Proposed Solution

In this section a full chip systematic yield prediction is proposed. Rather than using cdf, our approach is based on hot-spot definitions and their yield scores (or failure rates) [122]. Example of lithography hot spots were defined in Chapter 3 in Section 3.11.4.2 and illustrated in Figures 3.31, 3.34, and 3.39. The reader is strongly encouraged to review that section for a better understanding of typical examples of lithography hot spots. The total full-chip yield is calculated by combining all the individual hot-spot yield scores and considering their spatial correlations. The proposed solution is applicable to predicting any systematic yield loss that needs to consider spatial correlations. For example, the CMP yield prediction and the litho yield prediction are two of the applications of the proposed solution. This solution is also equally applicable to parametric yield prediction. Furthermore, given that yield models for “particle related” yield loss are simple, mature, and almost insensitive to design patterns it is quite easy to combine the random particle yield predictor with the yield predictor from this method for a full and pretty accurate yield solution.

In this section, we introduce the proposed solution from the following aspects:

- 1 The inputs needed and what makes them practical.
- 2 The main challenges associated with a good implementation of the proposed solution.

7.5.2.1 The Inputs

- (a) The definitions of hot spots. Ideally these definitions will be provided by fabrication facilities - see Table 7.2 for an example of CMP hot spot specifications. Process simulators can use the definition to identify hot-spots for a given layout. However, if this input is not provided by fabrication facilities there are simulation techniques that can generate those hot spot definitions. This is powerful for designs done around a process that is not fully developed yet.
- (b) The yield score of these hot spots. Again, these scores are either provided by fabrication facilities or are obtained by local process simulations. The scores have to be monotonic in failure probabilities, between 0 and 1, and needless to say the calculated total yield will be at the same accuracy level as the provided hot-spot yield scores.
- (c) The spatial correlation matrix for the yield measuring variables. Once again it is either provided by the fabrication facilities or generated by the assumption of pure distance dependency; not a bad assumption (fast, but less accurate). Another way of deriving that matrix is through repeated process simulations with all different process setups (more accurate, but slow).

As we repeatedly mentioned the ideal situation would be for the fabrication facilities to provide hot spot definitions and scores but that simulations are an equally satisfactory source of this data. Obtaining data from fabrication facilities is also ideal in that it allows one to verify and fine-tune the simulations derived hot-spot yield scores and spatial correlations.

7.5.2.2 The Main Challenge Solved by the Proposed Solution

The main challenge is how to incorporate correlations when combining individual hot-spot scores for the total full-chip yield calculation. The proposed solution uses a transformation operation “T” (derived in this section and shown in Figure 7.4) that will be applied directly to the hot-spot yield scores in such a way that the correlations are handled during the transformation such that the transformed yield scores are independent of each other. Hence, a direct multiplication of the individual transformed yield scores gives the total yield score of the whole chip in a manner that is easy to handle mathematically. This

Table 7.2. A Possible CMP Hot Spot Specifications for 65nm

Description	Spec	metal 1	metal x	top metal
metal vs. chipwide average	+/-%	20	20	20
topography vs. chipwide average	+/-%	25	25	25
oxide vs neighboring gap	A	750	750	N/A

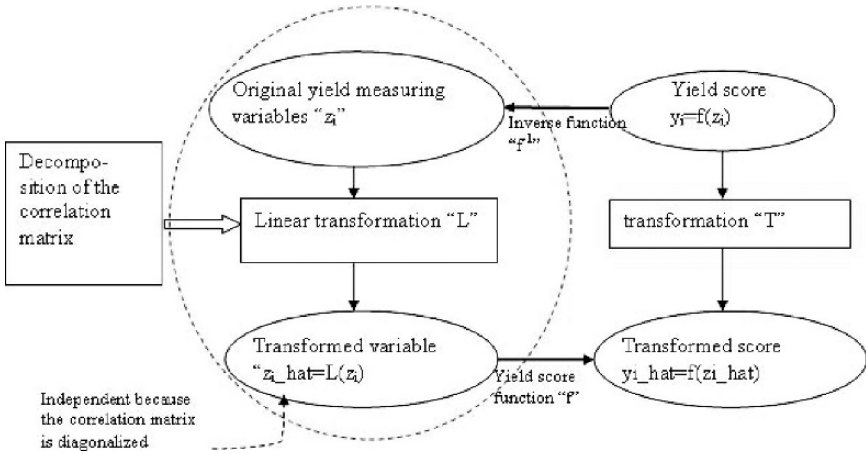


Figure 7.4. Derivation of the Transformation “T” for Hot-spot Yield Scores

approach provides a more practical way to predict full chip systematic yield with consideration to spatial correlations. This approach actually provides a universal framework for systematic yield and parametric yield prediction for any type of yield loss as long as the hot-spot definitions, individual hot-spot yield, and the spatial correlation of layout components are provided or can be simulated. With this proposed universal yield prediction framework integrating all different components of yield loss into total yield for a given layout is quite straightforward given the breakdown of correlated components to independent ones.

7.5.3 A Brief Description of the Key Ideas

7.5.3.1 Key Idea for the Hot Spots Yield Prediction Approach and Methodology

The key idea of the proposed yield prediction approach is to use provided hot spots and their yield scores. In order to consider spatial correlations, we propose a methodology of transforming the hot-spot scores directly such that after the transformation the correlations are decomposed and the transformed yield scores are rendered independent of each other.

7.5.3.2 Idea for Deriving the Transformation “T” for Hot-spot Yield Scores

As illustrated in Figure 7.4 the transformation “T” in the solid red box is what the method provides. Mathematically it is equivalent to the content in the dotted red circle. We use it to illustrate the key idea and the main derivation steps.

Decomposing the correlation matrix of the yield measuring variables gives us the linear transformation “L”. Applying “L” on the yield measuring variables

will transform them into independent ones. However, “L” is not the same as the transformation “T” that we need for the hot-spot yield scores. It is because the yield scoring function “f()” that relates the yield measuring variables to the yield scores is nonlinear. But “T” is related to “L” by the yield scoring function “f()”. We make use of this relation to derive the transformation “T”. As a result, directly applying the derived transformation “T” on the hot-spot yield scores will transform them into independent ones.

Although the yield scoring function $f()$ is a crucial link between “L” and “T” we do not request that the exact yield scoring function $f()$ and its inverse $f^{-1}()$ are implicitly used for the derivation of “T” instead of being explicitly used for calculating the yield measuring variables. As long as the input hot-spot yield scores satisfy the following criteria listed in Section 7.5.3.3, the transformation “T” can be derived for the proposed solution.

7.5.3.3 Hot-spot Yield Scores and Yield Scoring Function

The basic criteria for the input hot-spot yield scores are two obvious requirements:

- 1 The score being a number between 0 and 1.
- 2 The score being monotonic with severity of violation in terms the failure probabilities.

Hot-spot yield scores can be provided in many different ways. One way would be that the yield score values directly come from fabrication facilities’ measured data. Another would be calculating them from local process simulation using TCAD tools. In this section we will use the approximate functions for both yield scoring function $f()$ and its inverse $f^{-1}()$. It can be proved that the errors in approximating both $f()$ and its inverse $f^{-1}()$ will not propagate through the series of derivations, and are rather reduced and bounded. The reasoning behind that will be given in next subsection.

Yield scores can also be provided from the fabrication facilities’ provided specifications by score formulation procedures. Table 7.3 and Table 7.4 illustrate two such examples. One is for CMP yield scores and the other is the

Table 7.3. CMP Hot Spot Scoring (Based on CMP Hotspot Specifications)

Rules	Region	Score
M1 depth of focus	>900	0
	>800 and <900	0.5
	>700 and <800	0.8
	<700	1
M1 dishing

Table 7.4. Litho Hot Spot and Score Specifications (Derived from a Foundry Specs)

Rules	Region	Weight	Score
Line-type NILS	<0.9	Must fix	0
	>0.9, and <1.1	8	0.2
	>1.1, and <2	2	0.8
	>2	0	1
space-type NILS

lithography yield scores. In this case, we can use the yield scoring functions derived from the specified scores, for example in the form of piecewise linear functions. In either case the calculated total yield will be at the same accuracy level as the provided hot-spot yield scores.

7.5.3.4 Details on the Derivation of Transformation “T”

The main purpose of transformation is to make the transformed yield measuring variables independent of each other on all hot spots (see Figure 7.4). We are given the correlation matrix which is associated with the original yield measuring variable values on the hot spots. Decomposition (such as PCA, the Principal Component Analysis, or ICA, Independent Component Analysis) on this correlation matrix provides a linear transformation “L” on the yield measuring variable values. After transformation the correlation matrix associated with transformed yield measuring variables is diagonal. Thus the transformed variables are independent of each other.

However one should keep in mind that we don’t have the yield measuring variable values or their distributions. Instead, we only have the yield scores of the hot spots. The transformation “T” on yield scores is not the same as “L” on yield measuring variables. Yield score of a spot is a function of the yield measuring variable distribution (like mean and variance), and its bounds (See Figure 7.5). For example the scoring function can be

$$Y_i = \int_l^u pdf(z)dz = f(\mu, \sigma, l, u) \quad (7.12)$$

where z is the yield measuring variable, l and u are the lower and upper bounds. This function is highly non-linear. Hence the linear transformation “L” on x is not the same as “T” on y_i , where x is the measured variable distribution statistics, y_i is the yield score on sport “i”. But “L” and “T” are related by f . Therefore, we find an equivalent representation for “T” as:

$$T(y_i) = f\{L[f^{-1}(y_i)]\} \quad (7.13)$$

Note also that the yield score function is not used explicitly. We do not derive the exact yield measuring variables during the derivation. Instead we

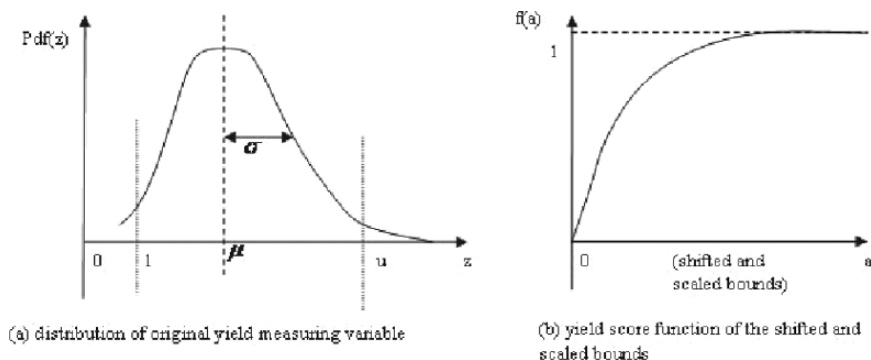


Figure 7.5. Distribution of Yield Measuring Variable and Yield Score Function

only make use of the relations and derive some intermediate variables which combine the information of the original bounds and the original yield measuring variables' means and variances. Ultimately those intermediate variables are all transformed back to yield scores. Next are the derivation details.

First, simplify the function “ f ” by centering and scaling. For each spot’s yield measuring variable value, we can perform “centering” and “scaling” to make the transformed variables be 0-mean and unit-variance. The “centering” amount is the variable’s nominal value. The “scaling” amount is the guided by the variance, which is the diagonal entry in the correlation matrix. With “centering” and “scaling”, the distribution of yield measuring variable on all hot spots have 0-mean and unit-variance. Although the yield measuring variables are not Gaussian distributed, given the limited amount of information available about them a Gaussian distribution assumption is not a bad one. In fact as we shall see it is a good enough one. And, the distributions on all locations are approximately the same. Hence the bounds “ l ” and “ u ” are shifted and scaled as well after “centering” and “scaling” operations. And therefore they are functions of the mean and the variance of the yield measuring variables (see Figure 7.4).

The linear transformation “ L ” on the yield measuring variables would include all the centering, scaling, and decomposition operations. This step dramatically simplifies the form of yield score function “ f ”, which now has the same form for all locations. It is a function of the shifted and scaled bounds. The original variable’s “mean” and “variance” information are both contained in the shifted bounds.

Since we approximate the yield measuring variable to be the same distributed with 0-mean and unit-variance after “centering” and “scaling” (Gaussian for example), we can approximate the yield score function f (scaled-and-shifted-bounds) by $g()$, and $f^{-1}(\text{yield-score})$ by $g^{-1}()$. Note that the yield score func-

tion is monotonic and is non-linear. We can use any approximation technique, or curve fitting to approximate it as polynomial. One example of such an approximation is to use a piece-wise linear approximation. Also note that this procedure is not limited to a particular approximation technique. If after real silicon data is made available we can replace the functions we have with a better approximation functions $g()$ and $g^{-1}()$ and then the same yield prediction methodology is applied.

The constraints on the approximation that we request are: the approximation error is bounded, and either $g() < f()$ always true, or $g() > f()$ always true. These constraints guarantee that the approximation error in $f^{-1}() - g^{-1}()$ before going through transformation “L” and the one in $f() - g()$ after “L” cancel each other. Hence the approximation errors do not propagate through the operations from $g^{-1}()$ to $L()$ and then to $g()$, but are rather reduced. It can be proved that the error “e” between the approximate $g^{-1}()$ and real $f^{-1}()$ on transformed yield measuring variables are bounded. Specially,

$$\begin{aligned}
 e &= L(g^{-1}(y_1), \dots, g^{-1}(y_n)) - L(f^{-1}(y_1), \dots, f^{-1}(y_n)) \\
 &\leq \max\{g^{-1}(y_i) - f^{-1}(y_i)\}
 \end{aligned}
 \tag{7.14}$$

The idea can be more clearly illustrated by Figure 7.6. In that figure, x_1 and x_2 are two values of the yield measuring variable corresponding to two yield scores y_1 and y_2 . They are derived by exact inverse yield score function $f^{-1}()$. \hat{x}_1 and \hat{x}_2 are the values calculated from y_1 and y_2 by approximate inverse yield score function g^{-1} . $L(x_1, x_2)$ and $L(\hat{x}_1, \hat{x}_2)$ are the transformed yield measuring variable, based on true variable values or approximate ones. “e” is the error between them. Since $L()$ is linear transformation, “e” is bounded by

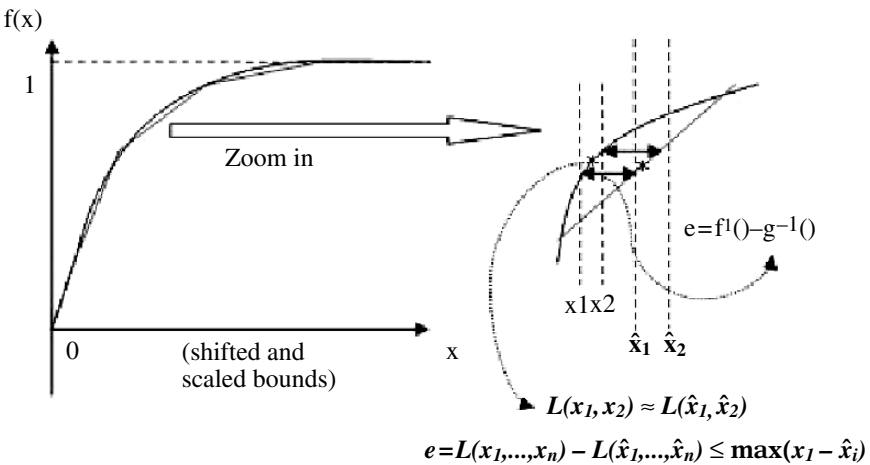


Figure 7.6. Approximation of $f()$ and $f^{-1}()$

Equation 7.14. Hence the error on the complete transformation “T” brought by approximation to the functions $f()$ and $f^{-1}()$ is bounded by the max approximation error between the exact $f^{-1}()$ and the approximate $g^{-1}()$.

Finally, after performing this transformation T on the given hot-spot yield scores, the transformed scores are associated with the independent yield measuring values. Hence they can be directly multiplied together to get the total yield score.

7.5.3.5 The complete flow for deriving transformation “T”

The whole procedure in the form of a flow diagram is illustrated in Figure 7.7. In summary we have introduced a comprehensive procedure for generating a comprehensive yield prediction model with a consideration of correlations.

7.5.4 Example and Results

In this section, we present some illustrative numerical examples to demonstrate the key benefits of proposed method for yield prediction: request reasonable inputs, easy to compute, and final error in yield prediction is very stable and small.

In the examples to be shown next, we studied 2 hotspots, with individual failure rates as $fr_1=7.2\%$, $fr_2=31\%$. The spatial correlations and variances of

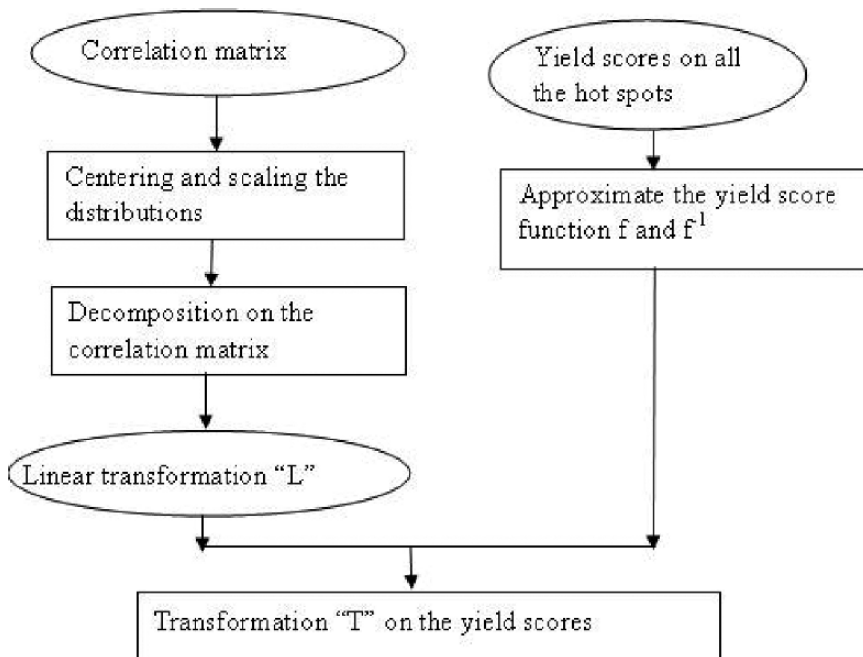


Figure 7.7. The Complete Flow for Deriving the Transformation “T”

the yield measuring variable on these two spots can be obtained from the covariance matrix: $\Sigma = [4 \ 0.81; 0.81 \ 9]$. The nominal values of the yield measuring variable on these two spots can be obtained from process simulation with nominal condition. Here they were set to $\mu = [3.8; 5.7]$. According to the given hot spot definitions, manufacturing bounds can be obtained. Specifically, the lower bound was 0, upper bound was 7.

We assumed some true distributions on these two hot spots, for example, Rayleigh with given means and variances. We used this information only to compute the real yield for comparison purposes.

We applied the hot spot based yield prediction method to compute the yield, and compared with the true yield value to calculate the prediction error. For comparison, we also implemented the “cdf” approach on these examples.

Before showing the simulation results, we would like to first show how much difference the insufficient knowledge of the distribution can make. In Figure 7.8, there are two distribution curves, with the same mean and variances. The blue curve is the true distribution (Rayleigh), the red one is the approximate distribution curve (Gaussian). Although they share the same means and variances, it can be clearly seen that the difference between the two curves is quite large. This is the main source of the final error in the predicted yield. For “cdf” approach, this difference is directly reflected in the final prediction error. Hence

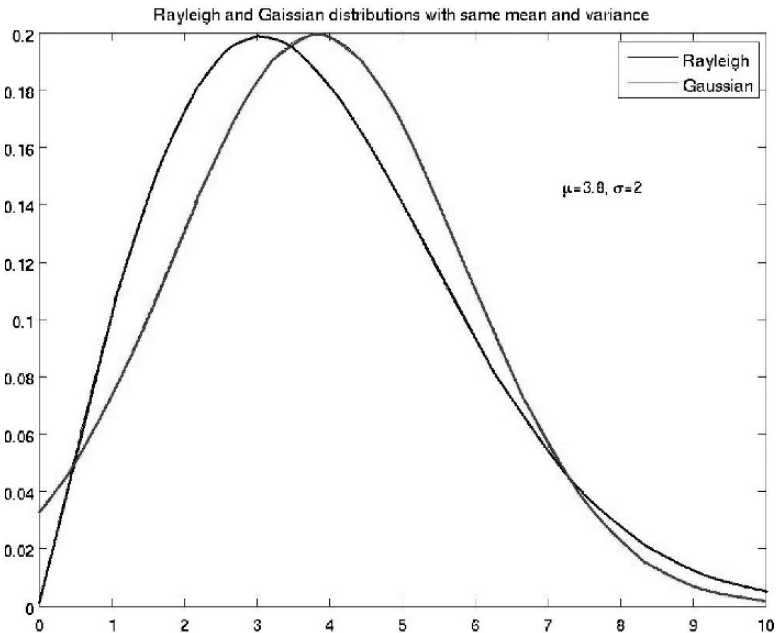


Figure 7.8. Rayleigh and Gaussian Distributions with Same Mean and Variance

Table 7.5. Simulation Results for the Case When True Distribution is Rayleigh ($\sigma_1 = 2$, $\sigma_2 = 3$)

σ_{12}	realY	hotspot approach		cdf approach	
		calcY	Err(%)	calcY	Err(%)
1	0.7738	0.7387	4.53	0.6844	11.55
0.81	0.7561	0.7246	4.17	0.6694	11.47
0.5	0.7198	0.6970	3.17	0.6405	11.02
0.3	0.6909	0.6759	2.17	0.6187	10.45
0	0.6394	0.6394	0	0.5816	9.04

the error can be large in some cases, small in the others. The error is quite unstable and unpredictable. On the other hand, with the hot spot based yield prediction method, both the forward yield scoring function and inverse yield scoring function are used. Consequently the errors in the approximation of each step do not propagate to the final error. Instead, the major portion of the errors is canceled, as is explained in last section. Hence the final error is greatly reduced and bounded.

Table 7.5 shows the simulation results for varies of situations with different correlations between the two hot spots. Covariance $\sigma_{12}=1$ means the two spots are fully correlated. Covariance $\sigma_{12}=0$ means the two spots are totally uncorrelated. The 2nd column shows the real yield values for these cases. The 3rd and 4th column show the results from the hot spot based method. The last two columns show the results from the “cdf” approach. It can be clearly seen that the approximation errors from our method are quite stable and stay within a small value range. Whereas the errors from “cdf” approach are quite large.

Table 7.6 shows the simulation results for the same set of examples. Except that the real distribution of the two hot spots are Laplacian. From this set of results, it can be clearly demonstrated that the prediction error from the “cdf” approach heavily relies on how close the approximated distribution is to the real distribution. In this set of experiments, they are very close. Hence the prediction error improves. But in reality, we can never know the exact distribution on the hot spots. Hence it is impossible to predict how large the error can be in the

Table 7.6. Simulation Results for the Case When True Distribution is Laplace ($\sigma_1=2$, $\sigma_2=3$; $\mu_1=3$, $\mu_2=3.5$)

σ_{12}	realY	hotspot approach		cdf approach	
		calcY	Err(%)	calcY	Err(%)
1	0.8056	0.8296	2.98	0.7891	2.05
0.81	0.7957	0.8172	2.7	0.7753	2.56
0.5	0.7763	0.7917	1.98	0.7476	3.70
0.3	0.7615	0.7716	1.33	0.7262	4.64
0	0.7356	0.7356	0	0.6889	6.35

predicted yield with “cdf” approach. However, the prediction error from the proposed hot spot based method stays within in a small value range, regardless how close the selected approximate distribution is to the real distribution. That is one of the key benefits provided by our method.

7.6 EDA Application II: Development of an IC Manufacturing Yield Model Encompassing Intra-Die Variations

A manufacturing yield model that takes into account the impact of physical layout and its interactions with manufacturing fluctuations into account is very powerful in the sense that it allows the designer to predict design-specific features that impact intra-die variability and thus yield and it allows the designer to alter those features and thus improve yield in a predictable manner with a known cost.

In this Section such a model is described and implemented where the intra-die systematic variations are evaluated using a physics-based model as a function of a design’s physical layout. The random variations and their across-die spatial correlations part of the model are obtained from data harvested from manufactured test structures.

The proposed algorithm is geared towards reducing the order of the numerical integration in the yield model. The model can be used to

- 1 predict manufacturing yields at the design stage.
- 2 enhance the layout of a design for higher manufacturing yield.

The proposed model and the listed examples were correlated and calibrated using data obtained from a well known fabrication facility [123, 124].

7.6.1 Background

In this chapter and in earlier chapters we have discussed how a typical IC manufacturing process involves complex physical and chemical interactions that result in the targeted end parameters having finite variations centered around their targeted intended values no matter how accurately controlled the manufacturing process is. We also discussed that traditionally these variations manifested themselves in the form of lot to lot, wafer to wafer, and die to die variations that were design independent and that resulted in some acceptable yield loss (the three corners model based design approach). Yield improvement under that scenario mainly involved tightening the process control over time. However, with feature sizes smaller than half the wavelength of the optically utilized light source and shrinking, and with corresponding tighter pitches, intra die variations has become the dominant and the most significant component in determining manufacturing yield.

There are two components to die-level variations: (1) *intra-die systematic variations* and (2) *intra-die random variations*. *Intra-die systematic variations* are strongly layout-dependent. Two typical examples of variations with a significant component of layout dependency are: (i) intra-die critical dimension (CD) variations due to microlithography and (ii) Cu & oxide thickness variations due to the Chemical-Mechanical Planarization (CMP) process. Empirical data shows that the intra-die systematic CD and thickness variations resulting from the layout pattern non-uniformity are becoming comparable to, even dominant over lot to lot, wafer to wafer, and die to die variations [125]. In recent years, a number of full-chip simulation tools have been developed to evaluate and predict intra-die systematic variations at the design step [6]para:3. In addition to the intra-die systematic variation, the *intra-die random variation* remains an important and significant component of the total die-level variation. This component reflects random fluctuations of process parameters within a die. The overall random variations tend to be spatially correlated in the current processes. When the lot to lot, wafer to wafer, and die to die random variations dominate the overall random variations, a perfect spatial correlation at die-level can be assumed. However, due to decreasing feature sizes and increasing die sizes, the spatial correlations of random variations between two intra-die locations do not exhibit ideal behavior any more. Instead the spatial correlation of intra-die variations decreases with increasing distances between locations. The non-perfect correlation between intra-die locations strongly impacts the total manufacturing yield. Yield loss due to layout dependent intra-die variations cannot be rectified without some intelligent compensation at the design stage. However, the first step towards a yield-aware enhanced design is to be able to predict manufacturing yield at each design stage with some degree of accuracy. Most yield prediction models tend to focus on on random defects related yield [126, 127]. Unfortunately such models do not consider the impact of spatial correlations of intra-die variations and are therefore not sufficient to predict manufacturing yield in current and future processes.

The model proposed in this section addresses the aforementioned factors. The key features of this model are:

- 1 A yield prediction methodology that can take into account both intra-die systematic variations and all known forms of random variation.
- 2 A model that predicts die yield after CMP and a computationally efficient algorithm to evaluate the model.

7.6.2 Variation Decomposition

In this section, we provide a brief overview of the different types of process parameter variations. Process parameters vary at different scales in time and space. These variations can be classified as lot-lot, wafer-wafer, die-die, and

intra-die [125]. The lot-lot and wafer-wafer variations are mainly temporal while the die-die variations are primarily spatial. Due to the long range nature of those variations, they are usually very low frequency in nature. This means their impact on two locations within a die are the same. Hence, it is reasonable to assume a perfect intra-die correlation for these components of random variations.

The intra-die variation can be decomposed into two components. One is the systematic spatial variation which is mainly caused by the layout dependencies of the process. A key example of this variation is the pattern and density dependencies of the intra-die oxide and Cu thickness in the CMP process. The other component of the intra-die variation is the random variation that is caused by typical process fluctuations around its nominal value and is spatially correlated.

Based on the above classification and discussion, a quality indicative value to describe a process parameter for a location (x, y) is denoted as $p(x, y)$ and can be expressed as

$$\begin{aligned} p(x, y) &= \mu + f_{l_l} + f_{w_w} + f_{d_d} + f_i(x, y) \\ &\quad + \varepsilon_{l_l} + \varepsilon_{w_w} + \varepsilon_{d_d} + \varepsilon_{f_f}(x, y) \\ &= \mu + f_{l_l} + f_{w_w} + f_{d_d} + f_i(x, y) + \varepsilon(x, y) \end{aligned} \quad (7.15)$$

where μ is the overall mean, f_{l_l} is the systematic lot-lot variation, f_{w_w} is the systematic wafer-wafer variation, f_{d_d} is the systematic die-die variation, $f_i(x, y)$ is the systematic intra-die variation, ε_{l_l} is the random lot-lot variation, ε_{w_w} is the random wafer-wafer variation, ε_{d_d} is the random die-die variation and $\varepsilon_i(x, y)$ is random intra-die variation.

In the following formulation, we assume that $f_{l_l} + f_{w_w} + f_{d_d} = 0$. It can be shown that this simplification does not affect our analysis. Therefore, Equation 7.15 can be simplified as

$$p(x, y) = \mu(x, y) + \varepsilon(x, y) \quad (7.16)$$

where $\mu(x, y) = \mu + f_i(x, y)$ and $\varepsilon(x, y) = \varepsilon_{l_l} + \varepsilon_{w_w} + \varepsilon_{d_d} + \varepsilon_{f_f}(x, y)$.

Note that if the random variation was dominated by lot-lot, wafer-wafer, and die-die random variation then the correlation of $\varepsilon(x, y)$ at two intra-die locations (x_1, y_1) and (x_2, y_2) would be close to 1. But, when intra-die random variation is much larger than the sum of lot-lot, wafer-wafer, and die-die random variations, the correlation is solely determined by the intra-die component $\varepsilon_{f_f}(x, y)$. In all other cases, the correlation lies somewhere between the correlations of intra-die random variations and 1.

7.6.3 Variations Handled by Hotspot Model

In this formulation, we make the following assumptions on the nature of the intra-die variations. These assumptions were made based on a detailed analysis of data obtained from a fab.

If there are n locations that we are interested in, we represent the random variables p at the n locations by an n -dimensional random variable vector \mathbf{p} . Equation 7.16 can be further written as

$$\mathbf{p} = \boldsymbol{\mu} + \boldsymbol{\varepsilon} \quad (7.17)$$

where $\boldsymbol{\mu}$ is a n -dimensional vector representing the systematic components of the variables and $\boldsymbol{\varepsilon}$ is a n -dimensional vector representing the overall random components. We assume that $\boldsymbol{\varepsilon}$ satisfies a multivariate normal distribution $N(0, \boldsymbol{\Sigma})$, where $\boldsymbol{\Sigma}$ is a $n \times n$ covariance matrix. Thus, \mathbf{p} satisfies a multivariate normal distribution $N(\boldsymbol{\mu}, \boldsymbol{\Sigma})$. Furthermore, it is assumed that (i) the variances σ^2 of $\boldsymbol{\varepsilon}(x, y)$ at each location are equal to each other. Then there is

$$\rho_{i,j} = \sigma_{i,j} / \sigma^2 \quad (7.18)$$

where $\sigma_{i,j}$ is the (i, j) th entry of $\boldsymbol{\Sigma}$, ρ is the correlation matrix and $\rho_{i,j}$ the (i, j) th entry of the correlation matrix. This assumption is usually valid for most process parameters. (ii) the correlation is solely a function of distances.

7.6.4 Application Example: CMP Yield

We use CMP as an example to demonstrate the yield model. CMP is one of the enabling processes for planarization as well as for patterning copper interconnect in the deep sub-micron IC fabrication. The Cu interconnect is patterned primarily by four sequential steps:

- (I) a deposition process to form a dielectric layer on the wafer
- (II) a plasma etch process to generate the trenches in the dielectric layer
- (III) a deposition process to fill up the trenches with copper, and
- (IV) a CMP process to remove the bulk copper from the top of the dielectric layer leaving copper in the trench as interconnect.

We have discussed Cu CMP earlier in the book so our description here will be brief for the benefit of this section only. An ideal CMP process should produce a perfectly flat Cu of uniform thickness across the wafer. However, this is not the case in reality because the Cu thickness at a location (x, y) on the wafer is affected by different layout patterns in a design, and a number of process parameters. The different layout patterns can be described by layout density, layout perimeters, line width, and so on [6]. The layout patterns are typically

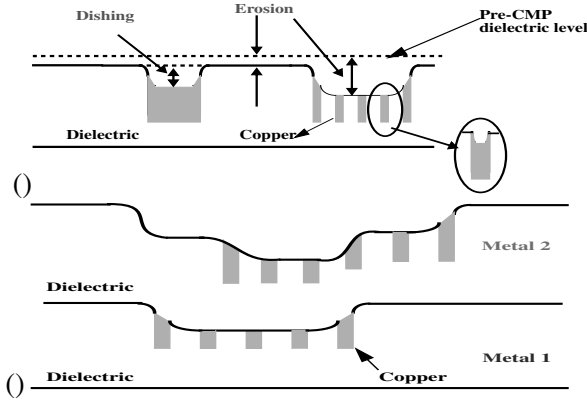


Figure 7.9. Typical Post-CMP Topography [6]

not uniform in a design. The process parameters include the incoming Cu deposition thickness, barrier deposition thickness, Cu polishing rate, barrier/oxide polishing rate, CMP down pressure, velocity, polishing time, and so on [84]. They usually fluctuate around their nominal values.

Figure 7.9 shows typical Cu thickness variation after CMP. The thickness variation can be caused by underlying layout differences or by random variations of the process parameters. They include copper dishing, dielectric erosion, and multi-layer cumulative topographies variation. When the thickness variation is large, it may cause a circuit open and/or a circuit short. For instance, when the copper is not totally removed from the top of the dielectric layers, a circuit short occurs. On the other hand, if the copper in the trench is over polished, a circuit open occurs. The variation can also cause defocus issues in the lithography process following CMP. This can result in zero yield in extreme cases.

7.7 CMP Yield Prediction Model

To ensure a chip's functionality and yield after CMP it is necessary to ensure that the Cu thickness falls within a specification bounded by an upper specification limit (USL) and a lower specification limit (LSL). This specification is dictated by the design requirements on one hand and manufacturing capabilities on the other.

We define **CMP Yield** as the probability that all thickness values across a die fall between USL and LSL.

Mathematically, yield Y can be expressed as:

$$\begin{aligned}
 Y &= \int_L^U \int_L^U \int_L^U \dots \Phi(\mathbf{p}) dp_1 dp_2 \dots dp_n \\
 &= \int_L^U \int_L^U \int_L^U \dots \frac{e^{(-0.5(\mathbf{p}-\boldsymbol{\mu})^T \boldsymbol{\Sigma}^{-1}(\mathbf{p}-\boldsymbol{\mu}))}}{\sqrt{(2\pi)^n |\boldsymbol{\Sigma}|}} dp_1 dp_2 \dots dp_n \quad (7.19)
 \end{aligned}$$

where U is used to denote USL and L is used to denote LSL, n denotes the number of locations where the thickness is monitored in the yield prediction process and Φ denotes the joint distribution of the thickness variation at these n locations. The joint distribution of the thickness at the n locations can be written as:

$$\Phi(\mathbf{p}) = \frac{e^{(-0.5(\mathbf{p}-\mu)^T \Sigma^{-1}(\mathbf{p}-\mu))}}{\sqrt{(2\pi)^n |\Sigma|}} \quad (7.20)$$

where \mathbf{p} is the n -dimensional random variable vector and $|\Sigma|$ is the determinant of the covariance matrix [128].

Typically, a large number of locations need to be tracked for good yield prediction. A typical number in the order of 10^5 to 10^6 is needed to predict the systematic thickness variation μ accurately. For example, for a chip size of $4\text{mm} \times 4\text{mm}$, a number of 160,000 locations are needed by meshing the chip into $10\mu\text{m} \times 10\mu\text{m}$ tiles.

A direct numerical integration of Equation 7.19 with dimension n is in the order of 10^5 to 10^6 and is not practically feasible. It would require a large amount of computation time and a huge amount of memory without guaranteeing any numerical accuracy.

Another issue with the above method is that a lot of manufacturing data would be needed to populate the covariance matrix. A chip of size $4\text{mm} \times 4\text{mm}$ with a mesh size of $10\mu\text{m}$ would contribute 160,000 locations across the chip. The covariance matrix Σ as a function of locations has to be obtained from manufacturing by using test structures similar to those in [129]. For our example, to obtain the covariance / correlation matrix needed, measurements at $(400^2 + 400^2)^{1/2} = 576$ locations (around one location every $10\mu\text{m}$) are ideally needed. This is an impractical and expensive proposition.

In the next section, we propose a computationally efficient algorithm that can reduce the order of numerical integration and also reduce the amount of test-data needed without sacrificing accuracy.

7.7.1 Yield Prediction Algorithm

We present in this and subsequent sub-sections yield prediction algorithms for two scenarios:

- 1 perfect correlation of random variations across the die.
- 2 correlation across the die that is decreasing with distance.

The first case can be used to predict yield for small dies or when correlation data is unavailable from a test chip or a fab. However, it is important to note that for large dies it is incorrect to assume a perfect correlation. Typical manufacturing data suggests that the correlation decreases gradually with

distance. For such cases, we propose a computationally efficient algorithm described in Section 7.7.1.2 for evaluating yield while taking spatial correlations into account.

7.7.1.1 Perfect Correlation across the Die

When assuming a perfect correlation between the random variations at any two intra-die locations all entries in the correlation matrix are equal to 1. This causes the rank of $\Sigma = 1 \leq n$ (or Σ to not be a full-rank matrix). Thus the inverse of Σ does not exist. In this case Equations 7.19 and 7.20 cannot be used to calculate the joint probability of the Cu thickness at the n locations. Assuming that the maximum nominal Cu thickness of the n locations is Max and that the minimum nominal Cu thickness is Min as shown in Figure 7.10 it follows that the probability for all Cu thickness to fall between the USL and LSL (therefore the yield) can be calculated as:

$$Y = \int_L^\infty PDF(Min, x)dx + \int_{-\infty}^U PDF(Max, x)dx - 1 \quad (7.21)$$

where PDF is the univariate normal distribution function. The first integral is the probability for all Cu thickness values to fall above LSL. The second integral is the probability for all Cu thickness values to fall below USL. Their sum minus 1 is the probability that all Cu thickness values fall between USL and LSL.

Equation 7.21 implies that the probability Y of all Cu thickness falling within the specification is solely determined by two locations: one with the maximum

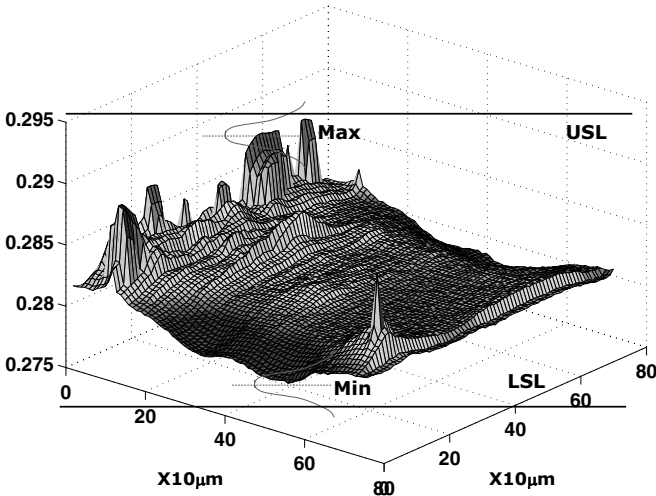


Figure 7.10. Yield Prediction for The Case of Perfect Across-chip Correlation

nominal thickness *Max* and the other with the minimum nominal thickness *Min*. All other locations do not affect the overall probability. Due to the full correlation of thickness variations within a die, thickness values at all locations keep co-varying and the variation amounts are the same everywhere. Therefore, the location with a maximum nominal thickness always have a maximum thickness and the location with a minimum nominal thickness always have a minimum thickness. Mathematically, this can be attributed to the degeneration of the $n \times n$ covariance matrix into a scalar. The probability of the two locations to be within the specification is the same as the probability that all thickness values within the die fall within the specification.

7.7.1.2 Correlation decreasing with distance

Experimental data shows that correlation decreases very gradually with increasing distance. The top graph of Figure 7.11 shows the correlation of post-CMP thickness values (normalized) obtained from manufacturing data for two locations which are $80\mu\text{m}$ away from each other. A high correlation of 0.99 was

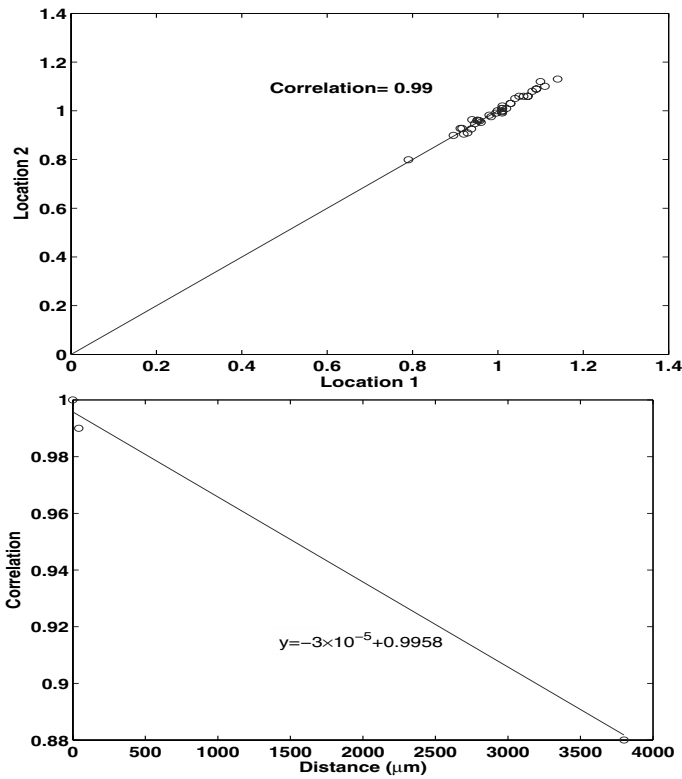


Figure 7.11. Spatial Correlations of Random Variation as Function of Distances

obtained. A relatively lower correlation of 0.88 was obtained for another two locations which are around $4000\mu\text{m}$ away from each other. Assume a linear reduction of correlation with distance, a function as that shown in the bottom graph of Figure 7.11 can be obtained, showing a gradual reduction of correlation. This leads us to believe that the correlation between locations within a certain distance, say $200\mu\text{m}$, is very close to 1. Thus, a much coarser grid can be used for sampling and obtaining manufacturing data. In addition, neighboring locations can be assumed to have near perfect correlation. This fact is used in our algorithm and greatly reduces the order of the numerical integration, thereby speeding up the computation.

To compute yield, we determine the probability that the thickness at all locations falls below USL (denoted as Y_{max}) and the probability that the thickness at all locations falls above LSL (denoted as Y_{min}). When the across-chip correlation of the random variation is relatively strong, the yield can be approximated as

$$Y = Y_{max} + Y_{min} - 1 \quad (7.22)$$

Note that Equation 7.22 is an exact solution for two cases: (i) $USL = \infty$ ($Y = Y_{min}$) and (ii) $LSL = -\infty$ ($Y = Y_{max}$). In the following paragraph we first discuss the computation of Y_{max} .

We use a symbolic chip with a small size of $120\mu\text{m} \times 130\mu\text{m}$ (shown in Figure 7.12) as our example. The chip is meshed into $10\mu\text{m} \times 10\mu\text{m}$ tiles. It is assumed that the nominal Cu thickness $\mu(x, y)$ in all tiles is obtained by a CMP simulator. The distance throughout which any two locations are assumed to have an almost-perfect correlation is 3.5 times the tile size, bounded by circles with radius = $35\mu\text{m}$ as shown in Figure 7.12. We will refer to the region where perfect correlation is assumed as a *perfect-correlation circle*.

First the tile with the maximum nominal thickness across the whole chip is found and is denoted as *Max1* (Figure 7.12). All the tiles in the perfect-correlation circle around *Max1* are contained in *circle 1*. Next, the tile with the maximum nominal thickness outside of *circle 1* is located and is denoted as *Max2* (Figure 7.12). The tile with the maximum nominal thickness outside of the union of *circle 1* and *circle 2* is denoted as *Max3*. The above procedure is repeated until all the tiles in the die are covered by a circle. The chip in Figure 7.12 is covered by 8 circles surrounding 8 maximum locations from *Max1* to *Max8*.

We assume that the almost-perfect correlation across the circle to be a perfect correlation of 1. Then the probability of thicknesses at tiles surrounding *Max1* (*mint green tiles*) to be smaller than USL is solely determined by *Max1* similar to that shown in the case of Figure 7.10. Outside the circle surrounding *Max1* tiles with the highest probability to be outside USL are those surrounding *Max2* (*red tiles*). Outside the union of circles surrounding *Max1* and *Max2* they are *Max3* and its surrounding tiles. After the above procedure the nominal thickness

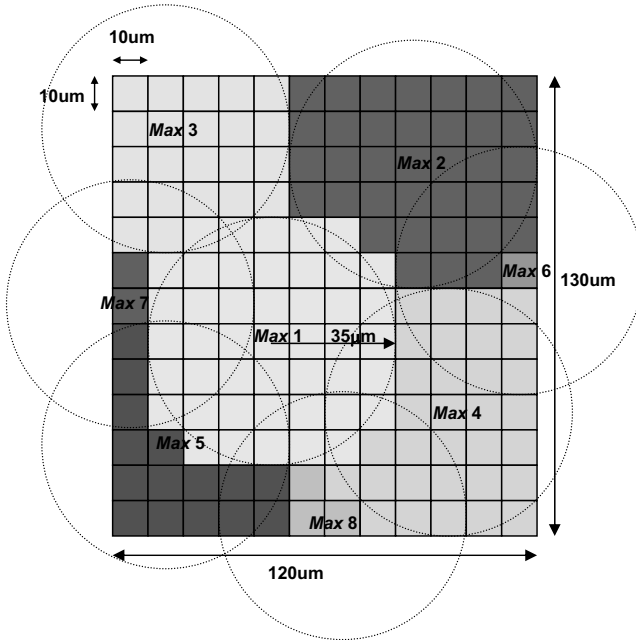


Figure 7.12. Perfect Correlation Circles Surrounding Maximum Thickness Values

values $Max1 \sim Max8$ at the 8 maximum locations as well as the correlations between the 8 locations (functions of their relative distances) are obtained. Note that because of the near-perfect correlation in the *perfect-correlation circles* the probability for the 8 locations to fall below the USL is close to the probability for all the locations on the die to fall below USL.

Knowing the correlation matrix ρ_{max} of the 8 locations we can obtain their covariance matrix \sum_{max} and calculate their joint distribution using Equation 7.19. The only difference here is that $-\infty$ should replace LSL L in Equation 7.19 to calculate Y_{max} . Note that the size of the correlation matrix is 8×8 . It is a much smaller size than that of $12 \times 13 \times 12 \times 13 = 156 \times 156$ obtained when applying Equation 7.19 directly to all the tiles. For a chip with a typical size of $4\text{mm} \times 4\text{mm}$, the size of the correlation matrix can be reduced from $160,000 \times 160,000$ to around $2,500 \times 2,500$. When the perfect-correlation distance is increased from the $35\mu\text{m}$ to $200\mu\text{m}$ the size of the correlation matrix (around 100×100) gets even smaller. The evaluation of a 100-dimensional integration is still not an easy task but much more tractable. In a later Section 7.7.1.3 we will discuss a specific algorithm by Genz [128] to calculate the integration after the above order reduction is performed.

Mathematically the above procedure is to replace the sub-matrix (whose elements are close to 1, which is surrounding the entries with a maximum

nominal value in the correlation matrix) with a sub-matrix whose elements all equal to 1. This makes the full-rank covariance matrix degenerate into a matrix with a rank smaller than n and thus reduces the order of the computation. This is similar to the case described in the last section where the whole correlation matrix degenerates into a scalar.

By placing another group of perfect correlation circles around the tiles with minimal nominal thickness values, a similar method can be used to evaluate the probability Y_{min} that all locations fall above the LSL.

To summarize the above yield model and associated algorithm a flow chart for Y_{max} calculation is plotted in Figure 7.13. A similar chart can be plotted for Y_{min} . The overall yield is then calculated by Equation 7.22.

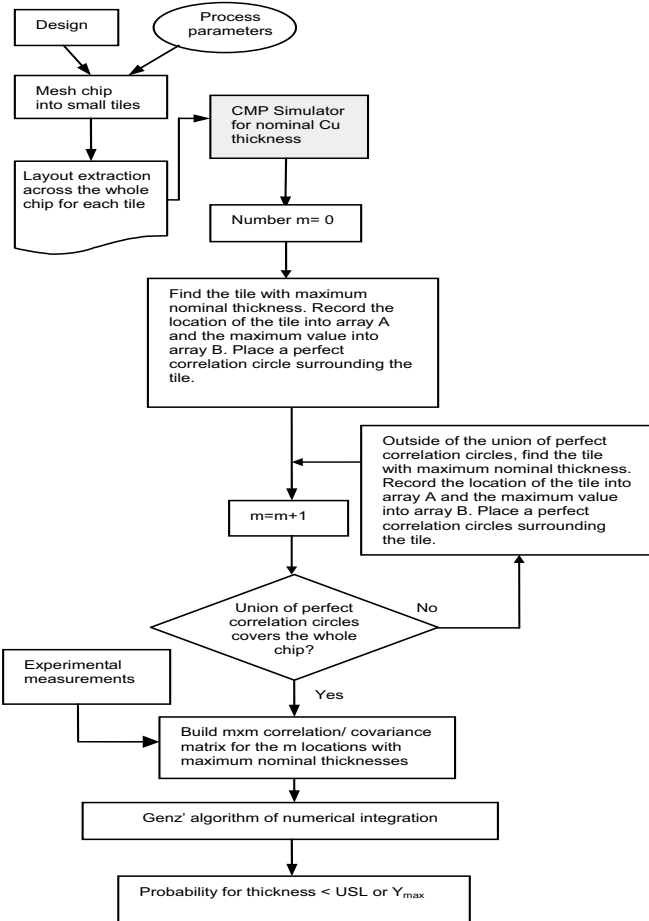


Figure 7.13. Flow Chart for Y_{max} Calculation

Using the proposed algorithm, the order of integration is much smaller. However, a typical integration order after the reduction is still in the range of several hundreds depending on the chip size and how quick the correlation drops with distance. In such a situation a direct numerical integration is still not feasible. A numerical algorithm in next subsection proposed by Genz is used to solve this problem.

7.7.1.3 Genz’s Algorithm for Multi-Dimensional Numerical Integration

The key of Ganz’s algorithm involves three transformations of the correlation matrix which is \sum_{max} after order reduction. They are described briefly below. For a detailed explanation the reader is referred to [128].

Transformation 1:

Because the covariance matrix is symmetric and positive definite it can be decomposed into two triangular matrices through Cholesky decomposition:

$$\sum = CC^T \tag{7.23}$$

where C is a lower triangular matrix and C^T is an upper triangular matrix. Let $p-\mu = Cy$, there is $dp = dp_1 dp_2 \dots dp_n = |C| dy = |C| dy_1 dy_2 \dots dy_n$ and

$$L-\mu \leq Cy \leq U-\mu \tag{7.24}$$

where y is a n -dimensional vector, y_1, y_2, \dots, y_n are the n components of the vector y , $L = (L, L, \dots, L)$ a n -dimensional vector representing the lower specification limit and $U = (U, U, \dots, U)$ a n -dimensional vector representing the upper specification limit.

For each component y_i in vector y , Equation 7.24 can be further written as

$$\frac{L - \mu_i - \sum_{j=1}^{i-1} (C_{ij}y_j)}{C_{ii}} \leq y_i \leq \frac{U - \mu_i - \sum_{j=1}^{i-1} (C_{ij}y_j)}{C_{ii}} \tag{7.25}$$

Note that C is an upper triangular matrix. Thus only y_m ($m < i$) determine y_i ’s upper limit and bottom limit. This property is critical for transformations 2 and 3.

Substitution of Equations 7.23- 7.24 into Equation 7.19 yields:

$$Y = \frac{1}{\sqrt{(2\pi)^n}} \int_{L'_1}^{U'_1} e^{-\frac{y_1^2}{2}} \dots \int_{L'_i}^{U'_i} e^{-\frac{y_i^2}{2}} \dots \int_{L'_n}^{U'_n} e^{-\frac{y_n^2}{2}} dy_n dy_{n-1} \dots dy_1 \tag{7.26}$$

where $L'_i(y_1, y_2, \dots, y_{i-1}) = \frac{L-\mu_i - \sum_{j=1}^{i-1} (C_{ij}y_j)}{C_{ii}}$

and $U_i'(y_1, y_2, \dots, y_{i-1}) = \frac{U - \mu_i - \sum_{j=1}^{i-1} (C_{ij}y_j)}{C_{ii}}$.

Transformation 2:

Let

$$Z_i = \Phi(y_i) = \frac{1}{\sqrt{2\pi}} \int_{-\infty}^{y_i} e^{-\frac{1}{2}x^2} dx \tag{7.27}$$

which is the standard univariate normal distribution function. Then Equation 7.26 can be further written as

$$Y = \int_{L_1''}^{U_1''} \dots \int_{L_i''(z_1, z_2, \dots, z_{i-1})}^{U_i''(z_1, z_2, \dots, z_{i-1})} \dots \int_{L_n''(z_1, z_2, \dots, z_{n-1})}^{U_n''(z_1, z_2, \dots, z_{n-1})} dz_n dz_{n-1} \dots dz_1 \tag{7.28}$$

where

$$U_i''(z_1, z_2, \dots, z_{i-1}) = \Phi\left(U - \mu_i - \sum_{j=1}^{i-1} C_{ij}\Phi^{-1}(z_j) \right) / C_{ii}$$

$$\text{and } L_i''(z_1, z_2, \dots, z_{i-1}) = \Phi\left(L - \mu_i - \sum_{j=1}^{i-1} C_{ij}\Phi^{-1}(z_j) \right) / C_{ii}.$$

Transformation 3:

The final transformation is to let

$$z_i = L_i'' + w_i(U_i'' - L_i''). \tag{7.29}$$

Equation 7.28 is written as

$$Y = \int_0^1 (U_1'' - L_1'') \int_0^1 (U_2'' - L_2'') \dots \int_0^1 (U_n'' - L_n'') dw_n dw_{n-1} \dots dw_1 \tag{7.30}$$

where $U_i'' = \Phi\left(U - \mu_i - \sum_{j=1}^{i-1} C_{ij}\Phi^{-1}\left(L_j'' + w_j(U_j'' - L_j'') \right) \right) / C_{ii}$

and $L_i'' = \Phi\left(L - \mu_i - \sum_{j=1}^{i-1} C_{ij}\Phi^{-1}\left(L_j'' + w_j(U_j'' - L_j'') \right) \right) / C_{ii}$.

Equation 7.30 can be evaluated by a variety of numerical integration algorithms. The advantage of the above transformations is that it forces a priority ordering on the integration variables. Among all integration variables in Equation 7.30 w_1 is the most important because all $(U_j'' - L_j'')$ depend on it while w_n is the least important. This priority ordering can make numerical integration methods such as subregion adaptive algorithm work more efficiently and save computation time [128]. A simple but effective Monte-Carlo algorithm

incorporating the transformations is proposed by Genz [128]. Besides Y , the algorithm can also output the numerical error estimate Err [128].

7.7.2 Simulation Examples

A Matlab program was written to implement the above algorithm. A chip (130nm technology) with size $4.8\text{mm} \times 7.5\text{mm}$ was used as an example to verify its efficiency. Metal layers 2-4 (M2-M4) were selected for our simulation. The USL, nominal value, and LSL of the copper thickness were set at 4580A, 3580A, and 2580A respectively, for all three layers. The standard deviation of the Cu thickness variation was $0.012\mu\text{m}$. The variance was $0.012 \times 0.012\mu\text{m}^2$. We assumed a linear reduction of correlation with distance and the function $y = -3 \times 10^{-5}x + 0.9958$ of Figure 7.11 was used.

We obtained the nominal Cu thickness variation from a CMP simulation tool, which meshes the chip into $10\mu\text{m} \times 10\mu\text{m}$ tiles. The nominal Cu thickness values in matrix (size= 480×750) form, the variances and the correlation function were then inputted into the Matlab program for yield prediction. The yield prediction was done on a SUN UltraSPARC-II machine (CPU: $4 \times 400\text{MHz}$, RAM: 4G).

Table 7.7 shows the yield prediction under different radii of ‘perfect correlation circles (PCC)’. It is seen that the yield prediction has converged at a radius of $1000\mu\text{m}$ for all three layers. This indicates that our algorithm works well from the convergence perspective. We tried several other chips and similar convergence at $1000\mu\text{m}$ was observed. The CPU time increased from 157 seconds at a radius of $1000\mu\text{m}$ to 1152 seconds at a radius of $350\mu\text{m}$ with no improvement in accuracy. Therefore, $1000\mu\text{m}$ can be chosen as the radius of ‘perfect correlation circles’ for both efficient and accurate yield prediction. Moreover,

Table 7.7. Yield Prediction under Different Radii of ‘Perfect Correlation Circles (PCC)’

PCC Radius (μm)	Yield (%)			Integration Order (Ymax / Ymin)			CPU Time (sec.)
	M2	M3	M4	M2	M3	M4	M2
10000	95.1	47.0	95.1	1/1	1/1	1/1	12
5000	94.3	43.8	95.1	2/2	2/2	2/2	19
4000	94.3	41.4	95.1	4/2	4/3	3/2	25
3000	94.3	39.8	94.9	5/6	5/5	5/2	39
2000	94.3	39.2	94.4	7/8	10/9	9/11	50
1000	94.3	36.7	93.9	26/29	28/23	28/30	157
800	94.3	36.7	93.9	41/35	44/38	41/42	214
600	94.2	35.2	93.8	62/71	72/63	66/68	369
500	94.2	34.1	93.7	90/107	106/89	83/99	551
350	94.2	34.1	93.6	193/204	205/193	195/201	1152

the simulation data implies that for different designs using the same fabrication process, the same optimal radius of ‘perfect correlation circle’ can be used for yield predictions.

Note that the numerical error Err increases with the order of the numerical integration (or the decrease of the radius of the ‘perfect correlation circles’ and the increase of the number of ‘perfect correlation circles’ covering the chip). However, no error larger than 0.8% was observed in our experiments.

M3 shows significantly lower yield than M2 and M4. A detailed study of the nominal thickness values of the three layers shows that it is because the minimal nominal thickness values on M3 are closer to LSL.

To further study how the yield changes with the correlation function, we assumed a correlation-distance function $y = -7 \times 10^{-5}x + 1$ and re-ran the yield prediction. Data in Table 7.8 shows that the yield prediction converges at a smaller radius of ‘perfect correlation circles’. In addition, the yield under the new correlation function is lower. The lower correlations of the random variations between intra-die locations contribute to the lower yields.

7.7.3 Recap and some conclusions

The above simulation shows that the intra-die systematic variation and the spatial correlation of random variations affect yield simultaneously. The intra-die systematic variation is primarily determined by the design layout. The random variation and its spatial correlation are determined by the manufacturing variability (fluctuation). Traditionally reducing peak-peak intra-die systematic variations, for example, the nominal thickness variation in CMP [130], is the sole objective of various layout design optimization algorithms. This methodology, without considering the random variations and their spatial correlation,

Table 7.8. Yield Prediction for a Quicker Decrease of the Spatial Correlation

PCC Radius (μm)	Yield (%)			Integration Order (Ymax /Ymin)			CPU Time (sec.)
	M2	M3	M4	M2	M3	M4	M2
10000	95.1	47.0	95.1	1/1	1/1	1/1	12
5000	93.5	39.4	95.0	2/2	2/2	2/2	19
4000	93.5	33.4	94.9	4/2	4/3	3/2	25
3000	93.5	30.3	94.5	5/6	5/5	5/2	43
2000	93.4	28.1	93.4	7/8	10/9	9/11	55
1000	93.4	24.0	92.3	26/29	28/23	28/30	155
800	93.4	21.9	92.2	41/35	44/38	41/42	223
600	93.4	19.7	92.1	62/71	72/63	66/68	381
500	93.4	18.9	92.1	90/107	106/89	83/99	565
350	93.4	18.6	91.2	193/204	205/193	195/201	1171

may not be sufficient. One example: Two chips have the same peak-peak range of systematic variations, one has one single peak, the other have more than one peak and the peaks are far away from each other. The yield for the chip with more peaks should be lower than the yield of the chip with one peak only considering the low correlation between the random variations at the peaks. Thus a dummy filling algorithm which trades off the peak-peak range and the number of peaks may be needed. The model in this section sheds some light on such an algorithm.

Note that the above model does not consider the lot-lot, wafer-wafer, and die-die systematic variations. These variations can be incorporated into the model easily. It is an area well developed in the literature as it is the classical area of yield since the early development of the IC industry. Also, the yield model and associated algorithm proposed here may be extended to other processes such as the lithography process, and plasma etch process. The reader is strongly encouraged to develop such algorithms as an exercise.

7.7.4 Summary and Conclusions

7.7.4.1 Variability Summary & Conclusions

It is a forgone conclusion that with continued scaling lithography induced intra-die variations are growing in significance to the point where they are dominant. Of the device parameters variability in I_{off} and in V_{th} is most pronounced; T_{ox} and LER are also affected but to a lesser degree. Statistical analysis of experimental data [103] indicates that there is a 30% intra-die variation of I_{on} in the 3σ variation of that parameter. Intra-die variations are both random and systematic. It is important to determine the systematic part of variability which can be mitigated to a certain degree most of the time. There is not much that can be done to impact the random part of variation but there are ways to design around that random variation using statistical approaches was discussed briefly in Chapter 6.

7.7.4.2 Yield Summary and conclusions

For yield the path is clear. It is the dominance of systematic yield loss over random yield loss with every scaling step. However, there is a lot that can be done to improve the systematic yield especially in the areas of lithography and design style. Within the lithography space there are steps we discussed at length in Chapter 3 related to lenses, illumination polarization, mask phase-shift techniques, etc. Also, within the design (physical design here) we covered RET techniques, model based metal fills, wire spreading, via doubling. Finally, while applying statistical design methodologies cannot impact intra-die variability it can mitigate the negative impact of this variation by picking design “focal points” that optimize a design’s yield given the inevitability of intra-die variability.

Chapter 8

CONCLUSIONS

8.1 The Case for a DFM/DFY Driven Design

We have established early on in this book that worrying about yield is not a FAB-only concern any more, and that manufacturability and yield driven design is a collective responsibility that starts with the designer and that should (and is) be addressed by the EDA tools at every step of the design. For the designer yield is not any more an area minimization or performance optimization game but is about getting the design to work and to yield in the first place to meet the time to market window and to alleviate the ever increasing engineering and tooling costs, and for the IDM and FAB it is getting the design to yield in a consistent manner over the life cycle of the design taking into consideration the systematic and the random variability of the process parameters that reduces yield significantly over the ever narrowing product life window.

In Figure 5.15 of Chapter 5 we showed the relative breakdown of yield as a function of technology node and showed that with every node further down the nano-scale of CMOS systematic yield loss as a function of total yield loss accounts for a bigger percent of the total yield loss. Figure 8.1 is an extensive, and almost exhaustive top-down categorization of manufacturability steps that collectively impact yield. Each and every single one of them can be a show-stopper by itself and, each includes several sub-steps that need to be understood, modeled, and addressed by the proper EDA tools. As can be seen from Figure 8.1 random defects concerns, while still there, are a small subset of the overall manufacturability and yield derailing factors. It also shows the need to integrate physics both in terms of new materials (example: etch and CMP) and in terms of atomistic understanding of phenomena (example: stress, EM) with EDA simulation tools (litho and CMP models) and with enhanced manufacturing tools (higher lens NA, steppers, etc) in order for the 45nm and

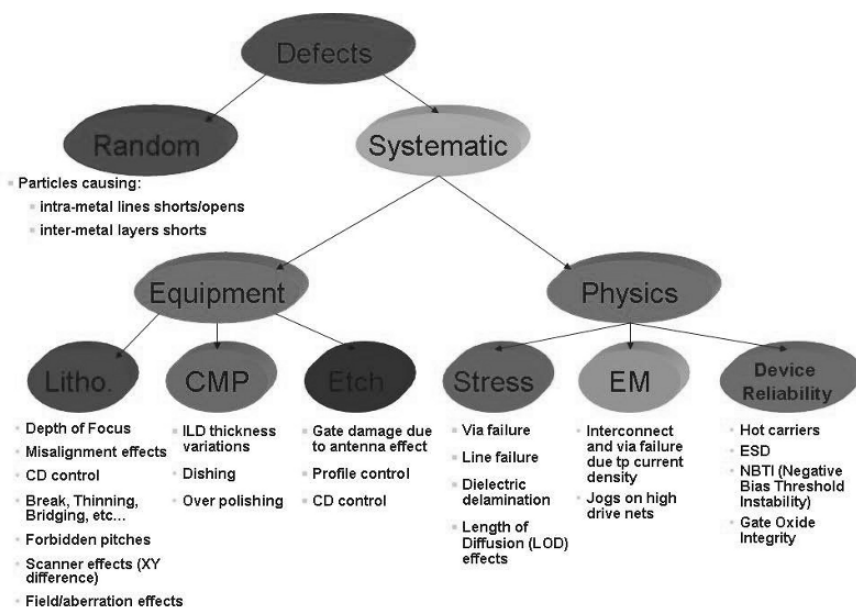


Figure 8.1. A Top-down View of Manufacturability and Yield Derailing Factors

beyond CMOS designs to happen. Also, in this Chapter we will touch in a summary and conclusion format on most of these categories for the sake of integrating them together towards a DFM/DFY driven design flow.

8.2 Design Intent Manufacturing (Lithography) Centric DFM

A design centric view of DFM starts with the stated goal of having the final printed and fully processed feature as close as possible to the intended design. In other words it is the lithography steps that are stressed here in terms of what needs to be done at every step of the design flow and mask making in light of the knowledge of the lithography effects associated with every step of the process flow.

However, it is important in the context of design intent to differentiate between the very costly and impractical attempt at trying to bring the final printed image as close as possible to the digitized image and between focusing at preserving the design intent in terms of performance and yield only.

A good example of that is model driven OPC. Figure 8.2 shows three alternatives to applying OPC, a full-menu OPC will result with a final image of highest integrity, but is costly in terms of area, computing, and storage associated with digitizing, fracturing, and financially in terms of mask cost. The just-enough OPC is a happy medium where the performance of the constructed

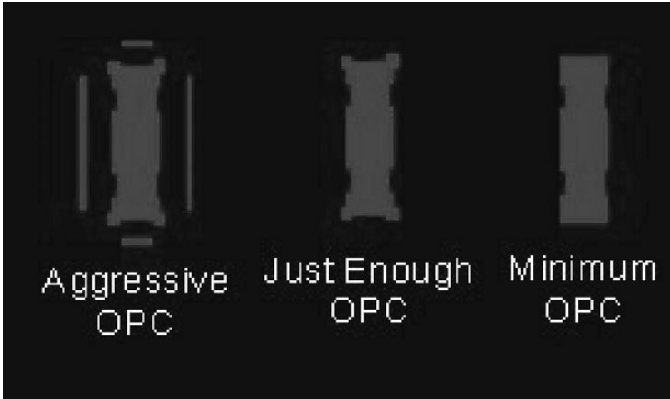


Figure 8.2. OPC Alternatives for a Digitized Geometry

device is almost fully preserved but a significant amount of area, cost, and effort is saved in the process, and finally a minimum OPC reflects a manufacturable and functional (and thus yielding) device where some acceptable “hit” is taken in performance and most definitely in artifacts such as end of line extension and poly gate over field, shapes that do not directly impact performance but could slightly impact yield.

8.3 Yield Centric DFM

A yield centric view of DFM has to start with ensuring manufacturability of a design in the first place but branches further to include design changes, lithography and process variations to improve yield. The list of actions that fit that description literally spans every point of every category shown in Figure 8.1. they will be enumerated and covered in Section 8.4. What is important to stress at this point is whether one looks at a design from a design intent centric point of view or a yield centric one (or both) one quickly finds that the design flow is a full-circle feedback loop encompassing the classical top down design flow with the yield and manufacturability driven bottoms-up approach and that all steps of the design flow influence each other and influence the overall yield and manufacturability of a design. Thus our assertion that there is a “collective” ownership by all participants of the design flow of all the manufacturability and yield issues.

8.4 DFM/DFY EDA Design Tools

Figure 8.3 is an EDA driven design flow that takes into account manufacturability and yield. In this flow we see the interaction of the classical top-down design flow with TCAD tools and with input from FABs test chips (DFM infrastructure) in coming up with DFM models capable of capturing beyond design

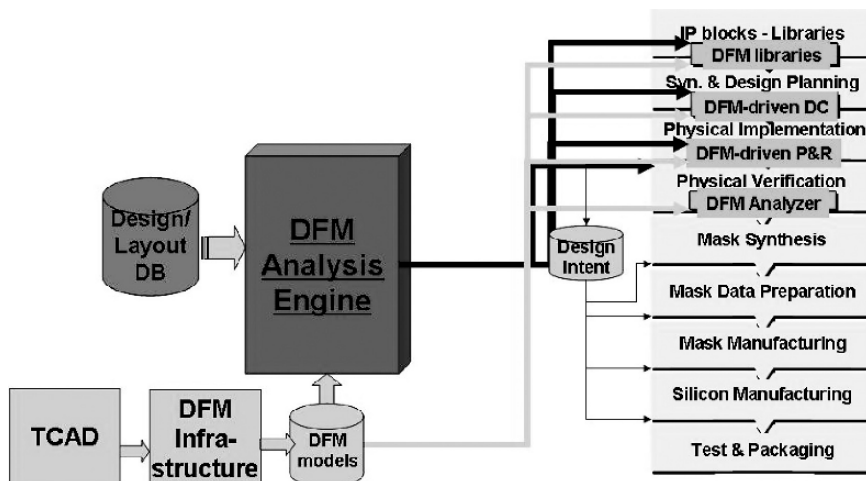


Figure 8.3. An EDA DFM/DFY Centric Design Flow

rules the nature of interaction of various processing steps with the design. Also, a major component of this flow is the DFM/DFY analysis engine that combines the three components of design intent, tools capabilities, and DFM models to optimize any particular design step for manufacturability and yield. Two points worth mentioning regarding Figure 8.3: every where DFM is mentioned it is automatically understood as DFM/DFY. The second point is that although there are many steps we covered in the area of mask synthesis, preparation, and inspection for the purposes of economics and practicality notice that no mention of DFM is tagged to the step in the design flow not due to any lack of significance but because by then all the significant manufacturability and yield implementation and optimization are complete.

In this Section we will be going over a summary of the areas of the design flow that are addressed by state of the art EDA tools and the steps done in each area and its significance to manufacturability and yield. The areas covered are:

- Implementation
- Physical Verification
- Mask Synthesis
- Mask Inspection
- TCAD

We will not be covering certain areas such as testability and packaging not due to any lack of importance but due to the fact that progress there has been

more evolutionary than disruptive and that the techniques while getting more elaborate and sophisticated all the time are beyond the realm of this book.

8.4.1 Implementation

8.4.1.1 Physical Library Design

Physical library design is the first step towards building a robust manufacturable and yielding design. There are several aspects to physical library design beyond the classical power, area, and speed. The additional features are mainly (but not limited to):

Critical Area Sensitivity. Critical area optimization is very straight forward. One has to take into account the over all critical area of opens and short and with that the overall impact on the cell area.

OPC Friendly Layout. An OPC friendly layout takes into account avoiding forbidden pitches by having uniform spacing (of poly for example) and by taking into consideration neighboring cells (including rotation, flipping, and mirror imaging) and what will that imply for OPC of the cell and of the block.

Performance Aware Layout. Here we are really getting into a TCAD related area where simulations can show a degradation of mobility as a function of gate spacing from active edge (STI), and mobility degradation as a function of gate stacking due to the stress profile. Obviously, if one is to take care of such considerations (say by avoiding S/D sharing for critical drivers) then that will come at a cost in area but nonetheless performance optimization is an option when needed.

Fracture Friendly Layout. Figure 8.4 is a simple example of what we refer to as fracture friendly layout. The more corners there are, the more “shots” that need to be written on a mask to represent the layout and the higher is the probability of a manufacturing error.

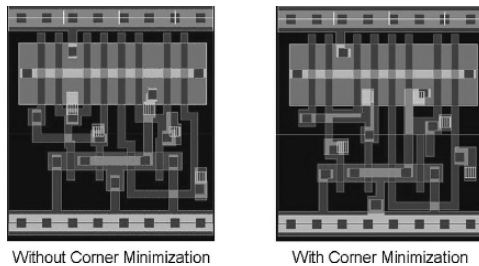


Figure 8.4. An Example of a DFM Optimized Cell Form

The bottom line is designing libraries with manufacturability and yield in mind. More on that in Section 8.4.2.

8.4.1.2 Synthesis

The most common (and easiest) type of library cell grading for yield is CA grading since there are many algorithms for doing that and since evaluating the accuracy of CA yield grading by the use of test chips is straight forward. As a result different versions of a given cell can be present in a library where in addition to the traditional arcs of area, delay, and power is the new arc of yield as a metric.

Figure 8.5 is an example of a cell with the arcs normalized for the “standard” automated layout of the cell. Other versions of the cell will be graded according to the normalized reference and the synthesis tool can optimize the design within a slack budget for any or all of the defined arcs. Synthesis tools capable of accommodating yield as an added arc are common place today.

8.4.1.3 Design Planning, Place and Route

The placement and routing stage is another area where several manufacturability and yield enhancement actions can be done and are currently automatically embedded in the most advanced placement and routing tools.

Boundary OPC Compliance During Placement. There is not much to be done at the placement stage other than checking that block to block interaction will not result in geometries that cannot be opc'd or that result in the presence of forbidden pitches for SRAF placements.

OPC Compliance During Routing. Figure 8.6 is an example of a typical routing jog that take place during routing. Such a jog is usually checked against built-in DRC rules but is additionally checked against OPC requirements to make sure it will not result in an un-opc'iable geometry. More on that in the LRC check.

Cell	ANF	delay	power	area	yield
lib1	1	1	1	1	1
lib2	0.98	1.1	0.9	1.1	1.05
lib2	0.99	1.08	.89	1.12	1.07
....					
lib4	4	.98	1.28	1.15	0.65

Figure 8.5. Table of Alternative Implementations of a Cell with Arcs

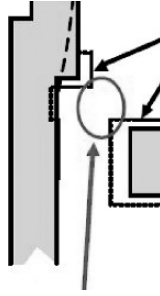


Figure 8.6. OPC Applicability Checking During Routing

Wire-spreading. Wire spreading as shown in Figure 8.7 is the most obvious way of improving CA shorts yield. However, there are two main caveats. It cannot be done at the expense of worsening the open CA number, also, if wire spreading includes making “U” jogs then that has to be evaluated in terms of OPC and corner aspects.

Wire-widening. The process of wire widening improves the open CA yield number, again, as long as it is not done at the expense of the shorts CA number. One word of caution though is that there are parasitic implications associated with higher area capacitance (but partially offset by lower resistance) and higher coupling capacitance if close to other wires which then becomes significant for performance. The bottom line is that no optimization step should be done without worrying about the potential adverse consequences.

Smart Metal Fill. Layer density rules with minimum and maximum bounds are not sufficient for good planarization at 65nm and beyond. Also, “dummy fills” in the form of blindly filling voids to meet density requirements results in too many edges to digitize, fracture, and write. Furthermore, the results obtained are sub-optimal. Figure 8.8 illustrates the concept of using metal fills to minimize the variability in ILD thickness, thus improve metal (and ILD) planarity as a stack of metal layers is progressively accumulated.



Figure 8.7. Wire Spreading

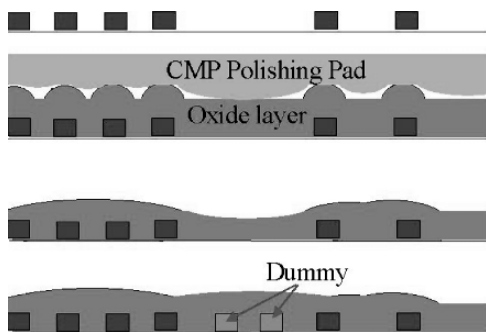


Figure 8.8. Smart Metal Fill to Minimize Local ILD and Metal Thickness Variation

A smart metal fill uses an optimization algorithm that takes the physics of the CMP process into account to minimize the local (more important than across die) variability of ILD. Also, an added benefit most of the time is less geometries to deal with as a smart metal fill usually achieves the objective at a lower layer density than rule driven metal fills.

Via-doubling. Opportunistic via doubling seems like a no-brainer choice in improving open via related yield if space is available. However, sometimes space (at the cost of added area) must be added and double vias is a requirement for certain critical nodes. Also, where to contact two layers of metals makes the difference between the applicability of the multi-vias or not as seen in Figure 8.9. Another aspect associated with via doubling (or multiple vias) is better printability given the problems we discussed in earlier chapters in printing isolated features.

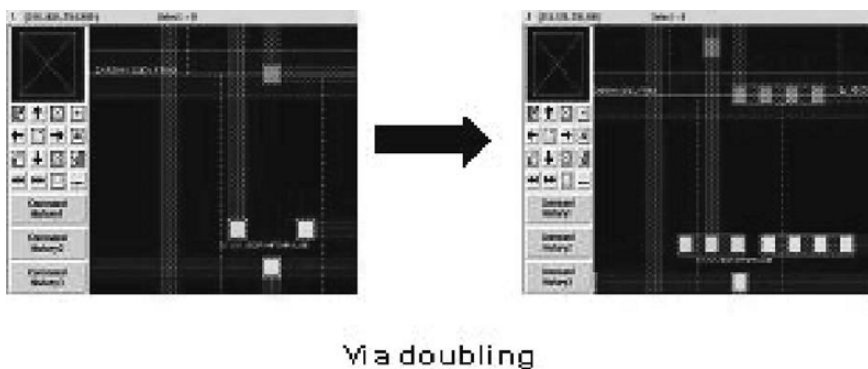


Figure 8.9. Illustration of Via Doubling

8.4.2 Physical Verification

Physical verification is one area of growing complexity and importance. The concept of design rule check is as old as the IC design flow, but with rule based DRC failing to account for all potential problems other techniques such as LRC based on pattern matching are increasingly implemented.

8.4.2.1 Design Rule Checking (DRC)

Rule based design rule checking is still performed as a first step in guaranteeing physical layout integrity but is by no means sufficient as a proof of manufacturability. Furthermore, there are plenty of rules that are classified as “recommended rules” and implementing all these rules as well will be a waste of area. A selective application of these recommended rules through the application of manufacturability models is part of what will be addressed in Section 8.4.3.

8.4.2.2 Lithography Rule Checking

Classical DRC falls short of accounting for OPC alterations to a layout and the feasibility of such alterations. One could try to capture such effects by writing an extensive set of conditional rules into a DRC deck. There are two problems with this approach. The first and minor one is the complexity of such effort. The bigger problem lies in all the false positives that such an algorithm flags resulting in endless hours of wasted engineering time.

An alternate solution that is currently being used and that is being expanded further is the use of a “look up” library of prohibited patterns that are either very difficult to OPC or that will print poorly. Figure 8.10 shows two examples of such patterns. Each pattern will be associated with a range of width and spacing of the geometries that will generate problems in order to assign a sensitivity measure as a function of this width and spacing. A further step that is now a

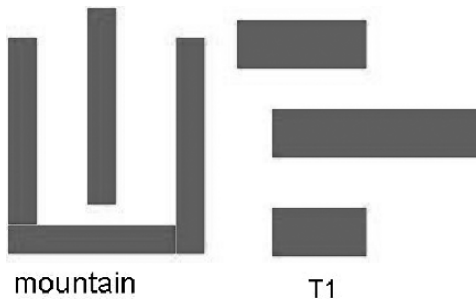


Figure 8.10. An Example of Prohibited Patterns

hot research area is algorithms that can predict such patterns in the first place based on printability simulations.

8.4.3 Mask Synthesis

There are several realities associated with nano-CMOS mask sets. These realities are progressing complexity and cost with every node and the fact that obtaining a defect free mask is a very difficult and costly proposition. Mask cost is a function of write time which is itself a function of the number of “shots” to be written, a number associated with the number of fractured geometries to be captured and the granularity of the technology. A lot of progress has been made in the field of parallel processing of masks, but that only shorten the duration of the write time of an individual mask but not the complexity or the total cost. Also, given the cost structure of the mask making it is obvious that various techniques are implemented at every step of mask preparation to minimize the number of shots to be written as long as the design intent is not compromised. Finally EDA tools that simulate the final image of the mask on silicon and comparing it to the design intent and, that can simulate the effect of mask faults on the final print to determine if a mask fault can be tolerated or not are proliferating.

8.4.3.1 Optical Proximity Correction Techniques

We covered at length the OPC aspects of general RET techniques to enhance the printability of a feature. The need of OPC stems from the fact that we are using a light source ArF with a $\lambda = 193$ nm to print features that are progressively less than half the wavelength of the light source. Model based OPC, the more mature form of OPC is the result of aerial simulations that will simulate the effect of added artifacts in the form of modified geometries or of scatter bars (SRAFS) on the final produced image using a lithography model. OPC for critical layers (such as poly gates) was needed at 90nm technology, but with every node the number of layers needing OPC increased, and the extent of OPC needed increased as well. ArF will still be the illumination source at 45nm (less than a quarter wavelength) and that explains the need for heavy use of OPC. However, given what we mentioned earlier about mask costs as a function of the number of shots needed to write a mask “smart” OPC, also referred to as “just enough OPC” is used based on EDA tools that simulate the whole lithography flow under a design intent constraints file to determine which OPC operation is a must and which one can be skipped without hurting either yield or performance.

8.4.3.2 Phase Resolution Enhancement Techniques

Beyond the 45 nm node the critical dimension of the features to be printed is smaller than a quarter wavelength and OPC procedures alone are not sufficient

to ensure printability. Manipulating the phase of the incident illumination by altering the thickness of the mask coating is needed to create an interference pattern where we make use of the phase cancellation of the wave portions below the energy threshold of the resist to print sharp features that are at or smaller than a quarter wavelength. In chapter 3 we discussed several flavors of phase alteration from full (180°) phase shift to attenuated varieties of phase shift. Also, we discussed the illumination options associated with each type such as off axis illumination.

Again in the process of assigning alternating phases to adjacent geometries the designer is faced with phase conflicts that need to be resolved. We covered phase resolution algorithms dedicated to that purpose.

8.4.3.3 Data Fracturing and Mask Preparation

Fig 11 is a basic illustration of a digitized layout that has been fully OPC'ed and then fractured in preparation for mask writing.

The Figure 8.11 clearly illustrates the need for selective OPC to avoid having the number of fragmented shots that need to be written on a mask grow out of control. Again EDA tools use extended lithography models to simulate silicon printout for various OPC alternatives. A way of identifying what is critical to performance (example gate thinning) is needed to ensure that full OPC is applied to such sections. The rest of the geometries are OPC'ed to the minimum needed to ensure printability and yield.

8.4.4 Mask Inspection

Figure 8.12 shows a typical flow for mask data inspection before writing (and after fracturing) the real mask. The process of fracturing does produce minor differences from the digitized and OPC'ed layout and thus need to be XOR'd against the original GDSII (after OPC) and the differences simulated based on lithography models to determine if the differences are of any significance. Such differences are then either waived as irrelevant or fixed. Then mask writing takes place usually using an e-beam machine. Write time is a direct function of the

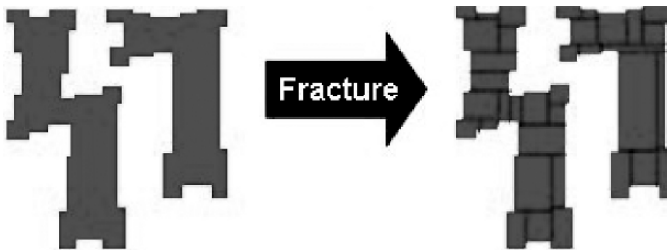


Figure 8.11. Data Fracturing

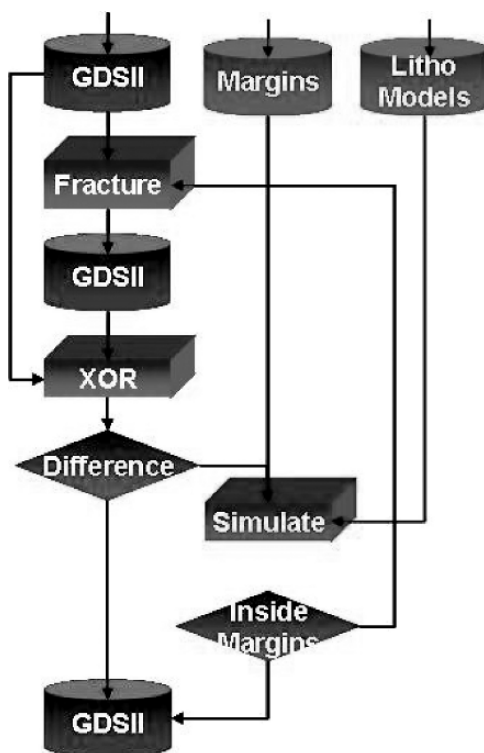


Figure 8.12. Mask Inspection Flow

number of shots to be written which is a direct one to one translation of the number of fractured polygons.

8.4.4.1 Mask defect simulation & repair

A similar flow to Figure 8.12 is also used for comparing the images on the written mask to the ones intended to be written. As pointed out in several locations an error free mask is very expensive if not also next to impossible. Therefore a lithography-model based simulation is performed on the mask errors to determine if the error when printed on silicon is:

- (I) Irrelevant and thus can be ignored and waived.
- (II) Cannot be ignored as it has functionality or yield significance but can be repaired.
- (III) Fatal fault → Mask needs to be scrapped and a new mask written.

8.4.5 TCAD

TCAD has always been at the forefront of the manufacturing process in the classical role of process and device development. However, with all the exotic techniques currently used such as strained silicon engineering and with the 3-D quantum mechanical nature of interactions at the device level TCAD has emerged to the forefront of DFM and DFY tools in terms of ramping up yield and in terms of identifying geometric and layout dependencies of various parameters for pointing out variability in performance and potential hot spots for manufacturing.

8.4.6 Process Modeling and Simulation

TCAD classical process simulation focuses on the front end process steps. It models manufacturing steps such as implantation, diffusion, oxidation, etching, and various types of depositions, as well as lithography. Certain aspects of modeling such as ion implantation, dopants diffusion, and oxidation are quite predictable and relatively easy to generate accurate models for. Other aspects such as deposition, etching, and CMP are three-dimensional and are modeled geometrically. They are more complex and less predictable.

8.4.6.1 Device Simulation

The next classical area of TCAD simulation is modeling device behavior. TCAD device modeling involves the modeling of the electrical, mechanical, and magnetic behavior of devices built on process models such as the ones described in the Section 8.4.5. Device models include static, small signal, large signal, and noise as well as modeling time dependent dynamic behavior.

With the advent and proliferation of 3-D devices (FinFETS, etc) a combination of process modeling capabilities and device modeling capabilities opens the door for powerful “what if” capabilities by TCAD tools based on disturbing one parameter in a particular process model and see the impact it has on the corresponding device. This allows special tuning of alternatives such as V_t , leakage, etc.

8.4.6.2 Physical Layout links (stress & hotspots)

One area of utmost importance in the design cycle that TCAD is particularly suited for is the link to manufacturability aspects including OPC and physical layout. With techniques such as stressed silicon TCAD tools are invaluable for evaluating layout dependencies of parameters such as V_t and mobility and in providing real time feedback to the designer.

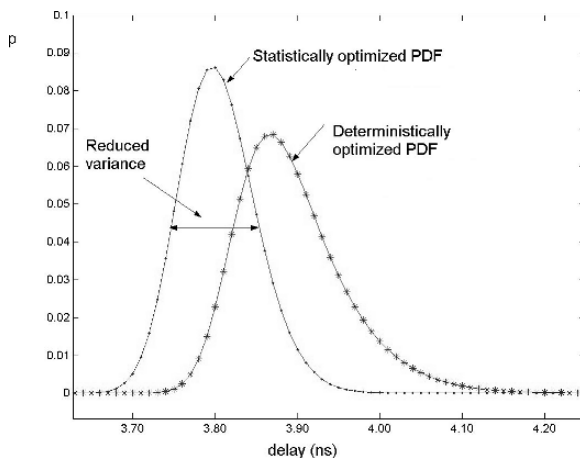


Figure 8.13. Statistical vs Deterministic Design Delay Slack

8.5 Design Variability

Parametric variability whether random or systematic is going to increase with every new technology node as long as we continue to push the envelop of Moore's law with existing lithography procedures. We have a tough combination of higher performance translating to smaller clock periods and higher variability translating to wider percentage of variation for each parameter.

Needless to say this translates to a paradigm shift in design methodology from the three-corner guard-banded design to a statistical design methodology where we start by characterizing the libraries using statistical spice models and where the delay and power arcs are themselves distribution functions.

Statistical design allows us to select optimal combinations of design and process parameters and by doing that shift the yield distribution inwards as shown in Figure 8.13 and thus reduce the unacceptable yield loss associated with over sensitivity to one design parameter or by guard-banding of the three-corner design model.

8.6 Closing Remarks

There are indeed mounting challenges as we go from the current state of the art technology of 45 - 32 nm to whatever the practical limits for CMOS scaling are (experimentally 6nm devices clocked at over 2.5 Tera Hz were demonstrated), And, most likely a EUV (extreme ultra-violet, $\lambda = 13$ nm) lithography or some other alternative to optical lithography will be used to commercially reach there; but there are also unlimited opportunities when one considers the possibilities of what can be achieved. What is more fascinating in considering the future possibilities is not the degree of scaling but the applications

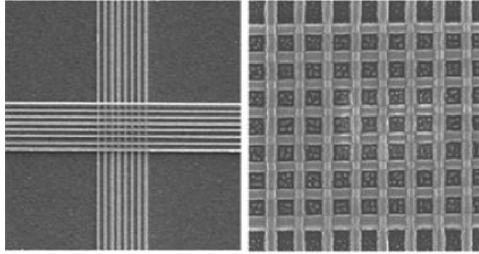


Figure 8.14. Cross-bar Molecular Memory

and the level of functional integration associated with that, made possible by that scaling.

Few thoughts we ponder is the integration of the bottoms up nano-technology with the classical top-down CMOS design flow. Cross-bar molecular memories developed using imprint lithography are thought to be 5 years away from being integrated into CMOS (Figure 8.14). Single walled carbon nanotubes (SCNT) as vias and carbon ribbon transistors (Figure 8.15) are candidates for sub 10 nm devices, nano-fluidic valves (Figure 8.16)), and DNA cavities for bio-medical applications are but a few of such possibilities. They are not far fetched. In fact most are already happening today but not wide spread or at economies of scale levels. Polymer based self-assembly techniques could find their way into integration with CMOS processes for interconnect insulation and other applications. Again the commercial applications for some of those exotic technologies are perhaps five to ten years from wide use, others will simply fade away against better alternatives.

Another integration that has been long in the making that is taking place today is the integration of MEMS (Micro Electro-Mechanical Systems) and



Figure 8.15. Carbon Nano-tube Transistor [pfq]

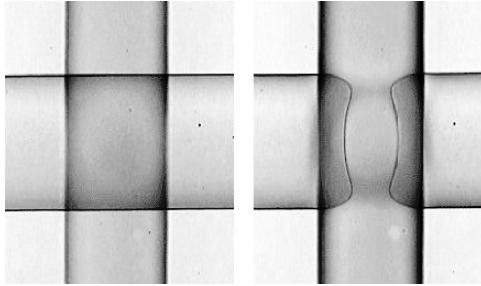


Figure 8.16. Nano-fluidic Valve [xyz]

NEMS (Nano Electro-Mechanical Systems) with standard CMOS processes. The EDA tools needed to make the integration processes seamless are still in their early stages mainly due to the economies of development cost. However, the spread of MEMS sensors and actuators in every day live applications is making this integration happen at a faster pace.

Where does that leave DFM/DFY? more important and critical than ever before. With that level of integration system cost and complexity will be more critical, and very small increments of yield will translate to the difference between failure and success.

References

- [1] T. H. Park, *Characterization and Modeling of Pattern Dependencies in Copper Interconnects for Integrated Circuits*, Ph.D. thesis, Dept. of EECS, MIT, Cambridge, MA, USA, 2002.
- [2] J. Reid, S. Mayer, E. Broadbent, E. Klawuhn, and K. Ashtiani, “Factors influencing damascene feature fill using copper pvd and electroplating,” *Solid State Technology*, July 2000.
- [3] A. Agarwal, D. Blaauw, V. Zolotov, and S. Vruthula, “Statistical timing analysis using bounds,” in *Proc. DATE: Design Automation and Test in Europe*, Feb. 2003, pp. 62–67.
- [4] A. Agarwal, V. Zoloto, and D. Blaauw, “Statistical timing analysis using bounds and selective enumeration,” in *IEEE Transactions on Computer-Aided Design of Integrated Circuits*, Sept. 2003, vol. 22, pp. 1243–1260.
- [5] M. Myazaki and et al., “A 1.2 gips/w uprocessor using speed adaptive vt cmos with forward bias,” *IEEE Journal of Solid-State Circuits*, Feb. 2002.
- [6] T. E. Gbondo-Tugbawa, *Chip-scale Modeling of Pattern Dependencies in Copper Chemical Mechanical Polishing Processes*, Ph.D. thesis, Dept. of EECS, MIT, Cambridge, MA, USA, 2002.
- [7] D. Anderson, *Design for Manufacturability & Concurrent Engineering*, CIM, 2003.
- [8] J. Kawa, C. Chiang, and R. Camposano, “Eda challenges in nano-scale technology,” in *Proc. Custom Integrated Circuits Conf.*, 2006.
- [9] W. Kuo and T. Kim, “An overview of manufacturing yield and reliability modeling for semiconductor products,” *proceedings of IEEE*, vol. 87, no. 8, pp. 1329–1344, 1999.
- [10] J. Cunningham, “the use and evaluation of yield models in integrated circuit manufacturing,” *IEEE Transaction on Semiconductor Manufacturing*, vol. 3, no. 2, pp. 61–70, 1990.
- [11] W. Maly, H. Heineken, J. Khare, and P.K. Nag, “Design for manufacturability in submicron domain,” in *Proc. Intl. Conf. on Computer-Aided Design*, 1996.

- [12] Y. Fei, P. Simon, and W. Maly, "New yield models for DSM manufacturing," in *Proc. of IEEE Electron Devices Meeting*, 2000.
- [13] D. M. H. Walker, "Critical area analysis," in *4th International Conference on Wafer Scale Integration*, 1992.
- [14] A. V. Ferris-Prabhu, "Modeling the critical area in yield forecasts," *IEEE Journal of Solid-State Circuits*, vol. SC-20, no. 4, pp. 874–878, 1985.
- [15] A. V. Ferris-Prabhu, "Defect size variations and their effect on the critical area of VLSI devices," *IEEE Journal of Solid-State Circuits*, vol. SC-20, no. 4, pp. 878–880, 1985.
- [16] I. Bubel, W. Maly, T. Waas, P. K. Nag, H. Hartmann, D. Schmitt-Landsiedel, and S. Griep, "AFFCCA: A tool for critical area analysis with circular defects and lithography deformed layout," in *IEEE International Workshop on Defect and Fault Tolerance in VLSI Systems*, 1995.
- [17] U. Lauther, "An $o(n \log n)$ algorithm for boolean mask operations," in *Proc. of the Design Automation Conf.*, 1981.
- [18] G. A. Allan and A. J. Walton, "Efficient extra material critical area algorithms," *IEEE Transactions on Computer-Aided Design of Integrated Circuits*, vol. 18, no. 10, pp. 1480–1486, 1999.
- [19] S. Fitzpatrick, G. O'Donoghue, and G. Cheek, "A comparison of critical area analysis tools," in *IEEE/SEMI advanced semiconductor manufacturing conference*, 1998.
- [20] G. A. Allan, "A comparison of efficient dot throwing and shape shifting extra material critical area estimation," in *Proc. of the IEEE Symposium on Defect and Fault Tolerance in VLSI Systems*, 1998.
- [21] P. K. Nag and W. Maly, "Hierarchical extraction of critical area for shorts in very large ICs," in *IEEE International Workshop on Defect and Fault Tolerance in VLSI Systems*, 1995.
- [22] W. A. Pleskacz, C. H. Ouyang, and W. Maly, "A DRC-based algorithm for extraction of critical areas for opens in large VLSI circuits," *IEEE Transactions on Computer-Aided Design of Integrated Circuits*, vol. 18, no. 2, pp. 151–162, 1999.
- [23] A. Dalal, P. Franzon, and M. Lorenzetti, "A layout-driven yield predictor and fault generator for VLSI," *IEEE Transaction on Semiconductor Manufacturing*, vol. 7, no. 1, pp. 77–82, 1993.
- [24] M. Chew and A. Strojwas, "Efficient circuit re-extraction for yield simulation application," in *Proc. Intl. Conf. on Computer-Aided Design*, 1987.
- [25] Y. Hamamura, K. Nemoto, T. Kumazawa, and H. Iwata, "Repair yield simulation with iterative critical area analysis for different types of failure," in *Proc. of the IEEE Symposium on Defect and Fault Tolerance in VLSI Systems*, 2002.
- [26] Q. Su, S. Sinha, and C. Chiang, "Fast calculation of average critical area for ic layouts," patent pending, Oct. 2004.
- [27] E. Huijbregts, H. Xue, and J. Jess, "Routing for reliable manufacturing," *IEEE Transaction on Semiconductor Manufacturing*, vol. 8, no. 2, pp. 188–194, 1995.

- [28] V. Chiluvuri and I. Koren, "Layout-synthesis techniques for yield enhancement," *IEEE Transaction on Semiconductor Manufacturing*, vol. 8, no. 2, pp. 178–187, 1995.
- [29] G. Allan, A. Walton, and R. Holwill, "An yield improvement technique for IC layout using local design rules," *IEEE Transactions on Computer-Aided Design of Integrated Circuits*, vol. 11, no. 11, pp. 1355–1362, 1992.
- [30] V. K.R. Chiluvuri and I. Koren, "New routing and compaction strategies for yield enhancement," in *IEEE International Workshop on Defect and Fault Tolerance in VLSI Systems*, 1992.
- [31] J. Fang, J.S.K Wong, K. Zhang, and P. Tang, "A new fast constraint graph generation algorithm for VLSI layout compaction," in *IEEE International Symposium on Circuits and Systems*, 1991.
- [32] U. Manber, *Introduction to Algorithms A Creative Approach*, Addison-Wesley Publishing Company Inc., 1989.
- [33] D. K. de Vries and P. L. C. Simon, "Calibration of open interconnect yield models," in *IEEE International Symposium on Defect and Fault Tolerance in VLSI systems (DFT'03)*, 2003.
- [34] Q. Su, S. Sinha, and C. Chiang, "A novel and flexible algorithmic framework for random yield improvement," patent pending, 2007.
- [35] S. Sinha and et al. "A novel and flexible algorithmic framework for random yield improvement," in *Proc. of International Symposium on Quality Electronic Design*, 2007.
- [36] C.N. Berglund, "Trends in systematic non-particle yield loss mechanisms and the implication for ic design," in *Proc. SPIE Optical Microlithography*, Feb. 2003, vol. 5040.
- [37] D. Flagello and et al. "Optimizing and enhancing optical systems to meet low k1 challenges," in *Proc. SPIE Optical Microlithography*, Feb. 2003, vol. 5040.
- [38] C. Pierrat and A. Wong, "The mef revisited: Low k1 effects versus mask topography effects," in *Proc. SPIE Optical Microlithography*, Feb. 2003, vol. 5040.
- [39] L. Melvin III, J. P. Shiely, M. Rieger, and B. Painter, "A methodology to calculate line-end correction feature performance as a function of reticle cost," in *Proc. SPIE Optical Microlithography*, Feb. 2003, vol. 5040.
- [40] C. Progler and G. Xiao, "Critical evaluation of photomask needs for competing 65-nm node ret options," in *Proc. SPIE Optical Microlithography*, Feb. 2003, vol. 5040.
- [41] A. K. Wong, *Resolution Enhancement Techniques in Optical Lithography*, SPIE Press, Washington, USA, 2001.
- [42] A. Kahng, X. Xu, and A. Zelikovsky, "Yield and cost driven fracturing for variable shape-beam mask writing," in *Proc. SPIE Optical Microlithography*, 2004, vol. 5567, pp. 360–371.
- [43] A. Kahng, X. Xu, and A. Zelikovsky, "Fast yield-driven fracture for variable shape-beam mask writing," in *Proc. SPIE Optical Microlithography*, 2006, vol. 6283.

- [44] N. Cobb, *Fast Optical and Process Proximity Correction Algorithms for Integrated Circuit Manufacturing*, Ph.D. thesis, University of California at Berkeley, 1998.
- [45] W. Xiong, M. Tsai, J. Zhang, and Z. Yu, "Direct: An efficient optimization scheme for mask generation using inverse lithography," in *NSTI Nanotech*, 2007.
- [46] J. Stirniman and M. Rieger, "Fast proximity correction with zone sampling," in *Proc. SPIE Optical Microlithography*, 1994, vol. 2197.
- [47] J. Stirniman and M. Rieger, "Quantifying proximity and related effects in advanced wafer processing," in *Proc. SPIE Optical Microlithography*, 1995, vol. 2440.
- [48] J. Stirniman and M. Rieger, "Spatial-filter models to describe ic lithographic behavior," in *Proc. SPIE Optical Microlithography*, 1997, vol. 3051.
- [49] N. Cobb and A. Zakhor, "Large area phase-shift mask design," in *Proc. SPIE Optical Microlithography*, 1994, vol. 2197.
- [50] N. Cobb and A. Zakhor, "Fast, low-complexity mask design," in *Proc. SPIE Optical Microlithography*, 1995, vol. 2440.
- [51] N. Cobb and A. Zakhor, "Fast sparse aerial image calculation for opc," in *Bacus Symposium on Photomask Technology*, 1995, vol. 1621.
- [52] K. Lucas and et al., "Process, design and optical proximity correction requirements for the 65 nm device generation," in *Proc. SPIE Optical Microlithography*, Feb. 2003, vol. 5040.
- [53] M. Reiger, j. Mayhew, and S. Panchapakesan, "Layout design methodologies for sub-wavelength manufacturing," in *Proc. of the Design Automation Conf.*, 2001, pp. 85–92.
- [54] C. Chiang, A. Kahng, S. Sinha, X. Xu, and A. Zelikovsky, "Fast and efficient bright-field aapsm conflict detection and correction," *IEEE Transactions on Computer-Aided Design of Integrated Circuits*, vol. 26, no. 1, pp. 115–127, Jan. 2007.
- [55] C. Chiang, A. Kahng, S. Sinha, and X. Xu, "Fast and efficient phase conflict detection and correction in standard-cell layouts," in *Proc. Intl. Conf. on Computer-Aided Design*, 2005, pp. 149–156.
- [56] C. Chiang, A. Kahng, S. Sinha, X. Xu, and A. Zelikovsky, "Bright-field aapsm conflict detection and correction," in *Proc. DATE: Design Automation and Test in Europe*, 2005, vol. 2, pp. 908–913.
- [57] V. Wiaux and et al., "Arf solutions for low-k1 back-end imaging," in *Proc. SPIE Optical Microlithography*, Feb. 2003, vol. 5040.
- [58] C. Mak, "The lithography expert: Off-axis illumination," in *Micro-Lithography World*, Aug. 2003.
- [59] T. Matsuo, A. Misaka, and M. Sasago, "Novel strong resolution enhancement technology with phase-shifting mask for logic gate pattern fabrication," in *Proc. SPIE Optical Microlithography*, Feb. 2003, vol. 5040.
- [60] S. Hsu and et al., "65nm full-chip implementation using double dipole lithography," in *Proc. SPIE Optical Microlithography*, Feb. 2003, vol. 5040.

- [61] D. Pan and M. Wong, "Manufacturability aware physical layout optimization," in *ICICDT*, May 2005.
- [62] M. Mukherjee, Z. Baum, J. Nickel, and T. Dunham, "Optical rule checking for proximity corrected mask shapes," in *Proc. SPIE Optical Microlithography*, Feb. 2003, vol. 5040.
- [63] T. Tsai and C. Chiang, "Lithography printability grading system in design stage," patent pending, 2007.
- [64] M. Tsai, D. Zhang, and T. Tang, "Modeling litho-constrained design layout," in *Proc. of the Design Automation Conf.*, 2007.
- [65] L. Liebman, "Layout impact of resolution enhancement techniques," in *Proc. of International Symposium on Physical Design*, 2003.
- [66] J. Mitra, P. Yu, and D. Z. Pan, "Radar:ret-aware detailed routing using fast lithography simulations," in *Proc. of the Design Automation Conf.*, June 2005, pp. 369–372.
- [67] L.-D. Huang and M. D. F. Wong, "Optical proximity correction (opc)-friendly maze routing," in *Proc. of the Design Automation Conf.*, June 2004, pp. 186–191.
- [68] S. Sinha and C. Chiang, "A range pattern definition of susceptibility of layout regions to fabrication issues," patent pending, Mar. 2006.
- [69] H. Yao, S. Sinha, C. Chiang, Y. Cai, and X.-L. Hong, "Efficient process-hotspot detection using range pattern matching," in *Proc. Intl. Conf. on Computer-Aided Design*, 2006, pp. 625 – 632.
- [70] R. Zhu and T. Takaoka, "A technique for two-dimensional pattern matching," in *Communication of ACM*, 1989, vol. 32, pp. 1110–1120.
- [71] R. A. Brualdi, *Introductory Combinatorics*, Prentice Hall, New York, 2004.
- [72] L. Borucki and et al., "Modeling planarization in chemical mechanical polishing," www.ima.umn.edu/modeling/mm02reports/mmrep1.pdf, June 2002.
- [73] T. E. Gbondo-Tugbawa, *Process Integration Issues of Low-Permiability Dielectrics with Cu for High-Performance Interconnects*, Ph.D. thesis, Stanford University, 1999.
- [74] T. P. Moffat, D. Wheeler, W. H. Huber, and D. Josell, "Superconformal electrodeposition of copper," *Electrochemical and Solid-State Letters*, vol. 4, pp. C26–C29, 2001.
- [75] D. Josell, D. Wheeler, W. H. Huber, J. E. Bonevich, and T. P. Moffat, "A simple equation for predicting superconformal electrodeposition in submicrometer trenches," *Journal of the Electrochemical Society*, vol. 148, pp. C767–C773, 2001.
- [76] Y. H. Im, M. O. Bloomfield, S. Sen, and T. S. Cale, "Modeling pattern density dependent bump formation in copper electrochemical deposition," *Electrochemical and Solid State Letters*, vol. 6, pp. C42–C46, 2003.
- [77] J. Luo, Q. Su, C. Chiang, and J. Kawa, "A layout dependent full-chip copper electroplating topography model," in *Proc. Intl. Conf. on Computer-Aided Design*, 2005, pp. 133–140.

- [78] Z. Stavreva, D. Zeidler, M. Plotner, G. Grasshoff, and K. Drescher, "Chemical-mechanical polishing of copper for interconnect formation," *Microelectronic Engineering*, vol. 33, pp. 249–257, 1997.
- [79] L. He, A. B. Kahng, K. Tam, and J. Xiong, "Design of ic interconnects with accurate modeling of cmp," in *Proc. SPIE Optical Microlithography*, 2005.
- [80] V. Mehrotra, *Modeling the Effects of Systematic Process Variation on Circuit Performance*, Ph.D. thesis, Dept. of EECS, MIT, Cambridge, MA, USA, 2001.
- [81] M. X. Yang, D. Mao, C. Yu, and et. al, "Sub-100nm interconnects using multistep plating," *Solid State Technology*, Oct. 2003.
- [82] J. Tower, A. Maznev, M. Gostein, and K. Otsubo, "Measurement of electroplated copper overburden for advanced process development and control," in *Advances in Chemical Mechanical Polishing, Material Research Society Spring Meeting*, 2004.
- [83] D. O. Ouma, *Modeling of Chemical Mechanical Polishing for Dielectric Planarization*, Ph.D. thesis, Dept. of EECS, MIT, Cambridge, MA, USA, 1998.
- [84] J. Luo and D. A. Dornfeld, *Integrated Modeling of Chemical Mechanical Planarization for Sub-Micron IC Fabrication: from Particle Scale to Feature, Die and Wafer Scales*, Springer-Verlag, Berlin, Germany, 2004.
- [85] T. E. Gbondo-Tugbawa, *Chip-scale Modeling of Pattern Dependencies in Copper Chemical Mechanical Polishing Processes*, Ph.D. thesis, Dept. of EECS, MIT, Cambridge, MA, USA, 2002.
- [86] R. Tian, D. Wong, and R. Boone, "Model-based dummy feature placement for oxide chemical-mechanical polishing manufacturability," *IEEE Transactions on Computer-Aided Design of Integrated Circuits*, vol. 20, no. 7, pp. 902–910, July 2001.
- [87] A. B. Kahng, G. Robins, A. Singh, and A. Zelikovsky, "New and exact filling algorithms for layout density control," in *Proc. Intl. Conf. on VLSI*, 1999.
- [88] Y. Chen, A. B. Kahng, G. Robins, and A. Zelikovsky, "Monte-carlo algorithms for layout density control," in *Proc. Asia and South Pacific Design Automation Conference*, 2000, pp. 523–528.
- [89] Y. Chen, A. B. Kahng, G. Robins, and A. Zelikovsky, "Practical iterated fill synthesis for cmp uniformity," in *Proc. of the Design Automation Conf.*, 2000, pp. 671–674.
- [90] X. Wang, C. Chiang, J. Kawa, and Q. Su, "Min-variance iterative method for fast smart dummy features density assignment in chemical-mechanical polishing," in *Proc. of International Symposium on Quality Electronic Design*, 2005, pp. 258 – 263.
- [91] B. Stine and et al., "The physical and electrical effects of metal-fill patterning practices for oxide chemical-mechanical polishing processes," in *Proc. of IEEE Electron Devices Meeting*, Mar. 1998, vol. 45, pp. 665–679.
- [92] A. B. Kahng, G. Robins, A. Singh, and A. Zelikovsky, "Filling algorithms and analyzes for layout density control," *IEEE Transactions on Computer-Aided Design of Integrated Circuits*, vol. 18, pp. 445–462, Apr. 1999.

- [93] W. Grobman, M. Thompson, R. Wang, C. Yuan, R. Tian, and E. Demircan, "Reticle enhancement technology: Implications and challenges for physical design," in *Proc. of the Design Automation Conf.*, 2001, pp. 73–78.
- [94] Y. Chen, A. B. Kahng, G. Robins, and A. Zelikovsky, "Monte carlo methods for chemical-mechanical planarization on multi-layer and dual-material models," in *Proc. SPIE Conf. Design and Process Integration for Microelectronic Manufacturing*, Mar. 2002.
- [95] A. B. Kahng, G. Robins, A. Singh, and A. Zelikovsky, "Area fill synthesis for uniform layout density," *IEEE Transactions on Computer-Aided Design of Integrated Circuits*, vol. 21, no. 10, pp. 1132–1147, Oct. 2002.
- [96] B. Stine and et al., "A closed-form analytic model for ild thickness variation in cmp processes," in *Proc. CMP-MIC Conference*, Mar. 2002.
- [97] D. Ouma, D. Boning, J. Chung, G. Shinn, L. Olsen, and J. Clark, "An integrated characterization and modeling methodology for cmp dielectric planarization," in *Proc. International Interconnect Technology Conference*, June 1998, pp. 67–69.
- [98] T. Yu, S. Cheda, J. Ko, M. Robertson, A. Dengi, and E. Travis, "A two dimensional low pass filter model for die-level topography variation resulting from chemical mechanical polishing of ild films," in *Proc. of IEEE Electron Devices Meeting*, Dec. 1999.
- [99] S. Sinha, J. Luo, and C. Chiang, "Dummy filling technique for improved planarization on chip surface topology," patent pending, Apr. 2006.
- [100] S. Sinha, J. Luo, and C. Chiang, "Model based layout pattern dependent metal filling algorithm for improved chip surface uniformity in copper process," in *Proc. Asia and South Pacific Design Automation Conference*, 2007, pp. 1–6.
- [101] S. Lakshminarayanan, P.J. Wright, and J. Pallinti, "Electrical characterization of the copper cmp process and derivation of metal layout rules," *IEEE Transaction on Semiconductor Manufacturing*, 2003.
- [102] J. Luo, Q. Su, and C. Chiang, "Simulating topography of a conductive material in a semiconductor wafer," patent pending, Nov. 2005.
- [103] H. Masuda, S. Ohkawa, A. Kurokawa, and A. Aoki, "Challenge: Variability characterization and modeling for 65-90 nm processes," in *Proc. Custom Integrated Circuits Conf.*, Sept. 2005.
- [104] H. Chang, V. Zolotov, and S. Narayan and C. Visweswariah, "Parameterized block-based statistical timing analysis with non-gaussian parameters, nonlinear delay functions," in *Proc. of the Design Automation Conf.*, 2005.
- [105] H. Masuda, S. Ohkawa, A. Kurokawa, and A. Aoki, "Challenge: Variability characterization and modeling for 65-90nm processes," in *Proc. Custom Integrated Circuits Conf.*, 2005.
- [106] H. Chang and S. S. Sapatnekar, "Statistical timing analysis considering spatial correlations using a single pert like traversal," in *Proc. Intl. Conf. on Computer-Aided Design*, 2003.

- [107] A. Agarwal, D. Blaauw, V. Zolotov, S. Sundareswaran, M. Zhao, K. Gala, , and R Panda, "Path-based statistical timing analysis considering inter- and intra-die correlations," in *ACM Intl. Workshop on Timing Issues in the Specification and Synthesis of Digital Systems*, 2002, pp. 16–21.
- [108] A. Agarwal, D. Blaauw, V. Zolotov, S. Sundareswaran, M. Zhao, K. Gala, and R Panda, "Statistical timing analysis considering spatial correlations," in *Proc. Asia and South Pacific Design Automation Conference*, Jan. 2003, pp. 271–276.
- [109] M. Berkelaar, "Statistical statistical delay calculation, a linear time method," in *ACM Intl. Workshop on Timing Issues in the Specification and Synthesis of Digital Systems*, Dec. 1997, pp. 15–24.
- [110] A. Devgan and C. V. Kashyap, "Block-based statistical timing analysis with uncertainty," in *Proc. Intl. Conf. on Computer-Aided Design*, Nov. 2003, pp. 607–614.
- [111] C. E. Clark, "The greatest of a finite set of random variables," in *Operational Research*, 1961, vol. 9, pp. 85–91.
- [112] J. Le, X. Li, and L. Pileggi, "Stac: Statistical timing analysis with correlation," in *Proc. of the Design Automation Conf.*, 2004.
- [113] C. Visweswariah, K. Ravindran, K. Kalafala, S.G. Walker, and S. Narayan, "First-order incremental block-based statistical timing analysis," in *Proc. of the Design Automation Conf.*, 2004.
- [114] S. Bhardwaj, P. Ghanta, and S. Vruthula, "A framework for statistical timing analysis using non-linear delay and slew models," in *Proc. Intl. Conf. on Computer-Aided Design*, 2006.
- [115] M. Orshansky, "Statistical design optimization techniques," in *Proc. DATE: Design Automation and Test in Europe*, 2006.
- [116] M. Mani, A. Devgan, and M. Orshansky, "An efficient algorithm for statistical minimization of total power under timing yield constraints," in *Proc. of the Design Automation Conf.*, 2005.
- [117] J. Kao, S. Narendra, and A. Chandrakasan, "Leakage reduction techniques," in *Proc. Intl. Conf. on Computer-Aided Design*, 2003.
- [118] B. Murphy, "Cost-size optima of monolithic integrated circuits," in *Proceedings of the IEEE*, 1964, pp. 1537–1545.
- [119] W. Ham, "Intrachip and spatial parametric integrity, an important part of ic process characterization," in *Proc. of IEEE Electron Devices Meeting*, 1977, pp. 406–309.
- [120] C. Berglund, "A unified yield model incorporating both defect and parametric effects," *IEEE Transaction on Semiconductor Manufacturing*, vol. 9, pp. 249–257, Aug. 1996.
- [121] C. Guardiani, N. Dragone, and P. McNamara, "Proactive design for manufacturing (dfm) for nanometer soc design," in *Proc. Custom Integrated Circuits Conf.*, 2004.
- [122] Q. Su and C. Chiang, "Hot-spot based yield prediction with consideration of correlations," patent pending, 2007.

- [123] J.Luo, S. Sinha, Q. Su, and C. Chiang, "Predicting ic manufacturing yield by considering both systematic and random intra-die variations," patent pending, Jan. 2006.
- [124] J. Luo, S. Sinha, Q. Su, J. Kawa, and C. Chiang, "An ic manufacturing yield model considering intra-die variations," in *Proc. of the Design Automation Conf.*, July 2006, pp. 749–754.
- [125] B. E. Stine, D. S. Boning, and J. E. Chung, "Analysis and decomposition of spatial variation in integrated circuit processes and devices," *IEEE Transaction on Semiconductor Manufacturing*, vol. 10, pp. 24–41, Feb. 1997.
- [126] A. R. Dalal, P. D. Franzon, and M. J. Lorenzetti, "A layout-driven yield predictor and fault generator for vlsi," *IEEE Transaction on Semiconductor Manufacturing*, vol. 6, pp. 77–82, 1993.
- [127] I. S. Wagner and I. Koren, "An interactive vlsi cad tool for yield estimation," *IEEE Transaction on Semiconductor Manufacturing*, vol. 8, pp. 130–138, 1995.
- [128] A. Genz, "Numerical computation of multivariate normal probabilities," *Journal of Computational and Graphical Statistics*, vol. 1, pp. 141–149, 1992.
- [129] J. P. Cain and C. J. Spanos, "Electrical linewidth metrology for systematic cd variation characterization and causal analysis," in *Proc. SPIE Optical Microlithography*, 2003, pp. 350–361.
- [130] R. Tian, X. Tang, and D. F. Wong, "Dummy feature placement for chemical-mechanical polishing uniformity in a shallow trench isolation process," *IEEE Transactions on Computer-Aided Design of Integrated Circuits*, vol. 21, pp. 63–71, 2002.

Index

- Attenuated phase-shift mask (APSM), 70, 71, 73, 74, 78, 80
- Chemical mechanical polishing (CMP), 3, 17, 75, 99–148, 200, 201, 202, 204, 212, 214–216, 219, 234
- Critical area (CA), 18, 22–26, 31, 34, 35, 36–39, 41–42, 232, 233
- Critical dimension (CD), 7, 22, 55, 57, 64, 155, 158, 212, 236
- Critical path method (CPM), 171–172, 181
- Design for manufacturability (DFM), 1–3, 5, 11–12, 13–14, 16, 17–19
- Design for yield (DFY), 1–3, 11–12, 13–14, 16, 17, 19, 53, 81, 227–228, 229–231, 239, 242
- Double dipole lithography (DDL), 73–74
- Dual Damascene process, 99–101
- Electronic design automation (EDA), 2, 12, 15, 17, 19, 200–201, 211–215, 229–231, 236, 237
- Electroplating (ECP), 102–109, 115–116, 119, 121, 139–147, 150
- Intellectual Property (IP), 199
- Inter-level dielectric (ILD), 4, 100, 101, 125–128, 233–234
- Line edge roughness (LER), 5, 152, 155–156, 168, 226
- The linear programming method (LPM), 127, 129, 135–136
- Lithography rule check (LRC), 75–78, 232, 235
- Mask error enhancement factor (MEEF), 69–70
- Metal fill (dummy filling)
 model based metal fill, 139–140, 164, 226
 Rule based metal fill, 125–126
- Numerical aperture (NA), 6–8, 54–55, 56, 58, 70, 73, 83, 105, 227
- Off axis illumination (OAI), 8, 70, 71–73, 74, 237
- Open critical area (Open CA), 22, 27, 31–34, 41–44, 45, 47–49, 50, 233
- Optical proximity correction (OPC), 8–9, 43, 46, 59–63, 73–74, 75, 78, 80, 228–229, 231–233, 235–237
- Parametric yield, 151, 166–168
- Phase shift mask (PSM), 8–9, 58, 65–69
- Probability density function (PDF), 178, 181, 185, 217
- Random defects, 21–51
- Range pattern, 85–95
- Range pattern matching (RPM), 85–86, 88–92, 94
- Rayleigh equations
 depth of focus (DOF), 6, 55, 56
 resolution (R), 6, 55
- Resolution enhancement techniques (RET), 8–9, 55–59, 63, 71, 73, 74, 75–76, 79–84, 236
- Short critical area (Short CA), 22, 27–31, 37, 41–42, 43–47, 49, 50–51
- Static timing analysis (STA), 170–172, 175–176, 177, 182
- Statistical static timing analysis (SSTA), 171, 175–176, 180–181, 183, 185, 187, 192

Sub-resolution assist feature (SRAF), 8, 34,
63–65, 236
Systematic yield, 53–96

Technology computer-aided design (TCAD), 11,
12, 13–14, 17, 204, 229, 231, 239

Variability, 13, 14, 75, 84, 126, 151–164, 168,
170, 172–173, 175, 178, 186–187, 195,
211, 240

Yield prediction, 195–226

About the Author

Charles Ching-Liu Chiang received his Bachelor degrees from the Department of Political Science, Tunghai University at Taichung, Taiwan in 1980, and Department of Computer Science, New Mexico State University, Las Cruces, New Mexico, USA in 1986. Then he had his Masters and Ph.D. degree from the Department of Electrical Engineering and Computer Science, Northwestern University, Illinois, USA in 1988 and 1991, respectively.

After working at IBM and EDA companies for 10 years, he joined the Advanced Technology Group at Synopsys, Inc. in 2001. His research interests include routing, placement, floorplan, and signal integrity. His main research focus is now on design for manufacturability (DFM).

Dr. Chiang has been a Senior Member of IEEE since 1998. He received the Superior Design Recognition award and the ADAL award from IBM Rochester in 1993 and 1994, respectively. He has served on the Technical Program Committee of ICCAD from 2004 to 2007, on that of Field Programming Logic (FPL) from 2002 to 2003, and of ASP-DAC in 2007. He is Synopsys Top 15 Inventor Award recipient in 2005 and 2006. He also is the first runner up of 2006 Synopsys Distinguished Inventor Award. He has published more than 50 technical papers and filed 13 US patents.

About the Authors

Jamil Kawa received his B.S. degree, EE in 1977 and his M.S. Degree, EE in 1978 from the University of Michigan at Ann Arbor. He also received an M.B.A. in 1988 from the University of Santa Clara. Mr. Kawa has worked as a circuit designer and as a circuit design manager at National Semiconductor, VLSI technology (Phillips), Actel, and Chips and Technologies (Intel). He is currently managing director of R&D at the Advanced Technology Group of Synopsys. He has served on the TPC of several IEEE conferences including DAC, ICCD, and CICC where he currently heads the custom and low power sub-committee. Mr. Kawa has 3 patents and over 18 publications.